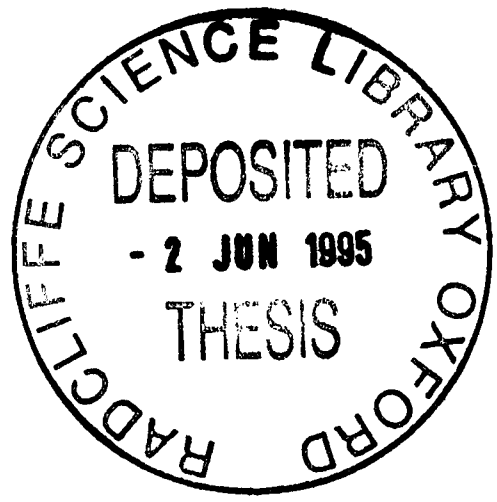
Nuclear Structure Studies involving polarised Iodine, Samarium and Europium: Experimental Techniques and Theoretical Models

Young Koh
St. Edmund Hall



A thesis submitted in partial fulfilment of the requirements
for the degree of Doctor of Philosophy
in the University of Oxford

Michaelmas Term 1994

To

My Parents,
my wife (Ji Yeon)
and
my sons(Chan Hee, Keon Hee)

Nuclear Structure Studies involving polarised Iodine, Samarium and Europium: Experimental Techniques and Theoretical Models

Young Koh
St. Edmund Hall

A thesis submitted in partial fulfilment of the requirements
for the degree of Doctor of Philosophy
in the University of Oxford
Michaelmas Term 1994

Abstract

Low Temperature Nuclear Orientation (LTNO) is an important technique in the study of nuclei far from stability. The theory of LTNO and its application to the measurement of static nuclear moments and other quantities of spectroscopic interest are reviewed.

The off-line facility at Oxford was used to study the decay of $^{133}I \rightarrow ^{133}Xe$ and $^{135}I \rightarrow ^{135}Xe$. ^{133}I having $Z = 53$ and $N = 80$ has three protons above the closed shell Z=50 and two neutrons holes in $N = 82$ shell, while ^{135}I has fully closed neutron shell since it has $N = 82$, and they are of considerable theoretical interest since a wide variety of the theoretical nuclear models may be used to describe the observed levels close to the stable double closed shell structure. Another aim is to search for the nuclear magnetic dipole moment of the ground state of ^{135}I. Nuclear orientation of ^{133}IFe and ^{135}IFe enabled the mixing ratios of several transitions in the decay scheme of ^{133}I and ^{135}I to be determined. From temperature dependence for ^{135}I, the nuclear magnetic moment of ^{135}I has been deduced. Also temperature dependence for ^{133}I, analysed using a simple model, gave value for the magnetic hyperfine field that differed from previous published values. The method of combining nuclear orientation with NMR has become a very popular technique in recent years for determining nuclear magnetic dipole moments very precisely. The purpose of the NMR/ON experiment was to measure the hyperfine field with greater precision and to get some idea of the proportion of nuclei subject to it.

Light Eu and Sm nuclei have attracted attention as systems with the number of protons right below the Z=64 subshell gap and the number of neutrons approaching N=82 major shell closure. Odd-proton, odd-neutron and odd-odd nuclei near the A=140 region have been investigated in the framework of the particle-triaxial rotor model. Main attention has been paid to explanation of experimental magnetic dipole and electric quadrupole moments of ground and isomeric states. Model predictions for deformation parameters of $^{136-142}Sm$ even-even cores have been extracted.

Acknowledgements

I would like to thank to Professor R. Cowley and Dr. J.Baker who allowed me to use the Clarendon Laboratory's facilities , where most of the experiment data in this thesis was produced, and to Professor R.Cashmore of the Nuclear Physics department for allowing me to use all of its facilities, and Dr. P.Hodgson who kindly loaned me material from his lectures.

I would like to express my appreciation of the patient supervision and guidance given to me during my three years at Oxford by my supervisor Dr N.J.Stone, and special thanks go to his wife, Dr Irena Stone who has given me assistance and encouragement on many occasions.

Also I would like to express my thanks to Professor D.H.Davis, Professor T.W.Jones of University College London, Dr. D.N.Tovee and Dr. M.Forshaw for many things.

I wish also to thank my good mates David , Andrew, Peter and Vivian. Because of them I never tired to come to the lab, whatever the hour !!! I will miss our extended tea time discussions about topics ranging from the national lottery to sometimes physics even !!!

There are still so many people I want to thank, not least Dr. M.G.Booth, Dr. D.Zakoucky, Dr. I.Oliveira, Dr. P.Harding and Dr. M.Veskovic, of course.

Then there are many of my Korean friends I would also like mention, but I am not going to do so, because if I missed one of them out I would be in trouble !. However I would like to mention only some of them: J.DO.Mun(now Dr. Mun), Dr. J.Dong.Lee, Mr. J.Whan.Song, H.Jong.Kim, Y.Doo.Cho, S.Hoon.Kim, H.Gu.Kang, J.Dae.Kim and M.Ho.Lee, Professor K.Tae.Chang - I always enjoyed their company. I would like to thanks to Dr. P.H.Han and Mr.W.H.Kwak for their caress and kindness.

I really would like to thank Dr. M.Month of Fermi lab, the U.S. D.O.E. for their financial support, all the staff of the Bates accelerator centre at M.I.T., and the people at Harvard University for their help and warm welcome. My thanks also go to Professor Fogelberg and Mr. R.Jacobson of Studsvik neutron research laboratory in Sweden for their warm reception during my stay there. Furthermore, I would like to thank the Scott fund and the college travel fund for their assistance.

My special thanks to my mother-in-law for her invaluable help to make me possible to write this thesis without any distraction despite her own very difficult situation.

My parents deserve very special thanks, without their support I could not possibly be here, and I would like to thank all of my family for their support. Specially I would like thanks to my mother for everything.

Finally, it is impossible to imagine how this thesis would have been completed without the help, support, nagging and extreme patience that my wife, Ji Yeon, has provided, and also my two sons (Chan Hee and Keon Hee) who make me laugh so often.

Contents

Chapter One Low Temperature Nuclear Orientation 1

1.1 Introduction 1
1.2 Quantum Mechanical formalism of Nuclear Orientation 2
1.2.1 Density matrix formalism 2
1.2.2 Statistical tensors 4
1.2.3 Nuclear states 5
1.2.4 Orientation parameters 6
1.2.5 Magnetic dipole orientation 7
1.2.6 Electric quadrupole orientation 9
1.3 Observation of g-radiation from oriented nuclei 9
1.3.1 Efficiency matrices and tensors 9
1.3.2 Time evolution of the density matrix 10
1.3.3 Multipole expansion of the radiation field 11
1.3.4 Final statistical tensors 12
1.3.5 Angular Distribution Function 15
1.3.6 De-orientation Coefficients 16
1.4 Extranuclear contributions 19
1.4.1 Solid angle correction factors 19
1.4.2 Fraction in Good sites 20
1.5 Hyperfine Interactions 21
1.5.1 The magnetic Hyperfine Interaction 21
1.5.2 NMR-ON in Ferromagnetic Hosts 22
1.6 Ion implantation 24
1.6.1 Dilute alloys for hyperfine interaction studies 24
1.6.2 Principles of implantation 25
1.7 Nuclear spin-lattice relaxation 27
References 32

Chapter Two Experimental Apparatus and Techniques 34

2.1 The $^{3}He/^{4}He$ dilution refrigeration 34
2.1.1 Introduction 34
2.1.2 Properties of liquid $^{3}He/^{4}He$ 34
2.1.4 Continuous operation below 10mK 38
2.1.5 Sample preparation and orientation 39
2.1.6 NMR/ON on $^{60}CoFe$ 41
2.2 The cooling power test 42
2.3 Top loading Dilution unit 43
2.4 Nuclear Thermometry 44
2.5 Data Acquisition system 46
2.6 Germanium Detectors 48
References 51

Chapter Three Data Analysis 52

3.1 Introduction 52
3.2 Spectrum Analysis 52
3.2.1 Markers and Calibration 52
3.2.2 Peak fitting routines 55
3.2.3 Normalised Anisotropies 58
3.2.4 Dead time correction 58
3.2.5 Half-life correction 60
3.2.6 Extraction of the A_2 and A_4 terms of the angular distribution 60
References 62

Chapter Four Nuclear Orientation decay studies of ^{133}I and ^{135}I 63

4.1 Introduction 63
4.2 Experimental details 64
4.3 Nuclear Orientation decay studies of ^{133}IFe 64
4.3.1 Introduction 64
4.3.2 Temperature dependence results 66
4.4 NMR/ON on ^{133}I 69
4.4.1 Experiment 69
4.4.2 Results 70
4.5 Nuclear Orientation decay studies of ^{135}I 70
4.5.1 Introduction 70
4.5.2 Temperature dependence results 71
4.6 Discussion 96
References 104

Chapter Five The Theory of Nuclear Models 107

5.1 Introduction 106
5.2 The Collective model 106
5.2.1 Deformation parameters 106
5.2.2 Surface oscillations about a spherical shape 108
5.2.3 Rotations and Vibrations for deformed shapes 110
5.2.3.1 The Bohr Hamiltonian 110
5.2.3.2. The axially symmetric case 114
5.2.3.3 The Asymmetric Rotor 117
5.3 The nuclear shell model 119
5.4. One-particle shell model of nuclei 121
5.4.1 Spins and parities of the ground states of nuclei 121
5.4.2. Single-particle magnetic dipole moments of nuclei 122
5.4.3. Single-particle electric quadrupole moments of nuclei 124
5.5 Deformed shell model 127
5.5.1. The Anisotropic harmonic oscillator 127
5.5.2. Nilsson Hamiltonian 129
5.6 The particle-plus-rotor model 130
5.6.1 Introduction 130
5.6.2 The axially symmetric case 133

5.6.3 The triaxial-rotor-plus-particle model 136
5.6.4 Electromagnectic Properties 137
References 139

Chapter Six Particle-triaxial-rotor calculation of light odd-A and odd- odd Eu and Sm nuclei (137≤A≤143) 142

6.1 Introduction 141
6.2 Calculation procedure and parameters of the model. 143
6.2.1.Odd-A nuclei 143
6.2.2. Odd-odd nuclei 145
6.3 Results 147
6.3.1 Negative parity states in 137-143Eu nuclei. 147
6.3.2 Negative parity states in 137-143Sm nuclei. 150
6.3.3 Positive parity states in 141-143Eu 153
6.3.4 Positive parity states in 139-143Sm 159
6.3.5 The odd-odd 138Eu nucleus. 162
6.4 Conclusions 165

Appendix A 169
Appendix B 173
Appendix C 176
Appendix D 178

Chapter One

Low Temperature Nuclear Orientation

The experiments described in this thesis involve the use of the techniques of low temperature nuclear orientation (LTNO), and nuclear magnetic resonance of oriented nuclei (NMR/ON). These techniques are used to study the hyperfine interactions of radioactive isotopes and the angular distribution of their decay products.

In this chapter, nuclear orientation formalism is discussed and the basic concepts of hyperfine interactions and nuclear magnetic resonance of oriented nuclei are reviewed. A brief review of nuclear spin-lattice relaxation is also given in chapter 1. In chapter 2, the experimental techniques, apparatus, and the method of sample preparation are described. The data analysis techniques and programs that are used in this thesis are described in chapter 3. Then, in chapter 4, the experimental results for ^{133}I and ^{135}I are presented. In chapter 5, the nuclear shell model, deformed shell model, collective model, particle-rotor model and particle plus triaxial-rotor model are discussed. Theoretical calculations of rare earth isotopes $^{137,139,141,143}Eu$ and $^{137,139,141}Sm$ are presented in chapter 6.

1.1 Introduction

In general the probability of emission of electromagnetic radiation from a decaying nucleus depends on the angle ϑ and φ between the expectation value $\langle \boldsymbol{J} \rangle$ of the total angular momentum vector $\boldsymbol{J}$ of the nucleus and the direction $\boldsymbol{K}$ in which the photons are observed. In the case of axial symmetry, the probability depends only on the polar angle ϑ.

If the individual $\boldsymbol{J}$ vectors of the nuclei are randomly oriented (i.e. $\langle \boldsymbol{J} \rangle = 0$) the observed radiation will be isotropic in space. In order to observe an anisotropic radiation pattern the angular momentum vectors of the nuclei should point towards some preferred direction so that $\langle \boldsymbol{J} \rangle \neq 0$ and the intensity and polarisation properties of the radiation will then depend on the angle between the orientation axis and the direction of observation $\boldsymbol{K}$. If the polarisation properties

are not observed in an experiment, the distribution is called the directional distribution $W(\vartheta)$ of the radiation and if they are observed, then it is called the polarisation distribution $W(\vartheta, \boldsymbol{P})$. The term angular distribution is used to refer to both directional or polarisation distributions and as used in this thesis refers to the directional distribution $W(\vartheta)$ since only directional distributions are studied.

An ensembled of nuclei can be oriented by three different means;

(i) extranuclear static and dynamic orientation (e.g. optical pumping)

(ii) orientation by observing a preceding emitted radiation with well defined direction and polarisation properties (e.g. angular correlations)

(iii) orientation by absorption of nuclear radiation of well defined direction and polarisation (e.g. Coulomb excitation)

The method of Low Temperature Nuclear Orientation (LTNO) falls into the first of the above categories since it involves the "brute-force" orientation of the static electric or magnetic moments of the nucleus with an external magnetic field. At very low temperature the energetically lower states, m-states in the case of magnetic interactions, must be unequally populated according to the Boltzmann distribution, and so their splitting should be at least comparable to the available thermal energy kT.

The remaining sections of this chapter will describe how the angular distribution of γ-radiation is related to various nuclear properties of interest and to the orienting interaction.

1.2 Quantum Mechanical formalism of Nuclear Orientation

1.2.1 Density matrix formalism

If every value of a complete set of commuting observables has been observed a physical system is then said to be in a pure state which can be described by a complete set of quantum numbers.

In an angular distribution measurement only ensemble averages are observed and the quantum mechanical description of such mixed states requires incoherent superpositions of pure quantum states. Such an ensemble can be described by a density matrix[9].

A pure state can be described by the state vector

$$|\Psi\rangle = \sum_{\phi} |\phi\rangle\langle\phi|\Psi\rangle$$

and (1.1)

$$\langle\Psi| = \sum_{\phi} \langle\Psi|\phi\rangle\langle\phi|$$

The expectation value of any operator $\hat{O}$ in the state $|\Psi\rangle$ has the form

$$\langle\Psi|\hat{O}|\Psi\rangle = \sum_{\phi,\phi'} \langle\Psi|\phi'\rangle\langle\phi'|\hat{O}|\phi\rangle\langle\phi|\Psi\rangle \tag{1.2}$$

A mixed state consisting of a number of independent nuclei may be described by an incoherent superposition of the possible pure states $|\Psi_n\rangle$, weighted with factors $g(n)$ which are proportional to the number of nuclei in the nth state and have the normalisation condition $\sum g(n)=1$. The expectation value of the operator $\hat{O}$ in such a mixed state is therefore given by the weighted average of the expectation values $\langle\Psi|\hat{O}|\Psi\rangle$

$$\langle\hat{O}\rangle = \sum_{n=1}^{N} g(n)\langle\Psi_n|\hat{O}|\Psi_n\rangle \tag{1.3}$$

Substituting (1.2) into (1.3) with the normalisation condition gives

$$\langle\hat{O}\rangle = \sum_{n,\phi,\phi'} \langle\phi|\Psi_n\rangle g(n)\langle\Psi_n|\phi'\rangle\langle\phi'|\hat{O}|\phi\rangle \tag{1.4}$$

or in terms of the density matrix ρ with matrix elements

$$\langle\hat{O}\rangle = \sum_{\phi,\phi'} \langle\phi|\hat{\rho}|\phi'\rangle\langle\phi'|\hat{O}|\phi\rangle \tag{1.5}$$

where

$$\langle\phi|\hat{\rho}|\phi'\rangle = \sum_{n=1}^{N} \langle\phi|\Psi_n\rangle g(n)\langle\Psi_n|\phi'\rangle \tag{1.6}$$

The density matrix can be regarded as a representation of the density operator

$$\hat{\rho} = \sum_{n=1}^{N} |\Psi_n\rangle g(n)\langle\Psi_n| \tag{1.7}$$

in the basis $|\phi\rangle$ and the density operator completely describes the state of the

ensemble.

1.2.2 Statistical tensors

In angular distribution problems the symmetries of the elements of the ensemble with respect to rotations are of interest. We choose the basis states $|\phi\rangle$ to be the eigenstates $|\eta jm\rangle$ of the angular momentum operator J^2 and its projection onto the z-axis, J_z. The symbol η represents the other quantum numbers which are needed to specify the states uniquely. The matrix elements of the density operator in this representation are

$$\hat{\rho}(\eta_1 j_1 \eta_2 j_2) = \langle \eta_1 j_1 m_1 | \hat{\rho} | \eta_1 j_1 m_1 \rangle = \sum_n \langle \eta_1 j_1 m_1 | \Psi_n \rangle g(n) \langle \Psi_n | \eta_2 j_2 m_2 \rangle \qquad (1.8)$$

and the angular momentum states $|jm\rangle$ transform under a rotation of the quantization axis from $S(xyz)$ to $\bar{S}(\bar{x}\bar{y}\bar{z})$ by

$$|jm\rangle_S = \sum_{\bar{m}} |jm\rangle_S D^{j*}_{m\bar{m}}(S \to \bar{S}) \qquad (1.9)$$

where the D-matrices[2] are elements of rotation matrices. The elements of the density matrix transform under the same rotation according to

$$\langle j_1 m_1 | \hat{\rho} | j_2 m_2 \rangle_{\bar{S}} = \sum_{m_1 m_2} D^{j_1}_{m_1 \bar{m}}(S \to \bar{S}) \langle j_1 m_1 | \hat{\rho} | j_2 m_2 \rangle_S D^{j_2 *}_{m_2 \bar{m}_2}(S \to \bar{S}) \qquad (1.10)$$

Making use of the Clebsh-Gorden series of D-matrices, equation (1.10) is

$$\begin{aligned} \langle j_1 m_1 | \hat{\rho} | j_2 m_2 \rangle_{\bar{S}} = \sum_{m_1 m_2 \lambda} \langle j_1 m_1 | \hat{\rho} | j_2 m_2 \rangle_S (-1)^{m_2 - \bar{m}_2} (2\lambda + 1) \begin{pmatrix} j_1 & j_2 & \lambda \\ m_1 & -m_2 & q \end{pmatrix} \\ \times \begin{pmatrix} j_1 & j_2 & \lambda \\ \bar{m}_1 & -\bar{m}_2 & \bar{q} \end{pmatrix} D^{\lambda *}_{q\bar{q}}(S \to \bar{S}) \end{aligned} \qquad (1.11)$$

After multiplying both sides of equation (1.11) by the factor

$$(-1)^{j_1 + \bar{m}_2} (2\lambda + 1)^{1/2} \begin{pmatrix} j_1 & j_2 & \lambda \\ \bar{m}_1 & -\bar{m}_2 & \bar{q} \end{pmatrix}$$

and summing over $\overline{m}_1$ and $\overline{m}_2$, keeping $\overline{q}$ fixed, the following equation is obtained because of the orthogonality relations of the Wigner 3-j symbols

$$\begin{aligned}&\left\{\sum_{\overline{m}_1}\langle j_1 m_1|\hat{\rho}|j_2 m_2\rangle_{\overline{S}}(-1)^{j_2+\overline{m}_2}(2\lambda+1)^{1/2}\begin{pmatrix} j_2 & j_1 & \lambda \\ -\overline{m}_2 & \overline{m}_1 & \overline{q}\end{pmatrix}\right\}\\ &=\sum_q\left\{\sum_{m_1}\langle j_1 m_1|\hat{\rho}|j_2 m_2\rangle_S(-1)^{j_2+m_2}(2\lambda+1)^{1/2}\begin{pmatrix} j_2 & j_1 & \lambda \\ -m_2 & m_1 & q\end{pmatrix}\right\}D^{\lambda *}_{q\overline{q}}(S\to\overline{S})\end{aligned} \tag{1.12}$$

The linear combinations of the elements of $\rho(j_1 j_2)$ enclosed in brackets transform like spherical tensors of rank λ. It is, therefore, more convenient to use their linear combinations than the matrix elements themselves in studying the rotational properties of an ensemble. Thus the statistical tensors $\rho^{\lambda}_q(j_1 j_2)$ can be defined as

$$\rho^{\lambda}_q(j_1 j_2)=\sum_{m_1}\langle j_1 m_1|\hat{\rho}|j_2 m_2\rangle(-1)^{j_2+m_2}(2\lambda+1)^{1/2}\begin{pmatrix} j_2 & j_1 & \lambda \\ -m_2 & m_1 & q\end{pmatrix} \tag{1.13}$$

with the normalisation condition $\rho^0_0(j_1 j_2)=(2j_1+1)^{-1/2}\delta_{j_1 j_2}$. The statistical tensors are linear combinations of the matrix elements of the density matrix and contain the same information as the density matrix. (1.13) represents the vector relationship $\lambda=\boldsymbol{J}_2-\boldsymbol{J}_1$, and so the rank of the statistical tensor is limited to the range $|j_2-j_1|$ to j_2+j_1.

1.2.3 Nuclear states

Consider a cylindrical symmetric ensemble of nuclei of spin I. The density operator (1.7) for such an ensemble may be expressed in the form

$$\hat{\rho}=\sum_{m=-I}^{I}|Im\rangle g(n)\langle Im| \tag{1.14}$$

where the eigenstates $|Im\rangle$ of the nuclear spin operator I_z are defined with respect to the symmetry z-axis. In the case of LTNO an axis is defined by the direction of an external magnetic field. The corresponding density matrix $\rho(I)$ in the angular momentum representation $|I\overline{m}\rangle$ chosen with respect to some representation-coordinate system $\overline{S}$ is

$$\langle I\bar{m}|\hat{\rho}|I\bar{m}'\rangle = \sum_{m} |I\bar{m}\rangle g(m) \langle Im|I\bar{m}'\rangle \tag{1.15}$$

If $S = \bar{S}$ the density matrix is diagonal

$$\langle Im|\hat{\rho}|Im'\rangle = g(m)\delta_{mm'} \tag{1.16}$$

where $g(m)$ is the relative population of state $|Im\rangle$ in the ensemble.

An ensemble of randomly orientated nuclei with spin I at room temperature must be invariant under three dimensional rotations since it has no fixed orientation axis in space in general. Thus the only non-vanishing statistical tensor is

$$\rho_0^0(I) = (2I+1)^{-½}$$

with corresponding density matrix

$$\rho(I) = (2I+1)^{-1} \boldsymbol{I}$$

1.2.4 Orientation parameters

When an ensemble of nuclei is oriented, unequal populations of the $|Im\rangle$ states occur. The statistical tensors are invariant with respect to rotation through an arbitrary angle α about the axis of cylindrical symmetry which is defined by the applied external magnetic field. This rotation can be represented by

$$D^{\lambda *}_{q\bar{q}}(\alpha, 0, 0) = e^{-iq\alpha}\delta_{q\bar{q}} \tag{1.17}$$

and leads to the condition

$$\rho^{\lambda}_{\bar{q}}(I) = \sum_{q} \rho^{\lambda}_{q}(I) D^{\lambda *}_{q\bar{q}}(\alpha, 0, 0) = \rho^{\lambda}_{q}(I) e^{-iq\alpha}\delta_{q\bar{q}} = \rho^{\lambda}_{q}(I) \tag{1.18}$$

Using $\rho^{\lambda}_{0}(I) = \rho^{\lambda}_{0}(j_1 j_2)$ if $j_1 = j_2 = I$, the corresponding statistical tensors can be found by substituting equation (1.16) into (1.13)

$$\rho^{\lambda}_{0}(I) = \sum_{m} (-1)^{I+m} (2\lambda+1)^{½} \begin{pmatrix} I & I & \lambda \\ -m & m & 0 \end{pmatrix} g(m) \tag{1.19}$$

Hence, to describe an axially symmetric ensemble the non-vanishing statistical

tensors have q=0. Thus, the orientation parameters $B_\lambda(I)$ can be described by the statistical tensors with cylindrical symmetry and have the form[3]

$$B_\lambda(I) = (2\lambda+1)^{1/2}\rho_0^\lambda(I) = \sum_m (-1)^{I+m}\left[(2I+1)(2\lambda+1)\right]^{1/2}\begin{pmatrix} I & I & \lambda \\ -m & m & 0 \end{pmatrix} g(m) \quad (1.20)$$

where $g(m)$ is the population of the nuclear substate $|m\rangle$ and is given by a Boltzmann distribution

$$g(m) = Ae^{-E(m)/k_BT}$$

where $E(m)$ is the energy splitting of the sublevels, T is the temperature in Kelvin and A is a normalisation constant.

1.2.5 Magnetic dipole orientation

In the case of interaction of the static nuclear magnetic dipole moment with an applied magnetic field the magnetic energy of the nuclear m-levels is

$$E(m) = -\frac{\mu B}{I}m \quad (1.21)$$

where μ and I are the nuclear magnetic moment and spin respectively and B is the applied magnetic field. The sublevel populations in thermodynamic equilibrium are then given by

$$g(m) = \langle m|\hat{\rho}|m\rangle = \frac{e^{m\beta}}{\sum_m e^{m\beta}} \quad (1.22)$$

with

$$\beta = \frac{\mu B}{Ik_BT}$$

Hence the statistical terms in this case are given by

$$\rho_0^\lambda(I) = (2I+1)^{-1/2}B_\lambda(I) = \left\{\sum_m e^{m\beta}\right\}^{-1}\sum_m (-1)^{I+m}(2\lambda+1)^{1/2}\begin{pmatrix} I & I & \lambda \\ -m & m & 0 \end{pmatrix} e^{m\beta} \quad (1.23)$$

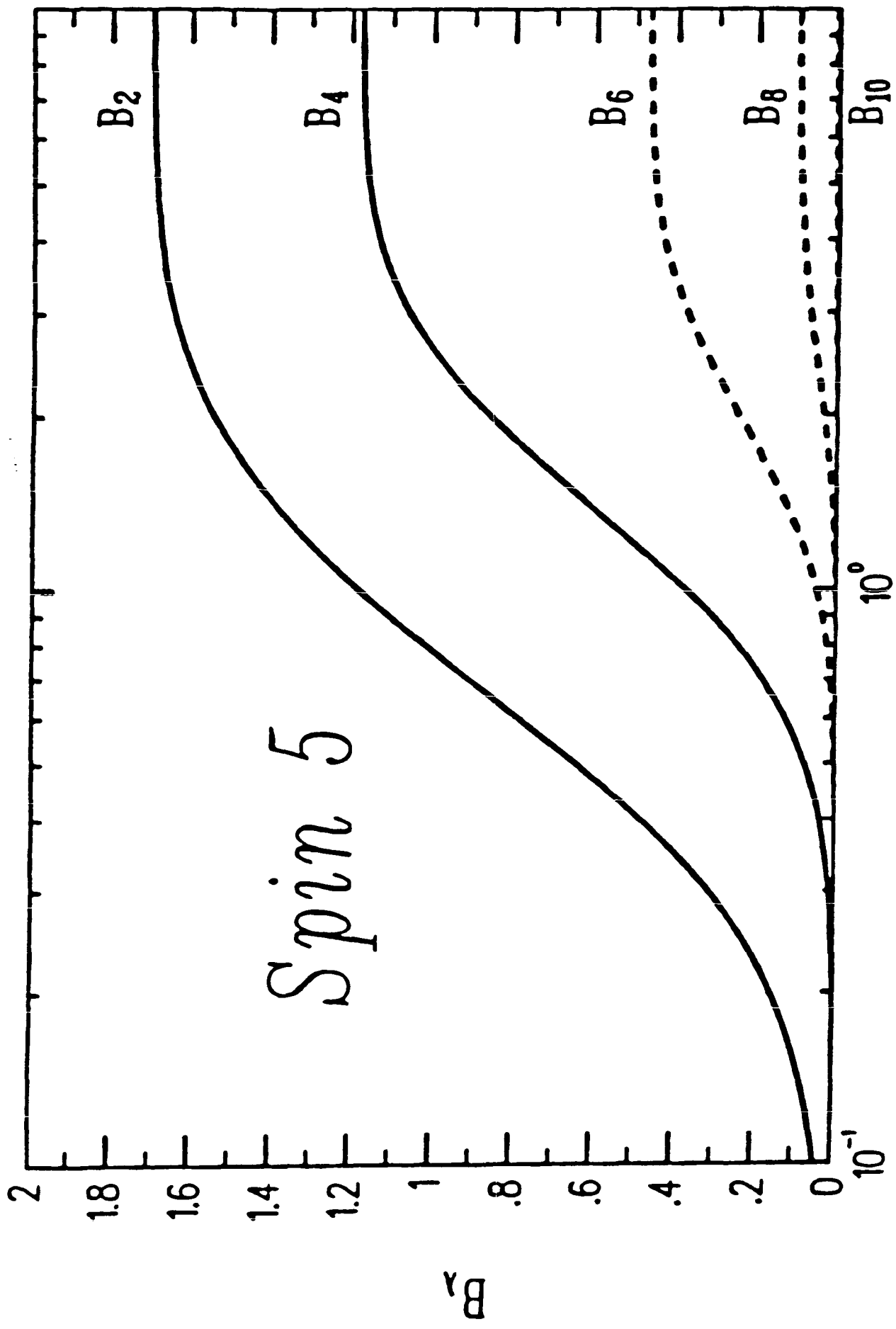


Fig 1.1 Orientation coefficients B_λ for spin 5 and $\frac{T_{int}}{T_L} = \frac{E(m)}{k_B T}$ [36]

1.2.6 Electric quadrupole orientation

The lowest order electric hyperfine interaction which gives rise to a splitting of the $|Im\rangle$ states, and can hence produces nuclear orientation, is the electric quadrupole interaction. This is zero for substitutional implantation to occupying substitutional sites of cubic symmetry. Since Fe is a cubic lattice and, consequently, the electric field gradient (EFG) of implants in Fe is small, the electric hyperfine interaction for IFe will be neglected in this thesis.

1.3 Observation of γ-radiation from oriented nuclei

1.3.1 Efficiency matrices and tensors

The probability $P(\phi_n)$ of finding a system described by the density matrix ρ in a pure state $|\phi_n\rangle$ is

$$P(\phi_n) = \langle \phi_n | \hat{\rho} | \phi_n \rangle \tag{1.24}$$

If the ensemble is observed by a measuring device which responds to the different pure states $|\phi_n\rangle$ of the ensemble with efficiency ε_n then the result of a measurement with the ensemble in an arbitrary state is

$$W = \sum_n \varepsilon_n P(\phi_n) = \sum_n \varepsilon_n \langle \phi_n | \hat{\rho} | \phi_n \rangle \tag{1.25}$$

where ε is a diagonal matrix with elements ε_n. The efficiency operator is defined as

$$\hat{\varepsilon} = \sum_n |\phi_n\rangle \varepsilon(n) \langle \phi_n| \tag{1.26}$$

Then the efficiency matrix can be described in some representation basis $|m\rangle$ as

$$\langle m|\hat{\varepsilon}|m'\rangle = \sum_n \langle m|\phi_n\rangle \varepsilon(n) \langle \phi_n|m'\rangle \tag{1.27}$$

Therefore, the efficiency tensor can be constructed according to (1.13)

$$\varepsilon^{\lambda}_{q(j_1 j_2)} = \sum_{m_1} \langle j_1 m_1 | \hat{\varepsilon} | j_2 m_2 \rangle (-1)^{j_1 + m_2} (2\lambda + 1)^{\frac{1}{2}} \begin{pmatrix} j_2 & j_1 & \lambda \\ -m_2 & m_1 & q \end{pmatrix} \tag{1.28}$$

The average results of measurements made with a measuring device characterised by the efficiency tensor $\varepsilon^{\lambda}_{q(j_1 j_2)}$ on an ensemble in the state given by the density matrix ρ is given by

$$W = \sum_{m,m'} \langle m|\hat{\varepsilon}|m'\rangle\langle m'|\hat{\rho}|m\rangle$$

or (1.29)

$$W = \sum_{j_1 j_2 \lambda q} \varepsilon^{\lambda^+}_q (j_1 j_2) \rho^{\lambda}_q (j_1 j_2)$$

where $\rho^{\lambda}_q (j_1 j_2)$ is the statistical tensor.

In the case of LTNO, measurements are made on the emitted radiation that give no information on a final nuclear state. In such cases, summation over the final unobserved states is implied and the measurement is represented by a unit efficiency matrix. If these states have angular momentum j_i then the efficiency tensor corresponding to the unit efficiency matrix with proper normalisation is

$$\varepsilon^{\lambda}_{q(j_1 j_2)} = (2j_1 + 1)^{1/2} \delta_{j_1 j_2} \delta_{\lambda} \delta_{q0} \quad (1.30)$$

1.3.2 Time evolution of the density matrix

For an ensemble of nuclei decaying by g-ray emission with a definite momentum $\boldsymbol{p}$ to a final nuclear state I_f, the final state density matrix can be represented as $\langle \boldsymbol{P}\tau I_f m_f | \hat{\rho} | I_f m'_f \boldsymbol{P}\tau' \rangle$. The time dependent Schrödinger equation is

$$i\frac{\partial}{\partial t}|\boldsymbol{\Psi}(t)\rangle = \hat{H}|\boldsymbol{\Psi}(t)\rangle \quad (1.31)$$

with a general solution

$$|\boldsymbol{\Psi}(t)\rangle = \hat{U}(t, t_0)|\boldsymbol{\Psi}(t_0)\rangle \quad (1.32)$$

where $\hat{U}(t, t_0)$ is the unitary time-evolution operator. The time evolution of the density operator, then, is given by

$$\hat{\rho}(t) = \sum_n \hat{U}(t, t_0)|\Psi_n(t_0)\rangle g(n)\langle\Psi_n(t_0)|U^+(t, t_0) = U(t, t_0)\hat{\rho}(t_0)U^+(t, t_0) \quad (1.33)$$

Therefore

$$i\frac{\partial}{\partial t}\hat{\rho}(t)=\left[H,\hat{\rho}(t)\right] \tag{1.34}$$

For decaying nuclei, the total Hamiltonian of the system is

$$H = H_0 + H_{int} \tag{1.35}$$

where H_0 is the Hamiltonian for the stationary states and H_{int} induces transitions between the eigenstates of H_0.

1.3.3 Multipole expansion of the radiation field

In semi-classical theory of the interaction of radiation with matter the Hamiltonian H_{int} is given by

$$H_{int} = -\int \boldsymbol{J}_N(\boldsymbol{r}')\boldsymbol{A}(\boldsymbol{r}',t)dv' \tag{1.36}$$

where $\boldsymbol{J}_N(\boldsymbol{r}')$ is the nuclear current density and $\boldsymbol{A}(\boldsymbol{r}',t)$ is the vector field potential describing the electromagnetic radiation. The vector field potential $\boldsymbol{A}(\boldsymbol{r}',t)$ can be decomposed into a series of multipole fields $\boldsymbol{A}^{\pi}_{LM}$ where π denotes the character of the electric/magnetic radiation and L, M are the total angular momentum and its z-component respectively. The multipolarity of the emitted radiation is 2^L and the parity is $(-1)^L$ for electric and $(-1)^{L+1}$ for magnetic transitions. For transition between an initial state $|I_i m_i\rangle$ of parity π_i, to a final state $|I_f m_f\rangle$ of parity π_f the emission matrix element is given by[5]

$$\begin{aligned}\left\langle I_f m_f \left| \boldsymbol{J}_N \boldsymbol{A}^{\pi *}_{LM} \right| I_i m_i \right\rangle &= (-1)^{L-M+1}\left\langle I_f m_f \left| \boldsymbol{J}_N \boldsymbol{A}^{\pi}_{L-M} \right| I_i m_i \right\rangle \\ &= (-1)^{L-M+1+I_f-m_f}\begin{pmatrix} I_f & L & I_i \\ -m_f & -M & m_i \end{pmatrix}\times\left\langle I_f \left\| \boldsymbol{J}_N \boldsymbol{A}^{\pi}_{L} \right\| I_i \right\rangle\end{aligned} \tag{1.37}$$

The Wigner 3-j symbol illustrates the conservation of angular momentum for electromagnetic transitions and parity conservation in the γ-decay process leads to the selection rules

$$\begin{aligned} &|I_f - I_i| \le L \le I_f + I_i \qquad (L>0) \\ &m_i = M + m_f \\ &\pi_i \pi_f = \begin{cases} (-1)^L & \text{for electric} \\ (-1)^{L+1} & \text{for magnetic} \end{cases} \end{aligned} \tag{1.38}$$

The condition $(L>0)$ implies that more than one multipolarity can contribute to a transition. For radiation of a fixed character, the probability of emission of radiation $\pi(L+1)$ is retarded over that for $\pi(L)$ by a factor of $\left(\lambda/a\right)^2$ where λ is the wavelength of the radiation and $a = 1.07A^{1/3} fm$ where A is a mass number. In addition, radiation $M(L)$ is retarded over $E(L)$ by a factor of $\left(\upsilon/c\right)^2$, where υ is the mean velocity of the nucleon in the nucleus and this factor is typically $\sim 10^{-2}$. In general, $M(L)$ and $E(L+1)$ can compete but it is rare for more than two multipolarities to contribute significantly to the electromagnetic decay of a nuclear state. The relative amplitude of two competing multipole orders L, L' can be described by the mixing ratio δ that is defined as the ratio of the reduced matrix elements.

$$\delta\left(\frac{\pi' L'}{\pi L}\right) = \frac{\left\langle I_f \left\| J_N A_{L'}^{\pi'} \right\| I_i \right\rangle}{\left\langle I_f \left\| J_N A_{L}^{\pi} \right\| I_i \right\rangle} \tag{1.39}$$

where the Steffen phase convention[5] is used.

1.3.4 Final statistical tensors

The unitary transformation of the Heisenberg representation, which means the wave function does not change with time but the operators corresponding to physical quantities change, gives the operators

$$\hat{H}(t) = exp\left(\frac{iH_0 t}{\hbar}\right) H_{int}\, exp\left(-\frac{iH_0 t}{\hbar}\right) \tag{1.40}$$

and

$$\hat{U}(t, t_0) = exp\left(\frac{iH_0 t}{\hbar}\right) U(t, t_0)\, exp\left(-\frac{iH_0 t}{\hbar}\right) \tag{1.41}$$

Expanding (1.34)

$$\hat{U}(t,t_0)=1-i\int_{t_0}^{t}\hat{H}(t')dt'+\cdots \tag{1.42}$$

Combining the second term in (1.42) with (1.32) and using first-order perturbation theory leads to

$$\begin{aligned}\left\langle \boldsymbol{P}\tau I_f m_f\left|\hat{\rho}(t)\right|I_f m_f'\boldsymbol{P}\tau'\right\rangle &=\left\langle \boldsymbol{P}\tau I_f m_f\left|exp\left(-\frac{iH_0t}{\hbar}\right)\right.\right\{\int_0^t exp\left(\frac{iH_0t'}{\hbar}\right)H_{int}\\ &\times\ exp\left(-\frac{iH_0t'}{\hbar}\right)dt'\left.\right\}\times\hat{\rho}(0)\left\{\int_0^t exp\left(\frac{iH_0t'}{\hbar}\right)H_{int}\,exp\left(-\frac{iH_0t'}{\hbar}\right)dt'\right\}\\ &\times exp\left(\frac{iH_0t}{\hbar}\right)\left|I_f m_f'\boldsymbol{P}\tau'\right\rangle\\ &=\left\langle \boldsymbol{P}\tau I_f m_f\left|H_{int}\right|I_i m_i\right\rangle\left\langle I_i m_i\left|\hat{\rho}(0)\right|I_i m_i'\right\rangle\\ &\times\left\langle I_i m_i\left|H_{int}^{+}\right|I_f m_f'\boldsymbol{P}\tau'\right\rangle\left|\int_0^t exp\,i\left(\omega+\frac{E_f-E_i}{\hbar}\right)t'dt'\right|^2\end{aligned} \tag{1.43}$$

The conservation of energy implies that the integral is only appreciably different from zero if $\hbar\omega=\hbar\omega_0=E_i-E_f$. In the Heisenberg representation the transition matrix elements of (1.41) are the time independent

$$\begin{aligned}\left\langle \boldsymbol{P}\tau I_f m_f\left|H_{int}\right|I_i m_i\right\rangle &=\int\left\langle I_f m_f\left|\boldsymbol{j}(\boldsymbol{r}')\right|I_i m_i\right\rangle\boldsymbol{A}(\boldsymbol{r}')dv'\\ &=\sqrt{\frac{2\pi}{L^3\omega}}\left\langle I_f m_f\left|\int\boldsymbol{j}(\boldsymbol{r}')\boldsymbol{e}_\tau^{*}exp\left(-i\frac{pr'}{\hbar}\right)dv'\right|I_i m_i\right\rangle\end{aligned} \tag{1.44}$$

Since the time dependence of $\boldsymbol{j}(\boldsymbol{r}',t)$, namely $exp\,i\left(E_f-E_i/\hbar\right)t$, is exactly compensated by that of $\boldsymbol{A}(\boldsymbol{r}',t)$, namely $exp(i\omega t)$. By integrating over ω and multiplying by the density of states, the last term in (1.43) results in a factor $L^3\omega_0^2 td\Omega/(2\pi)^2$ in the case of $t<<\left(\lambda_\gamma\right)^{-1}$, where λ_γ is the total transition probability. Otherwise t should be replaced by the radioactive decay factor $\left(1-exp\left(-\lambda_\gamma t\right)\right)\lambda_\gamma^{-1}$. Thus the elements of the final state density matrix are

$$\left\langle \boldsymbol{P}\tau I_f m_f \left|\hat{\rho}(t)\right| I_f m_f' \boldsymbol{P}\tau' \right\rangle = \frac{d\Omega}{2\pi}\omega \frac{\left(1-exp\left(-\lambda_\gamma t\right)\right)}{\lambda_\gamma} \left\langle I_f m_f \left| \int \boldsymbol{j}(\boldsymbol{r}') \boldsymbol{e}_\tau^* exp\left(-i\frac{\boldsymbol{pr}'}{\hbar}\right)\right.\right. \tag{1.45}$$
$$\times dv' \left| I_i m_i \right\rangle \times \left\langle I_i m_i \left| \hat{\rho}(0) \right| I_i m_i' \right\rangle \left\langle I_i m_i' \left| \int \boldsymbol{j}(\boldsymbol{r}') \boldsymbol{e}_\tau exp\left(i\frac{\boldsymbol{pr}'}{\hbar}\right) dv' \right| I_f m_f' \right\rangle$$

Introducing the absolute transition amplitudes $\gamma\left(\pi L, I_i \to I_f\right)^{(4)}$ which are proportional to the multipole expansions of (1.44), and again using Clebsh-Gordon series for the product of two D-matrices, gives

$$\left\langle \boldsymbol{P}\tau I_f m_f \left|\hat{\rho}(\infty)\right| I_f m_f' \boldsymbol{P}\tau' \right\rangle = \frac{d\Omega}{8\pi\lambda_\gamma} \sum_{mm'} \left(2I_i+1\right) \sum_{LL'\lambda} \left[(2L+1)(2L'+1)\right]^{\frac{1}{2}}$$
$$\times (2\lambda+1) \begin{pmatrix} I_f & L & I_i \\ m_f & M & -m_i \end{pmatrix} \begin{pmatrix} I_f & L' & I_i \\ m_f' & M' & -m_i' \end{pmatrix} \tag{1.46}$$
$$\times \begin{pmatrix} L & L' & \lambda \\ M & -M' & q \end{pmatrix} \begin{pmatrix} L & L' & \lambda \\ \tau & -\tau' & \mu \end{pmatrix} \left\langle I_i m_i \left| \hat{\rho}(0) \right| I_i m_i' \right\rangle$$

for times $\lambda_\gamma t \sim \infty$. The diagonal elements of this final state density matrix expression give the absolute probability that a photon with helicity τ is emitted into the solid angle $d\Omega$ in the direction $\boldsymbol{p}$ from the initial state $\rho(0)$ to form the final nuclear state $\left|I_f m_f\right\rangle$.

From this expression the final statistical tensor $\rho_{q_f}^{\lambda_f}\left(I_f, \boldsymbol{p}\right)$ may be constructed in accordance with (1.15). This is a 2x2 matrix in the helicity space τ, where four elements in $\left|Im\right\rangle$ space are

$$\left\langle \tau \left| \rho_{q_f}^{\lambda_f}\left(I_f, \boldsymbol{p}\right) \right| \tau' \right\rangle = \frac{d\Omega}{8\pi\lambda_\gamma} \sum_{\lambda_i \lambda_q q LL'} (-1)^{\lambda_i - q_i} \left(2\lambda+1\right)^{\frac{1}{2}} \left(\frac{2I_i+1}{2I_f+1}\right)^{\frac{1}{2}}$$
$$\times \begin{pmatrix} \lambda_f & \lambda & \lambda_i \\ q_f & q & -q_i \end{pmatrix} \rho_{q_i}^{\lambda_i}\left(I_i\right) D_{q\mu}^{\lambda *}\left(e_z \to \boldsymbol{k}\right) \left[\gamma(EL) + \tau\gamma(ML)\right]$$
$$\times \left[\gamma^*(EL') + \tau'\gamma^*(ML')\right] \frac{\begin{pmatrix} L & L' & \lambda \\ \tau & -\tau' & \mu \end{pmatrix}}{\begin{pmatrix} L & L' & \lambda \\ 1 & -1 & 0 \end{pmatrix}} F_\lambda^{\lambda_f \lambda_i}\left(LL' I_f I_i\right) \tag{1.47}$$

where the $F_\lambda^{\lambda_f \lambda_i}\left(LL' I_f I_i\right)$ are the generalised F-coefficient

$$F_{\lambda}^{\lambda_f\lambda_i}\left(LL'I_fI_i\right)=(-1)^{L'+\lambda_f+\lambda_i+1}\Big[(2I_i+1)(2I_f+1)(2L+1)(2L'+1)$$
$$\times(2\lambda_i+1)(2\lambda_f+1)(2\lambda+1)\Big]^{\frac{1}{2}}\begin{pmatrix}L & L' & \lambda\\ 1 & -1 & 0\end{pmatrix}\begin{Bmatrix}I_f & L & I_i\\ I_f & L' & I_i\\ \lambda_f & \lambda & \lambda_i\end{Bmatrix} \tag{1.48}$$

If one of the states is random, i.e. either λ_i or λ_f is zero, then the generalised F coefficients reduce to the ordinary F coefficients $F\left(LL'I_fI_i\right)$

$$F_{\lambda}^{0\lambda_i}\left(LL'I_fI_i\right)=F_{\lambda}\left(LL'I_fI_i\right)\delta_{\lambda_i\lambda}$$
$$F_{\lambda}^{\lambda_f 0}\left(LL'I_fI_i\right)=(-1)^{L+L'}F_{\lambda}\left(LL'I_fI_i\right)\delta_{\lambda_f\lambda} \tag{1.49}$$

1.3.5 Angular Distribution Function

The statistical tensor can be replaced by the orientation parameter (1.24) and the efficiency tensor is given by (1.36) since the final nuclear state is not observed. The electromagnetic photon are observed in a direction $\boldsymbol{k}$ with a detector described by the efficiency matrix ε. The probability of detection of the photon is then given by equation (1.35)

$$W(\boldsymbol{k})=\sum_{\tau\tau'}\langle\tau|\rho_0^0\left(I_f\right)|\tau'\rangle\langle\tau'|\varepsilon|\tau\rangle\left(2I_f+1\right)^{\frac{1}{2}} \tag{1.50}$$

where $\langle\tau|\rho_0^0\left(I_f\right)|\tau'\rangle$ is given by (1.40) with $\lambda_f=q_f=0$.

The detection of circularly polarised radiation with helicity τ by an ideal detector with efficiency matrix (1.39), that is $\tau=\tau'$ is[2]

$$W(\vartheta,\tau)=\frac{d\Omega}{8\pi\lambda_{\gamma}}\sum_{\lambda_q LL'}\tau^{\lambda+L+L'}B_{\lambda}\left(I_i\right)F_{\lambda}\left(LL'I_fI_i\right)$$
$$\times\left[\gamma(EL)+\tau\gamma(ML)\right]\left[\gamma^*(EL')+\tau\gamma^*(ML')\right]P_{\lambda}(\cos\vartheta) \tag{1.51}$$

where $P_{\lambda}(\cos\vartheta)=\left(D_{00}^{\lambda*}(\varphi,\vartheta,0)\right)$ are Legendre polynomials. The angles ϑ, φ are the polar angles of the observation direction $\boldsymbol{k}$ with respect to Cartesian coordinate system. With the parity selection rules for electromagnetic transitions, the circular polarisation distribution is obtained as

$$W(\vartheta,\tau)=\frac{d\Omega}{8\pi}\sum_{\lambda}\tau^{\lambda}B_{\lambda}(I_i)A_{\lambda}P_{\lambda}(cos\,\vartheta) \tag{1.52}$$

The directional distribution of γ-radiation emitted from an axially symmetric oriented source is then obtained by summing (1.52) over helicity states which yields a factor of 2 if $\lambda=$ even or 0 if $\lambda=$ odd. Thus the odd-λ terms vanish and (1.52) can be rewritten as

$$W(\vartheta,\tau)=\frac{d\Omega}{4\pi}\sum_{\lambda}B_{\lambda}(I_i)A_{\lambda}P_{\lambda}(cos\,\vartheta) \tag{1.53}$$

The coefficients A_{λ} are called the angular distribution coefficients and are given by[4]

$$A_{\lambda}=\frac{\sum_{LL'\pi\pi'}F_{\lambda}(LL'I_fI_i)\gamma(\pi L)\gamma^{*}(\pi'L')}{\sum_{L\pi}|\gamma(\pi L)|^2}=\frac{\sum_{LL'\pi\pi'}F_{\lambda}(LL'I_fI_i)\gamma(\pi L)\gamma^{*}(\pi'L')}{\lambda_{\gamma}} \tag{1.54}$$

with the normalisation $A_0=1$.

The angular distribution coefficients for two mixed multipoles L and $L'=L+1$ with amplitude mixing ratio $\delta=\gamma(\pi'L')/\gamma(\pi L)$ are then given in terms of the F-coefficients as[1]

$$A_{\lambda}=\frac{F_{\lambda}(LLI_fI_i)+2\delta F_{\lambda}(LL'I_fI_i)+\delta^2F_{\lambda}(L'L'I_fI_i)}{1+\delta^2} \tag{1.55}$$

1.3.6 De-orientation Coefficients

Generally in a LTNO experiment the radiation that is under investigation is not emitted directly from the oriented state I_0, but rather from a state I_i which is reached from I_0 through one or more unobserved intervening transitions. Hence it is necessary to integrate the final state statistical tensor over solid angle for each unobserved quantum. The final state statistical tensor $\rho_{q_n}^{\lambda_n}(I_n)$ that describes the ensemble after the emission of an unobserved $\gamma-$radiation γ_n from an initial state $\rho_{q_{n-1}}^{\lambda_{n-1}}(I_{n-1})$ is given by[4]

$$\rho_{q_n}^{\lambda_n}(I_n)=U_{\lambda_n}(\gamma_n)\rho_{q_{n-1}}^{\lambda_{n-1}}(I_{n-1})\delta_{\lambda_n\lambda_{n-1}}\delta_{q_nq_{n-1}} \tag{1.56}$$

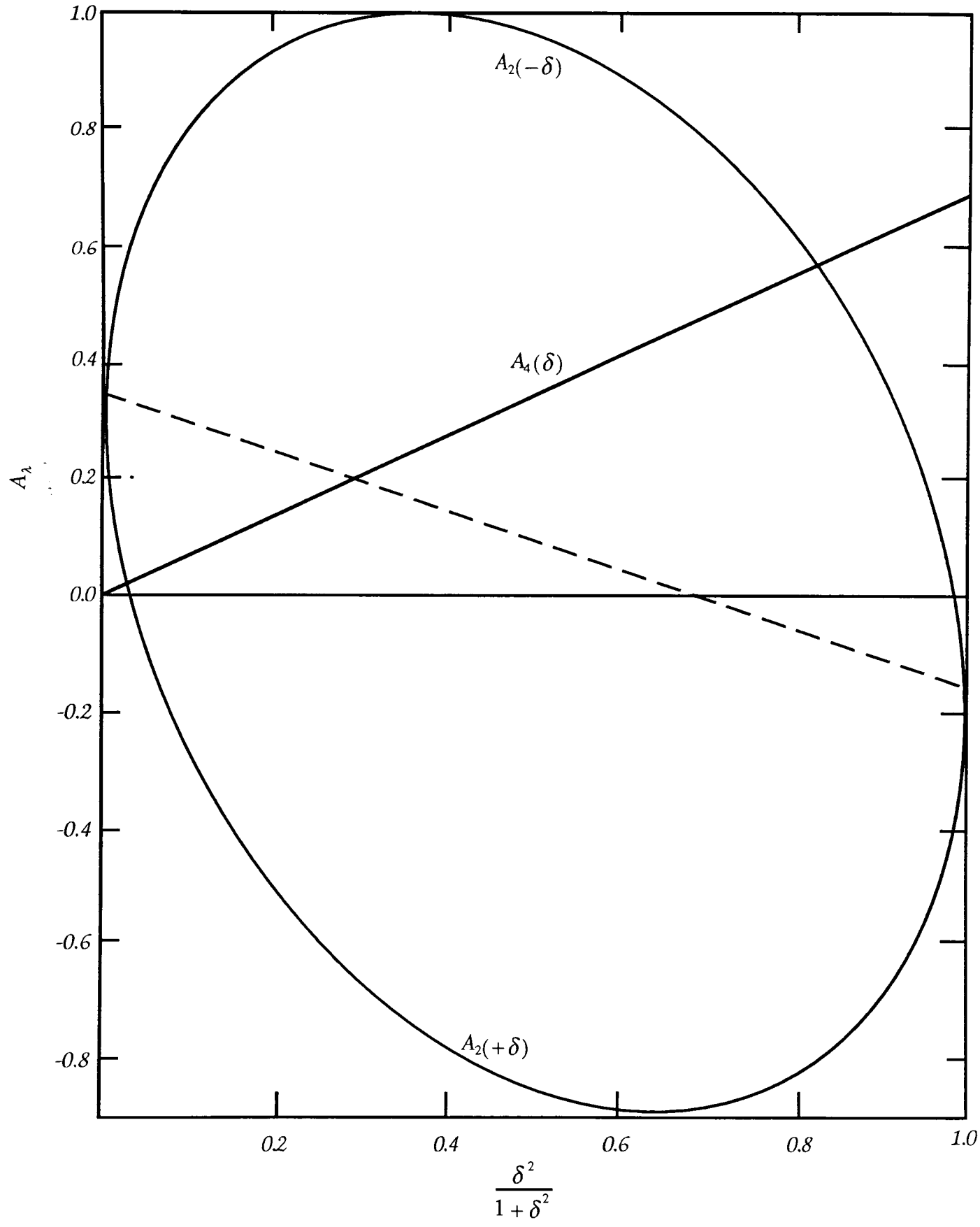


Fig 1.2 Angular Distribution Coefficients for λ=2,4 for a mixed L=1, L=2 transition with $I_i = 3$ and $I_f = 2$. The dashed line shows the division between positive and negative δ values.

where[3] $$U_\lambda = \sum_{L\pi} U_\lambda(I_i I_f L)\left|\gamma(\pi L)\right|^2 \Big/ \sum_{L\pi}\left|\gamma(\pi L)\right|^2$$

or in terms of δ[1] $$U_\lambda = \left\{U_\lambda(I_i I_f L) + \delta^2 U_\lambda(I_i I_f L')\right\}\Big/\left(1+\delta^2\right)$$

with the de-orientation factor U_λ is defined by[3]

$$U_\lambda(I_i I_f L) = (-1)^{I_i+I_f+\lambda+L}\left[(2I_i+1)(2I_f+1)\right]^{\frac{1}{2}}\begin{Bmatrix} I_i & I_i & \lambda \\ I_f & I_f & L \end{Bmatrix} \tag{1.57}$$

The de-orientation factors are normalised to unity, $U_0 = 1$. Hence for a cascade of n unobserved photons the final state statistical tensor is

$$\rho_q^\lambda(I) = U_\lambda(\gamma_n)U_\lambda(\gamma_{n-1})\cdots U_\lambda(\gamma_1)\rho_q^\lambda(I_0) \tag{1.58}$$

If there are many different branches which connect I_0 with I_i, the total U_λ is just the sum of the U_λ for each branch, weighted by the intensity w_n of that branch

$$U_\lambda(I_0\cdots I_i) = \sum_n w_n\left[U_\lambda(I_0\cdots I_i)\right]_n \tag{1.59}$$

The branching intensities are normalised so that $\sum w_n = 1$ and w_n represents the total intensity of each populating transition, e.g. including electron conversion. The directional distribution of a γ–radiation γ_{n+1} that is emitted from a state I_n, formed by the emission of an observed quantum from an axially oriented state I_0, as measure with polarization insensitive detectors, may be written[1]

$$W(\vartheta) = 1 + \sum_{\lambda=even} B_\lambda(I_0)U_\lambda A_\lambda Q_\lambda P_\lambda(\cos\vartheta) \tag{1.60}$$

$$B_\lambda(I_0) = 0 \qquad \text{if } \lambda > 2I_0$$

$$U_\lambda(I_i I_f L) = 0 \qquad \text{if } \lambda > 2I_i \text{ or } \lambda > 2I_f$$

$$A_\lambda(I_i I_f LL') = 0 \qquad \text{if } \lambda > L+L' \text{ or } \lambda > 2I_i$$

Since the γ–transition probability greatly reduces as the multipole order increments, transitions with $L > 2$ are experimentally rare. Thus in most cases and in the absence of further selection rules the directional distribution can be written as[1]

$$W(\vartheta) = 1 + B_2U_2A_2Q_2P_2(\cos\vartheta) + B_4U_4A_4Q_4P_4(\cos\vartheta) \tag{1.61}$$

where Q_λ is the solid angle correction factor described below. Then the axial and equatorial anisotropies can be defined as

$$W(0) = 1 + B_2(I_0)U_2A_2Q_2 + B_4(I_0)U_4A_4Q_4$$
$$W\left(\frac{\pi}{2}\right) = 1 - \frac{1}{2}B_2(I_0)U_2A_2Q_2 + \frac{3}{8}B_4(I_0)U_4A_4Q_4 \qquad (1.62)$$

1.4 Extranuclear contributions

1.4.1 Solid angle correction factors

Due to the finite solid angle subtended by the detector, the observed angular distribution will differ somewhat from the ideal distribution expected for point detectors. When the angular distribution is measured using a real detector the efficiency of the detector must be integrated over $d\Omega$. Consider the case of an axially symmetric detector centred along the radius vector with polar angle ϑ_0. In the polar angle co-ordinate system the useful absorption of γ−radiation is proportional to $\left(1-e^{-\tau(\gamma)x(\beta)}\right)$ where $x(\beta)$ is the path length through the active volume of the detector and $\tau(\gamma)$ is the full energy absorption coefficient for the detector material.

The measured directional distribution

$$\overline{W}(\vartheta) = \frac{\int W(\vartheta)\left\{1-e^{-\tau(\gamma)x(\beta)}\right\}d\Omega}{\left\{1-e^{-\tau(\gamma)x(\beta)}\right\}d\Omega} \qquad (1.63)$$

Taking out the angular terms from (1.70)

$$I_\lambda = \int P_\lambda\left(cos(\vartheta_0+\beta)\right)\left\{1-e^{-\tau(\gamma)x(\beta)}\right\}sin\beta d\beta d\varphi \qquad (1.64)$$

An expansion of $P_\lambda(cos\,\vartheta)$ about ϑ_0 using the spherical harmonic addition theorem[6] is

$$P_\lambda\left(cos(\vartheta_0+\beta)\right) = P_\lambda(cos\,\vartheta)P_\lambda(cos\beta)+\cdots \qquad (1.65)$$

where β is the angle between ϑ_0 and ϑ ($\vartheta=\vartheta_0+\beta$). Since these do not contribute to the integration over φ (1.64) reduces to

$$I_\lambda = 2\pi P_\lambda(\cos\vartheta_0)\int_0^{\Delta\beta} P_\lambda(\cos\beta)\left\{1-e^{-\tau(\gamma)x(\beta)}\right\}\sin\beta d\beta \qquad (1.66)$$

The solid angle correction factors Q_λ that can be calculated from the detector-source geometry for coaxial and closed end coaxial detectors may be defined as

$$Q_\lambda P_\lambda(\cos\vartheta_0) = \frac{I_\lambda}{I_0} \qquad (1.67)$$

1.4.2 Fraction in Good sites

The samples used in this work are prepared by direct implantation of radioactive ions from an isotope separator into a Fe-host matrix. Therefore, to interpret the static LTNO data, the parameters B_{hf} and f should be known. Beeler[7] shows that the entrant nucleus produces a series of primary lattice recoils which can go on to initiate independent subcascades. The local temperatures produced in these cascades can reach 5000K and last for about 10ps[8] during which time a degree of self-annealing can occur. As a result this often leaves the implant in an undamaged area of the lattice, with residual vacancies and interstitials several atomic spacings away. If the host and implant are compatible in size and electronegativity the ions come to rest in a substitutional site and experience the full hyperfine field. If the implant ions are larger than the host ions and/or have very different electronegativity the ions may come to rest in non-substitutional sites. The ions can also stop in a damaged lattice site or in a region of the lattice which is distorted by the presence of impurities or dislocations. In these cases the implanted ions can experience a negligibly small field or an intermediate field. The critical dose above which the fraction in substitutional sites falls rapidly has been established experimentally to be $\sim 10^{14}$ ions cm^{-2}[37]. In a typical LTNO sample the dose is only $\sim 10^{11} - 10^{13}$ ions cm^{-2}. The actual fraction of nuclei which occupy substitutional sites and the nature of any alternative sites depends on their solubility in the host lattice.

A simple but satisfactory model is the two site model in which a fraction f of the implanted ions are in the substitutional sites with full magnetic hyperfine field B_{hf} and the remainder (1- f) are in a second site with zero field. It has been used widely for both soluble and insoluble cases. Such a site may correspond to imperfectly implanted activity on the surface of the lattice as well as in the distorted sites referred to above. Therefore, (1.61) can be rewritten as

$$W(\vartheta) = 1 + f\{B_2 U_2 A_2 Q_2 P_2(\cos\vartheta) + B_4 U_4 A_4 Q_4 P_4(\cos\vartheta)\} \qquad (1.68)$$

A useful experimental check on the model is to examine the attenuations of B_2 and B_4 terms independently wherever possible.

1.5 Hyperfine Interactions

1.5.1 The magnetic Hyperfine Interaction

The orbital motion of the electrons of a free atom leads to an electronic current density $\boldsymbol{J}_e dr$ at a point $\boldsymbol{r}$ in a coordinate system centred at the nucleus. This current density will produce a magnetic field at the nucleus given by Ampere's law as

$$\boldsymbol{B}d\tau = \frac{\mu_0}{4\pi}\frac{\boldsymbol{r}\times\boldsymbol{J}_e}{r^3}d\tau \qquad (1.69)$$

Writing $\boldsymbol{J}_e d\tau = \boldsymbol{V}dq$, where $\boldsymbol{V}$ is the velocity of the charge element dq and noting that the electronic angular momentum is $\boldsymbol{l} = m_e\boldsymbol{r}\times\boldsymbol{V}$ gives

$$\boldsymbol{B}_{l_i} = -\frac{\mu_0}{4\pi}2\mu_B \boldsymbol{l}_i \left\langle r_{l_i}^{-3}\right\rangle \qquad (1.70)$$

Summing over i, the contributions from closed subshells disappear and in the L-S coupling limit

$$\boldsymbol{B}_L = -\frac{\mu_0}{4\pi}2\mu_B \boldsymbol{L}\left\langle r_e^{-3}\right\rangle \qquad (1.71)$$

The electron spin will also give rise to a magnetic field and this contribution should be evaluated separately inside and outside the nucleus. Electrons outside the nucleus give rise to a simple dipole sum field

$$\boldsymbol{B}_S = -\frac{\mu_0}{4\pi}g_S\mu_B\sum_i\left[3(\boldsymbol{S}_i\cdot\hat{r})\hat{r} - \boldsymbol{S}_i\right]\left\langle r_{S_i}^{-3}\right\rangle \qquad (1.72)$$

Electrons inside the nucleus give rise to

$$\boldsymbol{B}_F = -\frac{\mu_0}{4\pi}\frac{8\pi}{3}g_S\mu_B\left|\psi_S(0)\right|^2\boldsymbol{S} \qquad (1.73)$$

where $\boldsymbol{B}_F$ is so-called the Fermi contact term which is the interaction of nuclear dipole moment with a net electron spin density at the nucleus and is written in the L-S coupling limit.

In the solid state there are two mechanisms which give rise to such a contact field;

(i) Conduction electron polarization - In a ferromagnet the s-d exchange interaction between magnetic 3d electrons of the host and the s-like conduction electrons removes the degeneracy of the $s(\uparrow)$ and $s(\downarrow)$ conduction bands. This results in a net surplus of $s(\uparrow)$ electrons,

$$\boldsymbol{B}_F = -\frac{\mu_0}{4\pi}\frac{8\pi}{3} g_S \mu_B \left\{ \left|\psi_S^{\uparrow}(0)\right|^2 - \left|\psi_S^{\downarrow}(0)\right|^2 \right\} \boldsymbol{S} \qquad (1.74)$$

with $$\left|\psi_S^{\uparrow}(0)\right|^2 = \sum_i \left|\psi_i^{\uparrow}(0)\right|^2 - \sum_j \left|\psi_j^{\downarrow}(0)\right|^2$$

(ii) Exchange Core Polarization - Due to the overlap between the polarized conduction electrons of the magnetic host with the inner s-electrons of the non-magnetic impurity it is possible to induce a polarization of the impurity ion core. These polarized core s-electrons then contribute to the hyperfine field.

In the case of a thin foil that is magnetised in its plane, Knight shifts can be neglected and the effective field seen by the impurity is given by

$$\boldsymbol{B}_{eff} = \boldsymbol{B}_{hf} + \boldsymbol{B}_{app} \qquad (1.75)$$

1.5.2 NMR-ON in Ferromagnetic Hosts

Despite two major problems, the skin depth δ and the heating effect of applied RF power, some properties of ferromagnetic metals make them suitable as LTNO hosts in which NMR can be used to influence the nuclear substate populations $g(m)$ and hence measure the hyperfine splitting with high precision. Metallic samples (i.e. Fe-foil) can be cooled by conduction and the large internal hyperfine magnetic field produces a reasonable degree of orientation in most nuclei at accessible temperatures.

The penetration of the applied RF field into the sample is limited by the skin

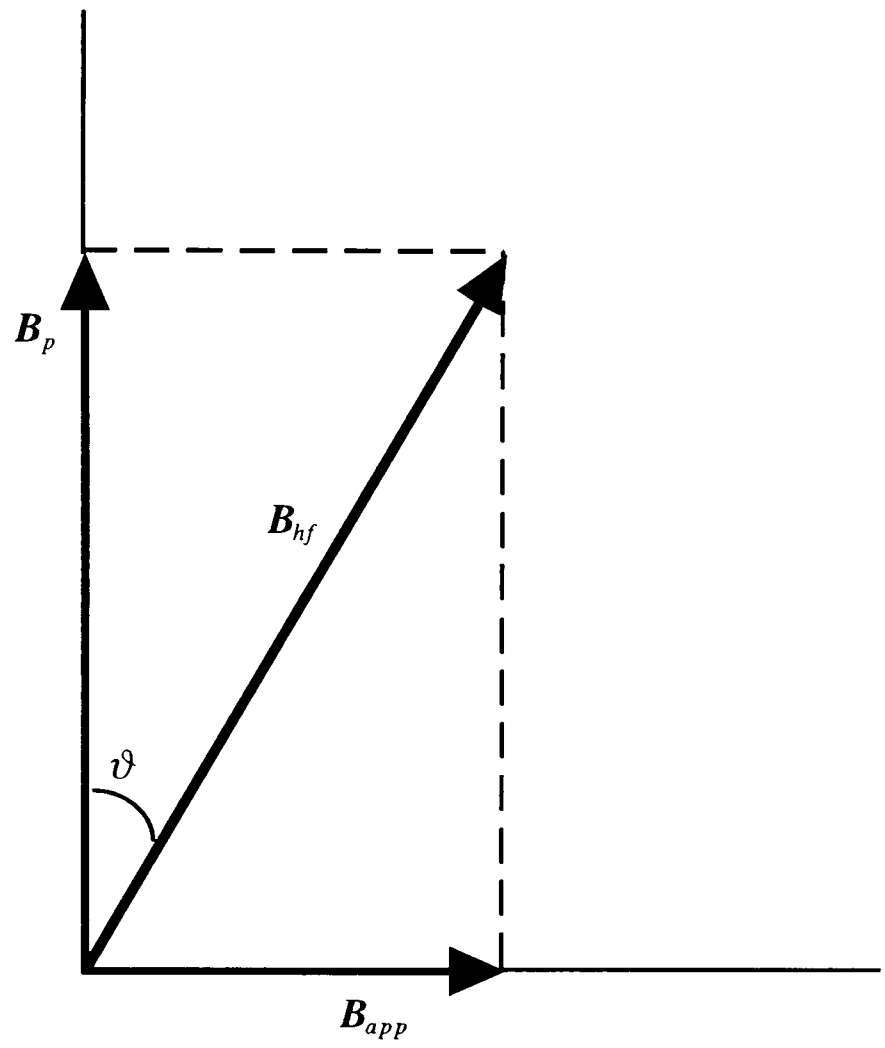


Fig 1.3 Vector diagram of $\boldsymbol{B}$ fields in NMR/ON experiment. $\boldsymbol{B}_p$ is the polarising field, $\boldsymbol{B}_{app}$ the applied RF field and $\boldsymbol{B}_{hf}$ is the hyperfine field.

depth δ, given by

$$\delta = \left(\frac{2\rho}{\omega \mu_r \mu_0} \right)^{\frac{1}{2}} \tag{1.76}$$

where ρ is the resistivity, μ_r the relative permeability of the metal and ω is the angular frequency of the RF field.

Since typical NMR-ON resonance frequencies are order of 100MHz the skin depth is ~ $1\mu m$. Therefore, only those nuclei which are within $1\mu m$ of the surface of the metal will contribute to the resonance signal while the rest will contribute a background noise. Hence it is important for a good signal to noise ratio to make the active sample very thin. This can be done by using a thin foil, by diffusing activity into the surface of the sample or by direct implantation of the activity at low energy (~ 60 keV), again achieving a thin active layer.

Non-resonant heating limits the maximum RF power that can be used. The RF field sets up eddy currents in the metal surface and these eddy currents lead to a power dissipation P in the sample

$$P = \frac{\rho B_{app}^2}{2\delta(\mu_r \mu_0)^{\frac{1}{2}}} \tag{1.77}$$

This causes the base temperature to rise resulting in a non-resonant destruction of anisotropy.

By applying a RF field at the nucleus, the direction of the hyperfine field is slightly tilted away from the direction of the applied field $\boldsymbol{B}_p$. Away from resonance the angle ϑ (fig 5.3) is small and is given by:

$$\vartheta \approx \frac{\boldsymbol{B}_{app}}{\boldsymbol{B}_p} = \frac{\boldsymbol{B}_{app}^{en}(n)}{\left(\boldsymbol{B}_{hf} + \boldsymbol{B}_p\right)} \tag{1.78}$$

The enhanced RF field seen by the nucleus $\boldsymbol{B}_{app}^{en}(n)$ is, then,

$$\boldsymbol{B}_{app}^{en}(n) = \boldsymbol{B}_{app}\left(1 + \frac{\boldsymbol{B}_{hf}}{\boldsymbol{B}_p}\right) \tag{1.79}$$

From (1.79), it can be seen that the lower $\boldsymbol{B}_p$ field the greater the enhancement of the RF field.

1.6 Ion implantation

1.6.1 Dilute alloys for hyperfine interaction studies

Nuclear orientation samples can be prepared by diffusing radioactivity impurity atoms into the ferromagnetic lattice. This procedure requires that the impurity element be soluble in the host at the required alloy concentration (typically $\leq$ 1 at %) and in most cases solubility corresponds to a substitutional lattice site occupation by the impurity atoms. The criteria which must be satisfied for an element to form an appreciable substitutional solid solution in a metal have been given by Hume-Rothery et al[15]. These are

(i) Atomic Size: The atomic diameters of solute and solvent atoms must differ by

less than about 15%; the size-factor is then favourable for the formation of a substitutional solution. The atomic diameter is defined as the smallest spacing between the atoms in the crystal structure of the pure element (for metal). Ideally one would choose a diameter which would take account of the electronic state of the impurity atom when in solid solution.

(ii) Electronegativity: The difference in electronegativity between the two elements must not be too large otherwise there will be a tendency to form an intermetallic compound or intermediate phase.

(iii) Valency: The valency of the solute atoms must be similar to or greater than that of the solvent atoms since a solute atom must have at least as many bonds available as a solvent atom.

For substitutionally soluble elements dissolved in iron, cobalt and nickel the hyperfine fields are mostly well known but gaps and uncertainties in the substitutional hyperfine field systematics exist in the region of insoluble elements or those for which conventional alloy preparation is hindered for reasons of sample chemistry. These include 1st and 2nd row light elements, inert gases, alkali metals, halogens and many rare earth and heavy metals. For such elements dilute alloys with ferromagnetic metals may be prepared by ion implantation in which accelerated impurity ions are injected into the host. Because implantation is a non-equilibrium process the ultimate impurity environment will be determined by factors different from those associated with thermal equilibrium alloy preparation. The location of such an implanted atom will depend on whether it is locally soluble (interstitially or substitutionally) or whether it forms a random or ordered precipitate. Furthermore since the implantation is damage producing, the influence of crystal defects and vacancies near the impurity atom must be considered. An implanted nucleus in a heavily damaged region may well experience a different hyperfine interaction from one in a less disordered region. Radiation damage and the stopping of ions during implantation are complex topics and they will not be considered in this thesis.

1.6.2 Principles of implantation

Ion energy, dose and sample temperature are important parameters in ion implantation (although in this work all implants were performed at room temperature so as to avoid thermally induced ion diffusion). The implantation energy must be sufficient for the impurity atom to ultimately stop behind the surface oxide layer and one usually implants at the maximum energy allowed by

the machine. The stopping power, S(E), is given by the equation

$$S(E) = \frac{dE}{dx} = \left(\frac{dE}{dx}\right)_{nuclear} + \left(\frac{dE}{dx}\right)_{electronic} \tag{1.80}$$

whilst the basic relation between the range and energy loss is simply

$$R = \int_0^E \frac{dE}{\left(-dE/dx\right)} \tag{1.81}$$

Experimentally the most useful quantity is the mean projected range, $\overline{R}_p$, measured parallel to the direction of the incident ion beam. For typical heavy impurities at implantation energies of ~ 60 keV the nuclear stopping term in equation (1.80) predominates and $\overline{R}_p$ ~ 60 to 300Å with a nearly Gaussian range straggling such that $\Delta R_p(\text{FWHM})/R_p \sim 0.3$.

Range and straggling calculations using a purely nuclear stopping model have been performed by Linhard[16] and the results agree broadly with experiment.

Choice of dose is governed by two factors. One desire the highest possible activity in a radioactive sample intended for nuclear orientation. However one is limited in hyperfine interaction measurements to a local impurity concentration sufficiently low that nearest neighbour interactions between impurity atoms are negligible. In addition the radiation damage introduced into the implanted region depends on dose. The mean number of vacancy-interstitial pairs (so-called Frenkel pairs) produced per bombarding ion has been given as[17]

$$\overline{n}(E) = 0.35\frac{E}{E_d}\left[\frac{4M_1M_2}{\left(M_1+M_2\right)^2}\right] \tag{1.82}$$

where E is the ion energy and E_d the threshold energy for Frenkel pair production, typically ~ 25 eV. However for implantation energies of several keV the elastic collision cross-section becomes very small and $\overline{n}(E)$ is approximately constant[16]. Therefore the radiation damage is largely independent of implantation energy but varies with the dose[18]. The distribution of damage resulting from implantation closely follows that of the implanted ions although its mean range is often slightly greater due to focused collision sequences.

Although the nuclear reaction recoil technique is often used in some implantations designed to measure hyperfine interactions, the use of isotope

separators provides a means of implanting the entire range of isotopes. In the present experiments the mass separator was used to implant ^{133}I and ^{135}I with implantation energy ~ 60keV at the neutron physics laboratory in Studsvik, Sweden.

When performing radioactive implantations the allowed local impurity concentration limits the sample activity. Hence the maximum activity will be determined by the source specific activity and the separator isotopic enhancement factor, defined as the ratio on target of the number of ions of mass A at position A to the number of ions of mass A at position A+1. The sample activity will be proportional to the enhancement factor for activity produced by neutron bombardment where the active isotope and inactive carrier isotope are separated in mass by one a.m.u. Often however sample activity is limited by isotopic contamination due to the presence of isobaric molecules or multiply charged impurities.

1.7 Nuclear spin-lattice relaxation

We will assume that a nuclear spin temperature does not exist in the system studied by nuclear orientation, because the nuclear spin system is very dilute. The nuclear spin-lattice relaxation in metals is determined by the interaction between the conduction electrons and the nuclei.

For weak coupling between the nuclear spin system and the lattice the Hamiltonian may be written as

$$\hat{H} = \hat{H}_S + \hat{H}_L + \hat{H}_{SL} \tag{1.83}$$

where $\hat{H}_S$ is the Zeeman interaction of the nuclear sub-levels, $\hat{H}_L$ is the lattice Hamiltonian and $\hat{H}_{SL}$ describes the spin-lattice interaction and is given by

$$\hat{H}_{SL} = A\hat{\boldsymbol{I}} \cdot \hat{\boldsymbol{S}} = AI_z S_z + \frac{1}{2}\left(S_+ I_- + S_- I_+\right) \tag{1.84}$$

where $\hat{\boldsymbol{I}}$ is the nuclear spin operator and $\hat{\boldsymbol{S}}$ the effective spin operator, which can be related to the orbital or/and spin operator of the conduction electrons.

We will restrict ourselves to the time evolution of the diagonal elements of the density matrix, i.e. the populations of the nuclear sublevels. This is justified for spin-lattice relaxation caused by a spherical symmetric perturbation; then the

density matrix will remain diagonal along the quantization axis.

Transitions induced by the non-diagonal elements link states differing by one unit in the magnetic quantum number. The corresponding transition probabilities, derived from Fermi's golden rule, are

$$W_{m+1,m} = \frac{\Delta E}{2kC_k} \frac{[I(I+1) - m(m+1)]}{1 - e^{-\Delta E/kT_L}} \tag{1.85}$$

and

$$\begin{aligned} W_{m+1,m} &= \frac{\Delta E}{2kC_k}[I(I+1) - m(m+1)]\left[1 + \frac{1}{e^{-\Delta E/kT_L} - 1}\right] \\ &= W_{m,m+1}\frac{\Delta E}{2kC_k}[I(I+1) - m(m+1)] \end{aligned} \tag{1.86}$$

where ΔE_n is the magnetic substate energy splitting and C_k, the Korringa constant, depend upon a system arising from the integral over electron states.

Under the conditions that the nuclear spin system is weakly coupled to the lattice and has a much smaller heat capacity, it can be shown that the spin density matrix remains diagonal at all times[19]. The time evolution of the (2I+1) diagonal elements of the density matrix p_m that describes the nuclear spin system is given by the master equation

$$\frac{dp_m}{dt} = \sum_n W_{nm}p_n - W_{mn}p_m \tag{1.87}$$

Without a spin-temperature the relaxation is entirely determined by the transition probabilities W_{mn} from state $|m\rangle \rightarrow |n\rangle$, given by (1.85). In matrix notation (1.87) can be written as

$$\frac{d\boldsymbol{p}}{dt} = \boldsymbol{R}\boldsymbol{p} \tag{1.88}$$

where $\boldsymbol{R}$ is the time independent relaxation "tri-diagonal" matrix because of the selection rules for the dipole transitions. The general solution of (1.88) is

$$\boldsymbol{p}(t) = exp(\boldsymbol{R}t)\boldsymbol{p}(0) \tag{1.89}$$

because $\boldsymbol{R}$ is independent of time.

If $\boldsymbol{R}$ has normalized eigenvectors $\vec{\eta}^{\lambda}$ ($\lambda = 0,1,...,2I$) and corresponding eigenvalues k_{λ}, then the matrix $\boldsymbol{U}$ with columns $\vec{\eta}^{\lambda}$ diagonalizes $\boldsymbol{R}$:

$$\boldsymbol{U}^{-1}\boldsymbol{R}\boldsymbol{U} = \boldsymbol{K} \qquad \text{with } K_{\lambda m} = k_\lambda \delta_{\lambda m} \tag{1.90}$$

Using $\boldsymbol{U}$, (1.88) can be written as

$$\boldsymbol{p}(t) = \boldsymbol{U}\, exp(\boldsymbol{K}t)\boldsymbol{U}^{-1}\boldsymbol{p}(0) \tag{1.91}$$

or in component form,

$$p_m(t) = \sum_{\lambda m'} U_{m\lambda}\, exp\left(k_\lambda t\right) U^{-1}_{\lambda m'} p_{m'}(0) \tag{1.92}$$

In experiments where the relaxation is measured with gamma-ray anisotropy, the populations p_m are only distantly related to the observable radiation distribution, which can be written as

$$W(\vartheta, t) = \sum_{\lambda=0}^{2I} \rho^\lambda(t) A_\lambda P_\lambda(cos\,\vartheta) \tag{1.93}$$

where ρ^λ are statistical tensors of order λ, which are linear combinations of the populations

$$\rho^\lambda = \sum_m (-1)^{I-m} \langle Im\, I - m | \lambda 0 \rangle p_m \tag{1.94}$$

Transforming p_m to ρ^λ with (1.94) gives

$$\begin{aligned} \rho^\lambda(t) = \sum_{mm'i\lambda'} (-1)^{2I-m-m'} \langle Im\, I - m | \lambda 0 \rangle U_{mi} e^{k_i t} U^{-1}_{im'} \\ \times \langle Im'\, I - m' | \lambda' 0 \rangle \rho^{\lambda'}(0) \end{aligned} \tag{1.95}$$

This equation can be written as a sum of exponentials:

$$\rho^\lambda(t) = \sum_{i=0}^{2I} R_{\lambda i} e^{k_i t} \tag{1.96}$$

The coefficients

$$R_{\lambda i} = \sum_{mm'\lambda'} (-1)^{2I-m-m'} U_{mi} U_{im}^{-1} \langle Im\, I-m|\lambda 0\rangle \times \langle Im'\, I-m'|\lambda' 0\rangle \rho^{\lambda'}(0) \tag{1.97}$$

depend both on the initial conditions $\rho^{\lambda}(0)$ and on the transformation $\boldsymbol{U}$ that diagonalizes $\boldsymbol{R}$.

A relaxation rate is given by

$$R_L = \frac{2kB}{\gamma_n^2} = \frac{1}{C_k \gamma_n^2} \tag{1.98}$$

Though the gyromagnetic ratio of the nucleus γ_n occurs in this expression, the Korringa constant $C_k = T_1 T_L$ can be shown to contain a factor $1/\gamma_n^2$, so that R_L is independent of the nuclear moment. Here T_1 and T_L denote the high temperature relaxation time and the lattice temperature, respectively.

Although the temperature dependence of spin-lattice relaxation rate of $^{133,135}IFe$ have not been measured in the present experiment, a short discussion of this may give some insight in the physics behind (1.96) and (1.97). The relaxation matrix $\boldsymbol{R}$ for $^{133,135}IFe$ with I=7/2 is

$$\boldsymbol{R} = -W \begin{pmatrix} 7Q & -7 & 0 & 0 & 0 & 0 & 0 & 0 \\ -7Q & 12Q+7 & -12 & 0 & 0 & 0 & 0 & 0 \\ 0 & -12Q & 15Q+12 & -15 & 0 & 0 & 0 & 0 \\ 0 & 0 & -15Q & 16Q+15 & -16 & 0 & 0 & 0 \\ 0 & 0 & 0 & -16Q & 15Q+16 & -15 & 0 & 0 \\ 0 & 0 & 0 & 0 & -15Q & 12Q+15 & -12 & 0 \\ 0 & 0 & 0 & 0 & 0 & -12Q & 7Q+12 & -7 \\ 0 & 0 & 0 & 0 & 0 & 0 & -7Q & 7 \end{pmatrix}$$

with $Q = exp(-\Delta E/kT_L)$. Let $X_L = (-\Delta E/kT_L)$.

In the high temperature limit ($X_L << 1$), $\boldsymbol{R}$ is symmetric with eigenvalues $k_\lambda = -W\lambda(\lambda+1)$ where λ= 0,1,...,2I. The matrix $\boldsymbol{U}$ is orthogonal, with components

$$U_{m\lambda} = (-1)^{I-m} \langle Im\, I-m|\lambda 0\rangle \tag{1.99}$$

Because of the symmetry properties of the Clebsch-Gorden coefficients, (1.96) reduces to

$$\rho^{\lambda}(t) = e^{k_{\lambda} t}\rho^{\lambda}(0) \tag{1.100}$$

At very low temperatures ($X_L \rightarrow \infty$), $\boldsymbol{R}$ becomes "bi-diagonal" with eigenvalues equal to the diagonal elements: 0, -2W(4I-6) (appearing once), -2WI, -2W(2I-1), ..., -2W(3I-3) (each appearing twice). The relaxation rate will be strongly influenced by the smallest eigenvalue -2WI, belonging to the transition between the lowest two levels. Provided the spin system is close enough to equilibrium that p_m can be neglected for all but the lowest two levels, all observables relax with a single exponential with relaxation time T_τ, given by

$$T_\tau = \frac{1}{2BhvI} = \frac{kC_k}{hvI} \tag{1.101}$$

This limit is reached for lattice temperatures

$$T_L << \frac{hvI}{k} \tag{1.102}$$

or

$$\frac{1}{T_L} >> 8.3(1)\mathrm{K}^{-1} \qquad \text{for } {}^{133}I$$

and

$$\frac{1}{T_L} >> 7.7(1)\mathrm{K}^{-1} \qquad \text{for } {}^{135}I.$$

References

[1] J.Rikovska et al., in Low-Temperature Nuclear Orientation, Chapter 4, eds. N.J.Stone and H.Postma (North-Holland, 1986)

[2] D.M.Brink and G.R.Satcher, in Angular momentum (Oxford, 1968)

[3] K.S.Krane, in Low-Temperature Nuclear Orientation, Chapter 2, eds. N.J.Stone and H.Postma (North-Holland, 1986)

[4] R.M.Steffen and K.Alder, in The Electromagnetic Interaction in Nuclear Spectroscopy, ed. W.D.Hamilton (North-Holland, 1975)

[5] K.S.Krane, Phys.Rev **C2**(1970) 724

[6] M.E.Rose, Phys.Rev **91**(1953) 610

[7] J.R.Beeler and M.F.Beeler, in Fundamental Aspects of Radiation Damage in Metals, **CONF-751006-P1**(1976) 28

[8] R.S.Averback et al., Nucl.Instr and Meth B33(1988)693

[9] U.Fano, Phys.Rev **90**(1953) 572

[10] H.Postma and N.J.Stone, in Low-Temperature Nuclear Orientation Chapter 1, eds. N.J.Stone and H.Postma (North-Holland, 1986)

[11] N.J.Stone, in Low-Temperature Nuclear Orientation, Chapter 8, eds. N.J.Stone and H.Postma (North-Holland, 1986)

[12] E.Klein, in Low-Temperature Nuclear Orientation, Chapter 12, eds. N.J.Stone and H.Postma (North-Holland, 1986)

[13] K.S.Krane, Introductory Nuclear Physics (John-Wiley, 1988)

[14] J.D.Jackson, in Classical Electrodynamics (2ed), (John-Wiley, 1975)

[15] W.Hume-Rothery et al., in The structure of metals and alloys (5th ed), (Institute of Metals, 1969)

[16] J.Lindhard et al., Mat. Fys. Medd. Dan. Vid. Selsk **33**(1963)14

[17] W.J.Snyder and J.S.Neufeld, Phys.Rev **99**(1955)1326

[18] R.B.Alexander, D.Phil Thesis (unpublished), Oxford University 1971

[19] A.Sher and H.Primakoff, Phys.Rev. **119**(1960)178

[20] R.Kirchner etal., Nucl. Instr and Meth **186**(1981) 295

[21] E.Klein, Hyp. Int **15/16** (1983) 557

[22] E.Klein, Hyp. Int **22** (1983) 557

[23] D.Spanjaard and F.Hartmann-Boutron, Solid State Comm **8**(1970)333

[24] B.G.Turrell, Hyp. Int **7**(1980)429

[25] F.Bacon etal., Phys Rev **B5**(1972)2397

[26] E.Klein, in Low-Temperature Nuclear Orientation
eds. N.J.Stone and H.Postma (North-Holland, 1986) ch 12

[27] A.Sher and H.Primakoff, Phys Rev **119**(1960)178

[28] C.P.Slichter, in Principles of Magnetic Resonances (Spring-verlag, 1978)

[29] J.Korringa, Physica **16**(1950)601

[30] N.J.Stone, in Hyperfine Interaction in Excited Nuclei,
eds G.Goldring and C.Kalish (Gordon and Breach, 1971)237

[31] N.J.Stone, Hyp. Int **22**(1985)3

[32] A.Narath, in Hyperfine Interactions, eds. A.J.Freeman and R.B.Frankel
(Acadenic Press, 1967) ch 7

[33] M.Kopp etal., Z. Phys **B44**(1981)73

[34] T.L.Shaw and N.J.Stone, ANDT **42**(1989)339

[35] N.J.Stone, in Low-Temperature Nuclear Orientation, Chapter 13,
eds. N.J.Stone and H.Postma (North-Holland, 1986)

[36] T.L.Shaw, D.Phil Thesis (unpublished), Oxford University 1987

[37] H.Pattyn et al., Hyp. Int **2**(1976)362

Chapter Two

Experimental Apparatus and Techniques

2.1 The $^3He/^4He$ dilution refrigeration

2.1.1 Introduction

To understand LTNO it is important to understand the relevant properties of liquid and solid matter involved in the attainment of low temperatures. Additionally experiments at low temperatures make no sense at all without good thermometry. Therefore, in this chapter these aspects of the work will be explained.

2.1.2 Properties of liquid $^3He/^4He$

There are two stable isotopes of liquid He, namely, ^3He and ^4He. ^4He is a bose particle and obeys Bose-Einstein statistics while ^3He is a fermion and obeys Fermi-Dirac statistics. When pure samples of the two isotopes are cooled, both liquefy and remain liquid down to the very lowest temperatures under their saturated vapour pressures. This occurs since both isotopes experience extremely weak Van der Waals binding forces that arise from the fluctuating polarisation charges induced in the electron shells of adjacent atoms.

Suppose an atom in the liquid is a free particle located in a $\boldsymbol{k}$-space formed by the adjacent atoms. Since they have the small atomic mass m, they have a large quantum mechanical zero-point energy, E_0

$$E_0 = \frac{h^2}{2mr^2} \tag{2.1}$$

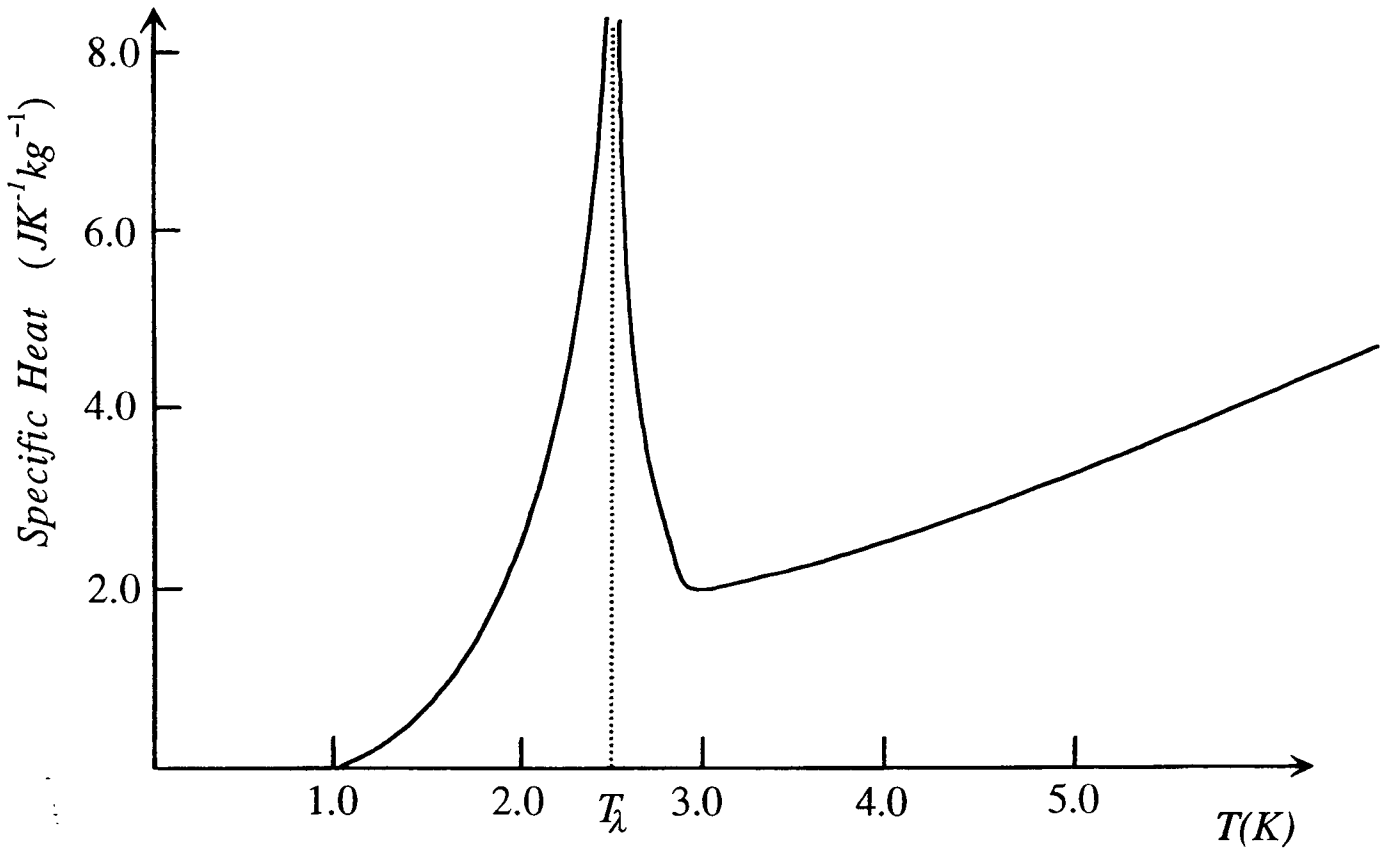


Fig 2.1 The specific heat of liquid ^4He under the saturated vapour pressure.

A schematic drawing of the temperature dependence of the specific heat of liquid ^4He under the saturated vapour pressure[12].

where $r = (V_m / N_A)^{1/3}$ is the distance between the atoms, V_m the molar volume and N_A is the Avogadro's number. As the zero-point energy is inversely proportional to the mass of the atom, ^3He is relatively more affected, leading to a molar volume of ~ $40\,cm^3$ compared to ~ $28\,cm^3$ for ^4He though the atoms are the same size. Also ^3He has a higher vapour pressure than ^4He at the same temperature.

The different statistics for the boson ^4He and for the fermion ^3He give rise to substantial differences in their low-temperature behaviour. The helium liquids are called quantum liquids because of the strong influence of quantum effects on their properties. ^3He fermi particles cannot undergo the analogue of a Bose momentum condensation into a superfluid state as the bosons ^4He do at the so called lambda transition temperature, T_λ (fig 2.1).

Figure 2.2 shows several of the remarkable features of helium isotopic liquid mixtures. Pure liquid ^4He becomes superfluid at $2.17K$ and this transition temperature is depressed when it is diluted with liquid ^3He. Eventually,

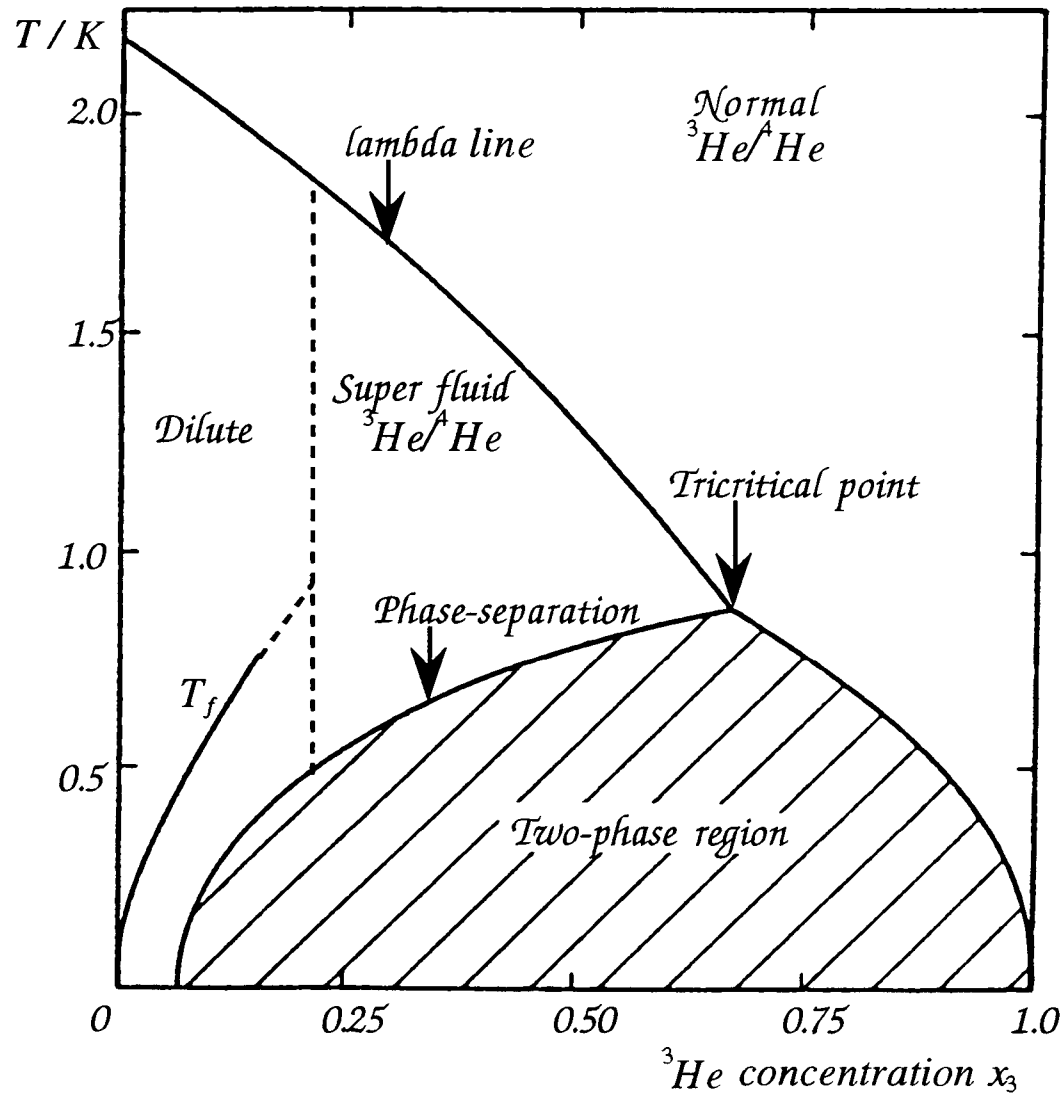


Fig 2.2 Phase diagram of liquid $^3He/^4He$ mixtures at saturated vapour pressure. Increasing the concentration of ^3He, x_3, shifts the lambda point to lower temperatures. Experimentally, $T_\lambda \cong T_\lambda^0(1-x_3)^{2/3}$ [12].

superfluidity ceases to exist for ^3He concentrations, $x_3 > 67\%$. At this concentration and at a temperature of $0.87K$ the λ-line meets the phase separation line. If a He mixture with $x_3 > 6.5\%$ is cooled down below $0.87K$ the heat motion of the ^4He content has almost completely disappeared, and its entropy and specific heat are very much less than those of ^3He. Hence, ^4He in the solution behaves only as a background fluid, in which the ^3He atoms move about rather as a gas of atoms in a vacuum. The mixture will eventually separate into two phases - one rich in ^3He and the other rich in ^4He, and the interaction between them will be weak. The dilute ^3He atoms behave like a perfect Fermi gas and the ^3He rich phase will float on top of the ^4He rich phase as the density of ^3He is lower than that of ^4He. If the temperature is decreased to close to absolute zero, the ^3He rich liquid becomes pure ^3He. However, the concentration of ^3He in the dilute phase has a constant value of 6.5% at saturated vapour pressure even at $0K$. This finite solubility is of utmost importance for $^3He/^4He$ dilution refrigeration technology.

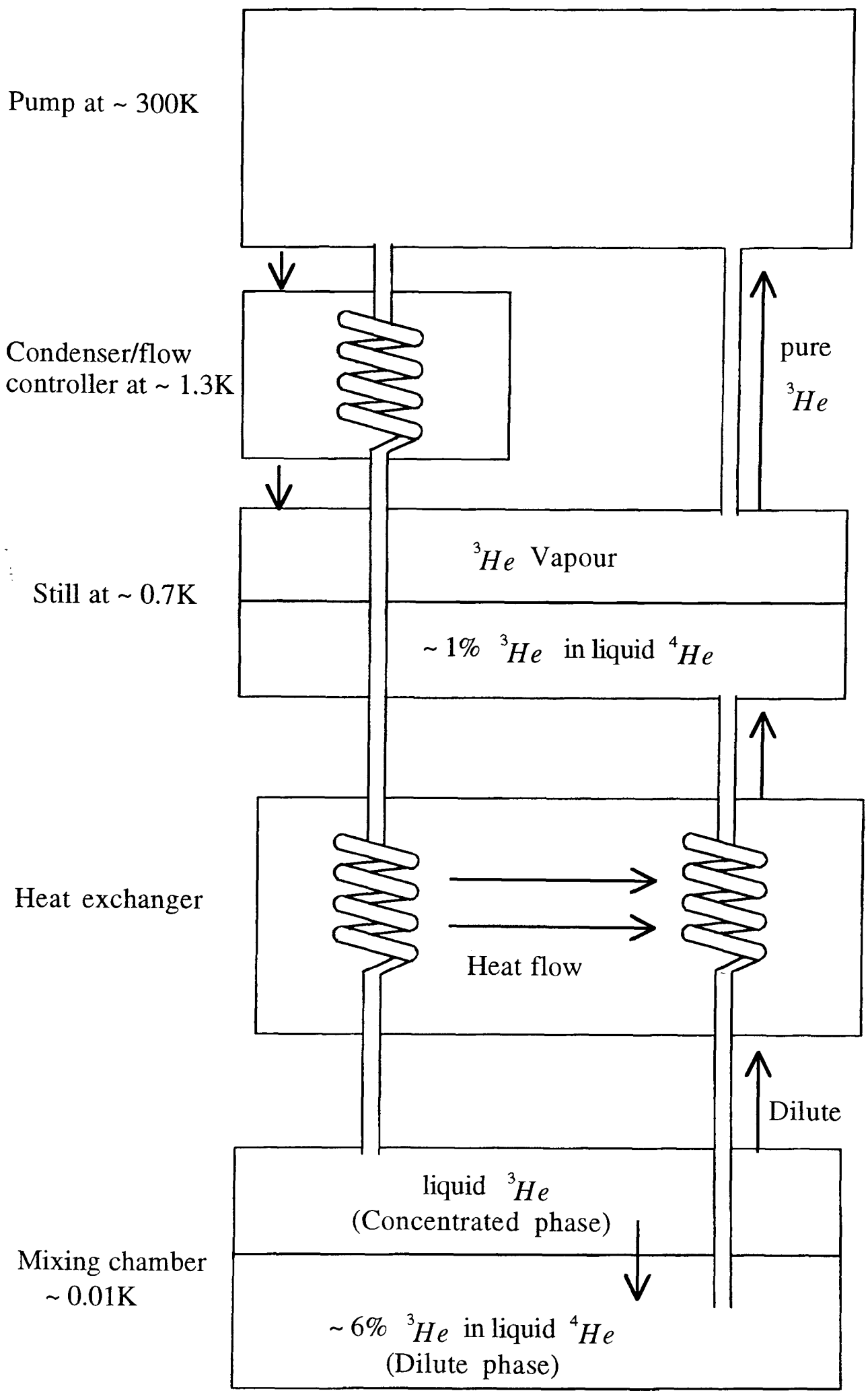


Fig 2.3 A schematic layout of a dilution refrigerator

A ^3He atom passing from the concentrated phase to the dilute phase will result in cooling because the specific heat of a ^3He atom is larger in the dilute phase than in the concentrated phase. Because of this finite solubility of ^3He in ^4He a cooling power will decrease only with T^2 and not exponentially as in the evaporation cooling process.

Due to the substantial difference between the vapour pressures of ^3He and ^4He at the same temperature, circulation of almost pure ^3He can be achieved. An osmotic pressure will drive the ^3He from the mixing chamber up into the still if they are at different temperatures in a cryogenic apparatus.

2.1.4 Continuous operation below $10mK$

The evaporation of low boiling point liquids is the usual method of maintaining a low temperature. A temperature bath between $4K$ - $5K$ can be easily obtained on liquid ^4He in a dewar.

The same liquid, evaporated at a lower pressure by using a pumping system, can maintain a lower temperature since the saturated vapour pressure decreases with temperature, and the size of the pumping system is limited, there is a lowest accessible temperature. For ^4He this is ~ $1K$ and ^3He is ~ $0.3K$.

To obtain steady temperatures down to a few mK the essence of the method is to dilute a ^3He - ^4He mixture. A schematic view of the main features of a conventional continuous operation $^3He/^4He$ dilution refrigerator is shown in (fig. 2.4). The Oxford dilution refrigerator used for experiments in this thesis is an Oxford Instruments model 300TL, with a base temperature of $<6mK$ and a nominal cooling power of $300\mu W$ at $100mK$.

In stable operation, the concentrated phase-dilute phase boundary must lie in the mixing chamber which is the coldest part of the refrigerator. The dilute phase in the mixing chamber is connected to the still via a series of heat exchangers. The still is pumped by a large diffusion pump backed by a sealed rotary pump. By pumping the still, ^3He is caused to cross the phase boundary from the concentrated phase to the dilute phase producing cooling. An optimal circulation rate of ^3He in the system is produced by an electric heater which maintains the still at a temperature ~ $0.8K$.

^3He from the rotary pump exhaust re-enters the cryostat after removing any air that may have leaked into the circulating tube by passage, through liquid nitrogen traps (called cold traps). The ^3He is re-cooled to ~ $1.2K$ by thermal

contact with a pumped ^4He pot and is then liquefied in the condenser which comprises a fine capillary tube of high impedence which is needed to keep the pressure of the ^3He sufficiently high for condensation to occur.

The ^3He is cooled to ~ $0.8K$ by passage through a wrap around heat exchanger on the still, and then returns to the mixing chamber through a concentric tube continuous heat exchanger and four sintered silver step heat exchangers, where cooling is performed by the out-going ^3He of the dilute phase. The efficiency with which the returning ^3He can be pre-cooled before entering the mixing chamber is one of the limitations on the base temperature attainable.

The conventional cryostat design consists of an Inner Vacuum Can (IVC), a main liquid ^4He bath of capacity ~ 30 litres, and an Outer Vacuum Can (OVC). There is a radiation shield maintained at $77K$ by a liquid nitrogen reservoir within the OVC. The IVC, which contains the dilution unit, is maintained at a pressure of $\leq 10^{-6}\tau$ during stable operation, with the main helium bath acting as a $4.2K$ radiation shield. Additional reduction in radiation heating of the dilution unit is achieved by an the $0.8K$ heat shield that is attached to the still.

The still, $25mK$ plate and mixing chamber temperatures can all be monitored during circulation using resistors. In normal operation, the temperature can be measured by use of a standard nuclear orientation thermometer (see sec. 2.4) soldered to a copper cold finger, which is screwed to the base of the mixing chamber to ensure good thermal contact.

2.1.5 Sample preparation and orientation

In this work the host lattices have all been polycrystalline Fe-foils of ~ 99.998% purity. These are prepared by cold-rolling an Fe sheet down to a thickness of $< 1mm$. Before polishing the Fe-foil it is chemically etched in a solution of 54 vol % H_3PO_4 (86%), 36 vol % H_2O_2 (30%),8.5 vol % distilled water and 1.5 vol % butoxyethanol for 10 - 30 seconds if necessary. After such an etch foil it is thoroughly washed. The surface of the foil is then polished using a $0.3\mu m$ alumina polishing suspension, and the foil is then annealed in a dry hydrogen environment at a temperature ~ $860^{\circ}C$ for ~ 12 hours (at $960^{\circ}C$ a Fe phase transition occurs) and is cooled slowly over about ~ 10 hours.

The loaded sample and thermometer lie at the centre of a $1.5Tesla$ superconducting split coil magnet which is used to polarise the magnetic domains in the foil. In an experiment, typically a field of ~ $0.7T$ is applied. This magnetic field ensures that the solder is not superconducting, and hence good thermal

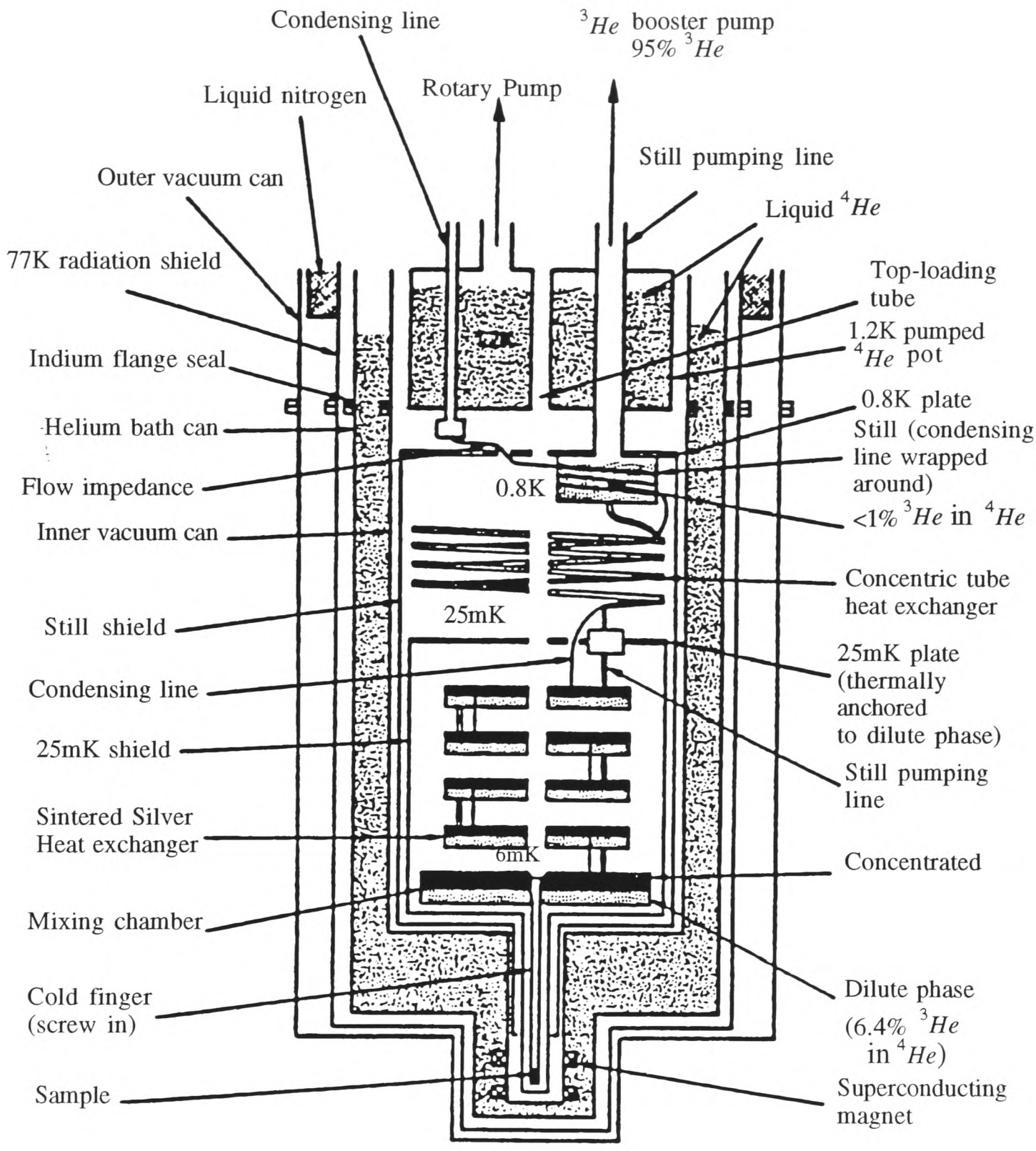


Fig 3.4 Schematic view of the conventional Oxford $^3He/^4He$ dilution refrigerator, showing the main features necessary for continuous operation at temperature down to ~ $6mK$[14].

contact to the cold finger is achieved. The field produced by the magnet has a homogeneity of ~ 1% over the sample volume.

2.1.6 NMR/ON on $^{60}CoFe$

In order to test the r.f. equipment, NMR/ON on $^{60}CoFe$ was performed. A $0.7\times1.5\ cm^2$ $0.2\mu m$ Fe foil with dilute HCl solution containing ^{60}Co activity evaporated onto the surface was diffused in a holder at $860^{o}C$ for ~ 12 hours. The active $^{60}CoFe$ sample was soldered to the cold finger, cooled ~ 14 mK and polarized in $0.7T$. With RF signal frequency modulated over +/-1MHz a search in 0.5MHz steps was made starting at 159.5MHz. Expected resonance frequency was 163 MHz. The observed resonance is shown in fig 2.5.

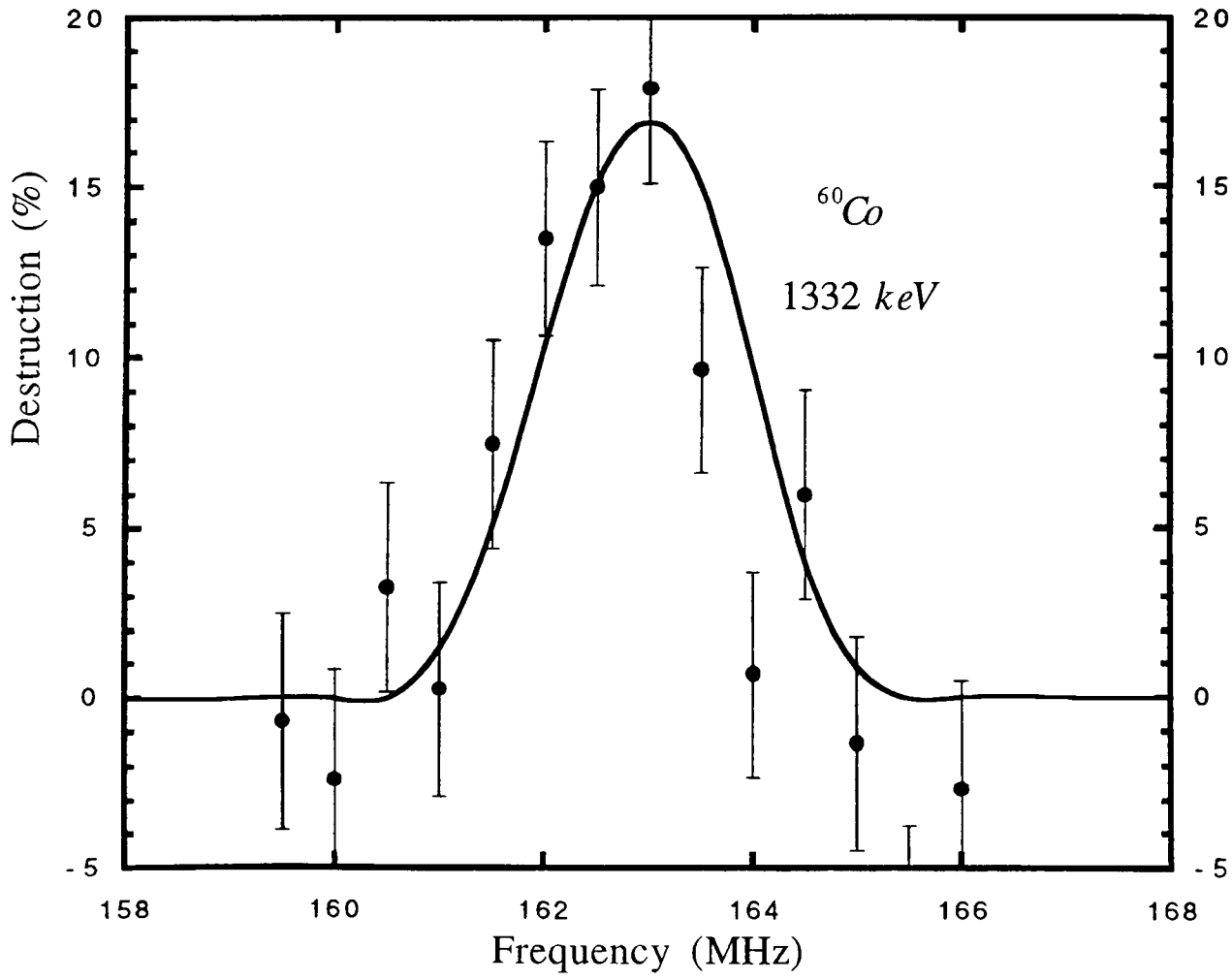


Fig 2.5 Observed resonance on $^{60}CoFe$

2.2 The cooling power test

The cooling power is given by

$$\dot{Q} = \dot{n}_3(107 - 24)T^2 = 84\dot{n}_3T^2(W) \qquad \text{for} \quad T < 0.1K \tag{2.2}$$

It is desirable to vary the temperature of the mixing chamber, and hence that of the sample. This can be done by passing current through a 415Ω resistor, thermally attached to the mixing chamber. If the external heating of the mixing chamber is denoted by $\dot{Q}$, then from the cooling power of the refrigerator as a function of temperature, it can be shown that[1]

$$\dot{Q} = C\left(T_{mc}^2 - T_{base}^2\right) \tag{2.3}$$

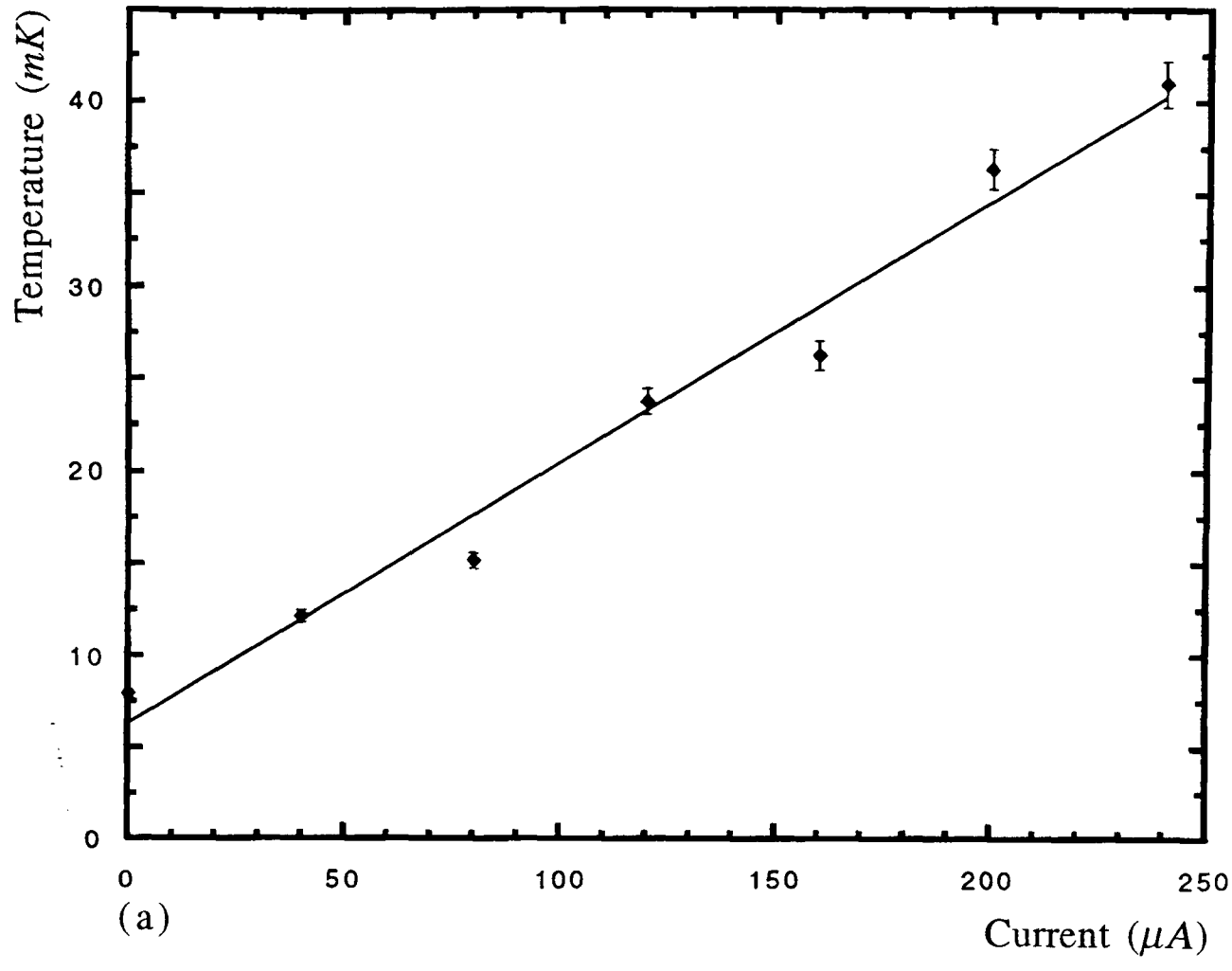
where T_{mc} is the temperature of the mixing chamber and T_{base} is the minimum temperature that can be attained. C is a constant for a particular set of refrigerator operating conditions. (2.3) can be rewritten as

$$T_{mc} = \left(\frac{\dot{Q}}{C} + T_{base}^2\right)^{\frac{1}{2}} = T_{base}\left\{\frac{R_{mc}}{C}\left(\frac{i}{T_{base}} + 1\right)\right\}^{\frac{1}{2}} \approx i\left(\frac{R_{mc}}{C}\right)^{\frac{1}{2}} \quad \text{for} \quad \left(\frac{T_{mc}}{T_{base}}\right)^{\frac{1}{2}} >> 1 \tag{2.4}$$

For the Oxford refrigerator, the ^3He circulation rate for optimum performance is ~ 400μmol/s and base temperature can be obtained as low as ~ $5mK$. A plot of $T_{mc}(mK)$ against current i (μA), and $T_{mc}(mK)$ against cooling power $\dot{Q}$ (μW) are shown in fig 2.6. The experimental points have been fitted using (2.4), giving the values

$$\begin{aligned} C &= 0.0206(1)\ \mu W \\ T_{base} &= 6.3(1)\ mK \end{aligned} \tag{2.5}$$

T_{base} agrees with the temperature that is currently achieved by the Oxford refrigerator. The cooling power at $25mK$ is ~ $10\mu W$ using the parameters in (2.5), which agrees with the specifications quoted by Oxford Instruments. From these results, a required temperature can be achieved by choosing the appropriate current for the mixing chamber heater.



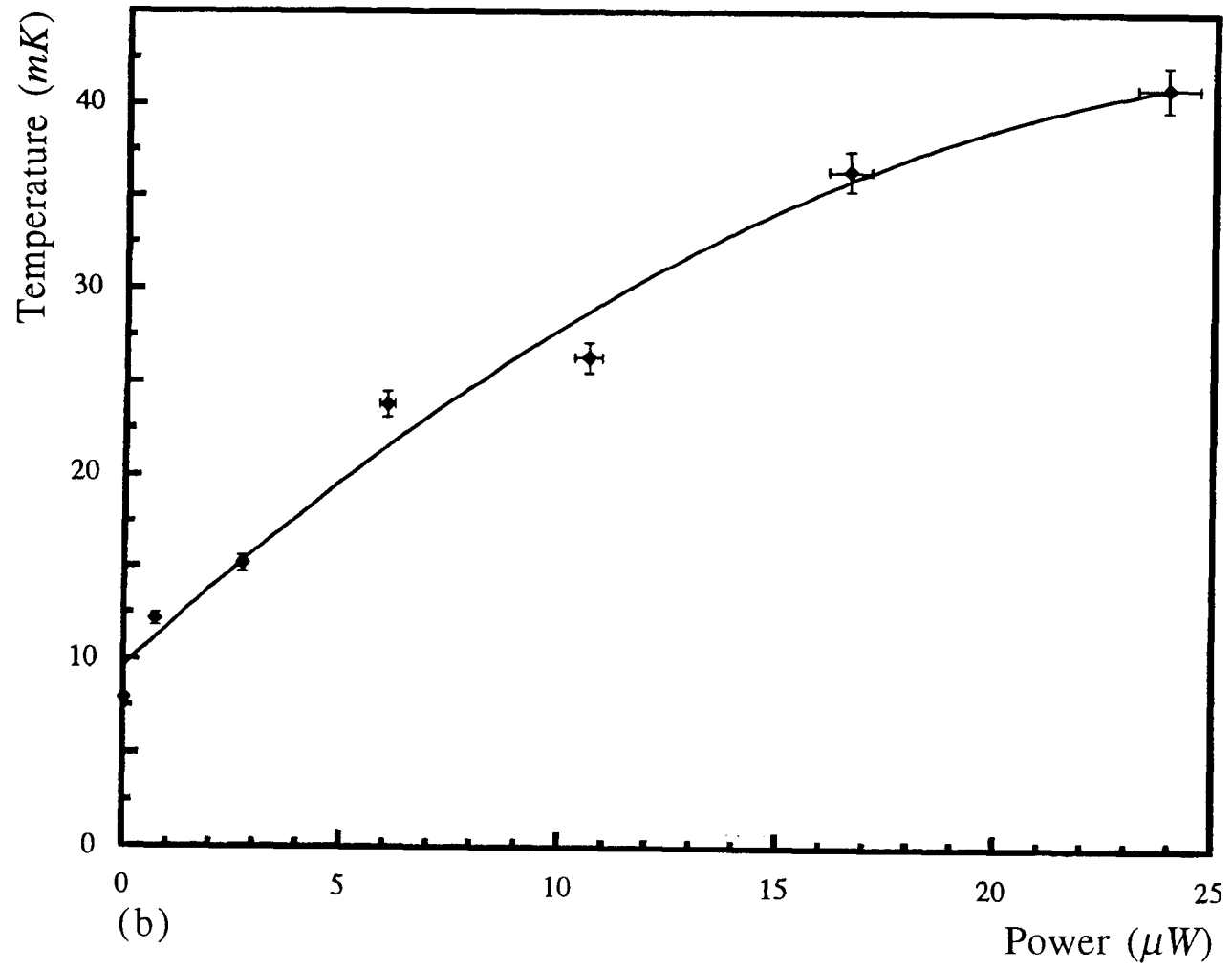


Fig 2.6 Cooling power of the Oxford refrigerator (a) the mixing chamber temperature is plotted against the current in the mixing chamber resistor (b) the mixing chamber temperature is plotted against cooling power.

2.3 Top loading Dilution unit

The top loading facility allows a sample at room temperature to be loaded directly into a cold dilution refrigerator without warming the refrigerator above $1K$ and cooled to base temperature within a few hours (~ 3 hours). The cold finger is mounted onto a long vacuum insulated top loading syphon and this is then lowered into the central access tube of the cryostat, through a vacuum lock and sliding seal arrangement, until the sample holder is just above the $1.2K$ pot. Liquid ^4He is then transferred from the main liquid ^4He bath through the top loading syphon to a small chamber at the bottom of the syphon and then up through a second tube within the top loading syphon. The helium circulation is maintained using a rotary pump in the outlet of the syphon. The liquid helium collecting in the chamber at the bottom of the syphon cools the sample holder by conduction. The temperature of the sample holder is ~ $4K$ after ~ 20 minutes circulation.

The top loading tube is fitted with a series of moveable baffles which act as radiation shielding during the normal operation of the refrigerator after the top loading system has been removed.

2.4 Nuclear Thermometry

In any LTNO experiment accurate measurement of the temperature of the sample is of the utmost importance. Therefore it is necessary to use a well known source for the temperature determination. An experimentally feasible LTNO thermometer must satisfy several important conditions;

(i) the hyperfine interaction is well known and a ~ 100% occupation of full substitutional sites in the host lattice can be relied upon

(ii) the decay scheme is as simple as possible with accurately known $U_\lambda A_\lambda$ coefficients

(iii) the nuclear spin-lattice relaxation time is short

(iv) reasonably long half-life with small radioactive heating

The nuclear orientation thermometer that has been used for this work has been $^{192}IrFe$ because of its high temperature sensitivity. $^{192}IrFe$ thermometer was produced by wrapping ^{192}Ir powder in Fe-foil and then melting in the furnace. The resulting dilute $^{192}IrFe$ alloy was then rolled to a suitable thickness and cut.

The useful temperature range of a thermometer can be defined in terms of the sensitivity function $T\,\partial W(\vartheta,T)/\partial T$. The properties for some of the most

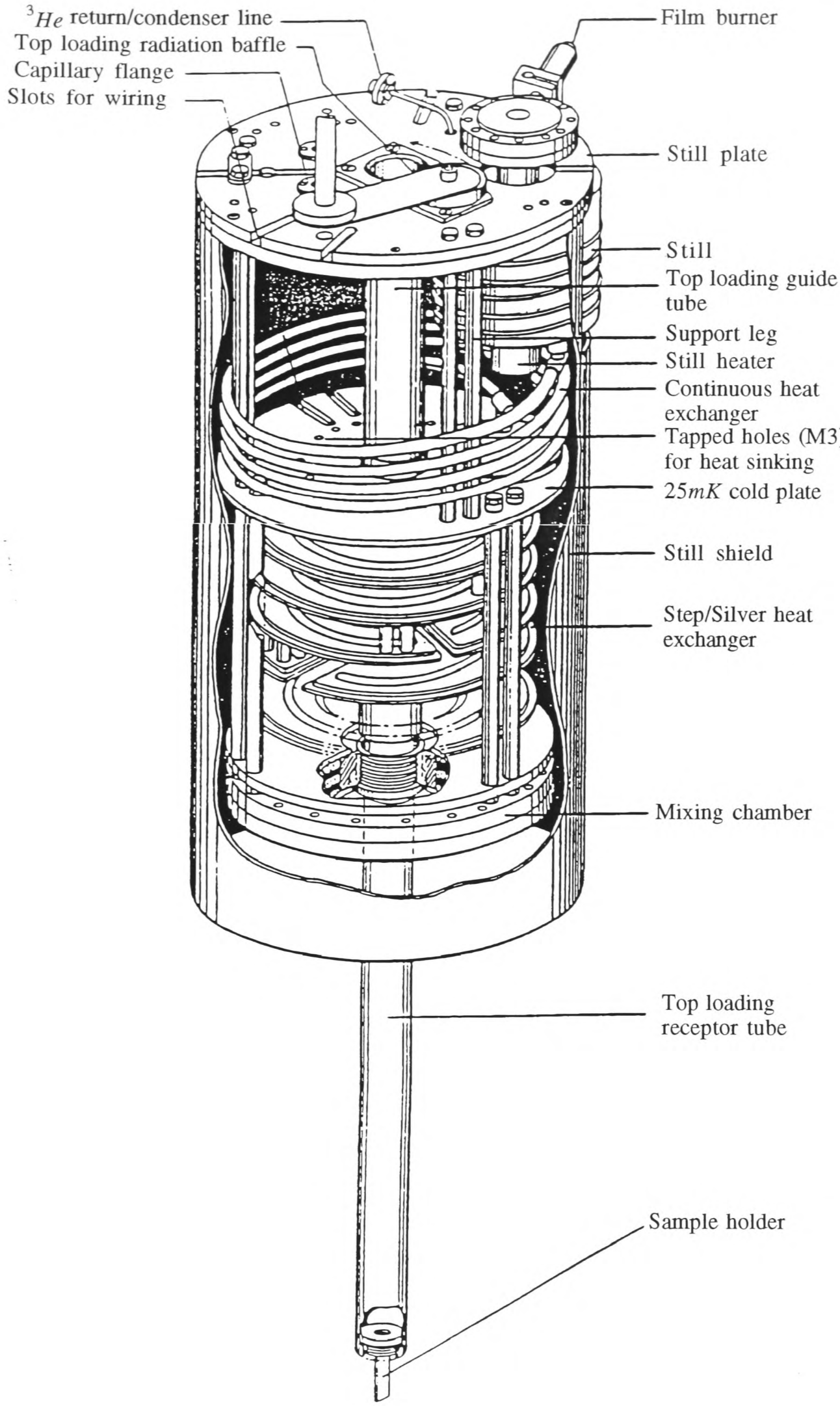


fig 2.7 A typical top loading dilution unit[14]

frequently used LTNO thermometers are shown in table 2.1, and their sensitivity functions and partial decay schemes are shown in fig 2.8.

2.5 Data Acquisition system

For the work described in this thesis, γ-rays have been detected using $Ge(Li)$ detectors and these measurements are recorded by the data acquisition system for subsequent analysis. Fig 2.9 shows schematic diagram of a typical singles mode data acquisition system. At Oxford both On-line and Off-line analysis can be done using PC based data acquisition system which can be connected to upto 16 ADCs at the same time.

The preamplifier is situated close to the detector so that the pick-up of stray signals and input capacitance is reduced. The most common type of preamplifier is the charge-sensitive type. The main amplifier amplifies and shapes the signal from the preamplifier for further processing. The Multi-Channel Analyser (MCA) digitises the incoming pulse with an Analogue-to-Digital Converter (ADC). The MCA then takes this number and increments a memory channel whose address is proportional to the value. The resulting spectrum, acquired over a chosen period of time, is written to the hard disk of the acquisition computer. These spectra can then be analysed as described in the next chapter.

Isotope	$E_\gamma(KeV)$	L	δ	Γ	U_2	U_4	A_2	A_4
^{192}Ir	316.5	E2	-	0.38	.34(2)	.015(7)	- .592615	-1.069046
	468.1	E2	-	0.22	.8521(5)	.505(17)	- .4477	- .3044

Table 2.1 The properties of the LTNO ^{192}Ir thermometer used in this work. L is the multipolarity and Γdenotes the transition probability.

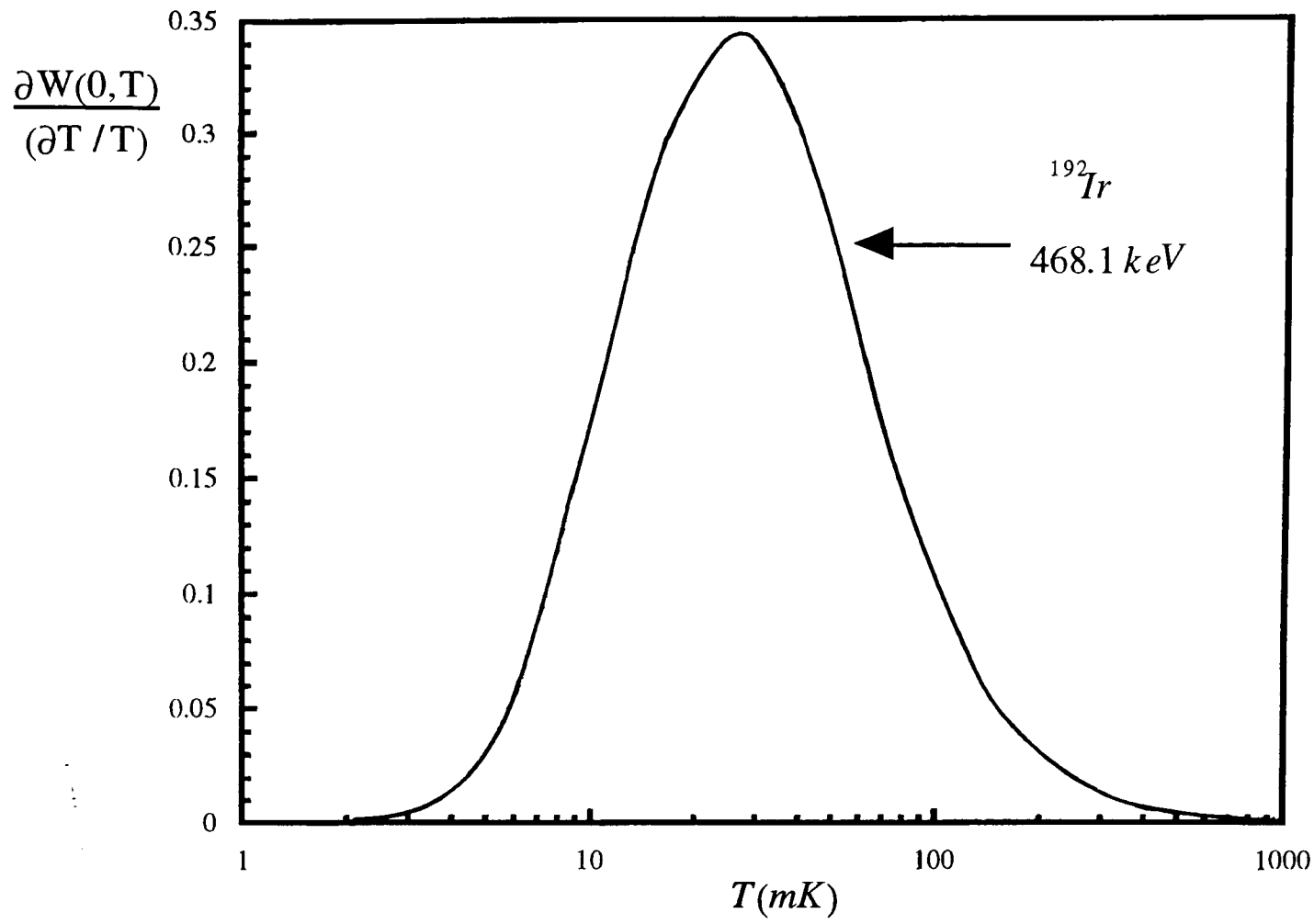


Fig 2.8 (a) Sensitivity Function for the $^{192}IrFe$ γ−ray thermometer
(b) The partial decay scheme of ^{192}Ir

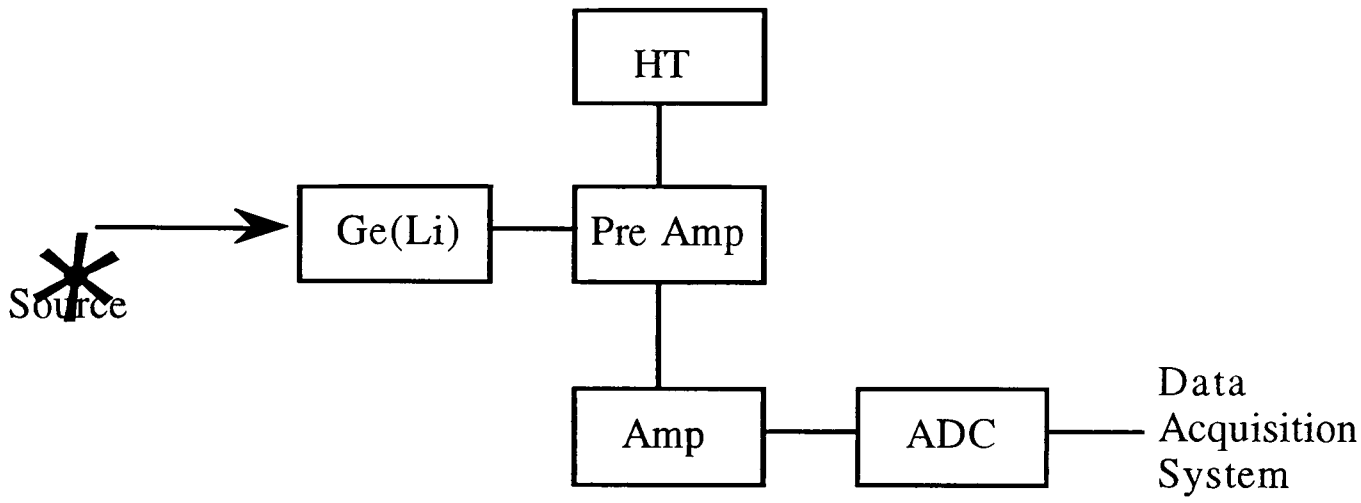


Fig 2.9 Schematic diagram of a typical singles mode data acquisition system

2.6 Germanium Detectors

To detect γ- rays, the thickness of detector must be much greater than that of detectors for the detection of α- particles and other short range radiations. The thickness of the depletion region is given by

$$\eta = \left(\frac{2\varepsilon V}{e\kappa} \right)^{\frac{1}{2}} \tag{2.6}$$

where V is the reverse bias voltage and κ is the net impurity concentration in the bulk semiconductor material. As it can easily be seen from (2.6), the only way to achieve greater depletion depths at a given voltage is to make the value of κ as small as possible.

There are two types of the germanium detectors. One of them is called a high-purity germanium ($HPGe$) or intrinsic germanium detector, because it is manufactured from ultrapure germanium. It has the an impurity concentration of $\sim 10^{10} \text{atoms} / cm^3$ and depletion depth of $\sim 10mm$. The other type is called a $Ge(Li)$ detector since it is produced by the lithium ion drifting process.

The $HPGe$ detectors have several advantages over the $Ge(Li)$ detectors.

The *HPGe* detectors are allowed to warm to room temperature when they are not used, whereas the *Ge(Li)* detectors must always be maintained at ~ $77K$ through the use of an insulated dewar in which a reservoir of liquid nitrogen is kept in thermal contact with the detector to prevent a catastrophic redistribution of the drifted lithium that will quickly take place at room temperature. Another advantage of using the *HPGe* detectors over the *Ge(Li)* types is that it can be repaired by annealing the detector when radiation damage occurs. It has been shown[2] that lightly damaged $\left(< 4\times10^{9} n/cm^{2}\right)$ n-type the *HPGe* detectors can be recovered to their original resolution performance if it is annealed at ~ $120^{\circ}C$ for 72 hours.

The detector must be contained in a vacuum-tight cryostat to prevent thermal conductivity between the crystal and the surrounding air, and its liquid nitrogen capacity must be ~ 30 litres to avoid filling the dewar more than once a week. It is also advantageous to locate the preamplifier as near the detector as possible to minimise capacitance. The input stages of the preamplifier normally are also cooled along with the detector to reduce electronic noise (see fig 2.10).

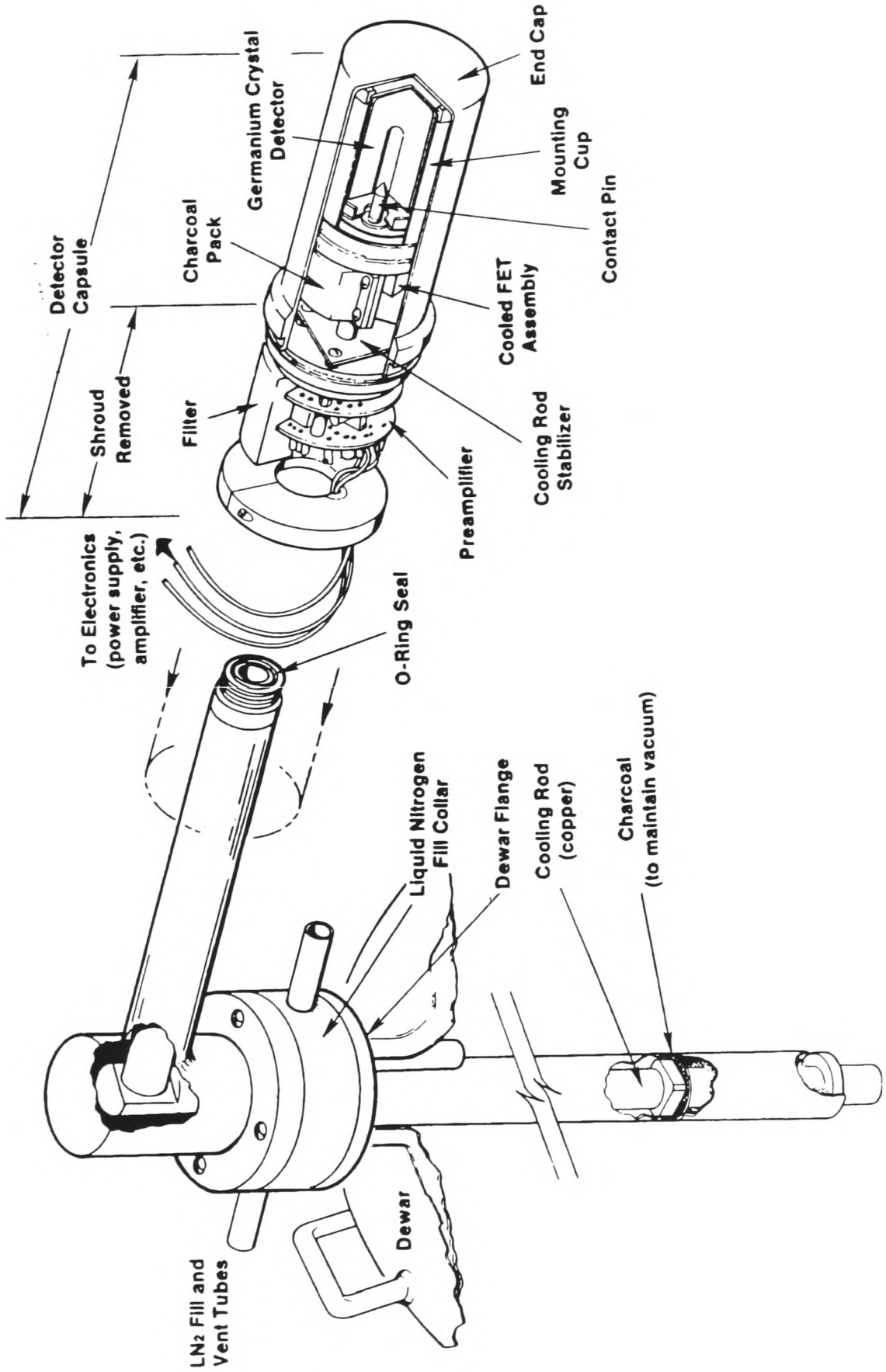


Fig 2.10 Schematic diagram showing the location of a *Ge(Li)/HPGe* detector within its vacuum capsule [15].

References

[1] O.V.Lounasmaa, in Experimental principles and methods below 1K, (Academic Press, 1974) Ch3

[2] T.W.Raudorfetal., IEEE Trans. Nucl. Sci. **NS-31** (1984) 253

[3] H.Postma and N.J.Stone, in Low-Temperature Nuclear orientation eds. N.J.Stone and H.Postma (North-Holland, 1986) ch 1

[4] N.J.Stone, in Low-Temperature Nuclear orientation eds. N.J.Stone and H.Postma (North-Holland, 1986) ch 13

[5] H.Marshak, in Low-Temperature Nuclear orientation eds. N.J.Stone and H.Postma (North-Holland, 1986) ch 16

[6] P.N.Cooper, in Introduction to nuclear radiation detectors (CUP, 1986)

[7] K.Mendelssohn, in The Quest for Absolute Zero (World University Library, 1966)

[8] G.A.Armantrout, IEEE Trans. Nucl. Sci. **NS-21** (1974)287

[9] R.H.Phel etal., IEEE Trans. Nucl. Sci. **NS-20** (1977)68

[10] G.H.Nakano etal., IEEE Trans. Nucl. Sci. **NS-24** (1977)68

[11] T.L.Shaw, D.Phil Thesis (unpublished, 1987)

[12] F.Reif, in Fundamentals of statistical and thermal physics (McGraw-Hill, 1965)

[13] F.Mandl, in Statistical Physics (John Wiley & Sons, 1988)

[14] Oxford Instruments LTD (1979)

[15] G.F.Knoll, Radiation Detection and Measurement (2ed) (John Wiley & Sons, 1989)

Chapter Three

Data Analysis

3.1 Introduction

It has been shown in chapter 1 that the angular distribution of gamma radiation from an oriented source is the combined effect of a many different properties of the nuclear system.

A typical experiment at Oxford can last a few days depending upon the half-life and strength of source. During the experiment some on-line analysis is done to monitor the spectra and the progress of the experiment. The real analysis is performed off-line using the spectrum analysis package GENDAT[1] (General Data Analysis) and the fitting program package MINUIT[2] on the Oxford University Nuclear Physics Vax 8700 computer or on the NOG Dec Alpha work station AV2.

A collection of spectra from an experiment is written to the hard disk of the PC-based data acquisition system and is transferred then to AV2 or the Vax. The program MPTOGEN is used to translate each spectrum into a form which GENDAT can read. Each spectrum is taken over a period of time, the so-called live time at a known geometry with respect to the orientation axis.

In this chapter, the data analysis technique used in this work will be briefly described. The full data analysis routine for preliminary (individual) and final (summed) spectra is shown in fig 3.1 and 3.2.

3.2 Spectrum Analysis

3.2.1 Markers and Calibration

The spectra analysed in this work are 8K channels wide and GENDAT provides three methods of extracting the gamma ray peak areas, namely, CEN, GAS and FTA. These three peak fitting routines will be explained in the next section with examples.

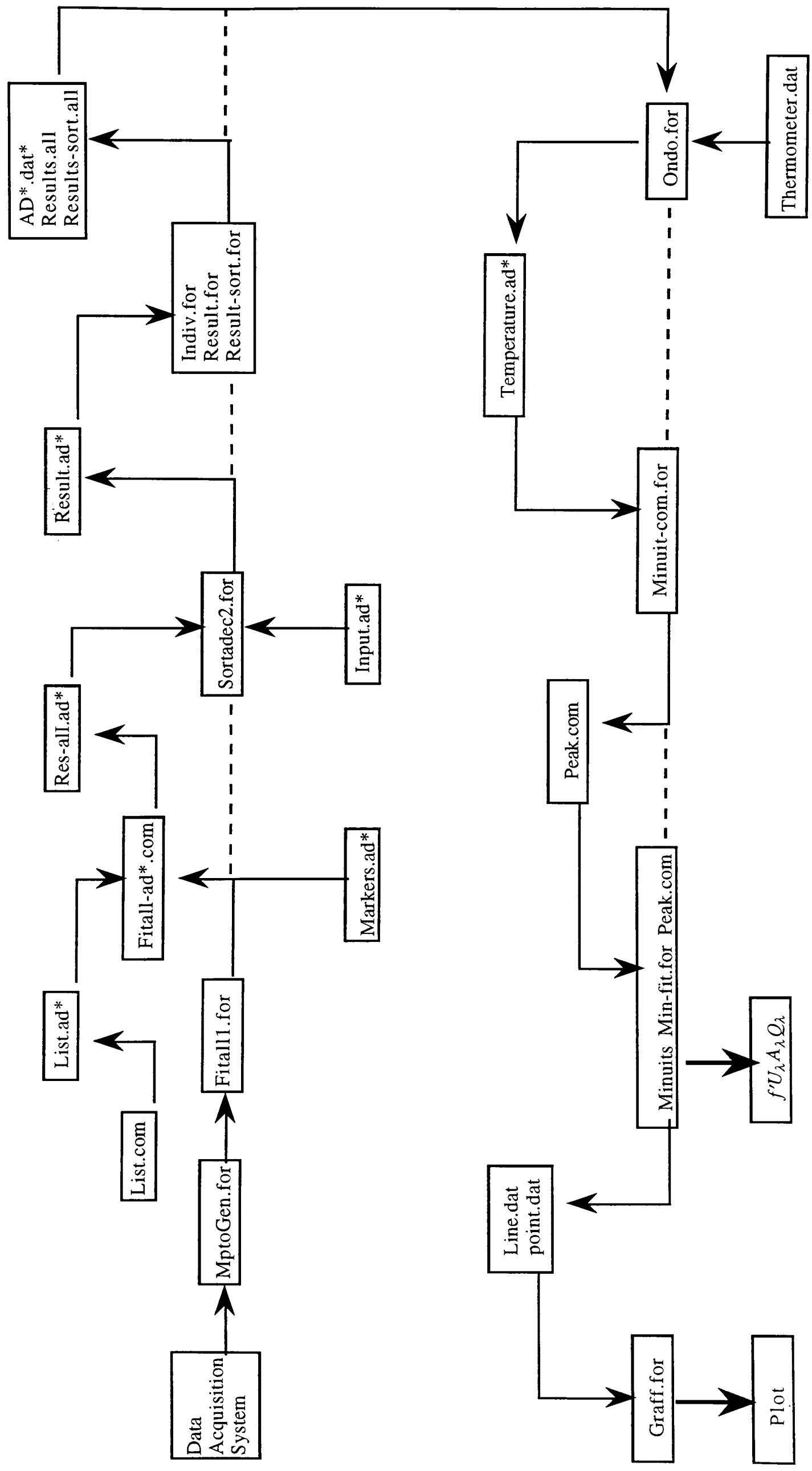


Fig 3.1 A flow chart for the preliminary analysis of all indvidual spectra

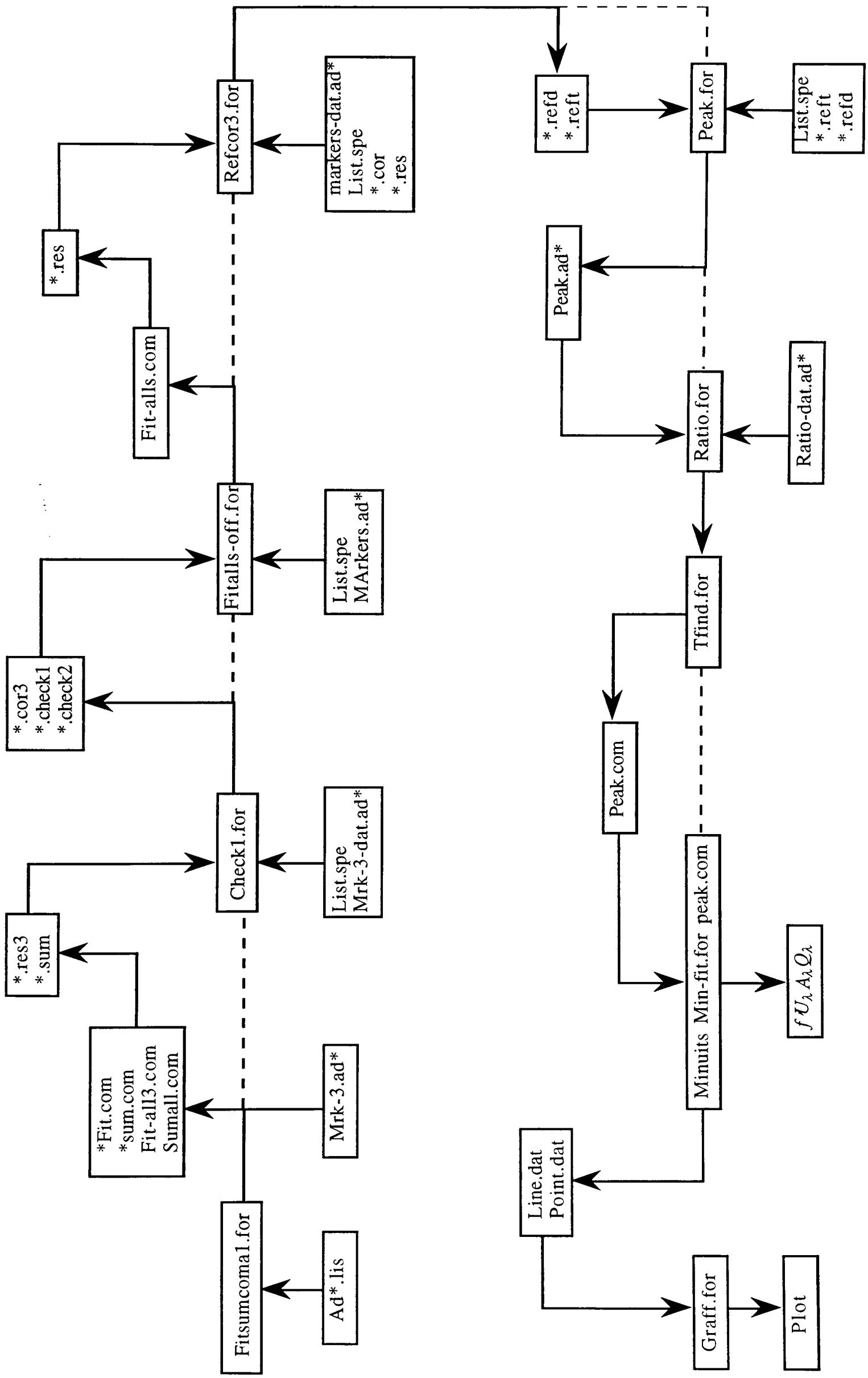


Fig3.2 A flow chart for summed spectra analysis

In GENDAT, markers are set on the displayed spectrum and perform three main functions;
(i) a region for full screen expansion can be defined
(ii) for the peaks of a particular spectrum the channel number, number of counts and energy (if the spectrum is calibrated) can be indicated
(iii) regions of interest (windows) around a peak/group of peaks for the purpose of peak area analysis/calibration can be defined
A set of markers can be stored in the transient program memory (SAV) or permanently in a disc file (SAM).

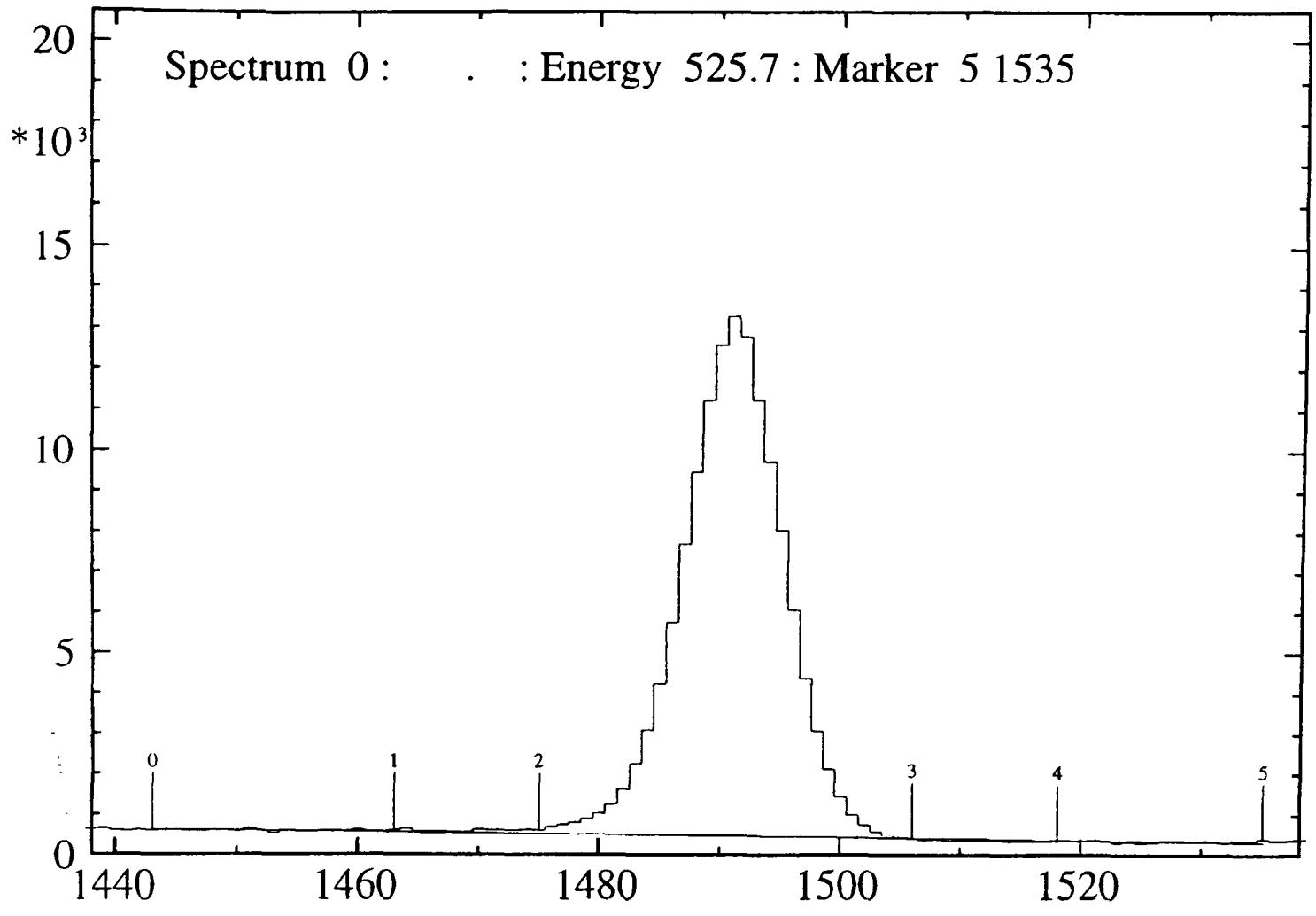
One advantages of GENDAT is its capability of performing large scale analysis automatically once the windows have been set. The results of this analysis are written to data files which will be used by further analysis programs.

In GENDAT, there are two types of energy calibration. One is the simple linear two-point calibration and the other one is the comprehensive least squares multi-point calibration that supersedes the two-point calibration. In both cases, calibration points are supplied by the user, which can be taken from known transition lines in the spectrum over the whole energy range.

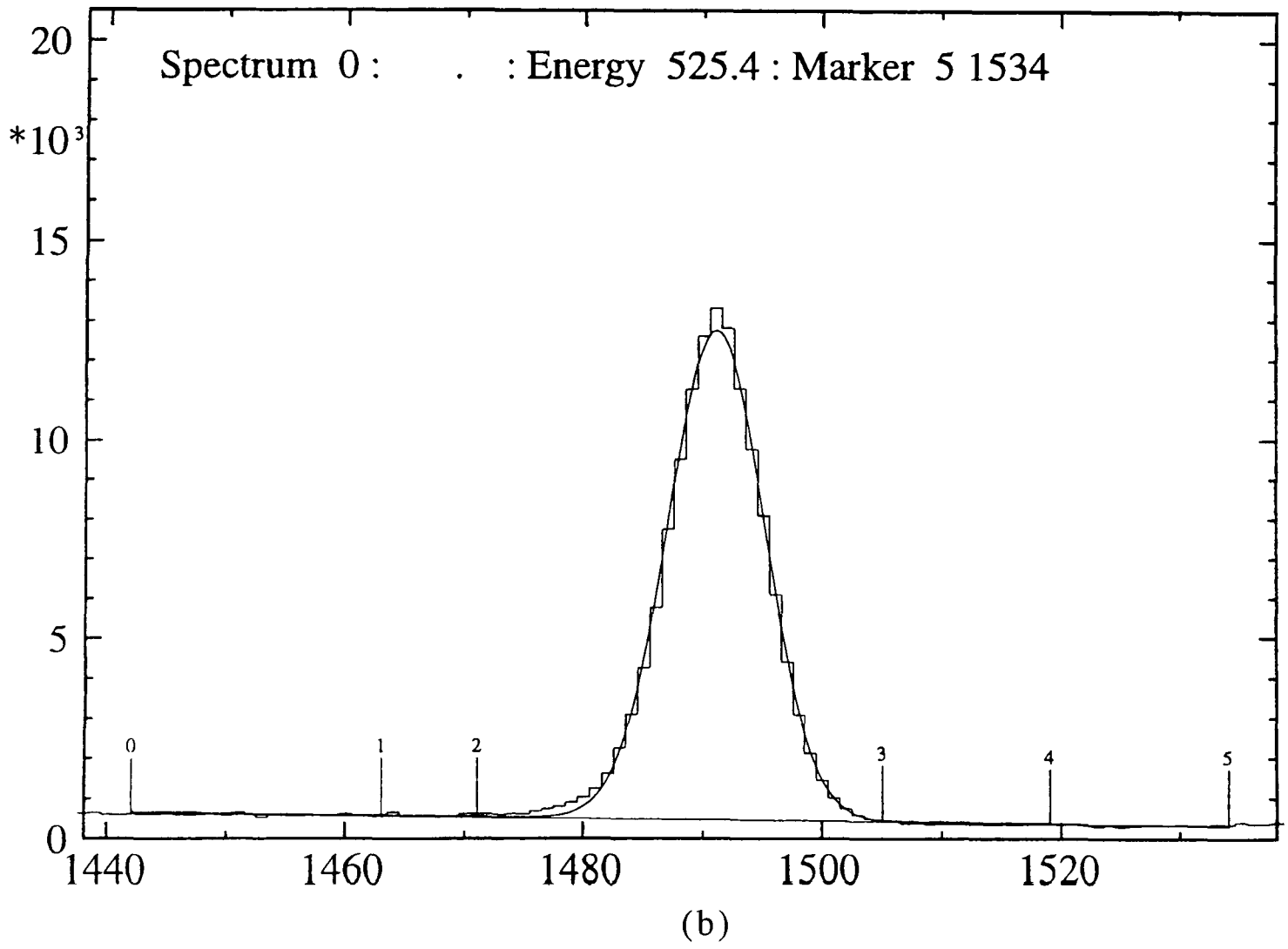
3.2.2 Peak fitting routines

Usually a γ-ray spectrum has many γ-peaks which are sometimes unresolved and a non-constant and often large Compton scattered background under each peak. Therefore, the user may have to decide which of the fitting routines described below to use;
(i) CEN takes simply the total number of counts in the channels lying below the peak and between the peak markers, and subtracts a linear background. Then it fits a single Gaussian to the peak but does not display it. The background, the area and error are displayed (see fig 3.3a).
(ii) GAS is essentially the same as CEN but the fitted Gaussian is displayed in full together with the fit parameters. (see fig 3.3b).
(iii) FTA is a multiple Gaussian fitting program[3], allowing unresolved multiplets to be analysed. The function that is fitted to the observed channel counts N_k is of the form[4]

$$y_{fit}(k) = \left(b_1 + b_2 k + b_3 k^2\right) + \sum_{i=1}^{n} A_i \, exp\left[-\frac{1}{2}\left(\frac{k - C_i}{\sigma_i}\right)^2\right] \qquad (3.1)$$



(a)



(b)

Fig 3.3 Examples of (a) CEN background subtraction (b) GAS fitting

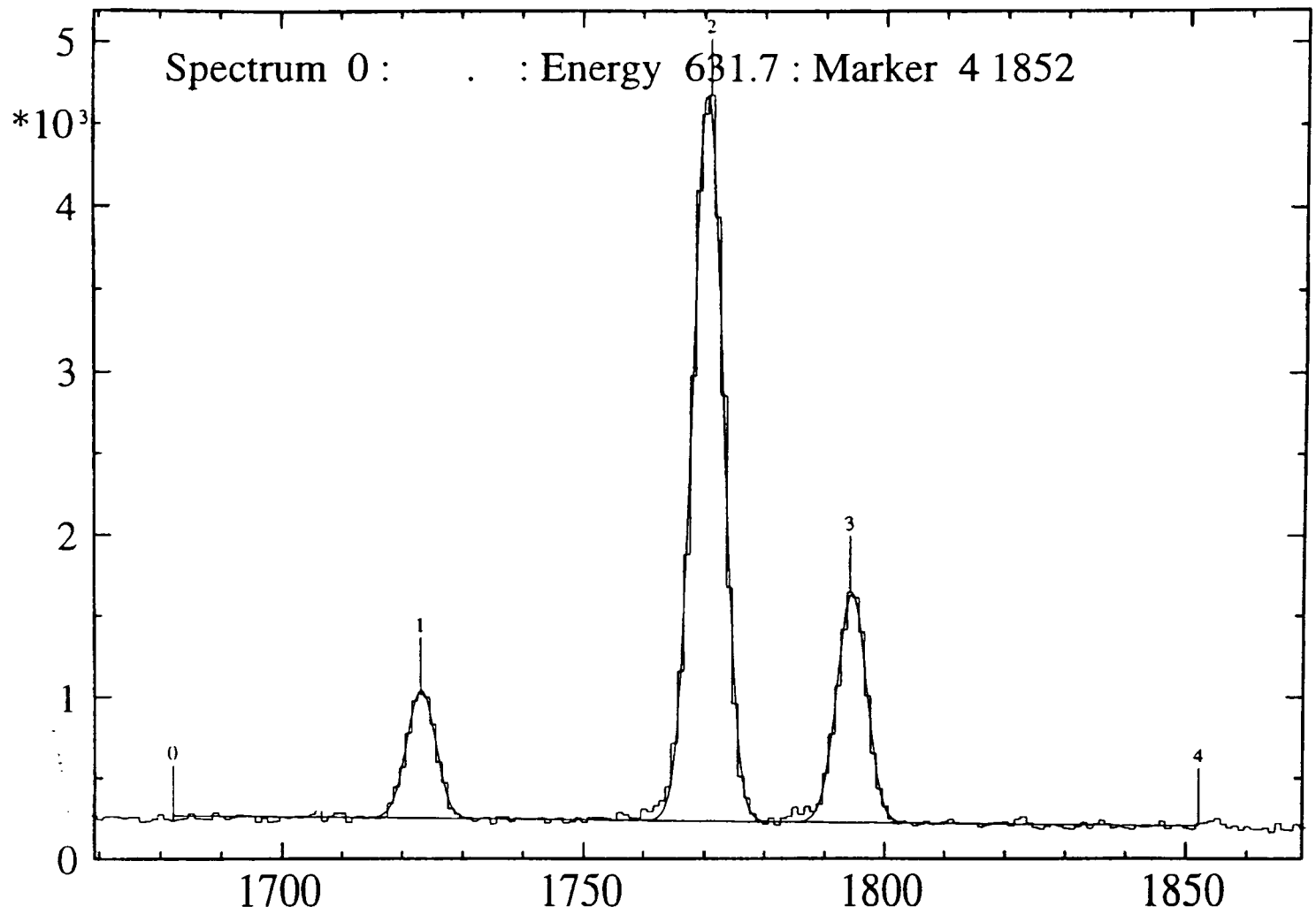


Fig 3.4 An example of FTA fitting

where k denotes a channel number, $b_{1,2,3}$ are linear, quadratic and cubic background terms, and each of the n Gaussian peaks has 3 parameters, A_i, C_i (centroid) and σ_i (FWHM). A region of upto 256 channels may be fitted using a combination of the above parameters. The first and last markers define the background levels and the other markers are first guesses for centroids for the fitting routine. There are options to fix the background type - Constant, Linear, Quadratic and also to fix either or both the FWHM and/or the centroid or to have both as free parameters. When both the FWHM and the centroid are fixed, a maximum of 23 peaks can be fitted but only 7 peaks if both are free parameters. An example of FTA fitting is shown in fig 3.4.

3.2.3 Normalised Anisotropies

The normalised directional distribution of γ - radiation from an axially symmetric oriented ensemble, as measured with polarization insensitive detectors, is given by equation (1.68) where the $\lambda = 0$ term describes an ensemble of randomly oriented nuclei.

Experimentally, normalisation is achieved by taking ratios of the peak areas measure from the nuclei when cold to the corresponding areas measured when the ensemble is warm and randomly oriented. The normalised angular distribution is then

$$W(\vartheta) = \frac{\text{cold area}}{\text{warm area}} = \frac{C_{cold}(\vartheta)}{C_{warm}(\vartheta)} \tag{3.2}$$

The anisotropy $\Lambda(\vartheta)$ can be defined as a percentage

$$\Lambda(\vartheta) = [W(\vartheta) - 1] \times 100\% \tag{3.3}$$

However, for on-line experiments where the source is continually being produced, both by implantation and through the decay of parent nuclei, it is necessary to eliminate the problem of unknown source strength by taking the ratio of the axial (ϑ=0) and the equatorial (ϑ=90) count rates $\Gamma(\vartheta)$, where

$$\Gamma(\vartheta) = \left[\frac{W(0)}{W(90)} - 1\right] \times 100\% \tag{3.4}$$

3.2.4 Dead time correction

Dead time refers to a minimum amount of time that must separate two events in order that they can be recorded as two separate pulses. Usually the preset live time is fixed for a spectrum acquisition to ensure that changes in count rate, and hence changes in dead time, do not introduce any errors in calculating the count rate.

There are two models of dead time behaviour of a counting system, namely, paralyzable and nonparalyzable response. In the paralyzable case, the true interaction rate, n, is given by

$$n = me^{n\tau} \tag{3.5}$$

where m is the recorded count rate and τ is the dead time.
In the case of nonparalyzable, n is given by

$$n = \frac{m}{1 - m\tau} \tag{3.6}$$

For low rates $(n << 1/\tau)$, (3.5) and (3.6) reduce to

$$\begin{aligned} m &= ne^{-n\tau} \cong n(1 - n\tau) \\ m &= \frac{n}{1 + n\tau} \cong n(1 - n\tau) \end{aligned} \tag{3.7}$$

As can be seen from (3.7) the two modes lead to identical results in the limit of small dead time losses.

To correct for the dead time without involving mathematical complication, it is necessary to normalise the total counts collected to the live time rather than the real time of the counting period. The relationship between real time, dead time τ, and live time is

$$T_{real} = T_{live} + \tau \tag{3.8}$$

Dead time can be corrected by introducing a regular count rate pulser into the system to be recorded as part of the spectrum. However, the pulser introduces its own dead time into the system which can not be corrected for. To overcome this problem, the count rate of the pulser should be small compared to the total count rate. Introducing pulser normalisation into (3.2)

$$W(\vartheta) = \frac{C_{cold}(\vartheta)}{C_{warm}(\vartheta)} \cdot \frac{P_{warm}(\vartheta)}{P_{cold}(\vartheta)} \tag{3.9}$$

where $P_{warm}(\vartheta)$ and $P_{cold}(\vartheta)$ are pulser counts in the warm and cold spectra respectively. The pulser technique for dead time correction was used in this work and the pulsar rate was set to a value that creates negligible dead time compared to the dead time due to the source under observation. As the pulsar sources ^{22}Na and ^{207}Bi were used for the experiments ^{133}I and ^{135}I, respectively.

3.2.5 Half-life correction

If N radioactive nuclei are present at time t and if there is no supply of nuclei to the sample, the decay constant/disintegration rate is given by

$$\lambda = -\frac{(dN/dt)}{N} \tag{3.10}$$

Integrating (3.10) gives the exponential law of radioactive decay

$$N(t) = N(0)e^{-\lambda t} \tag{3.11}$$

where $N(0)$ is the original number of nuclei present at t=0.

If spectra of period Δt are measured consecutively so that the first spectrum begins counting at t=0 and the n-th spectrum start at $n\Delta t$, then the correction factor Ξ_n which must multiply the n-th spectrum is

$$\Xi_n = \frac{N(0)\Delta t}{\int_{n\Delta t}^{(n+1)\Delta t} N(t)dt} = \frac{\lambda \Delta t e^{\lambda n \Delta t}}{\left[1 - e^{-\lambda \Delta t}\right]} \tag{3.12}$$

This correction must be included in the determination of the anisotropy otherwise the anisotropy of an ensemble at a constant temperature would vary with time.

3.2.6 Extraction of the A_2 and A_4 terms of the angular distribution

As discussed in (1.3.5), to describe the angular distribution $W(\vartheta)$ only the $\lambda = 2, 4$ terms are usually needed. Therefore, from (1.62)

$$\begin{aligned} W(0) &= 1 + fB_2U_2A_2Q_2^{ax}P_2^{ax} + fB_4U_4A_4Q_4^{ax}P_4^{ax} \\ W(90) &= 1 + fB_2U_2A_2Q_2^{eq}P_2^{eq} + fB_4U_4A_4Q_4^{eq}P_4^{eq} \end{aligned} \tag{3.13}$$

where $Q_\lambda^{ax,eq}$ are the solid angle corrections and $P_\lambda^{ax,eq}$ are the Legendre polynomial terms for the axial ($\vartheta = 0$) and the equatorial ($\vartheta = 90$) detectors. Solving (3.13) in terms of $fB_2U_2A_2$ and $fB_4U_4A_4$ gives

$$fB_2U_2A_2 = \frac{Q_4^{eq}P_4^{eq}[W(0)-1]-Q_4^{ax}P_4^{ax}[W(90)-1]}{Q_2^{ax}P_2^{ax}Q_4^{eq}P_4^{eq}-Q_2^{eq}P_2^{eq}Q_4^{ax}P_4^{ax}}$$

$$= \frac{3[W(0)-1]-8\left(\frac{Q_4^{ax}}{Q_4^{eq}}\right)[W(90)-1]}{Q_2^{ax}\left\{3+4\left[\frac{(Q_4^{ax}/Q_4^{eq})}{(Q_2^{ax}/Q_2^{eq})}\right]\right\}} \qquad (3.14a)$$

$$fB_4U_4A_4 = \frac{Q_2^{ax}P_2^{ax}[W(90)-1]-Q_2^{eq}P_2^{eq}[W(0)-1]}{Q_2^{ax}P_2^{ax}Q_4^{eq}P_4^{eq}-Q_2^{eq}P_2^{eq}Q_4^{ax}P_4^{ax}}$$

$$= \frac{4[W(0)-1]_8\left(\frac{Q_2^{ax}}{Q_2^{eq}}\right)[W(90)-1]}{Q_4^{ax}\left\{4+3\left[\frac{(Q_4^{ax}/Q_4^{eq})}{(Q_2^{ax}/Q_2^{eq})}\right]\right\}} \qquad (3.14b)$$

with $P_2^{ax} = P_4^{ax} = 1$, $P_2^{eq} = -1/2$ and $P_4^{eq} = 3/8$.

For the case $Q_\lambda^{ax} = Q_\lambda^{eq} = Q_\lambda$, (3.14) simplifies to

$$fB_2U_2A_2Q_2 = \frac{1}{7}\{3[W(0)-1]-8[W(90)-1]\}$$
$$fB_4U_4A_4Q_4 = \frac{4}{7}\{[W(0)-1]+2[W(90)-1]\} \qquad (3.15)$$

Under the assumption that a fraction f of the ensemble nuclei experience the full hyperfine interaction, the remainder being unoriented, it is possible, when the temperature and the hyperfine interaction, and hence the B_λ orientation parameters are known, to determine the products $fU_\lambda A_\lambda$ experimentally.

With knowledge of $U_\lambda A_\lambda$ coefficients for a particular gamma ray the fraction in good sites, f, can be determined by temperature dependence fitting, and, consequently, $U_\lambda A_\lambda$ can then be calculated for other transitions in the same decay using this value of f.

References

[1] D.Sinclair and T.Fox, Nuclear Physics Laboratory, Oxford (1973)

[2] F.James and M.Ross, Comp. Phys. Comm. **10**(1975)343

[3] D.W.O.Rogers, Nuclear Physics Laboratory, Oxford (1973)

[4] P.R.Bevington, in Data reduction and error analysis for the physical sciences (McGraw-Hill, 1969)

[5] K.S.Krane, in Introductory Nuclear Physics (John-Wiley, 1988)

[6] J.Rikovska et al., in Low-Temperature Nuclear Orientation, Eds. N.J.Stone and H.Postma (North-Holland, 1986) ch 4

Chapter Four

Nuclear Orientation decay studies of ^{133}I and ^{135}I

4.1 Introduction

^{133}I having $Z = 53$ and $N = 80$ has three protons above the closed shell Z=50 and two neutrons holes in $N = 82$ shell, while ^{135}I has fully closed neutron shell since it has $N = 82$, and they are of considerable theoretical interest since a wide variety of the theoretical nuclear models may be used to describe the observed levels close to the stable double closed shell structure.

From a measurement of the directional distribution of $\gamma-$ rays emitted by an ensemble of oriented nuclei one can extract several nuclear quantities. At a given degree of orientation of the parent nuclei the directional anisotropy of a $\gamma-$ transition is determined by the final and initial spins of the transition, by the mixing ratio of the multipoles contributing to the transition and by changes of orientation parameters due to the coupling of angular momenta in preceding $\beta-$ and $\gamma-$ transitions. The anisotropy of a $\gamma-$ radiation in a NO experiment is given by (3.13). In a LTNO spectroscopy experiment, f, Q_λ and B_λ must be known since they contain all the information about to experimental geometry and the orientation of the parent state in the host lattice. The product $A_\lambda U_\lambda$ contains the information about $\beta-$ decay and subsequent transitions between levels of the daughter. f can be determined from (3.13) for a transition in which the $A_\lambda U_\lambda$ coefficients are calculable from the decay scheme. The Q_λ can be calculated from the detector-source geometry. In this experiment, they are $Q_2 = 0.97(1)$ and $Q_4 = 0.89(1)$.

Using the large hyperfine field felt by iodine nuclei in an iron lattice, it is relatively easy to obtain a high degree of nuclear orientation with the LTNO techniques.

In this chapter, spin assignments of ^{133}I and ^{135}I will not be discussed since all observed levels are well established and the experimental details and results will be presented and discussed.

4.2 Experimental details

At OSIRIS the activity was produced by the thermal fission of neutron irradiated ^{235}U, ionised and accelerated to ~ 60 keV. Sources of ^{133}I and ^{135}I were implanted separately at room temperature into polycrystalline iron foils. Before implantation the foils were annealed for ~ 12h at 840^0C in a hydrogen atmosphere. The sources were subsequently studied at Oxford at temperature down to ~ 20 mK using the $^3He/^4He$ dilution refrigerator.

Three Ge(Li) detectors were placed equatorially and one Ge(Li) detector was placed axially relative to the axis of orientation, defined by a 0.7 T polarising field. A number of external factors, such as detector geometry, absorbers between source and detector and electronics were kept the same throughout the measurement.

The data taken at different temperatures are normalised and half-life corrected to data taken at a temperature where the polarisation is insignificant.

4.3 Nuclear Orientation decay studies of ^{133}IFe

4.3.1 Introduction

In the decay of ^{133}I, most of the low-lying $(5/2)^+$ and $(7/2)^+$ states in ^{133}Xe are populated by allowed Gamow-Teller transitions with $log\,ft \geq 7$. The population of these states through $\pi g_{7/2} \rightarrow \nu g_{7/2}$ may be due to configuration admixtures which are small and or which involve incoherent contributions from different components. Its partial decay scheme is shown in fig 4.1.

The spin of the ^{133}I ground state has been measured[1] as $(7/2)^+$. The spin of the ^{133}Xe ground state was obtained from the $^{134}Xe(d,t)$ reaction[1] and from the characteristics[1] of the $\beta-$ decays of ^{133}I to ^{133}Xe and ^{133}Xe to ^{133}Cs. Also the magnetic moment of ^{133}I ground state has been measured by a " flop-in " atomic-beam magnetic resonance[3] to be $2.856(5)\mu_N$.

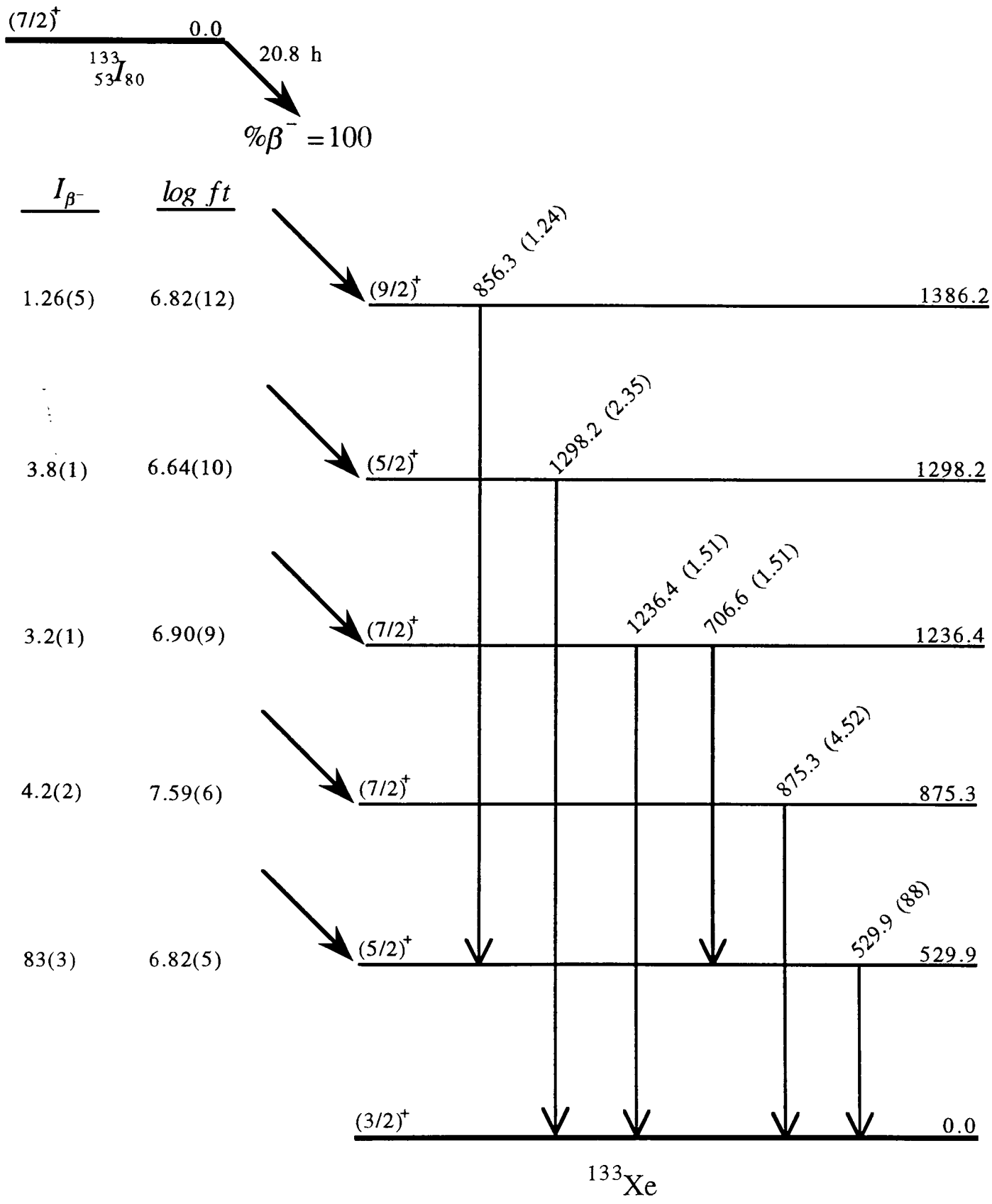


Fig 4.1 A partial decay scheme of ^{133}I

4.3.2 Temperature dependence results

529.9 level($J^{\pi} = \left(\frac{5}{2}\right)^{+}$)

The 529 keV level in ^{133}Xe is almost entirely populated by the pure Gamow-Teller $\left(\frac{7}{2}\right)^{+}$ to $\left(\frac{5}{2}\right)^{+}$ $\beta-$ decay. This level has direct $\beta-$ feeding of ~ 83% and indirect $\beta-$ feeding of ~ 3.7% (the percentages refer to total decays of ^{133}I). The weak feeds were ignored because the uncertainty they introduce into the decay parameters is much less than the experimental error.

The 529.9 keV level is well established and its theoretical de-orientation coefficients U_λ are

$$U_2 = 0.874 \qquad U_4 = 0.58$$

and, from measured anisotropy of the 529.9 keV transition, U_2A_2 =-0.76(3) and U_4A_4 =0.27(2), the angular distribution coefficients A_λ are calculated as

$$A_2 = -.87(3) \qquad A_4 = .47(4)$$

Thus the deduced E2/M1 mixing ratio for the this $\frac{5}{2}^{+} \rightarrow \frac{3}{2}^{+}$ transition is

$$\delta(529.9) = 2.4(2)$$

The experimental value of U_4A_4 = 0.27(2) eliminated another mixing ratio. The deduced mixing ratio is in broad agreement, within error, with the value given by Achterberg et al[6] (see Table 4.1).

With these data, the temperature dependence fitting gives

$$f \sim 79(3)\ \%$$

This value of f is used in all analysis of ^{133}I decays.

The product μB of magnetic moment ×hyperfine field of ^{133}I was found to be $312(4)\mu_N T$ by least square fitting of the temperature dependence of the 529.9 keV gamma-ray transition (see fig 4.2). This means that if we accept μ = $2.856(5)\mu_N$then the B_{hf} = 109.2(1.4)T which differs from the B_{hf}=114.4(2)[29]. Green et al[24], previously, obtained B_{hf} = 103.5(9)T by fitting integral nuclear orientation data on a cold-implanted, room temperature annealed, source of ^{131}I in

Fe. These results on the interaction strength are discussed in section 4.6.

<u>875 keV level</u>($J^{\pi} = \left(7/2\right)^{+}$)

The 875 keV level is populated $\left(7/2\right)^{+}$ to $\left(7/2\right)^{+}$ and has direct $\beta-$ feeding of ~ 4.2% and indirect $\beta-$ feeding of ~ 0.4%. According to Saxena and Sharma[28], the 875 keV gamma-ray is a possible unresolved doublet but we did not observe its double character.

The 875 keV transition has E2 character where we have assumed M3 contribution is negligible, $\left(7/2\right)^{+}$ to $\left(3/2\right)^{+}$ giving its theoretical values of A_{λ} as

$$A_2 = -0.468 \qquad A_4 = -0.358$$

Therefore we obtained the experimental value of U_{λ} from the measured anisotropy $U_2A_2 = -0.378(14)$ and $U_4A_4 = -0.154(29)$ as

$$U_2 = 0.81(3) \qquad U_4 = 0.43(8)$$

These are consistent with predominantly Gammow-Teller decay, for which $U_2 = 0.8095$ and $U_4 = 0.3651$. A pure Fermi decay would have $U_2 = U_4 = 1.0$.

<u>1236.4 keV level</u>($J^{\pi} = \left(7/2\right)^{+}$)

This level has direct $\left(7/2\right)^{+}$ to $\left(7/2\right)^{+}$ beta decay feed of ~ 3.2%. The 1236 keV $\gamma-$transition is a $\left(7/2\right)^{+}$ to $\left(3/2\right)^{+}$ E2 transition giving its theoretical value of A_{λ}, if we assume M3 contribution is negligible, as

$$A_2 = -0.468 \qquad A_4 = -0.358$$

The experimental deorientation coefficients U_{λ} are then calculated from the measured anisotropy of the 1236.4 keV transition $U_2A_2 = -0.416(19)$ and $U_4A_4 = -0.20(5)$as

$$U_2 = 0.89(4) \qquad U_4 = 0.56(13)$$

which indicate a considerable Fermi admixture in the beta transition.

Using the these data, analysis of the $\left(7/2\right)^{+}$ to $\left(5/2\right)^{+}$ transition at 706.6 keV

yields its M1/E2 mixing ratio as

$$\delta(706.6)= 4.4(3) \text{ or } .46(2)$$

The small value of U_4A_4 selects the lower E2/M1 mixing ratio

$$\delta(706.6)= 0.46(2)$$

which is in good agreement with the lower value given by Koen et al[8].

1298.2 keV($J^\pi = (5/2)^+$)

The 1298.2 keV level is populated by the Gamow-Teller $(7/2)^+$ to $(5/2)^+$ direct $\beta-$ decay feeding of ~ 3.8%. Therefore, the theoretical values of U_λ are

$$U_2 = 0.874 \qquad U_4 = 0.580$$

The 1298.2 keV gamma transition is a mixed (E2/M1) character in $(5/2)^+$ to $(3/2)^+$. From the measured anisotropy U_2A_2 =-0.546(2) and U_4A_4 =0.08(1), A_λ have been deduced for this transition as

$$A_2 = -0.625(2) \qquad A_4 = 0.14(2)$$

The extracted E2/M1 mixing ratio is then

$$\delta(1298.2)= 4.1(3) \text{ or } .59(2)$$

The low experimental value of U_4A_4 ~0.08, favours the smaller δ value

$$\delta(1298.2)= 0.59(2)$$

in disagreement with the dominant E2 strength reported by Krane et al[9].

1386.2 keV($J^\pi = (9/2)^+$)

This level has direct beta decay feed of ~ 1.26%. The experimental U_2A_2 = -0.426(19) value of the 856.3 keV transition to the $5/2^+$ state allows the assignments $J(1386) = 7/2, 9/2$. J=5/2 being eliminated by the absence of a

transition to the J=3/2 ground state. In the case of $J(1385) = 7/2$ the mixing ratio obtained from the U_2A_2 term requires $U_4A_4 > 0$. Thus the experimental value U_4A_4 = -0.16(3) excludes $7/2$. For $J(1386) = 9/2$, the theoretical values of U_λ are

$$U_2 = 0.925 \qquad U_4 = 0.749$$

From these the experimental values of A_λ for the 1368.2 keV transition are

$$A_2 = -.46(2) \qquad A_4 = -.22(4)$$

The theoretical values of A_λ for a 9/2 to 5/2 pure E2 transition are:

$$A_2 = -.432 \qquad A_4 = -.268$$

Therefore we conclude that the spin of the 1386.2 keV level is $9/2^+$ and the 856.3 keV transition is pure E2 character.

4.4 NMR/ON on ^{133}I

4.4.1 Experiment

The method of combining nuclear orientation with NMR has become a very popular technique in recent years for determining nuclear magnetic dipole moments very precisely (see section 1.5.2). The purpose of the NMR/ON experiment was to measure the hyperfine field with greater precision and to get some idea of the proportion of nuclei subject to it.

The hyperfine magnetic field of I in Fe had been measured using the Mössbauer technique[1]. Their measurement was on a source prepared by implantation of $^{129}Te^m$ into Fe at ~ 50 keV. The spectra obtained were consistent with *Te* atoms being distributed between two kinds of site, one experiencing a large magnetic field, the other giving an unresolved contribution to the spectra characteristic of *Te* atoms in low field or non-magnetic sites. In the present experiment *I* was implanted directly so that the hyperfine field would be expected to be the same but the distribution of the *I* atoms would probably be rather different.

The Fe foil, together with a $^{192}IrFe$ nuclear orientation thermometer, was

soldered with Wood's metal to a copper cold finger and top-loaded into the dilution refrigerator. An axial detector was used to detect the gamma-rays with respect to 0.7 *T* polarising field. The ^{133}I sample was cooled down to ~ 20 mK and resonance was searched for in steps of 0.5 MHz with the RF signal frequency modulation 1MHz between frequencies of 707 MHz and 716 MHz. The resonance search was done with the frequency modulation off (FM off) and then on (FM on) for each frequency point with the 529 keV gamma-ray of ^{133}I being used as the monitoring peak. A weak resonance of ^{133}I was observed (destruction of ~ 4%). This small peak destruction may be a consequence of the large linewidth of the polycrystalline resonance.

4.4.2 Results

The data for the 529 keV gamma-ray line of ^{133}I (fig 4.4) was analysed to give the destruction of anisotropy given by the equation:

$$D(\%) = \frac{N_{off} - N_{on}}{N_{off}} \times 100 \qquad (4.1)$$

where N_{off} is the anisotropy with unmodulated rf and N_{on} is the anisotropy with frequency modulation rf. A least squares fit of a Gaussian line shape to the data points gave a centre frequency at 712.25(25) MHz with a FWHM=2.25 MHz. The total integrated destruction of the resonance was deduced to be 34(6)%. If we take the magnetic moment of ^{133}I to be $\mu = 2.856(5)\mu_N$[3] and assume a zero Knight shift the calculated magnetic hyperfine field is:

$$B_{hf}\left(^{133}IFe\right) = 114.51(24)T \qquad (4.2)$$

in full agreement with the previous NMR/ON results of James[29] and Visser[30].

4.5 Nuclear Orientation decay studies of ^{135}I

4.5.1 Introduction

Since the ^{135}Xe has only a single neutron hole in the N = 82 shell, the energy

levels of ^{135}Xe are of particular interest. Higher energy states of ^{135}Xe are likely to result from coupling between excited core and single-hole states or from a three-quasiparticle excitation while the low-energy levels of ^{135}Xe are expected to be largely single-hole states in the neutron shell.

Two samples were prepared as described in section (4.2) and two independent experiments were performed. In each experiment, the sample and a $^{192}IrFe$ nuclear orientation thermometer were soldered onto the cold finger with Wood's metal, and then it was top-loaded into the Oxford dilution refrigerator. A polarizing field of 0.7 Tesla was applied to the sample and the dilution refrigerator was cooled down to ~ 20 *mK*.

The levels and transitions in ^{135}Xe have been studied by measuring a total of 15 gamma-rays from the levels populated through the β^- – decay of ^{135}I. A partial level decay scheme is shown in (fig 4.5). In this section, only one value of mixing ratio for each mixed transition is given. It was possible to select it by their A_4 coefficient term wherever possible, otherwise two mixing ratios are given if they can not be distinguished from each other by A_4 (see section 4.3.2).

4.5.2 Temperature dependence results

A magnetic moment and the fraction of good sites were extracted from the 1260 keV gamma transition (which is the most intense transition), 1038 keV E1 transition and 1706 keV E1 transition by simultaneous least squares fits (see fig 4.6 - 4.8 for example of the temperature dependence fit). The good site fractions for the two samples were found to be, due to the different implantation conditions,

$$f_1 \sim 74(3)\% \quad \text{and} \quad f_2 \sim 86(3)\%$$

The magnetic moment of ^{135}I was found to be $\mu B = 290.6(23)$ from the combined fits and, from this, we have deduced the magnetic moment assuming two different values of B_{hf} as

$$\mu = 2.54(2)\mu_N \qquad \text{with } B_{hf} = 114.4(2)$$
$$\mu = 2.66(6)\mu_N \qquad \text{with } B_{hf} = 109.2(1.4)$$

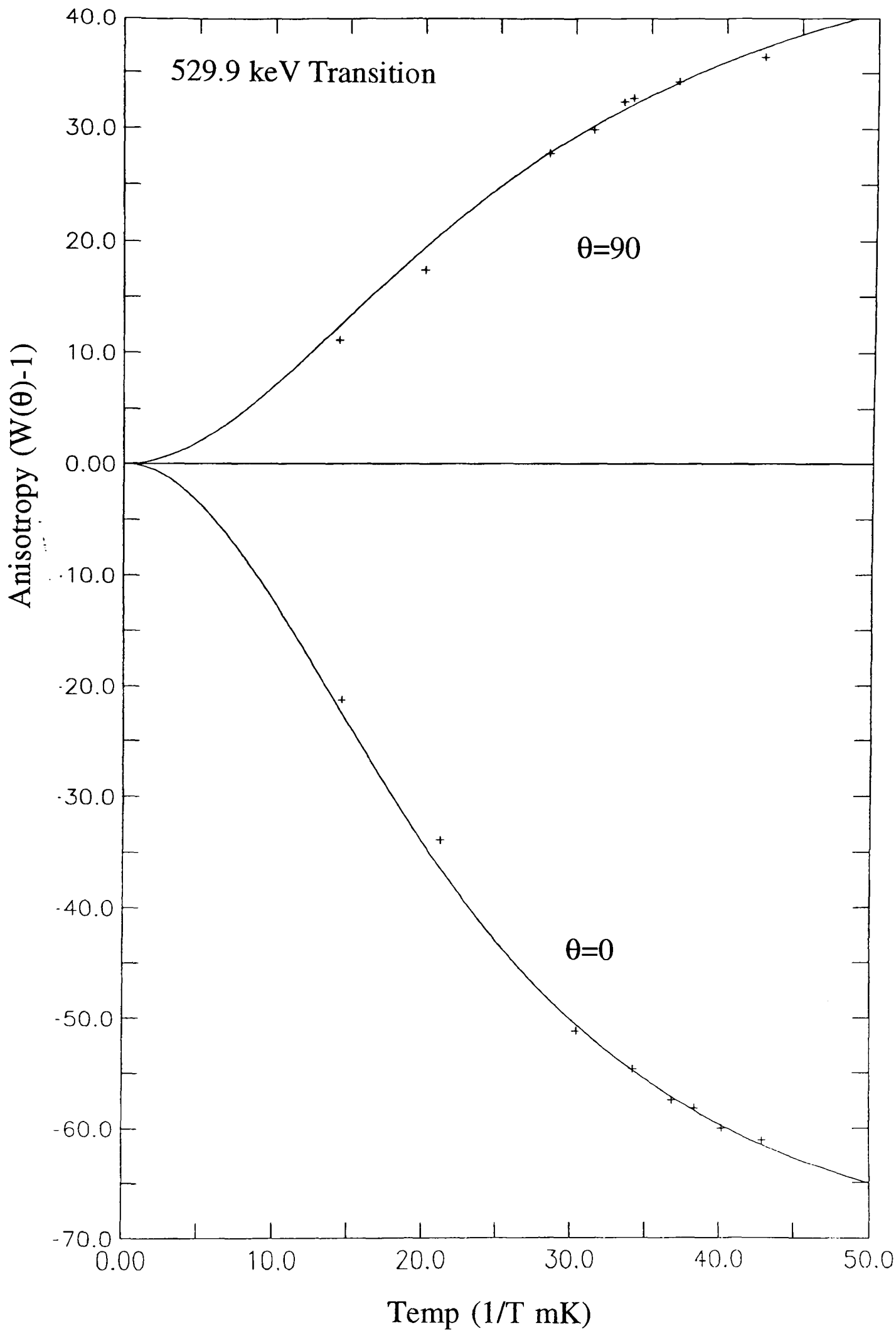


Fig 4.2 Axial/Equatorial anisotropy for the 529.9 keV transition as a function of 1/T seen in the decay of ^{133}I (in Fe)

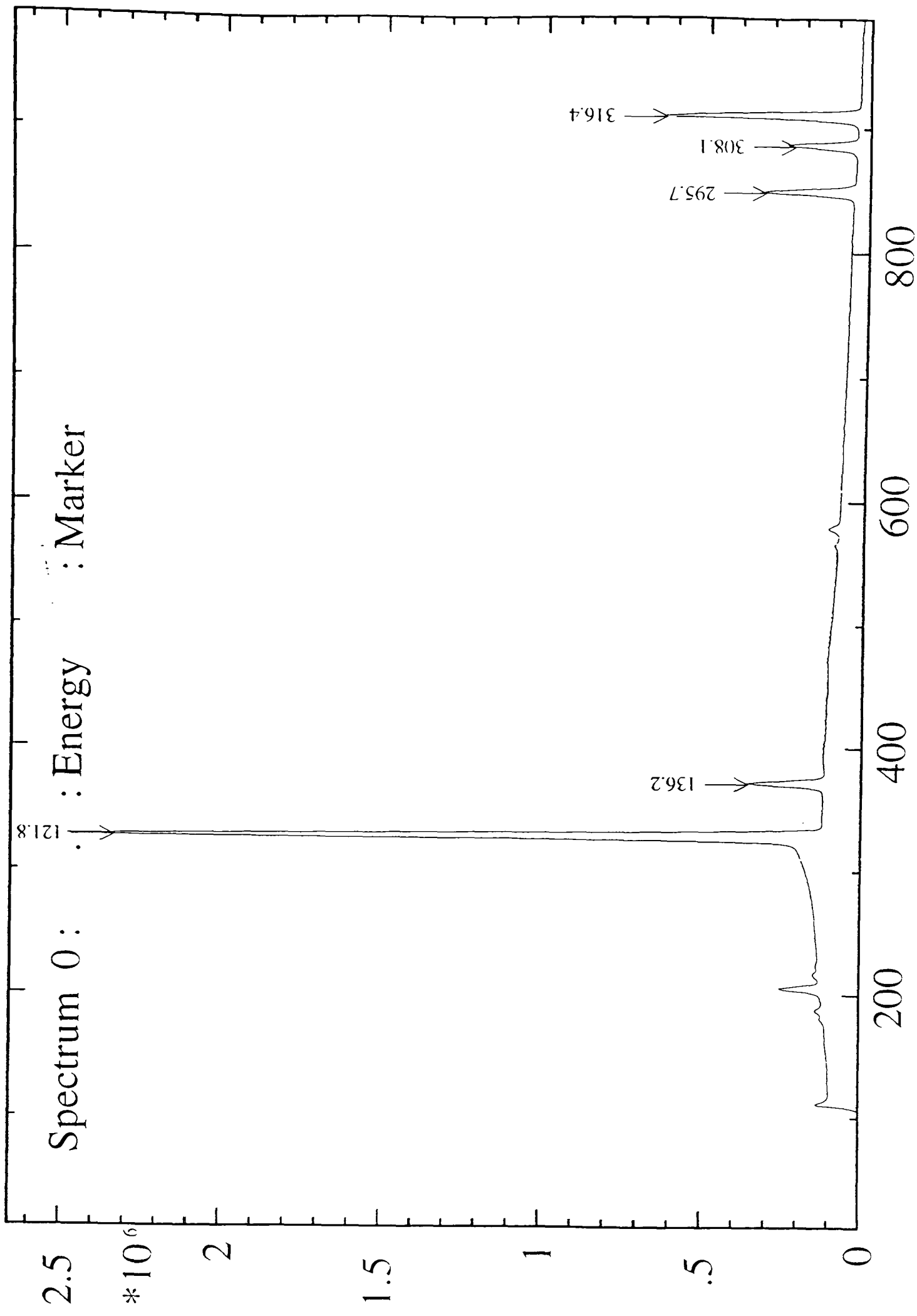


Fig 4.3 (a) Part of a gamma-ray spectrum of ^{133}I with ^{57}Co, ^{192}Ir thermometers and ^{22}Na sample used as a pulsar. The energies shown above are the energies in keV for the channel nearest to the peak centre and are correct to within ~ 0.5keV. The accurate fitted energies are given in table 4.1. (Channel numbers 0 to 1000).

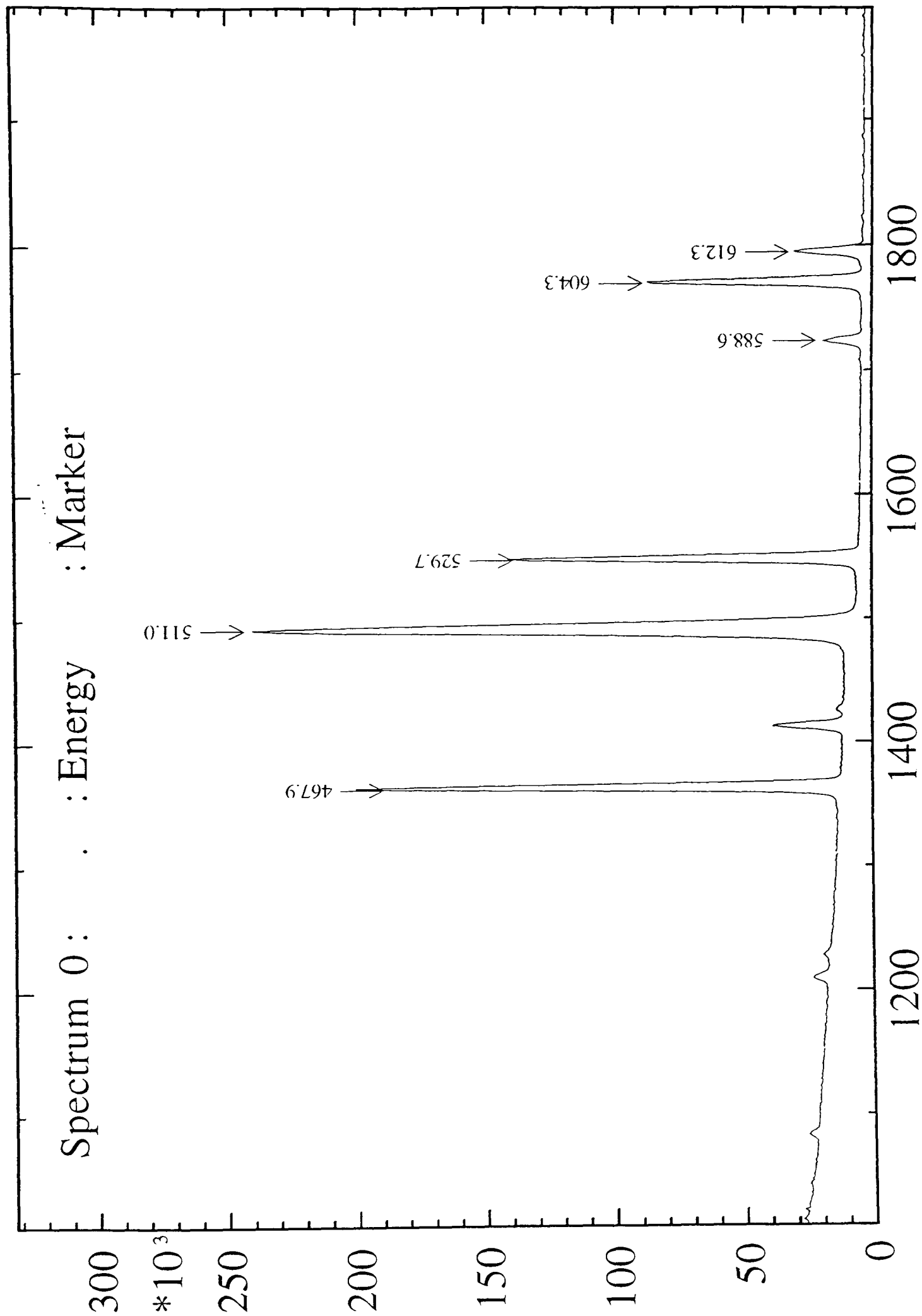


Fig 4.3(b) Part of a gamma-ray spectrum of ^{133}I (Channel numbers 1000-2000).

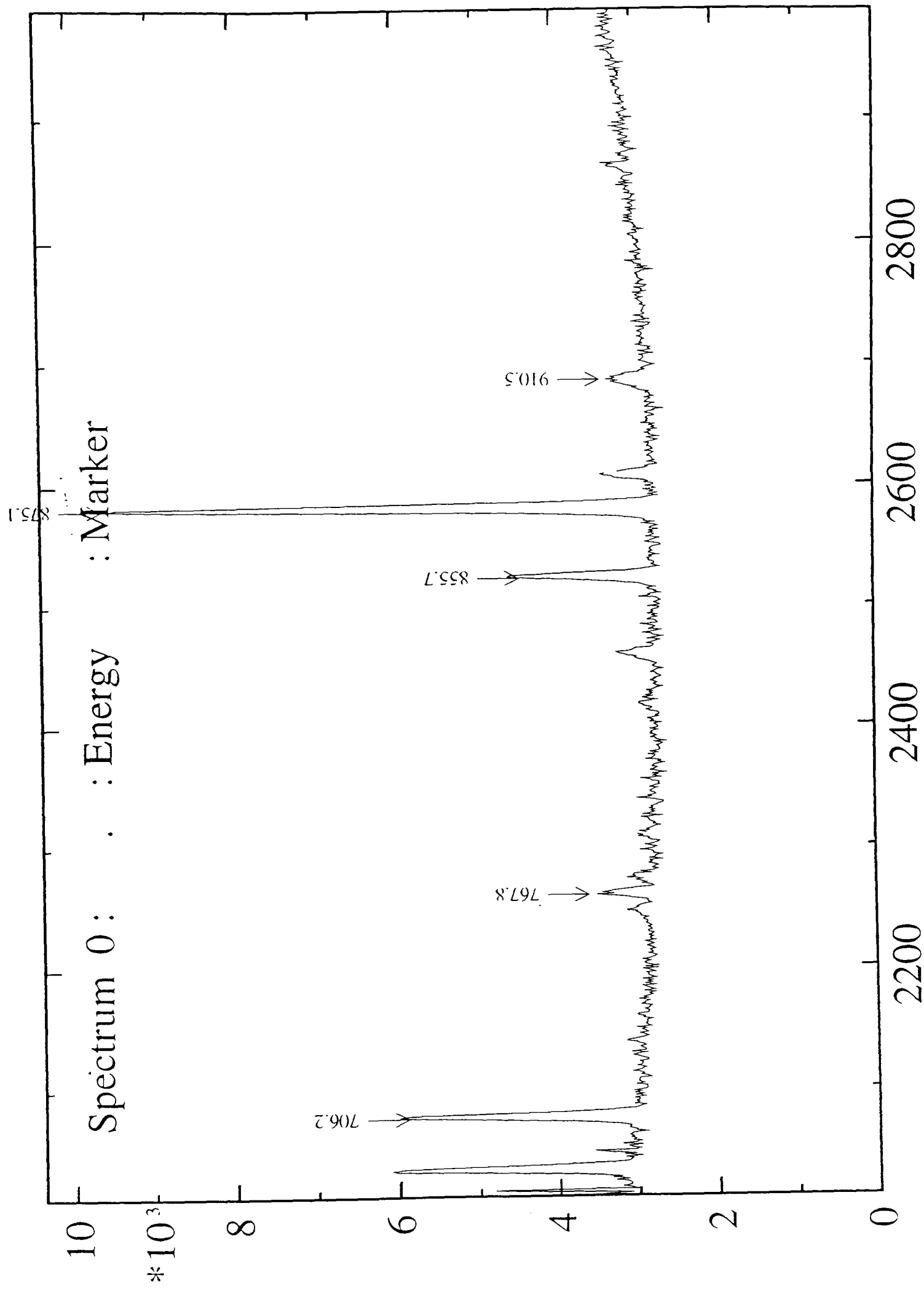


Fig 4.3(c) Part of a gamma-ray spectrum of ^{133}I (Channel numbers 2000-3000).

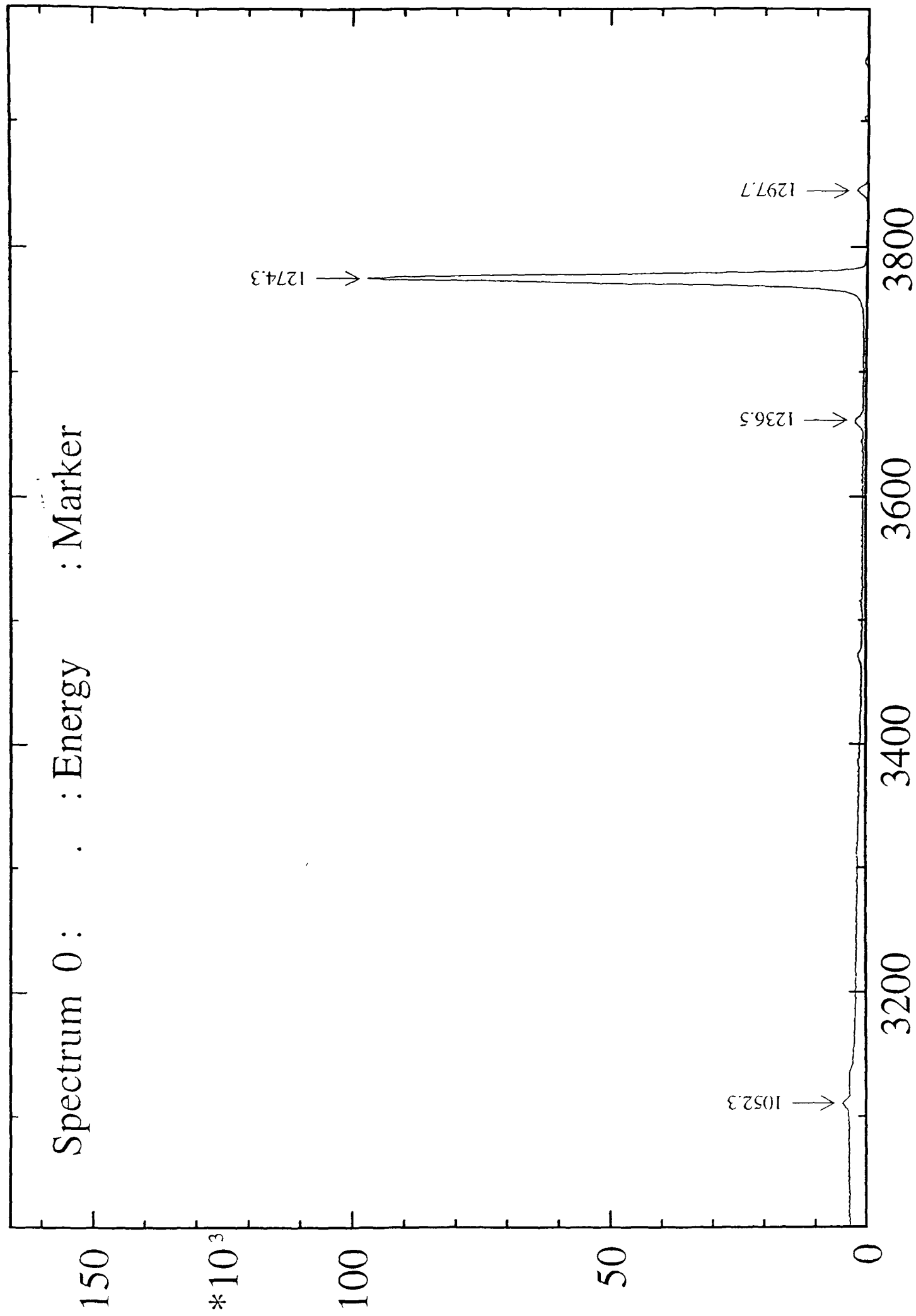


Fig 4.3(d) Part of a gamma-ray spectrum of ^{133}I (Channel numbers 3000-40000).

E_x	E_γ	I_γ	U_2	U_4	J_I^π J_f^π	Mult.	A_2	A_4	$\delta(Exp)$	$\delta[ref]$
529.9	529.9	1000	0.874†	0.580†	$(5/2)^+$ $(3/2)^+$	E2/M1	-0.87(3)	0.47(4)	2.4(2)	1.85(20)[6] 1.5(+11/ -7)[7]
875.3	875.3	51	0.81(3)	0.43(8)	$(7/2)^+$ $(3/2)^+$	E2	-0.468†	-0.358†		
1236.4	706.6 1236.4	17 17	0.89(4)	0.56(13)	$(7/2)^+$ $(5/2)^+$ $(7/2)^+$ $(3/2)^+$	E2/M1 E2	-0.48(2) -0.468†	-0.10(4) -0.358†	0.46(3)	4.31(4) / .46(3)[8]
1298.2	1298.2	27	0.874†	0.580†	$(5/2)^+$ $(3/2)^+$	E2/M1	-0.625(2)	0.14(2)	0.59(2)	4.2(3)[9]
1386.2	856.3	14	0.925†	0.749†	$(9/2)^+$ $(5/2)^+$	E2	-0.46(2)	-0.22(4)		

†: Theoretical value

Table 4.1 Results of ^{133}I

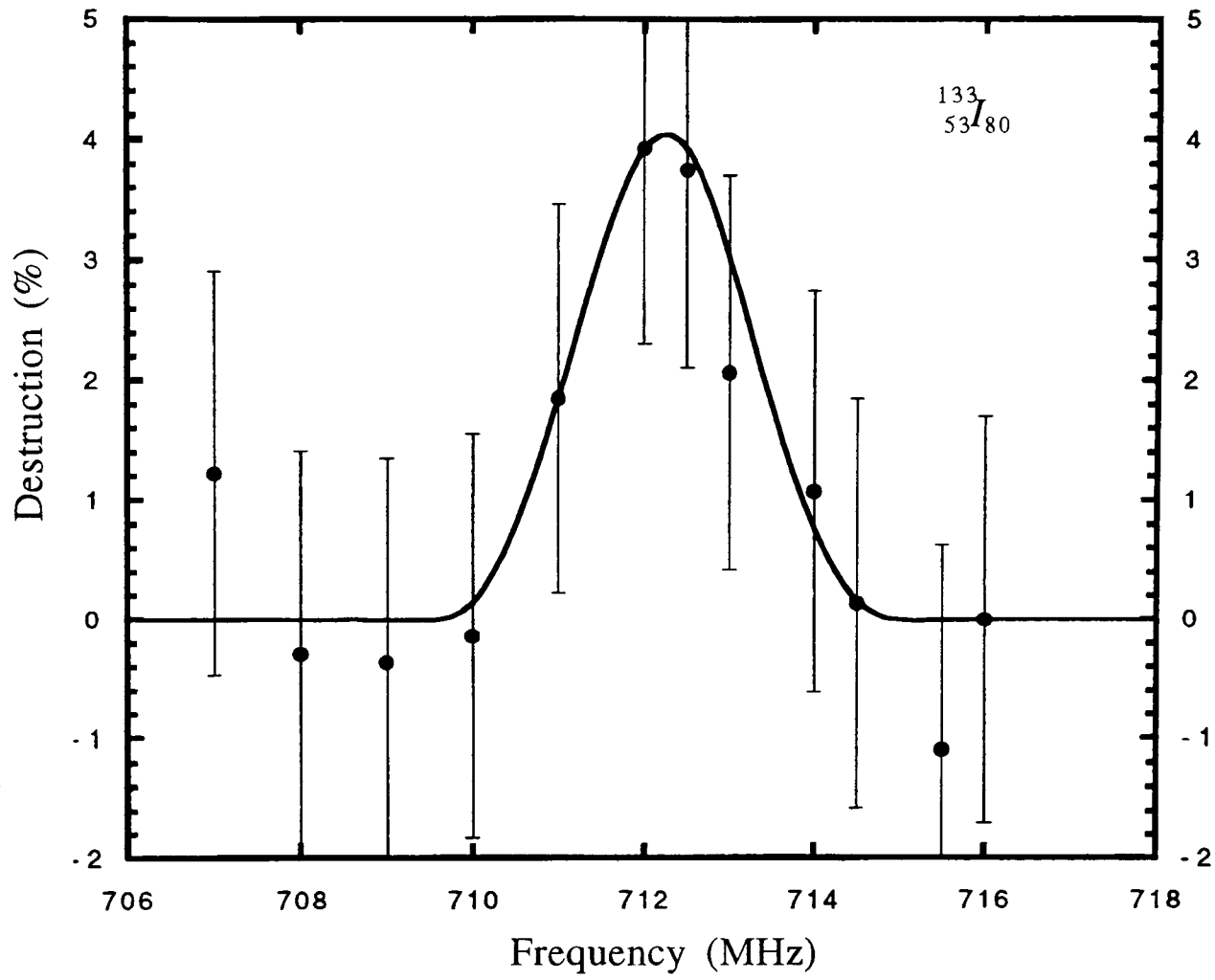


Fig 4.4 Resonance spectrum of the destruction in the decay of ^{133}I oriented at low temperature of ~ 20 *mK*.

which corresponds to the resonance frequency of $\nu(^{135}IFe) =$ 633(5)MHz and $\nu(^{135}IFe) =$ 663(15)MHz, respectively (see 4.3). These results are discussed in section 4.6.

<u>1131.5 keV level</u>($J^{\pi} = (7/2)^{+}$)

The 1131.5 keV level is populated from $(7/2)^{+}$ to $(7/2)^{+}$ by beta decay, and this level has only about 1.3% of direct $\beta-$ decay feeding while indirect feeding via higher levels is ~ 21.4%.

The 1131.5 keV gamma transition is a $(7/2)^+$ to $(3/2)^+$ E2 transition if we assume that the contribution of M3 is negligible. Hence the theoretical values of A_λ are

$$A_2 = -0.468 \qquad A_4 = -0.358$$

From measured anisotropy $U_2A_2 = -0.383(47)$ and $U_4A_4 = -0.14(1)$, U_λ can be deduced as

$$U_2 = 0.82(1) \qquad U_4 = 0.39(3)$$

<u>1260.4 keV level</u>($J^\pi = (5/2)^+$)

The 1260 keV level has strong direct beta feeding of 23.8% and the indirect feeding is ~ 6%. This beta decay is a pure Gammow-Teller $(7/2)^+$ to $(5/2)^+$ transition. The two transitions (417.6 keV transition from 1678.1 keV level and 972.6 keV from 2233.0 keV) contribute most of the indirect feeding. Analysis of the 417.6 keV transition and 972.6 keV transition (E2 transition) gives U_λ for the 1260 level as

$$U_2 = 0.839(8) \qquad U_4 = 0.500(5)$$

The 1260 keV $(5/2)^+$ to $(3/2)^+$ gamma transition has E2/M1 character. From the measured anisotropy $U_2A_2 = -0.604(8)$ and $U_4A_4 = 0.120(5)$, we have then

$$A_2 = -0.72(1) \qquad A_4 = 0.24(1)$$

From this the mixing ratio can be deduced as

$$\delta(1260.4) = 0.72(2)$$

which more precise than the value given by Krane[2], but in broad agreement.

<u>1457.6 keV level</u>($J^{\pi} = \left(\frac{5}{2}\right)^{+}$)

This level is populated by the pure Gammow-Teller $\left(\frac{7}{2}\right)^{+}$ to $\left(\frac{5}{2}\right)^{+}$ beta decay, with direct beta decay feeding of ~ 7.5% and indirect feeding of ~ 2% via higher levels. The de-orientation coefficients U_{λ} have been calculated as

$$U_2 = -0.858 \qquad U_4 = 0.544 \qquad \text{from all feeds.}$$

The measured anisotropy was $U_2A_2 = -0.515(9)$ and $U_4A_4 = -0.38(38)$.
The level decays to lower energy levels by two transitions:

The 1169.0 keV transition is E2 character $\left(\frac{5}{2}\right)^{+} \rightarrow \left(\frac{1}{2}\right)^{+}$ and its experimental values are

$$A_2 = -0.6(1) \qquad A_4 = -0.7(7)$$

The theoretical values of A_{λ} are

$$A_2 = -0.535 \qquad A_4 = -0.617$$

The theoretical values and the experimental values are in good agreement. Therefore the pure E2 in character is confirmed.

The 1457.6 keV transition is M1/E2, $\left(\frac{5}{2}\right)^{+} \rightarrow \left(\frac{3}{2}\right)$, and its angular distribution coefficients A_{λ} have been deduced as

$$A_2 = 0.77(3) \qquad A_4 = 0.2(4)$$

and the extracted mixing ratios are

$$\delta(1457.6) = -0.25(2) \text{ or } -1.7(1).$$

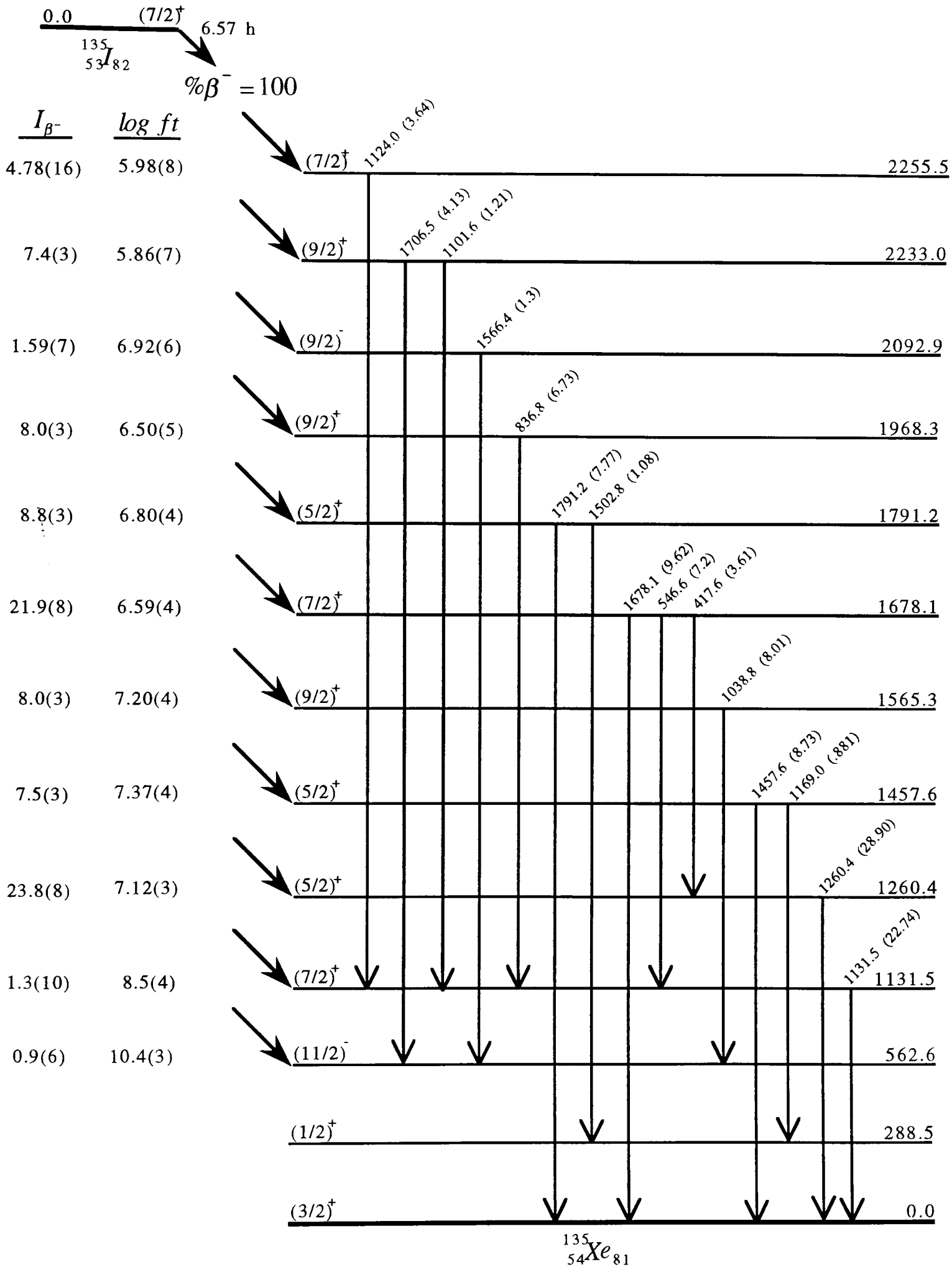


fig 4.5 A partial decay scheme of ^{135}I

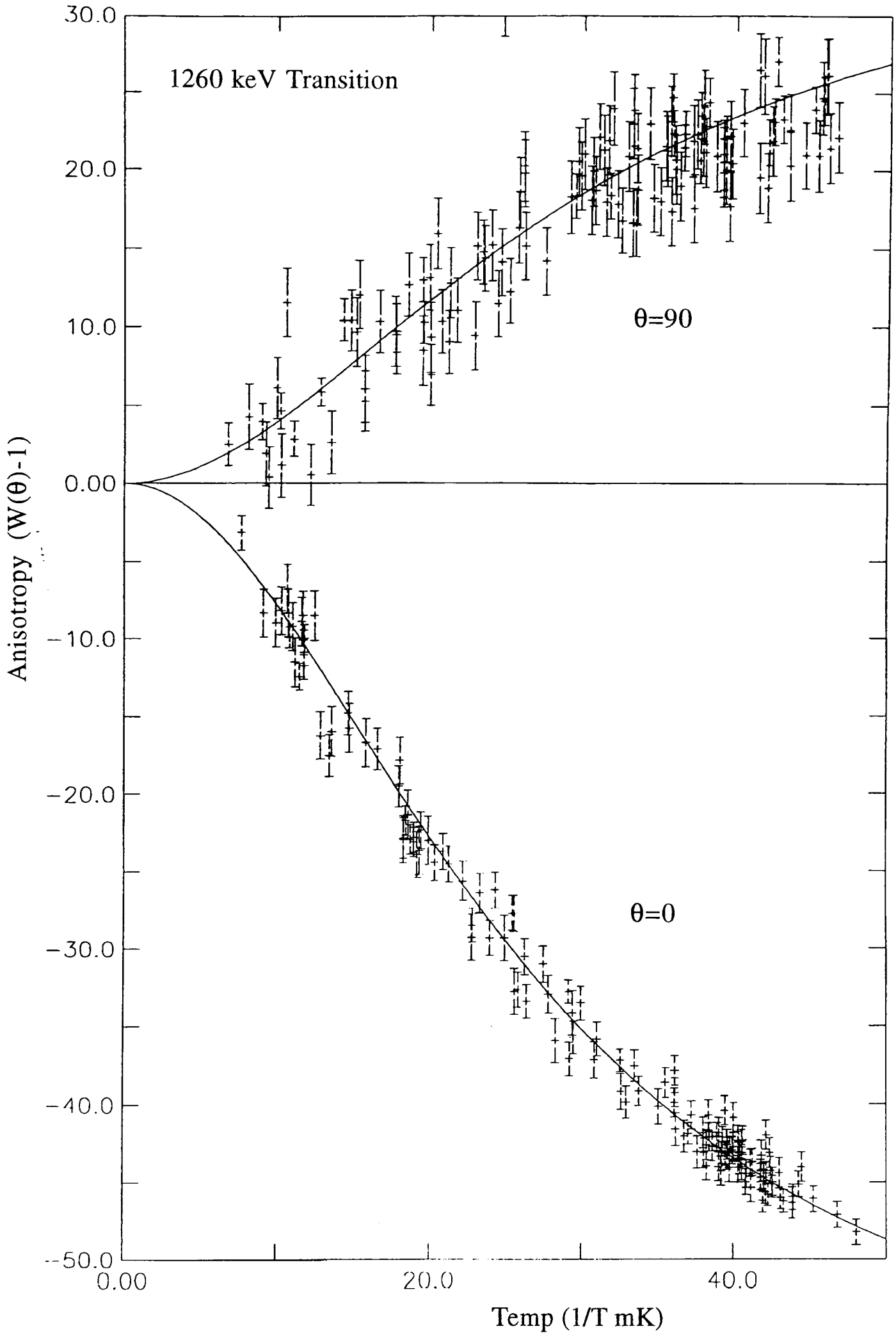


Fig 4.6 Axial/Equatorial anisotropy for the 1260 keV transition seen in the decay of ^{135}I (in Fe)

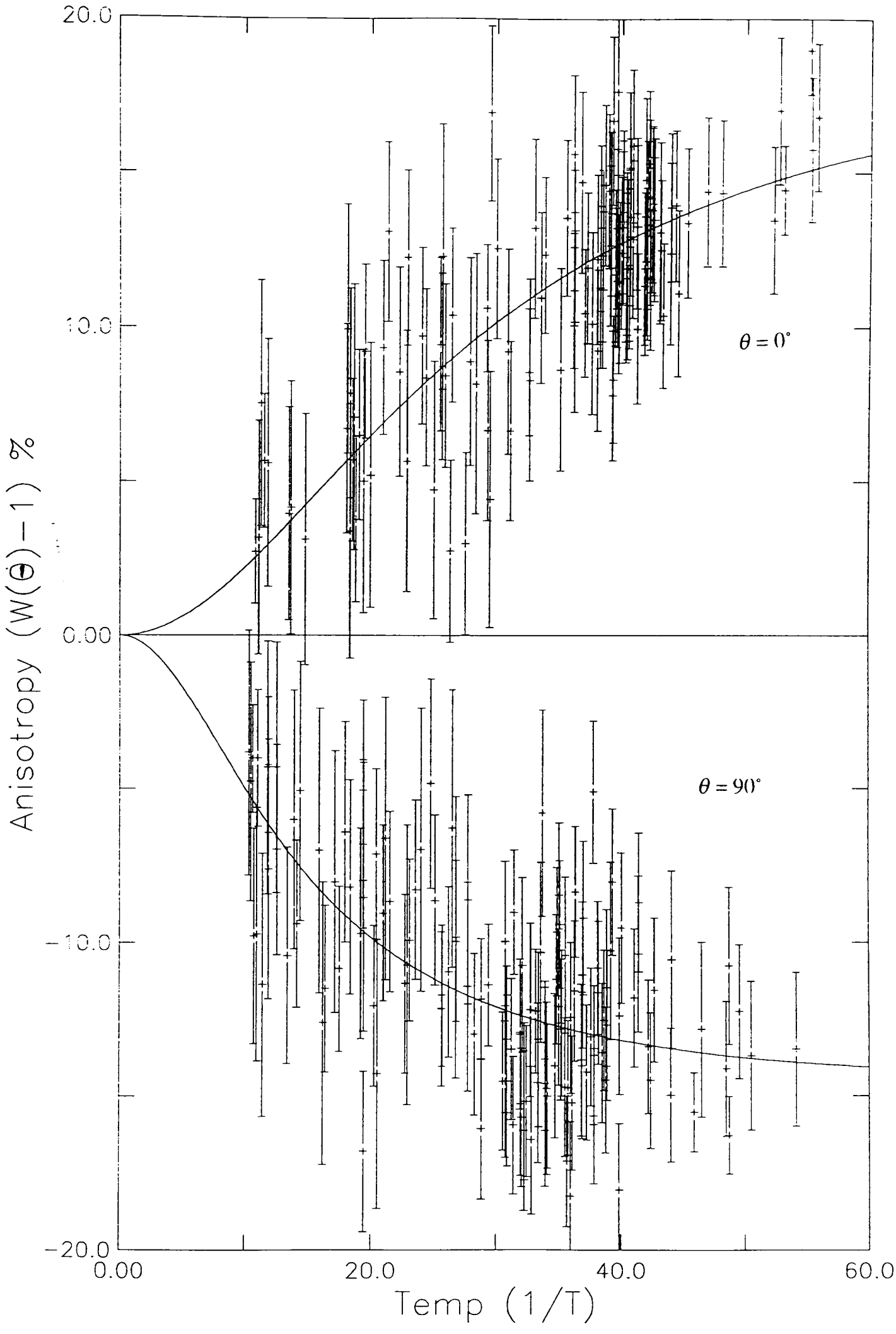


Fig 4.7 Axial/Equatorial anisotropy for the 1038 keV transition seen in the decay of ^{135}I (in Fe)

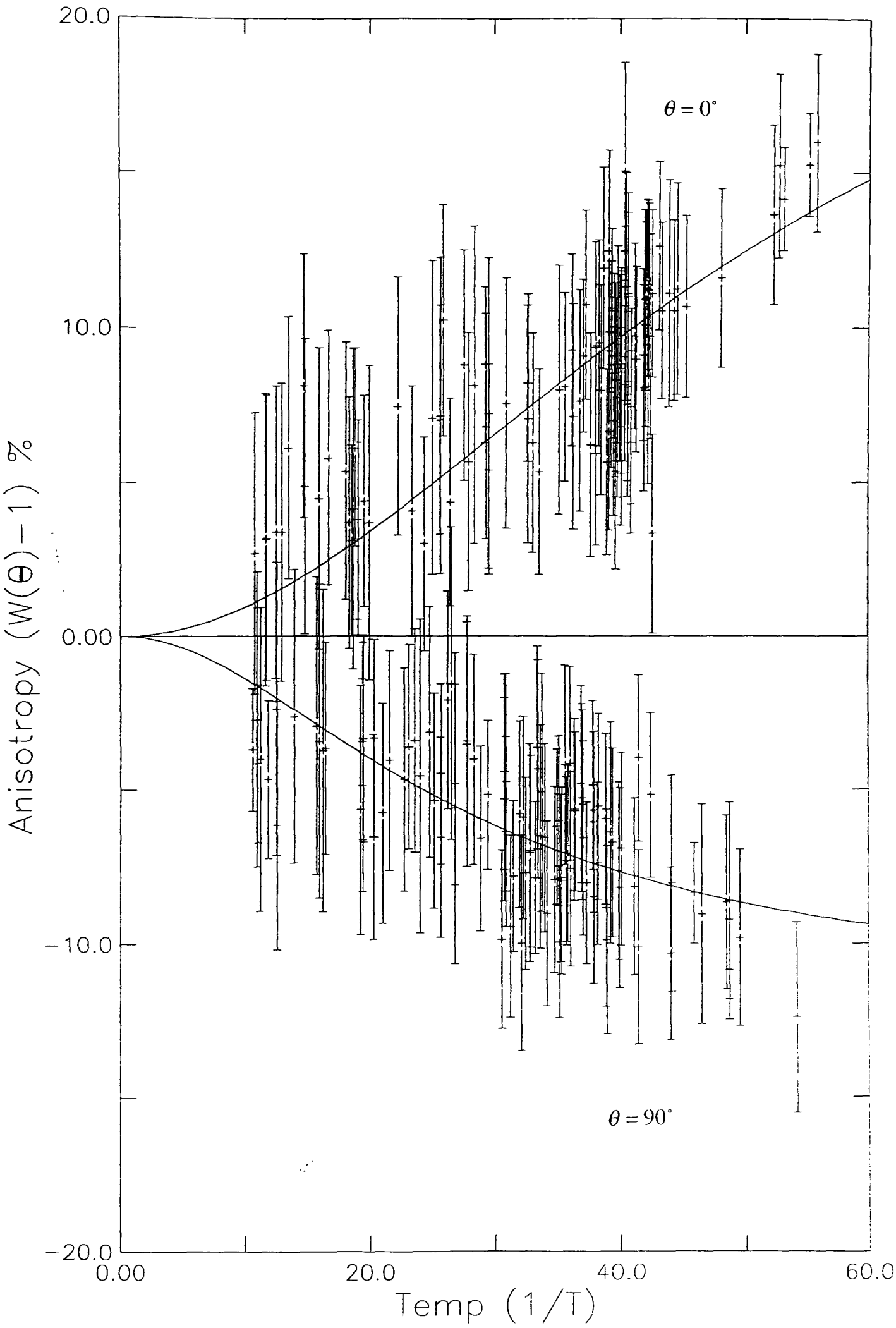


Fig 4.8 Axial/Equatorial anisotropy for the 1706 keV transition seen in the decay of ^{135}I (in Fe)

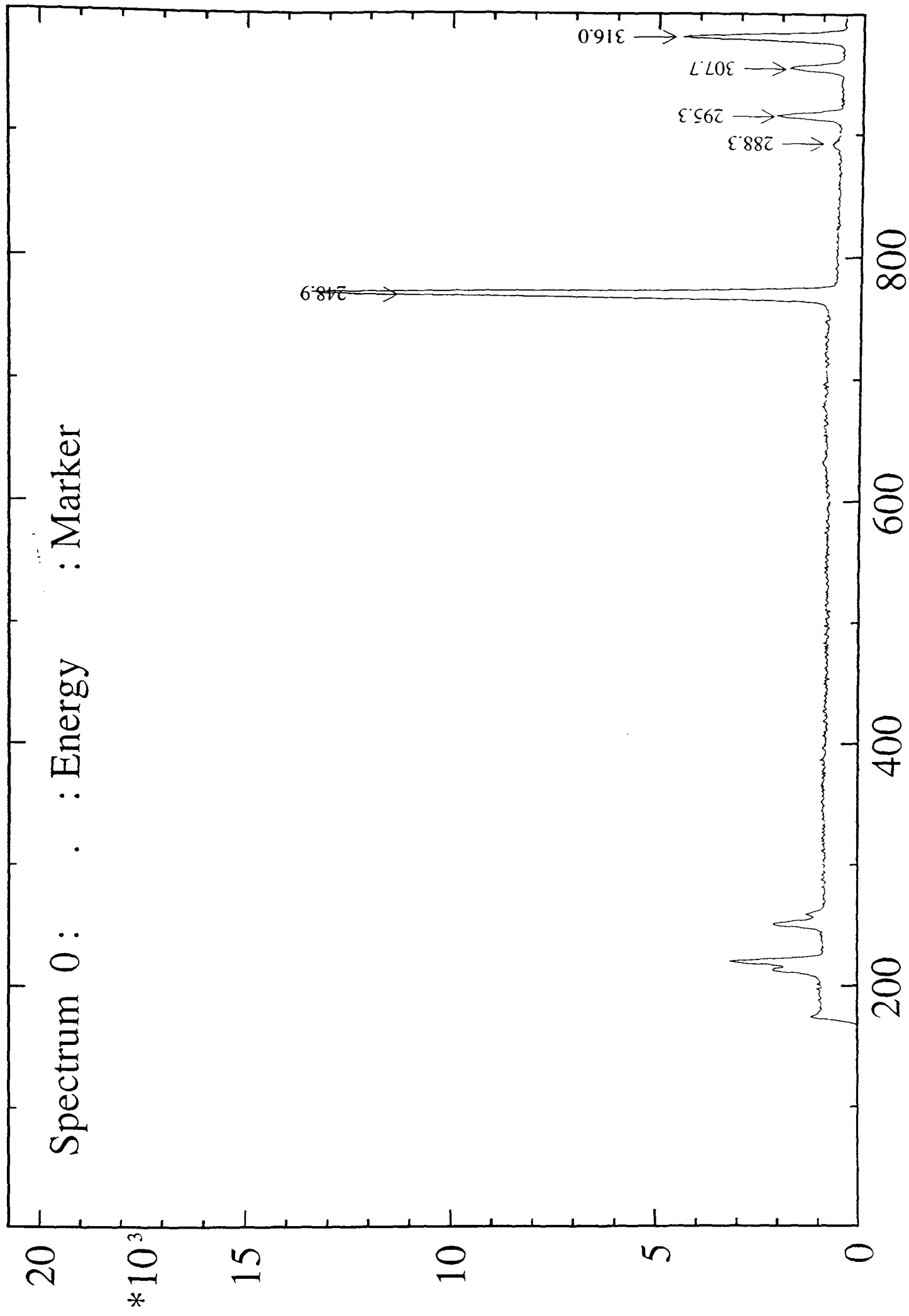


Fig 4.9(a) Part of a gamma-ray spectrum of ^{135}I with ^{192}Ir thermometer and ^{207}Bi sample used as a pulsar. The energies shown above are the energies in keV for the channel nearest to the peak centre and are correct to within ~ 0.5keV. The accurate fitted energies are given in table 4.1. (Channels number 0 to 1000).

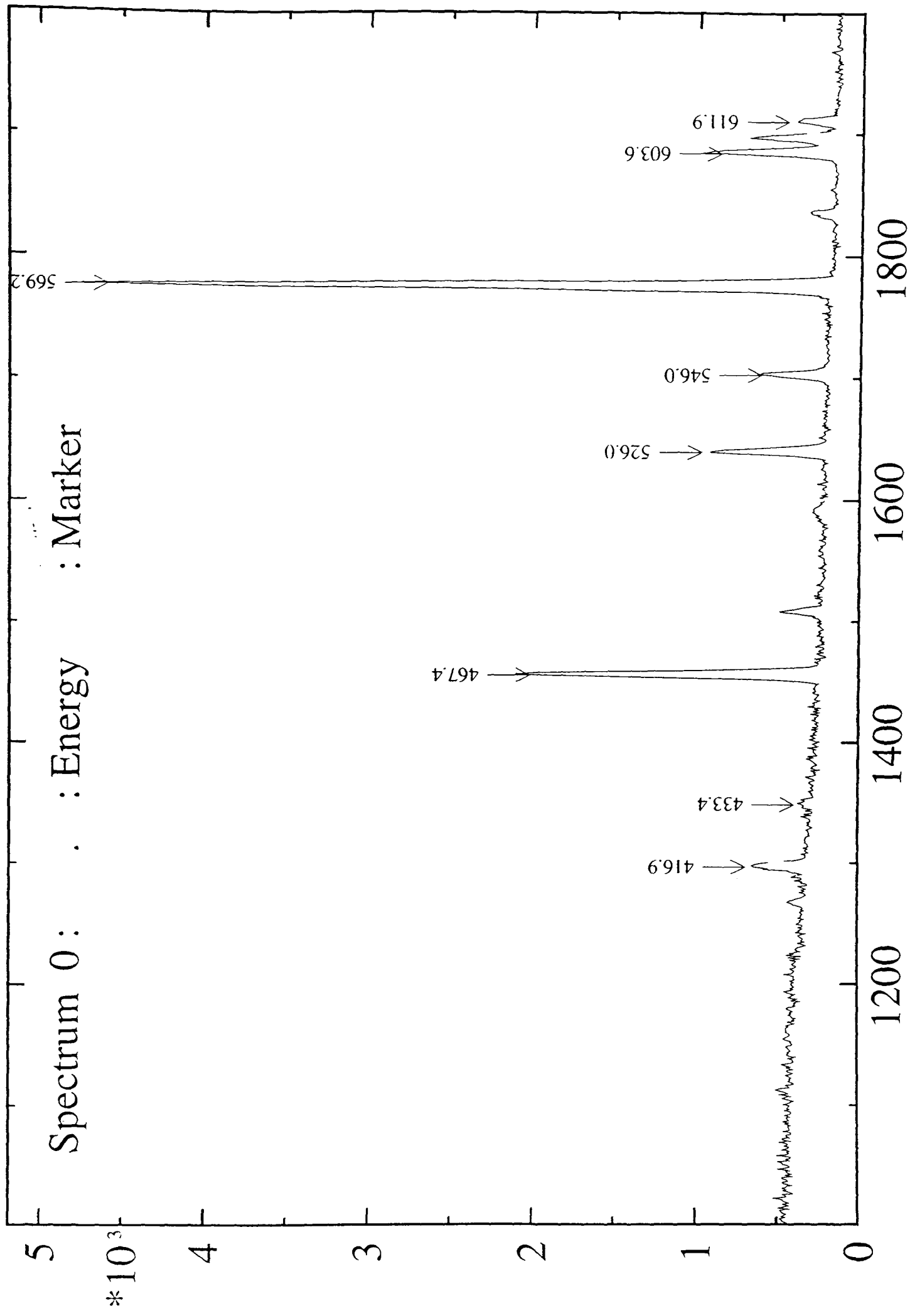


Fig 4.9(b) Part of a gamma-ray spectrum of ^{135}I (Channels number 1000-2000).

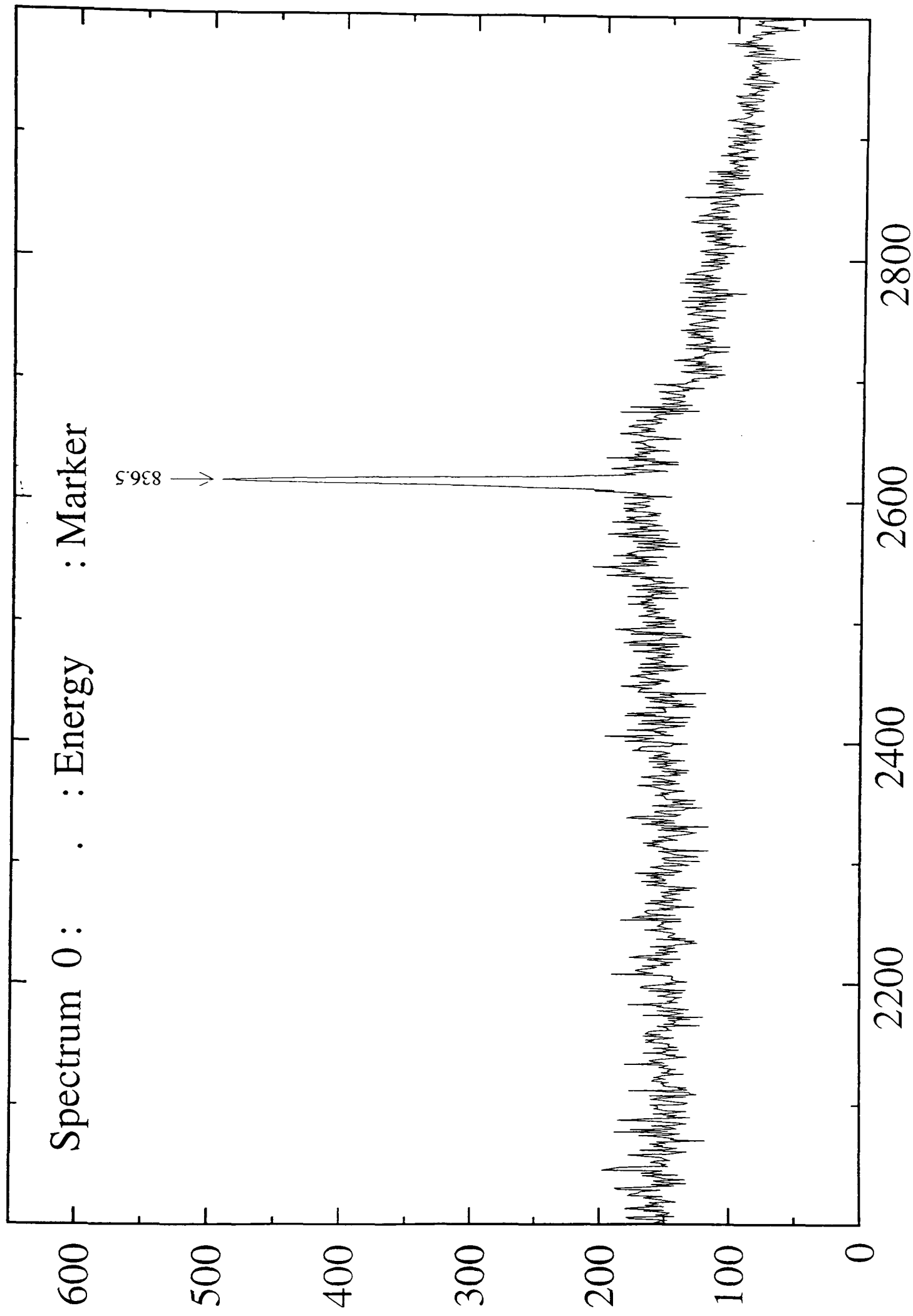


Fig 4.9(c) Part of a gamma-ray spectrum of ^{135}I (Channel numbers 2000-3000).

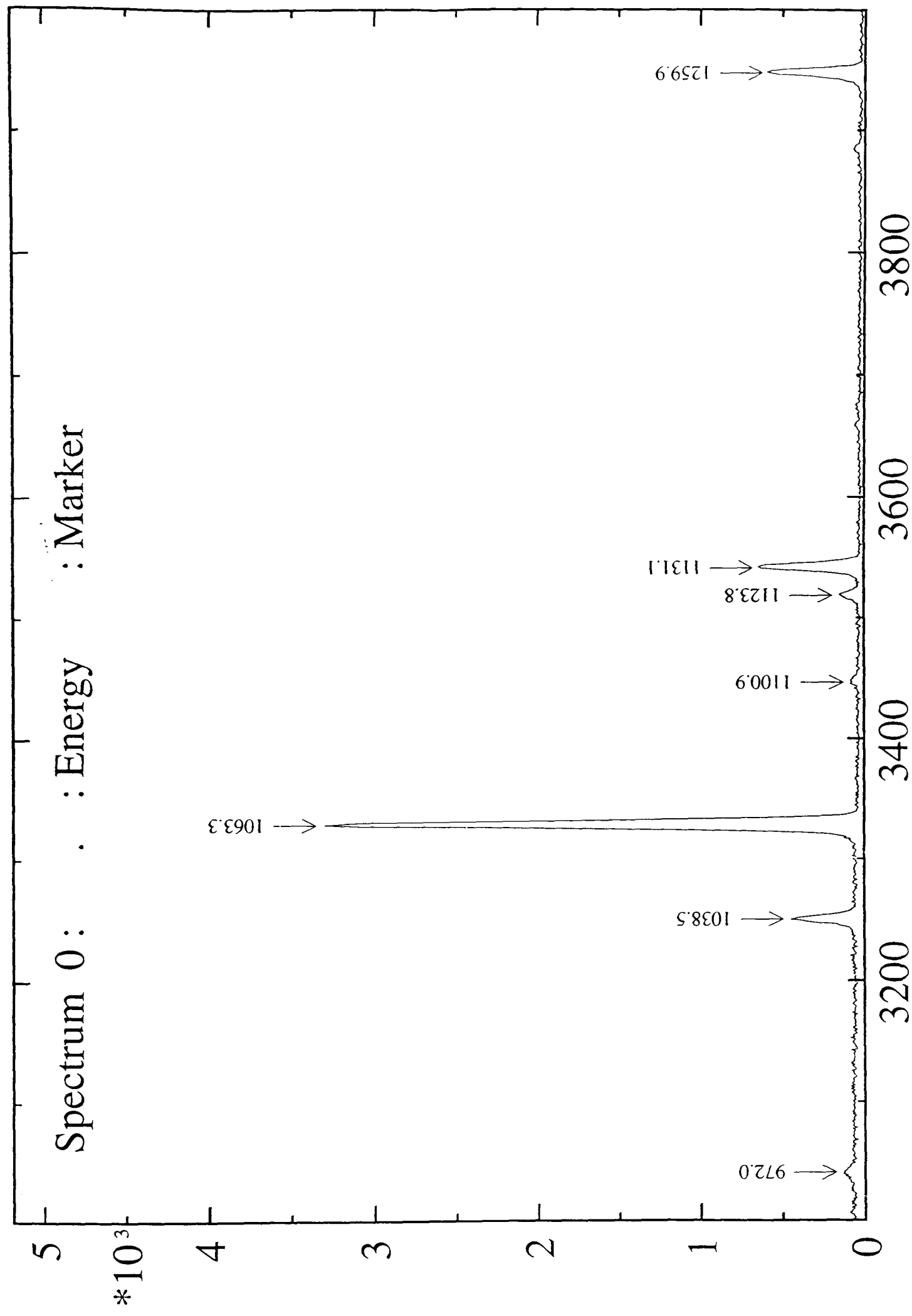


Fig 4.9(d) Part of a gamma-ray spectrum of ^{135}I. (Channel numbers 3000-4000).

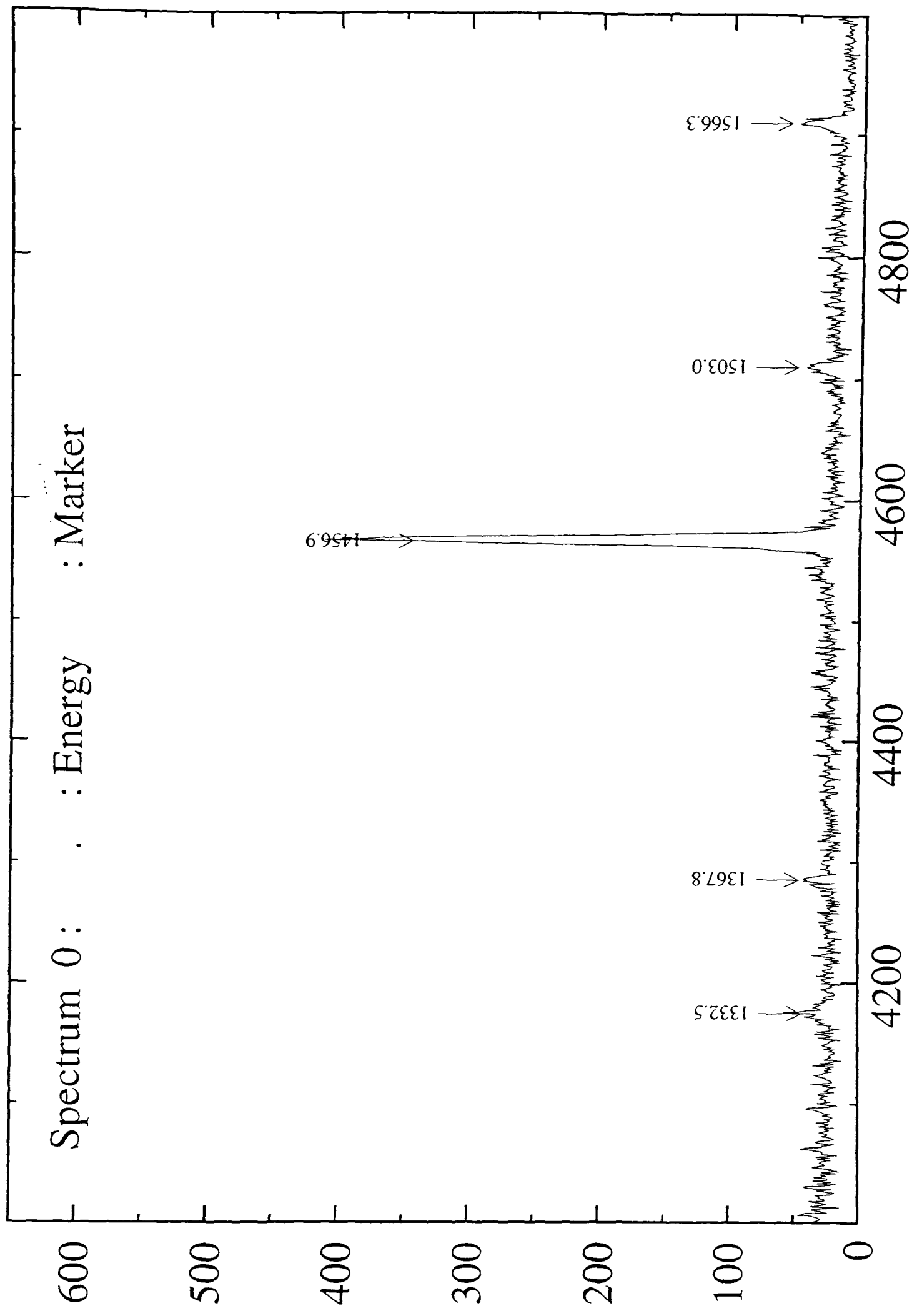


Fig 4.9(e) Part of a gamma-ray spectrum of ^{135}I. (Channel numbers 4000-5000).

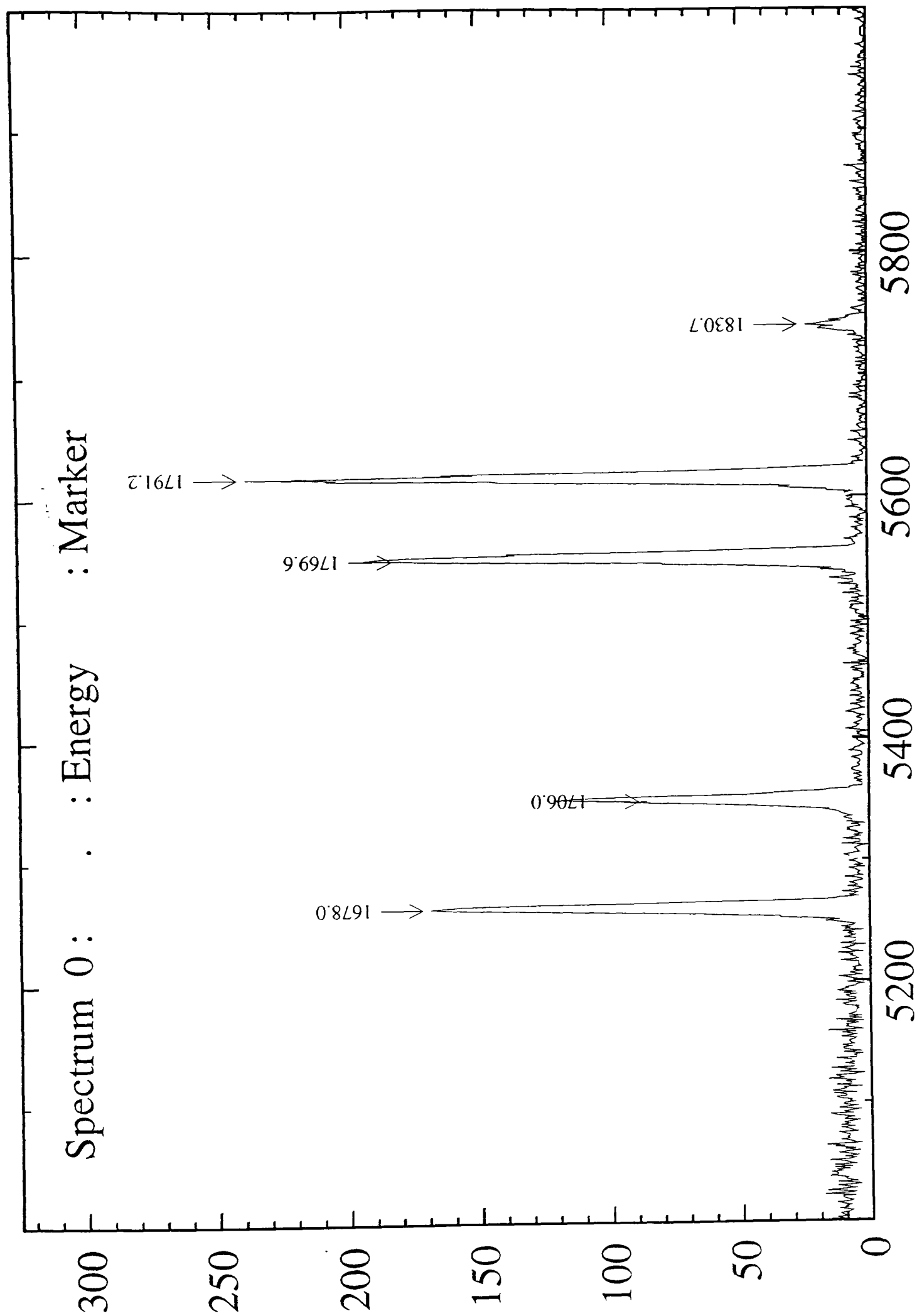


Fig 4.9(f) Part of a gamma-ray spectrum of ^{135}I. (Channel numbers 5000-6000).

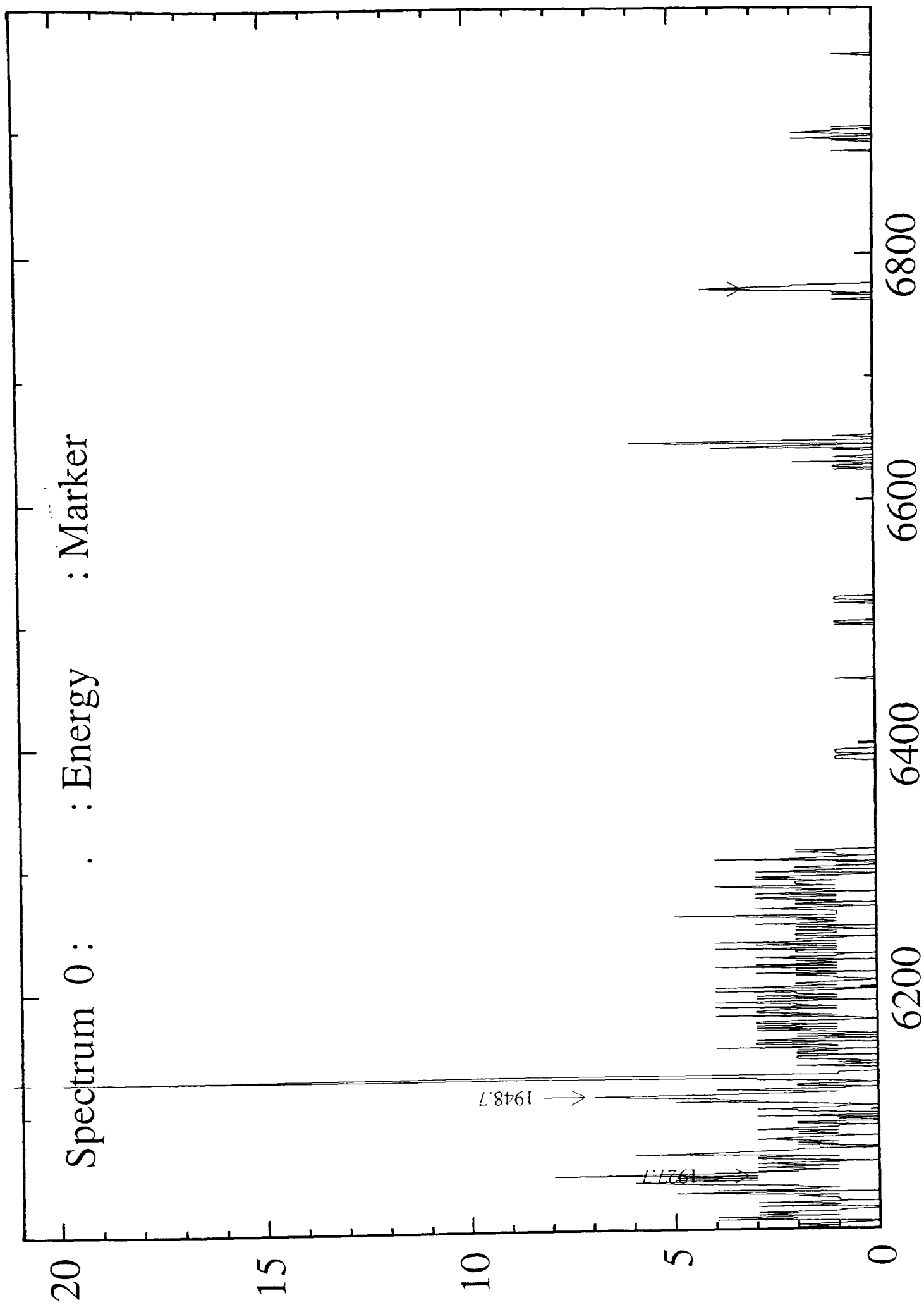


Fig 4.9(g) Part of a gamma-ray spectrum of ^{135}I. (Channel numbers 6000-7000).

1565.3 keV level($J^{\pi} = \left(\frac{9}{2}\right)^{+}$)

The 1565.3 level has direct beta decay feeding of ~ 8% and indirect beta decay feeding of ~ 0.6% and is populated by a pure Gamow-Teller transition $\left(\frac{7}{2}\right)^{+}$ to $\left(\frac{9}{2}\right)^{+}$. The theoretical values of U_{λ} are then

$$U_2 = 0.925 \qquad U_4 = 0.749$$

The 1038.8 keV transition is E1 in character, a $\left(\frac{9}{2}\right)^{+}$ to $\left(\frac{11}{2}\right)^{-}$ transition, and its angular distribution coefficients A_{λ} have been deduced from measured anisotropy $U_2A_2 = 0.176(3)$ and $U_4A_4 = 0.75(75)$ as

$$A_2 = 0.19(3) \qquad A_4 = 0.1(1)$$

The theoretical values of this E1 transition are

$$A_2 = 0.165 \qquad A_4 = 0.0$$

Both the experimental and the theoretical values of A_{λ} are in good agreement each other (see table 4.2) and, therefore, we conclude that this transition is a pure E1 transition.

1678.1 keV level($J^{\pi} = \left(\frac{7}{2}\right)^{+}$)

This level has direct beta decay feeding of ~ 21.9% with negligible indirect beta decay feeding. Since this β−decay could have either L=0 or L=1, U_{λ} coefficients have been deduced from the observed anisotropy of the 1678.1 keV transition which has E2 character, $\left(\frac{7}{2}\right)^{+}$ to $\left(\frac{3}{2}\right)^{+}$. Its theoretical A_{λ} values are

$$A_2 = -0.468 \qquad A_4 = -0.358$$

From the measured anisotropy $U_2A_2 = -0.379(47)$ and $U_4A_4 = -0.129(11)$, the de-orientation coefficients U_{λ} can be deduced as

$$U_2 = 0.81(1) \qquad U_4 = 0.36(3)$$

These are consistent with a pure Gamow-Teller beta transition.

The 417.6 keV transition has mixed E2/M1 character, $(7/2)^+$ to $(5/2)^+$, and its angular distribution coefficients A_λ have been deduced from the measured anisotropy U_2A_2 =0.49(8) and U_4A_4 =0.22(16)as

$$A_2 = 0.6(1) \qquad A_4 = 0.6(4)$$

From this, the E2/M1 mixing ratio has been calculated as

$$\delta(417.6) = \text{-}2.6(6)$$

where the large δ value is chosen based on the large A_4 coefficient.

From the measured anisotropy U_2A_2 =-0.25(5) and U_4A_4 =-0.14(23), A_λ have been deduced for 546.6 keV gamma transition, $(7/2)^+$ to $(7/2)^+$, as

$$A_2 = \text{-}0.31(6) \qquad A_4 = \text{-}0.4(6)$$

From this its E2/M1 mixing ratio has been deduced as

$$\delta(546.6) = \text{-}0.2(1) \text{ or } 0.14(9)$$

The A_4 term is too inaccurate to give a choice between the two possible δ values in this case.

1791.2 keV level($J^\pi = (5/2)^+$)

This level has direct beta decay feeding of ~ 8.8% and its indirect beta decay feeding is negligible. It is populated by a pure Gamow-Teller transition, $(7/2)^+$ to $(5/2)^+$. The theoretical values of U_λ are

$$U_2 = 0.858 \qquad U_4 = 0.544$$

The 1502.8 keV gamma transition has E2 character, from $(5/2)^+$ to $(1/2)^+$, and the experimental values of A_λ have been calculated with the theoretical values of U_λ, from the measured anisotropy U_2A_2 =-0.515(86) and U_4A_4 =-0.33(22), as

$$A_2 = -0.6(1) \qquad A_4 = -0.6(4)$$

The theoretical values of A_λ for this E2 transition are

$$A_2 = -0.535 \qquad A_4 = -0.617$$

Therefore this transition is accepted as being E2 in character.

The 1791.2 keV transition is E2/M1 character $(5/2)^+ \rightarrow (3/2)^+$, and its mixing ratio has not previously been determined. The angular distribution coefficients A_λ are calculated from the measured anisotropy $U_2A_2 = -0.14(7)$ and $U_4A_4 = 0.5(5)$,as

$$A_2 = -0.16(8) \qquad A_4 = 0.1(1)$$

Thus the E2/M1 mixing ratio for this transition has been deduced as

$$\delta(1791.2) = 0.14(2)$$

1968.3 keV level($J^\pi = (9/2)^+$)

This level is populated by the pure Gamow-Teller transition $(7/2)^+$ to $(9/2)^+$, with direct beta feeding of ~ 8.3%. The theoretical de-orientation coefficients U_λ are

$$U_2 = 0.925 \qquad U_4 = 0.749$$

Thus the angular distribution coefficients A_λ for the 836.8 keV transition $(9/2)^+$ to $(7/2)^+$ have been calculated from the measured anisotropy $U_2A_2 = 0.065(55)$ and $U_4A_4 = -0.38(45)$ as

$$A_2 = 0.07(6) \qquad A_4 = -0.5(6)$$

The deduced E2/M1 mixing ratio for this transition in this experiment

$$\delta(836.8) = 0.10(6)$$

somewhat smaller than the value $\delta = 0.31(12)$ of Begzhannov et al[4].

2092.9 keV level($J^{\pi} = \left(9/2\right)^{-}$)

This level has direct beta decay feeding of ~ 7.4% and is populated by the pure Gamow-Teller transition $\left(7/2\right)^{+}$ to $\left(9/2\right)^{-}$. The theoretical de-orientation coefficients U_{λ} are

$$U_2 = 0.925 \qquad U_4 = 0.749$$

Therefore A_{λ} for 1566 keV gamma transition, $\left(9/2\right)^{-}$ to $\left(11/2\right)^{-}$ have been calculated from the measured anisotropy $U_2A_2 = 0.093(93)$ and $U_4A_4 = 0.15(7)$ as

$$A_2 = 0.1(1) \qquad A_4 = 0.2(1)$$

The E2/M1 mixing ratio for this transition is not known and, from this experiment, has been deduced as

$$\delta(1566.4) = -7(+4/-\infty)$$

2233.0 keV level($J^{\pi} = \left(9/2\right)^{+}$)

This level is populated by the pure Gamow-Teller beta transition $\left(7/2\right)^{+}$ to $\left(9/2\right)^{+}$ with intensity ~ 7.4%. The theoretical de-orientation coefficients U_{λ} are

$$U_2 = 0.925 \qquad U_4 = 0.749$$

The 1706.5 keV gamma transition is E1 in character, from $\left(9/2\right)^{+}$ to $\left(11/2\right)^{-}$ and its experimental values of A_{λ} have been deduced from the measured anisotropy $U_2A_2 = -0.10(2)$ and $U_4A_4 = 0.00(6)$ as

$$A_2 = 0.11(2) \qquad A_4 = 0.00(8)$$

The theoretical values for pure E1 transition of A_{λ} are

$$A_2 = 0.165 \qquad A_4 = 0.0$$

Therefore this transition is accepted as being E1 in character.

The experimental values of A_λ for the 1101.6 keV transition $(9/2)^+$ to $(7/2)^+$ are

$$A_2 = -0.53(10) \qquad A_4 = 0.1(2)$$

and E2/M1 mixing ratio in this transition has been deduced as

$$\delta(1101.6) = 0.5(1)$$

which is considerably lower than the value given by Conçalves[5] (see table 4.2).

2255.5 keV level($J^\pi = (7/2)^+$)

This level has direct beta decay feeding of ~ 7.4% ($(7/2)^+$ to $(7/2)^+$). Assuming a pure Gamow-Teller transition as for the feed to the 1678 level, we deduced the angular distribution coefficients A_λ for the 1124.0 keV gamma transition of E2/M1 character, $(7/2)^+$ to $(7/2)^+$, from the measured anisotropy $U_2A_2 = -0.41(8)$ and $U_4A_4 = -0.33(4)$ as

$$A_2 = -0.5(1) \qquad A_4 = -0.9(1)$$

and the deduced E2/M1 mixing ratio is large and positive, but incompatible with a pure Gamow-Teller feed as the A_4 term is outside the physical limits.

4.6 Discussion

The results of the LTNO experiments in this chapter indicated that when *I* is implanted into Fe not all of the *I* atoms reside in a unique site. This is confirmed by the NMR/ON experiment. The NMR/ON resonance observed indicated that at least 30% of the *I* atoms reside in a site experiencing a hyperfine field of ~114.5*T* measured by NMR/ON on ^{133}I. The NO data showed that ~80% of *I* atoms could experience this field depending on the implantation conditions but was not sufficiently sensitive to enable any further deductions to be made. Thus the

simplest model consistent with the data so far is that ~80% of *I* atoms reside in a substitutional site experiencing a hyperfine field of ~114.2*T*, the remaining ~20% experiencing zero or near zero field perhaps as a result of residing in very damaged regions of the lattice.

The result of Green et al, gave a B_{hf}= 103.5(9)*T* when the ^{131}I nuclei were *cold* implanted into an iron foil host and this hyperfine field was derived using a two site model fit to the temperature dependence of anisotropy in the *I* isotope. The difference between Green's result and the result in this chapter appears to be due to a difference between *cold* and *warm* implantation and a difference in a polarizing field of 0.1*T* (Green)and 0.7*T* used in this work. It is useful here to explain the effect that temperature can have in influencing interactions between the impurity atoms and various associated defects of the lattice. The mobility of a particular defect usually occurs at a distinct temperature and is known as a recovery stage. Turos et al[27] show that at temperature greater than ~200 K free migration of vacancies and interstitial atoms occurs and that a temperature of ~700 K is needed to anneal residual damage in iron. Also they show that at temperature below ~50 K it is generally considered that very little movement of defects can take place.

Green et al showed a fit using the 'two site' model which shows that, in this model 95% of nuclei experienced a field of 103.5*T*, ~9.4% lower than B_{hf}=114.2*T*. In this work, the temperature dependance analysis of ^{133}I using the same model show 79% of nuclei experienced a field 109.2*T*, ~4.4% lower than B_{hf}=114.2*T*. From their results they suggest that all iodine moments measured at DOLIS-COLD are small by 10%. The results of the ^{133}I experiment suggested that iodine does not feel a full hyperfine field. However we must consider several factors:

(i) The value of *f* extracted will vary with implant quality since the two site mean field is an average over sites. Pattyn et al[25], performed a series of experiments with Xe isotopes implanted with different total implant dose into polycrystalline iron foils. They found that for a dose of 3.6×10^{13} atoms/cm^2 the fraction of good sites was 64(6)%, while at a dose of 1×10^{11} atoms/cm^2 the fraction in good sites was 90(10)%. Also, it is known that *cold* implantation for insoluble implants generally produces more in good field sites because the implants are frozen in, and the movement of vacancies and other impurities is restricted.

(ii) There are possibly quadrupole effects for IFe and this has been studied by Visser[30] by NMR/ON.

Any field obtained by the temperature dependence fit can be model dependent and, possibly, isotope and implant character dependent as well. Further investigation of this problem could be rewarding, if combined with a more direct study of site

distribution e.g. by channelling[29].

For the structure of iodine nuclei, Kisslinger and Sorensen particle+vibration phonon model has been used in 1960's [31]. Later, Hicks et al[16] described the ^{133}I nucleus within the framework of the cluster-vibration model(CVM)[17-23]. In this model, a dynamical cluster consisting of three protons is coupled to the core quadrupole vibration. The magnetic moment of the ground state calculated in this model was to be $\mu = 2.2\mu_N$. In this model, there is a choice between a coupling scheme involving the 3p cluster + Sn core or one proton + Te core for iodine nuclei. This choice can be based on similarity in trend between the neutron number dependence of energies of the first 2^+ states of the core and energies of excited states in the odd-A nucleus, corresponding to particle (cluster) coupling to the core. We show in fig 4.16 upto five low-lying $(5/2)^+$ states in odd-mass I nucleides plotted with the energies of the appropriate even-even Sn core. For these $(5/2)^+$ states, it appears that the cluster plus Sn core is marginally more appropriate description than the one proton plus Te core. But, for most other states, like the $I^{\pi}=1/2^+$, the particle plus Te core configuration seems to be more suitable. Of course, this rather simple experimental guidance must be taken as the first approximation.

Fig 4.11 shows the levels of ^{133}Xe plotted with the levels predicted by assuming the basic structure of ^{133}Xe to be that of a neutron in the $h_{11/2}$, $d_{3/2}$, or $s_{1/2}$ orbitals coupled to the ^{132}Xe core[10]. With a parent spin and parity of $(7/2)^+$, strong β decay should be observed to the $(5/2)^+$, $(7/2)^+$ and $(9/2)^+$ levels with weaker decay to the $(5/2)^-$, $(7/2)^-$ and $(9/2)^-$ levels.

Earlier work[28] had indicated existence of a level at 1405 keV that decayed only to the 530 keV level by an 875 keV gamma-ray. However, in this experiment, we observed no evidence for doublet character for the 875 keV peak. We also note that the $(7/2)^+$ at 1386 keV, whose suggested configuration is $|\frac{3}{2}24\rangle$, has relatively weaker branch to the ground state than does the $(7/2)^+$ 1236 keV level with a proposed $|\frac{3}{2}12\rangle$ configuration. The $(5/2)^+$ level at 1298 keV shows high δ values for its stronger transitions and strong feeding to the $(3/2)^+$, $(5/2)^+$ and $(7/2)^+$ members of the $|\frac{3}{2}12\rangle$ multiplet. The other $(5/2)^+$ level at 1350 keV has relatively stronger branches to the $(3/2)^+$ and $(1/2)^+$ single-particle levels. These suggest that the 1298 keV level has a sizeable $|\frac{3}{2}24\rangle$ component and the 1350 keV level a sizeable $|\frac{3}{2}22\rangle$ component. Therefore, the levels of ^{133}Xe can be

explained largely as a single neutron coupled to the ^{132}Xe. The expression $|\frac{3}{2}12\rangle$ is the $d_{3/2}$ single-particle coupled to the first 2^+ vibration and so on.

The energy levels of ^{135}Xe are particularly interesting due to a single neutron hole in the 82-neutron shell. The levels and their properties are discussed and compared elsewhere[11-14].

The low energy levels of ^{135}Xe seem to fit the expected pattern for a single-hole state in the 82 neutron shell. As expected, the ground state and the two lowest energy states are strongly excited in the (d,t) reaction presenting a single hole in either the $2d_{3/2}$, $3s_{1/2}$, or $1h_{11/2}$. The change in configuration allows the $(5/2)^+_2 \rightarrow (5/2)^+_1$ decay to proceed readily. For example, if we assume a little E2 in the 1457 keV transition, then the $(5/2)^+_2 \rightarrow (5/2)^+_1$ transition has equal probability to the $(5/2)^+_2 \rightarrow (3/2)^+$ ground state transition. The ^{135}Xe can be described as a hole coupled to the ^{136}Xe core vibrations. Walters and his co-workers[15] carried out large scale shell-model calculations for ^{135}Xe with four particles and a hole beyond ^{132}Sn giving an accurate description of the level structure of ^{135}Xe. The odd-mass iodine nuclei and their excitations provide the possibility of testing the CVM on a three-proton cluster (Z=53) interacting with varying degrees of quadrupole vibrational core softness for closed-shell ^{135}I. More recently, Paar[26] calculated the nuclear magnetic dipole moment of ^{135}I , $\mu = 2.52\mu_N$ in the frame work of CVM.

E_x	E_γ	I_γ	U_2	U_4	J_I^π J_f^π	Mult.	A_2	A_4	$\delta(Exp)$	$\delta[ref]$
1131.5	1131.5	787	0.82(1)	.39(3)	$(7/2)^+ (3/2)^+$	E2	-0.468†	-0.358†		
1260.4	1260.4	1000	0.839(8)	.500(5)	$(5/2)^+ (3/2)^+$	E2/M1	-0.72(1)	0.24(1)	0.72(2)	0.50(11)[2]
1457.6	1169.0	30	0.858†	.544†	$(5/2)^+ (1/2)^+$	E2	-0.6(1)	-0.7(7)		
	1457.6	302			$(5/2)^+ (3/2)^+$	E2/M1	0.77(3)	0.2(4)	-.25(2) / -1.7(1)	
1565.3	1038.8	277	0.925†	.749†	$(9/2)^+ (11/2)^-$	E1	0.19(3)	0.1(1)		
1678.1	417.6	123	0.81(1)	.36(3)	$(7/2)^+ (5/2)^+$	E2/M1	0.6(1)	0.6(4)	-2.6(6)	-1.2(+8/-12)[2]
	546.6	249			$(7/2)^+ (7/2)^+$	E2/M1	-0.31(6)	-0.4(6)	-0.2(1) / 0.14(9)	-0.5(+5/-6)[2]
	1678.1	333			$(7/2)^+ (3/2)^+$	E2	-0.468†	-0.358†		
1791.2	1502.8	38	0.858†	0.544†	$(5/2)^+ (1/2)^+$	E2	-0.6(1)	-0.6(4)		
	1791.2	269			$(5/2)^+ (3/2)^+$	E2/M1	-0.16(8)	0.1(1)	0.14(2)	
1968.3	836.8	233	0.925†	0.749†	$(9/2)^+ (7/2)^+$	E2/M1	0.07(6)	-0.5(6)	0.10(6)	0.31(12)[4]
2092.9	1566.4	45	0.925†	0.749†	$(9/2)^- (11/2)^-$	E2/M1	0.1(1)	0.2(1)	-7(+4/-∞)	
2233.0	1101.6	56	0.925†	0.749†	$(9/2)^+ (7/2)^+$	E2/M1	-0.53(10)	0.1(2)	0.5(1)	1.8(2)[5]
	1706.5	143			$(9/2)^+ (11/2)^-$	E1	0.11(2)	0.00(8)		
2255.5	1124.0	126	0.81(1)	0.36(3)	$(7/2)^+ (7/2)^+$	E2/M1	-0.5(1)	-0.9(1)	Large +ve	0.16(6)[2]

†: Theoretical value

Table 4.2 Results of ^{135}I

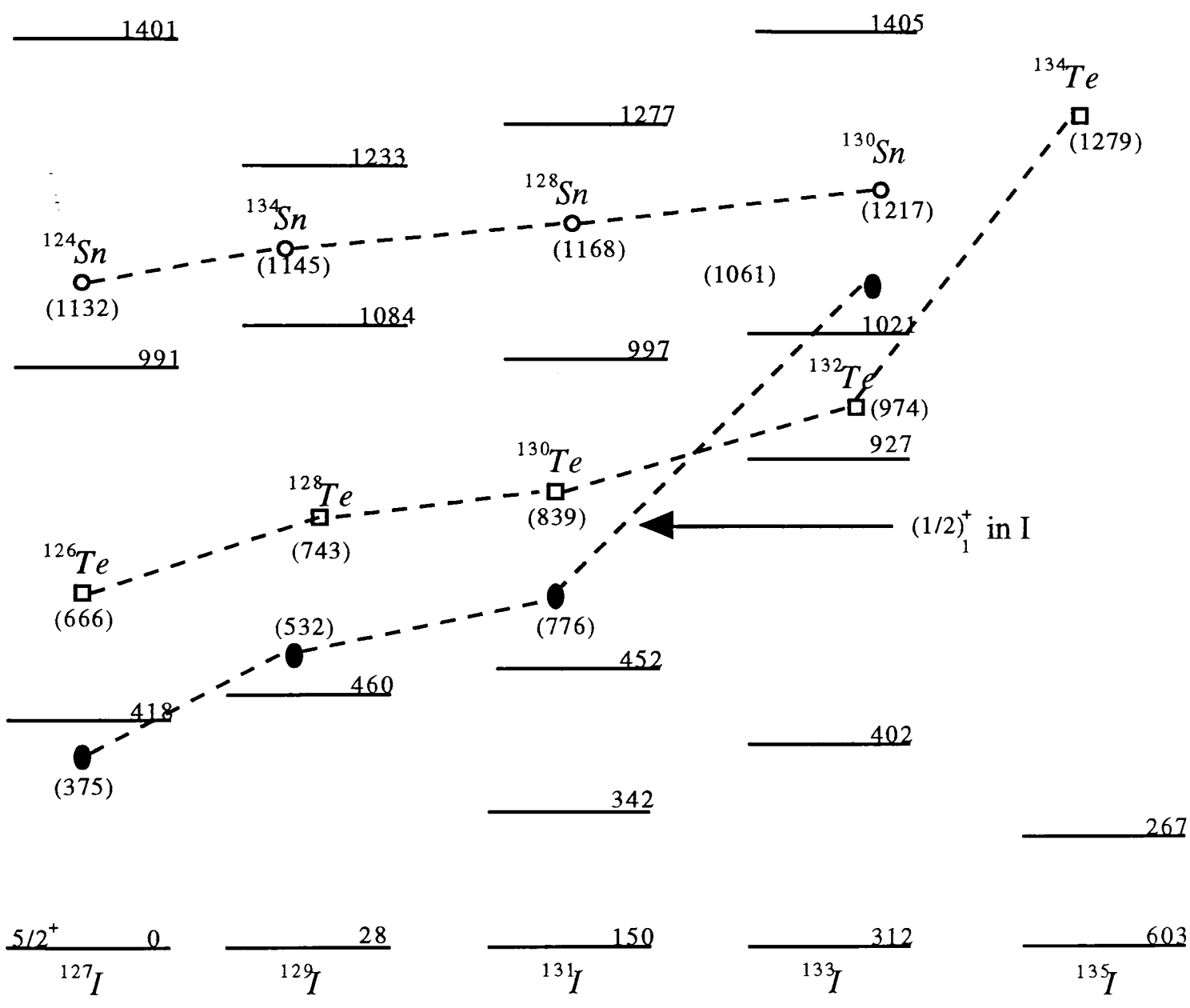


Fig 4.10 Systematics of the $\left(5/2\right)^+$ states in I nucleides compared with the first 2^+ states in the neighbouring Te and Sn cores and with the first $\left(1/2\right)^+$ states in I

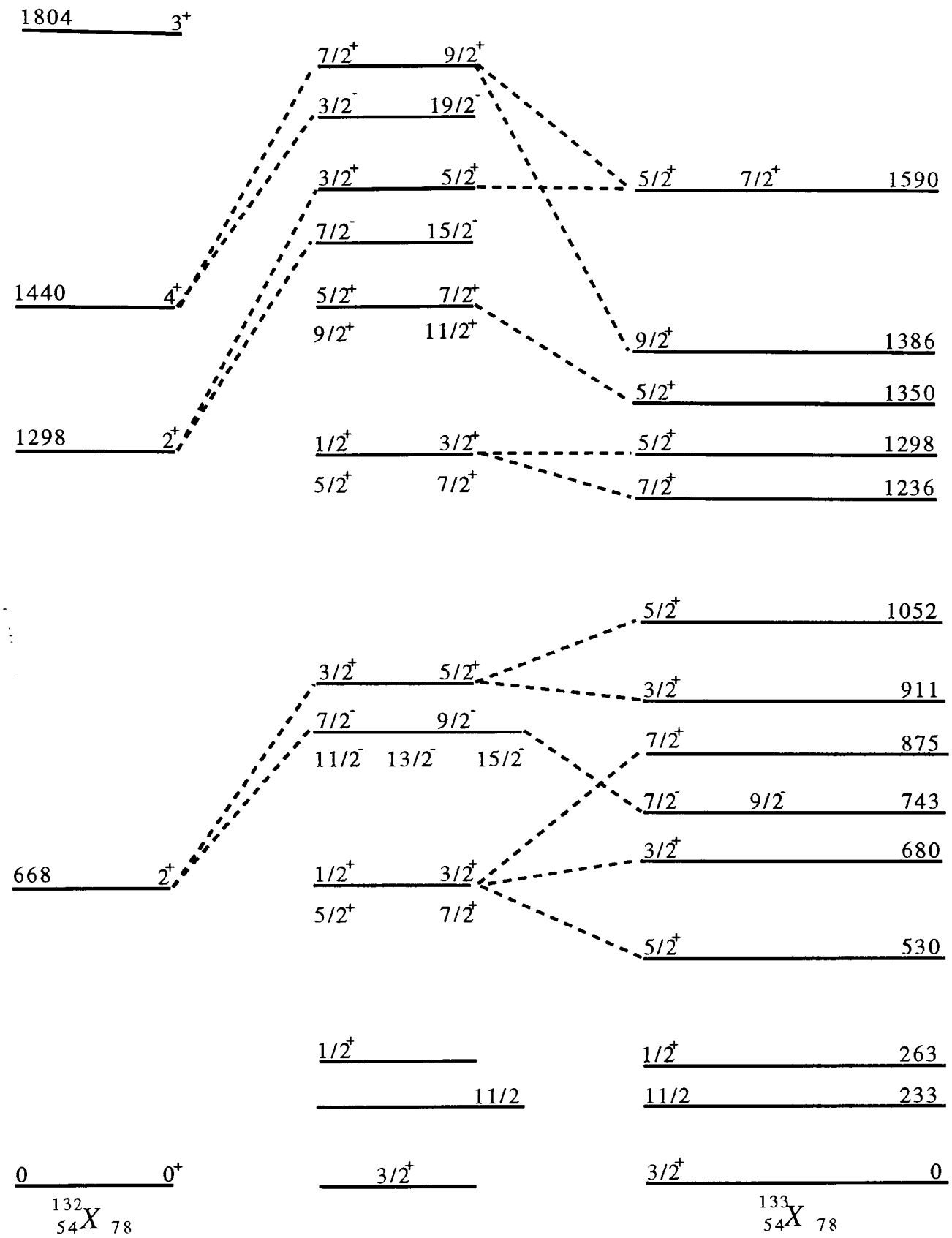


Fig 4.11 Levels of ^{133}Xe that arise from a zero-order coupling of the known single-particle states of ^{133}Xe to the known ^{132}Xe core excitations.

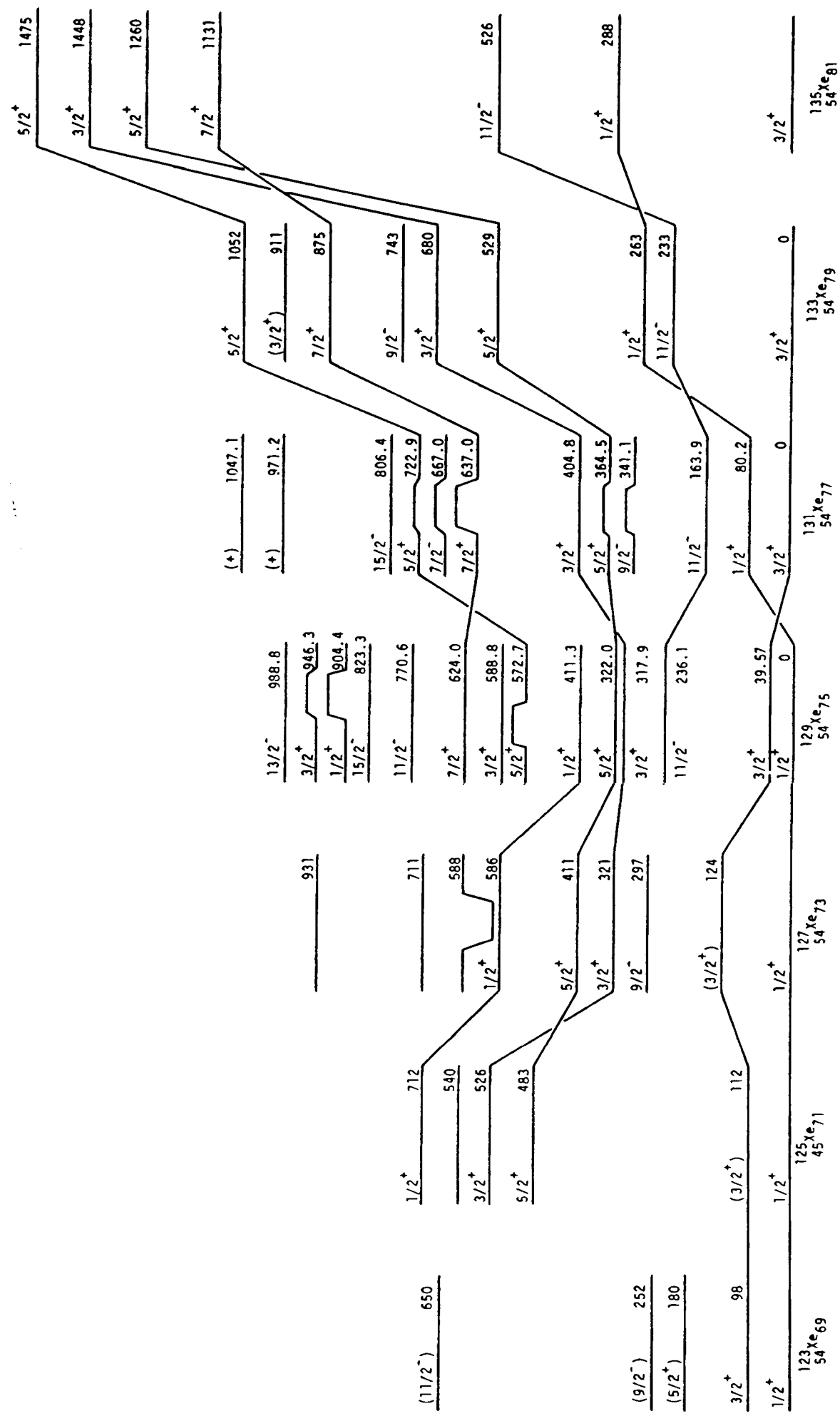


Fig 4.12 Systematics of odd-mass Xenon nuclei [32,33]

References

[1] H.de Waard and S.A.Drentje, Phys.Lett **20**(1966)38

[2] K.S.Krane, ADND **19**(1977)363

[3] S.S.Alpert et al. **UCRL-9850**(1961)

[4] R.B.Begzhannov et al., Phys. Ser **36**(1973)2190

[5] J.A.C.Conçalves and R.N.Saxena, Phys. Rev **C43**(1991)2586

[6] E.Achterberg et al., Phys. Rev **C5**(1972)1759

[7] K.S.Krane et al., Phys. Rev **C5**(1972)1671

[8] B.K.S.Koene et al., Nucl. Phys **A235**(1974)267

[9] K.S.Krane., ANDT **19**(1977)363

[10] J.H.Hamilton et al., Phys. Rev **C1**(1970)666

[11] E.S.Macias et al., Nucl. Phys **A147**(1970)513

[12] E.J.Shineid and B.Rosner, Phys. Rev **148**(1966)1241

[13] P.A.Moore et al., Phys. Rev **175**(1968)1516

[14] E.S.Macias and W.B.Walters, Nucl. Phys **A169**(1971)305

[15] W.B.Walters et al., Phys. Rev **C26**(1982)2273

[16] H.G.Hicks et al., Phys. Rev **C27**(1983)2203

[17] G.Alaga and G.Ialongo, Nucl. Phys **A97**(1967)600

[18] V.Parr, Phys. Phys. Rev **C11**(1975)1432

[19] V.Parr, Phys. Rev **C13**(1976)2532

[20] R.A.Meyer et al., Phys. Rev **C16**(1977)417

[21] R.Almar et al., Phys. Rev **C6**(1972)187

[22] G.V.Berghe, Z. Phys **266**(1974)139

[23] D.Visser, Ph.D thesis (unpublished), Groningen 1981.

[24] V.R.Green et al., Daresbury Annual Report (1986/87)

[25] H.Pattyn et al., Hyp. Int **2**(1976)362

[26] V.Paar, private communication (1995)

[27] A.Turos et al., Nucl. Inst. and Meth. **B19/20**(1987)123

[28] R.N.Saxena and H.D.Sharma, Nucl. Phys **A171**(1971)593

[29] P.K.James, D.Phil thesis, Oxford 1975

[30] D.Visser, Ph.D thesis, Groningen 1981

[31] L.S.Kisslinger and R.A.Sorensen., Rev Mod. Phys **35**(1963)853

[32] S.Jha et al., Phys. Rev **C6**(1972)2193

[33] J.C.Wells et al., Bull Am Phys. Soc **20**(1975)1188

Chapter Five

The Theory of Nuclear Models

5.1 Introduction

In this chapter, the collective and shell models of the nucleus are described and then the two models are combined and extended to describe well deformed odd-*A* nuclei in particle-core coupling models.

The theoretical work given here is based on the works by Eisenberg and Greiner[1], deShalit and Feshbach[2], and Bohr and Mottleson[3].

5.2 The Collective model

The liquid drop model (LDM) of the nucleus was one of the first models used to describe the different properties of the nucleus. This model is based on the assumption of the existence of strong coupling between the nucleons, as a result of which the mean free path of a nucleon in nuclear matter is small compared with the dimensions of the nucleus, and collective excitations associated with a simultaneous change of the states of many nucleons are taken into account. Collective degrees of freedom associated with change of the shape of the nucleus and of its orientation in space are taken into account.

5.2.1 Deformation parameters

Assume that the nucleus has a sharp surface and undergoes dynamical shape or surface oscillations. The length of the radius vector pointing from the origin to the surface is given by

$$R = R(\vartheta,\varphi) = R_0\left(1+\alpha_{00}+\sum_{\lambda=1}^{\infty}\sum_{\mu=-\lambda}^{\lambda}\alpha^{*}_{\lambda\mu}Y_{\lambda\mu}(\vartheta,\varphi)\right) \tag{5.1}$$

where R_0 is the radius of a sphere of the same volume and α_{00} is a constant that describes changes of the nuclear volume. Because of the assumption of the incompressibility of the nuclear fluid in this model the volume is kept constant for all deformations as $V = \frac{4}{3}\pi R_0^3$. The constant α_{00} is defined as

$$\alpha_{00} = -\frac{1}{4\pi}\sum_{\lambda \geq 1,\mu}\left|\alpha_{\lambda\mu}\right|^2 \tag{5.2}$$

The term $\lambda = 1$ describes mainly a translation of the whole system. The three parameters $\alpha_{\lambda\mu}$ can be fixed by the condition that the origin coincides with the centre of mass $\int_V r d^3r = 0$.

The condition on R is that R should be invariant under reflection and rotation of the coordinate system, and the $\alpha_{\lambda\mu}$ must be multiplied by a factor $(-)^\lambda$ under a parity transformation and must behave like $Y_{\lambda\mu}(\vartheta,\varphi)$ under a rotation of the coordinate system to satisfy the condition on R.

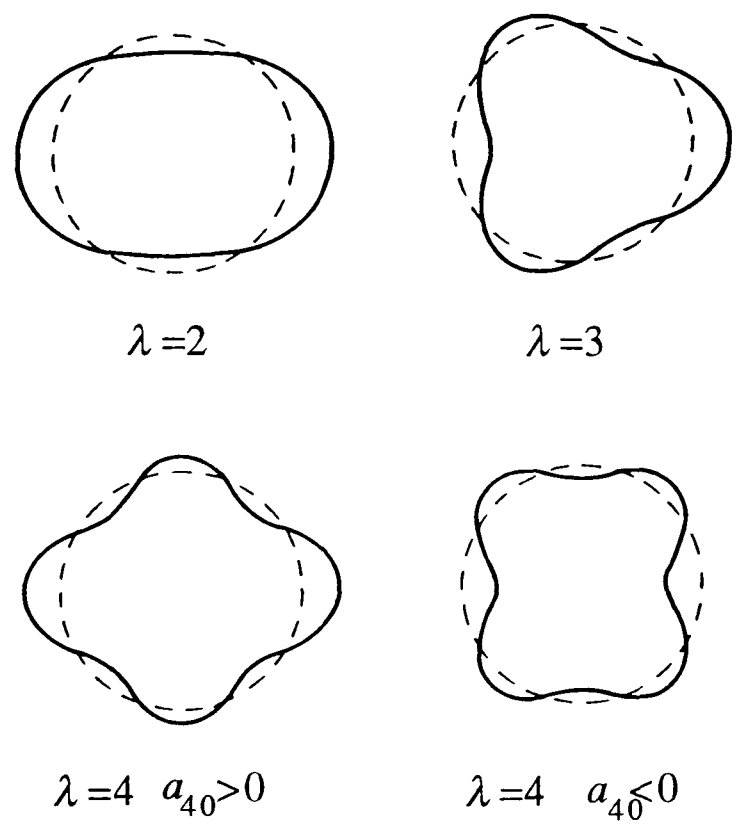


Fig 5.1. Nuclear shapes with quadrupole (λ=2), octupole (λ=3) and hexadecapole (λ=4) deformation.

$$\left(Y_{\lambda\mu}\right)_{\text{new}} = \sum_{\mu'} D^{\lambda}_{\mu'\mu}(\Omega)\left(Y_{\lambda\mu'}\right)_{\text{old}}$$
$$a_{\lambda\mu} = \sum_{\mu'} D^{\lambda}_{\mu'\mu}(\Omega)\alpha_{\lambda\mu'} \tag{5.3}$$

where $D^{\lambda}_{\mu'\mu}(\Omega)$ are the Wigner functions of the rotation and $a_{\lambda\mu}$ are the deformation parameters in the new system. For R to be real,

$$Y^{*}_{\lambda\mu} = (-)^{\mu} Y_{\lambda-\mu}$$
$$\alpha^{*}_{\lambda\mu} = (-)^{\mu} \alpha_{\lambda-\mu} \tag{5.4}$$

For axially symmetric deformation, the z-axis is chosen as the symmetry axis and the $\alpha_{\lambda\mu}$ vanish except for $\mu = 0$. The deformation parameters $\alpha_{\lambda 0}$ are usually called B_{λ}.

For the quadrupole deformation $(\lambda = 2)$ there are five parameters, three of which are correspond to the Euler angles and two real independent variables a_{20} and $a_{22} = a_{2-2}$ $(a_{21} = a_{2-1} = 0)$, and these give a complete description of the system. Introducing Hill-Wheeler[1] coordinates $\beta(>0)$, γ through the relation

$$a_{20} = \beta\cos\gamma$$
$$a_{22} = \frac{1}{\sqrt{2}}\beta\sin\gamma \tag{5.5}$$

Then

$$\sum_{\mu}\left|\alpha_{\alpha\mu}\right|^{2} = a^{2}_{20} + 2a^{2}_{22} = \beta^{2} \tag{5.6}$$

and

$$R(\vartheta,\varphi) = R_{0}\left\{1 + \beta\sqrt{\frac{5}{16\pi}}\cos\gamma\left(3\cos^{2}\vartheta - 1\right) + \sqrt{3}\sin\gamma\sin^{2}\vartheta\cos 2\varphi\right\} \tag{5.7}$$

5.2.2 Surface oscillations about a spherical shape

Surface oscillations are the first kind of excitations and the surface coordinates $\alpha_{\lambda\mu}(t)$ are functions of time with $\lambda \geq 2$.

The classical Hamiltonian function H_{coll} for small oscillations around spherical equilibrium shape is

$$H_{coll} = T + V = \frac{1}{2}\sum_{\lambda,\mu}\left\{B_\lambda\left|\dot{\alpha}_{\lambda\mu}\right|^2 + C_\lambda\left|\alpha_{\lambda,\mu}\right|^2\right\} \tag{5.8}$$

where the parameters of inertia B_λ and of stiffness C_λ are real constant.

Assuming the system is irrotational and incompressible, the kinetic energy of the surface vibrations is given by

$$T = \frac{m}{2}\rho\int_V V^2(\boldsymbol{r})d^3r = \frac{m}{2}\rho\int_V\left|\nabla\Phi\right|^2 d^3r = \frac{m}{2}\rho\oint_s\Phi^*\nabla\Phi ds \tag{5.9}$$

where ρ is the constant density of a nucleus of mass m. Using the gradient formula for spherical harmonics, the expression in the approximation of small deformations is obtained

$$T = \frac{R_0^5 m\rho}{2}\sum_{\lambda\mu}\frac{\left|\dot{\alpha}_{\lambda\mu}\right|^2}{\lambda} \tag{5.10}$$

The mass parameter B_λ is obtained by comparing (5.8) with (5.9)

$$B_\lambda = \frac{R_0^5 m\rho}{\lambda} = \frac{3}{4\pi\lambda}AmR_0^2 \tag{5.11}$$

The potential energy of a liquid drop with a surface deformation characterized by the parameters $\alpha_{\lambda,\mu}$ can be obtained from the coefficient of equation (5.2) if pairing energy with deformation and changes of the symmetry are neglected.

The deformation energy is defined as the difference in energy of the deformed and spherical drop

$$V(\alpha) = E_s(\alpha) - E_s(0) + E_c(\alpha) - E_c(0) \tag{5.12}$$

where the surface energy E_s and the Coulomb energy E_c is given by

$$E_s(\alpha) = \sigma\oint_s ds = E_s(0) + \frac{1}{2}\sum_{\lambda\mu}(\lambda-1)(\lambda+2)R_0^2\sigma\left|\alpha_{\lambda,\mu}\right|^2 \tag{5.13}$$

$$E_c(\alpha) = (Ze)^2\iint_v\frac{d^3r_1 d^3r_2}{\left|\boldsymbol{r}_1 - \boldsymbol{r}_2\right|} = E_c(0) - \frac{1}{2}\sum_{\lambda\mu}\frac{3(\lambda-1)(Ze)^2}{2\pi(2\lambda+1)R_0}\left|\alpha_{\lambda,\mu}\right|^2 \tag{5.14}$$

where σ is the surface tension.

From equations (5.8) and (5.13) the stiffness coefficients $(\lambda \geq 2)$ is as follows

$$C_\lambda = (\lambda - 1)(\lambda + 2)R_0\sigma - \frac{3(\lambda - 1)}{2\pi(2\lambda + 1)}\frac{(Ze)^2}{R_0} \tag{5.15}$$

The calculation of lifetimes and transition probabitlities require knowledge of $B(E\lambda)$ and $B(M\lambda)$ which are defined by

$$B\left(\begin{Bmatrix} E \\ M \end{Bmatrix}\lambda, I_i \to I_f\right) = \frac{1}{2I_i + 1}\left|\left\langle I_f \left\| \begin{Bmatrix} \hat{Q}_\lambda \\ \hat{M}_\lambda \end{Bmatrix} \right\| I_i \right\rangle\right|^2 \tag{5.16}$$

Since the $M1$-operator conserves angular momentum, $M1$-transitions are forbidden in this model. Therefore the most important transitions are $E2$-transitions.

Experimentally, it has been found that there is a strong correlation between the $B(E2)$ value of the first 2^+ state and its energy $E_{2^+} = \Omega_2$

$$E_{2^+} B\left(E2, 2_1^+ \to 0^+\right) \approx (25 \pm 8)\frac{Z^2}{A}\left[MeV\, e^2\, fm^4\right] \tag{5.17}$$

This empirical relation holds for all the nuclei throughout the nuclear table. Equation (5.16) shows the same energy dependence, but the A dependence is different. The strong shell effects in the low-lying 2^+ states indicate that they can not be pure quadrupole surface oscillations and that there are other states which also have the character of such collective vibrations.

5.2.3 Rotations and Vibrations for deformed shapes

5.2.3.1 The Bohr Hamiltonian

The pure LDM has a stable equilibrium only for spherical surfaces. Due to shell effects the potential $V(\alpha)$ in the collective Hamiltonian has minima at finite non-vanishing values of $\alpha = \alpha_0$. In this case the nucleus can have a stable ground state deformation and can exhibit collective rotations, which can be described by time-dependent surface parameters $\alpha_{\lambda,\mu}$ in the laboratory frame.

In a quantum mechanical description, a system with an axis of symmetry is

given by a wave function which is an eigenfunction of the angular momentum operator J_z, and any rotation about this axis produces only a phase. The rotating system has, therefore, the same wave function as the ground state and the same energy. With the body-fixed system that is defined by the principal axes of the mass distribution the potential in (5.8) has the form

$$V(\beta,\gamma)=\frac{1}{2}C_{20}\left(a_{20}(\beta,\gamma)-\dot{a}_{20}\right)^2+C_{22}\left(a_{22}(\beta,\gamma)-\dot{a}_{22}\right)^2 \tag{5.18}$$

This corresponds to a quadratic approximation in the vicinity of a deformed minimum at β_0 and γ_0. The nucleus has a deformation in its ground state, and the excitations are rotations and small oscillations around this equilibrium deformation. Transforming the kinetic energy in (5.8) to the body-fixed system and applying (5.3), the Bohr Hamiltonian is

$$T=T_{rot}+\frac{1}{2}B_2\left(\dot{\beta}^2+\beta^2\dot{\gamma}^2\right) \tag{5.19}$$

with

$$T_{rot}=\frac{1}{2}\sum_{\kappa=1}^{3}\zeta_\kappa\omega_\kappa^2$$

where ω_κ is the angular velocity around the body-fixed κ-axis and ζ_κ is a function of (β,γ) given by

$$\zeta_\kappa=4B_2\beta^2\sin^2\left(\gamma-\frac{2\pi}{3}\kappa\right),\qquad \kappa=1,2,3 \tag{5.20}$$

Using (5.11) and (5.20) the irrotational moment of inertia is

$$\zeta_\kappa^{irr}=\frac{3}{2\pi}mAR_0^2\beta^2\sin^2\left(\gamma-\frac{2\pi}{3}\kappa\right),\qquad \kappa=1,2,3 \tag{5.21}$$

which differs from the moment of inertia of a rigid body with the same deformation

$$\zeta_\kappa^{rig}=\frac{2}{5}mAR_0^2\left(1-\sqrt{\frac{5}{4\pi}}\beta\cos\left(\gamma-\frac{2\pi}{3}\kappa\right)\right),\qquad \kappa=1,2,3 \tag{5.22}$$

The experimental moment of inertia $\zeta_\kappa^{\exp}$ can be found from the energy of the first 2^+ state of a rotational band $\zeta_\kappa^{\exp}=\frac{3}{E_{2^+}}(MeV)$. Using euqations (5.17) and (5.35)

$$\zeta_{\kappa}^{\exp} = \frac{27}{8\pi^2} r_0^4 \frac{A^{4/3}\beta^2 (Ze)^2}{E_{2^+} B(E2)} \approx \frac{27(1.2)^4 \beta^2 A^{7/3}}{80\pi^2 25} \approx \frac{\beta^2 A^{7/3}}{400} (MeV) \qquad (5.23)$$

In the case of well deformed nuclei $(\beta - 0.2 \sim 0.4)$, ζ^{irr} is usually smaller by a factor of 2-3 than the experimental values while ζ^{rig} is large by a factor of 2

$$\zeta^{irr} < \zeta^{\exp} < \zeta^{rig} \qquad (5.24)$$

This shows that the flow structure of the nuclei is not irrotational or a rigid rotor. To quantize the classical Hamiltonian (5.19), the classical kinetic energy, which has the form

$$T = \frac{1}{2} \sum_{ij}^{k} g_{ij}(\xi) \dot{\xi}_i \dot{\xi}_j \qquad (5.25)$$

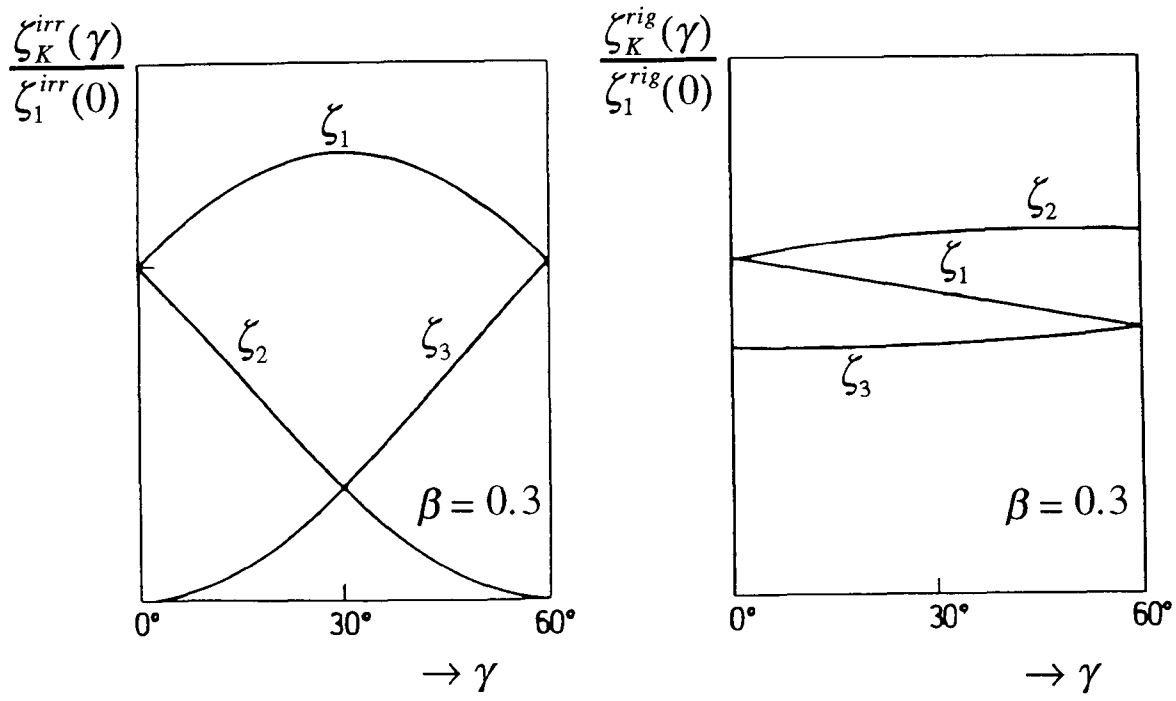


Fig 5.2. The γ-dependence of the irrotational and the rigid moments of inertia for fixed values of β[17]

then the quantized form is

$$\hat{H}_{kin} = -\frac{\hbar^2}{2}\sum_{ij} g^{-1/2}\frac{\partial}{\partial\xi_i} g^{1/2}\left(g^{-1}\right)_{ij}\frac{\partial}{\partial\xi_{ij}} \tag{5.26}$$

where g is the determinant and g^{-1} is the inverse matrix of g.

Applying equations (5.18) and (5.19),

$$\hat{H}_{coll} = -\frac{\hbar^2}{2B_2}\left[\beta^{-4}\frac{\partial}{\partial\beta}\left(\beta^4\frac{\partial}{\partial\beta}\right)+\frac{1}{\beta^2\sin 3\gamma}\frac{\partial}{\partial r}\left(\sin 3\gamma\frac{\partial}{\partial r}\right)\right]+\hat{T}_{rot}+V(\beta,\gamma) \tag{5.27}$$

where the rotation energy is

$$\hat{T}_{rot} = \frac{\hat{I}_1^2}{2\zeta_1}+\frac{\hat{I}_2^2}{2\zeta_2}+\frac{\hat{I}_3^2}{2\zeta_3} \tag{5.28}$$

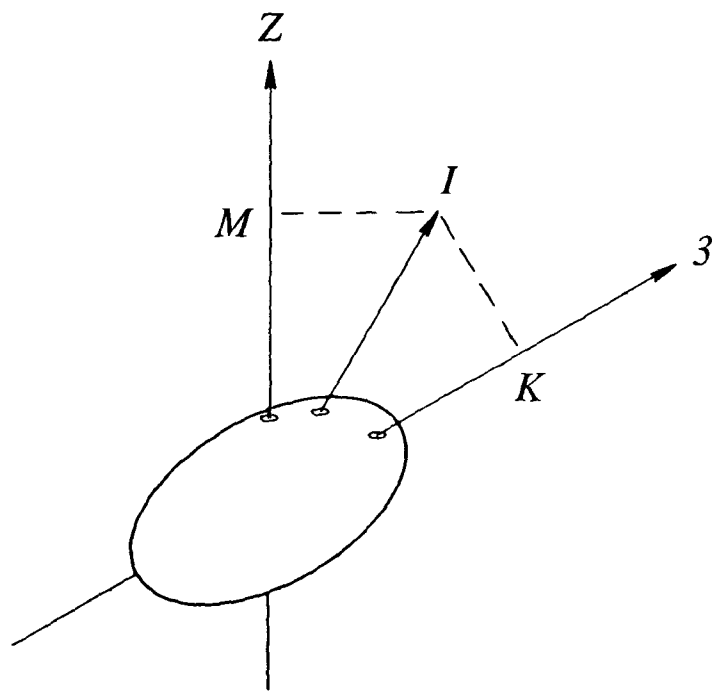


Fig 5.3 The relation between the total angular momentum I and its projection M onto the laboratory z-axis and its projection K onto the body-fixed 3-axis.

The operators $\hat{I}_k$ are the projections of the total angular momentum $\hat{I}$, represented in the Euler angles onto the body-fixed axes. Fig (5.3) shows the total angular momentum and its components $\hat{I}_2 = M$ and $\hat{I}_3 = K$. The eigenfunctions of $\hat{\boldsymbol{I}}^2$, $\hat{I}_z$ and $\hat{I}_3$ are given by

$$|IMK\rangle = \sqrt{\frac{2I+1}{8\pi^2}} D^{I*}_{MK}(\Omega) \tag{5.29}$$

Since $\hat{H}_{coll}$, $\hat{\boldsymbol{I}}^2$ and $\hat{I}_z$ commute, the eigenfunctions of the collective Hamiltonian (5.27) have the general form

$$\left|\Psi^I_M\right\rangle = \sum_k g_k(\beta,\gamma)|IMK\rangle \tag{5.30}$$

The triaxial rotor has certain discrete symmetries. $\hat{H}_{coll}$ is invariant under the point group D_2. Therefore eigenstates can be classified according to the irreducible representations of this group.

5.2.3.2. The axially symmetric case

In the case of very pronounced minima in the potential surface at axially symmetric deformations $\beta = \beta_0$ and $\gamma = 0$, rotations and small vibrations of the nuclear surface are expected. Expanding (5.28) around these points the Hamiltonian of an axially symmetric rotor with the moment of inertia $\zeta_0 = \zeta_1(\beta_0,0) = \zeta_2(\beta_0,0)$ to zeroth order, we obtain

$$T'_{rot} = \frac{\hat{\boldsymbol{I}}^2 - \hat{I}_3^2}{2\zeta_0} \tag{5.31}$$

The term $\hat{I}_3^2/2\zeta_3$ in H_{coll} couples rotations and vibrations since first-order terms are proportional to the deviation $(\beta - \beta_0)$ and γ and are mixture of rotational and vibrational degrees of freedom. Also ζ_3 vanishes for $\gamma = 0$ it can not be expanded and commutes with $\hat{I}_3$ and K.

(i) $K = 0$ bands $(I_3 = 0)$

In this case the rotational and vibrational motions decouple, and the wave function is

$$\left|\Psi^I_{M0}\right\rangle = g_0(\beta,\gamma)|IM0\rangle \tag{5.32}$$

where $g_K(\beta,\gamma)=(-1)^{I+K}g_{-K}(\beta,\gamma)$.

The motion in the coordinate a_{20} (β-vibration) decouples from the motion in the coordinate a_{22} (γ-vibration). Axial symmetry with respect to the 3-axis is preserved by the β-vibrations (quantum number n_β), but violated by the γ-vibrations (quantum number n_γ). (See fig 5.5)

Superimposed on each vibrational state (n_β,n_γ) is a rotational band and the spectrum is given by

$$E_{n_\beta n_\gamma}=E_{n_\beta n_\gamma}(0)+\frac{\hbar^2}{2\zeta_0}I(I+1) \tag{5.33}$$

with the band head

$$E_{n_\beta n_\gamma}(0)=\hbar\omega_\beta\left(n_\beta+\frac{1}{2}\right)+\hbar\omega_\gamma\left(2n_\gamma+1\right)\qquad n_\beta,n_\gamma=0,1,2\cdots \tag{5.34}$$

where ω_β and ω_γ are the frequencies of β- and γ-vibrations with $\omega_\beta=\left(C_{20}/B_2\right)^{1/2}$ and $\omega_\gamma=\left(C_{22}/B_2\right)^{1/2}$. These bands have been observed in many even-even nuclei as ground state bands $(n_\beta=n_\gamma=0)$ and β-bands $(n_\beta=1,n_\gamma=0)$.

The stretched $B(E2)$ values in a rotational band for K=0 bands are

$$B(E2,I+2\to I)=Q_0^2\frac{5}{16\pi}\frac{3}{2}\frac{(I+1)(I+2)}{(2I+3)(2I+5)} \tag{5.35}$$

(ii) $K\neq 0$ bands

The wavefunction has the form

$$\left|\Psi^I_{MK}\right\rangle=g_K(\beta,\gamma)\frac{1}{\sqrt{2}}\left\{|IMK\rangle+(-1)^I|IM-K\rangle\right\} \tag{5.36}$$

Bands have the spin sequence $I=|K|,|K|+1,\cdots$. The motion in a_{20} (β-vibration) can be separated from the rest but the term $\hat{I}_3/2\zeta_3=K^2/16B_2a_{22}$ couples the γ-vibrations with the rotation around the 3-axis. The spectrum is given by

$$E_{K,n_\beta,n_\gamma}(I)=E_{K,n_\beta,n_\gamma}(0)+\frac{\hbar^2}{2\zeta_0}\left\{I(I+1)-K^2\right\} \tag{5.37}$$

with the band-heads

$$E_{K,n_\beta,n_\gamma}(0)=\hbar\omega_\beta\left(n_\beta+\frac{1}{2}\right)+\hbar\omega_\gamma\left(2n_\gamma+1+\frac{|K|}{2}\right) \tag{5.38}$$

These bands are observed as γ-bands in many deformed nuclei, which have the quantum numbers $K=2,\ n_\beta=0,\ n_\gamma=1$. Since $\gamma=0$ implies $\zeta_3=0$ only the quantum mechanical zero point vibration in the γ-direction makes this possible. Fig (5.4) shows the qualitative structure of the collective $(\lambda=2)$ excitation in deformed and spherical nuclei.

For a theoretical description of deviation from the $I(I+1)$ law in the deformed nuclei, the rotational-vibrational coupling terms in $\hat{H}_{coll}$ should be taken into account. This rotational-vibrational interaction causes changes in the moment of inertia of a band and corresponds to a change of the nuclear shape under the influence of the rotation (stretching effect).

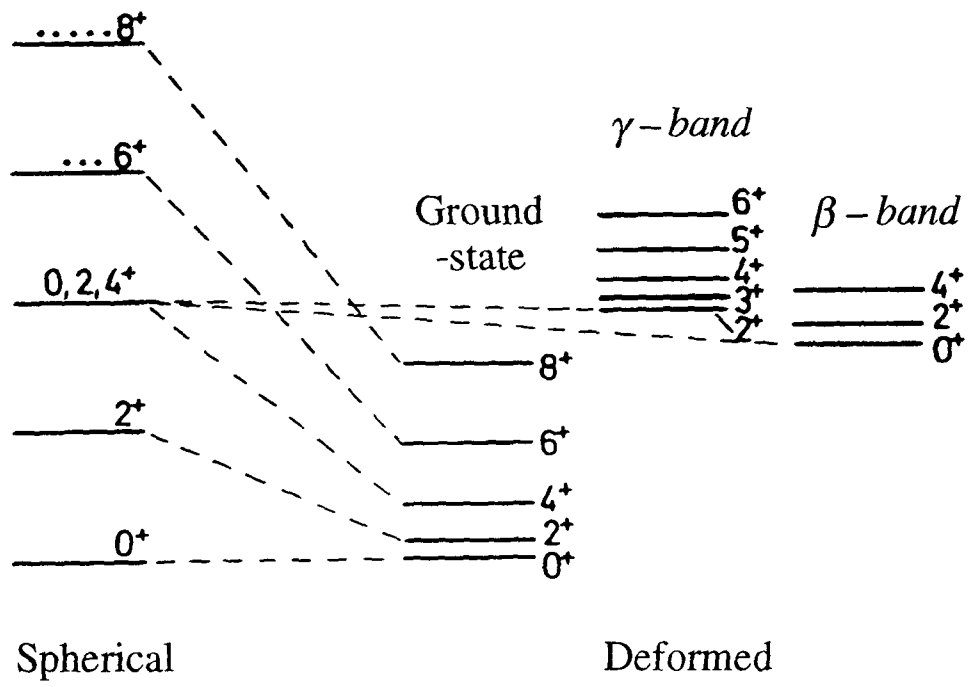


Fig 5.4 Schematic level schemes of spherical $(E=n\hbar\omega)$ and deformed nuclei $(E=I(I+1)\hbar^2/2\zeta)$

5.2.3.3 The Asymmetric Rotor

The wave function has the form

$$\left|\Psi_M^I\right\rangle = \sum_K g_K \left\{ |IMK\rangle + (-1)^I |IM-K\rangle \right\} \qquad K = 0,2,4\cdots \tag{5.39}$$

By assuming a maximal triaxiality $(\gamma = 30^\circ)$ the level structure of triaxial nuclei can be estimated roughly. The projection α of I onto the 1-axis is a good quantum number and

$$E_\alpha(I) = \frac{3\hbar^2}{8\zeta_0}\left[4I(I+4) - 3\alpha^2\right] \tag{5.40}$$

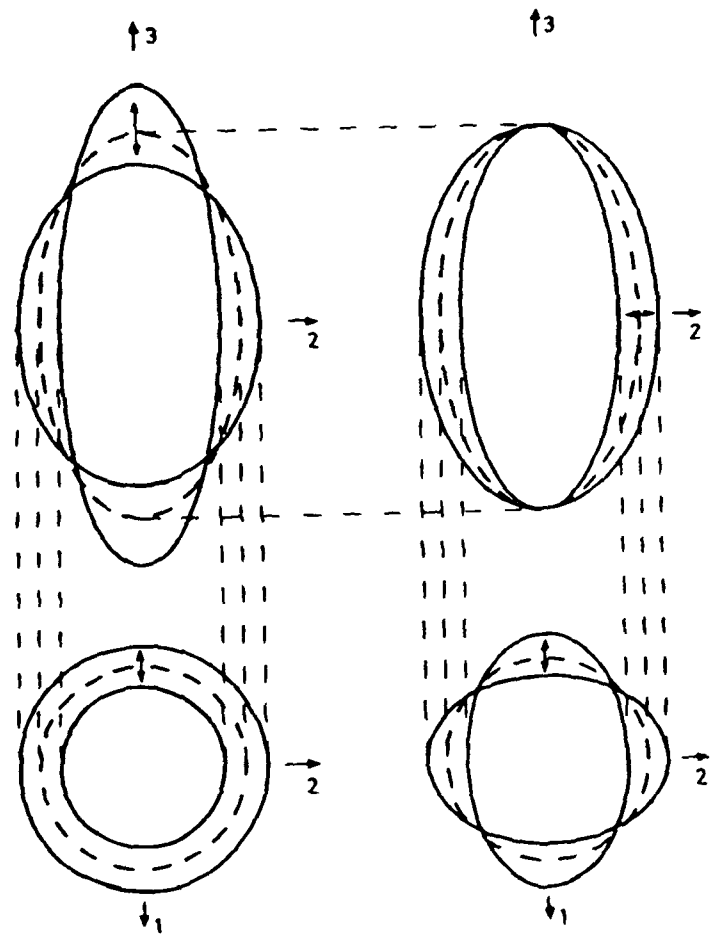


Fig 5.5 Schematical representation of β– and γ–vibrations by a cut along the (1,3) and (1,2) planes[1,3]

where $\zeta_2 = \zeta_3 = \frac{1}{4}\zeta_1 = \frac{1}{3}\zeta_0$ and ζ_0 is the moment of inertia at r=0. For each I the yrast level has $\alpha = I$. Next in energy comes the band with $\alpha = I-2$ and $\alpha = I-4$, and so on. Therefore a sequence of bands can be characterized by the "Wobbling" quantum number $n = I - \alpha$. States with the same n which are connected by large $E2$-transition probabilities can be calculated and from (5.40) their spectrum is

$$E_n(I) = \frac{3\hbar^2}{8\zeta_0}\left[4I(I+4) + 3n(2I-n)\right] \tag{5.41}$$

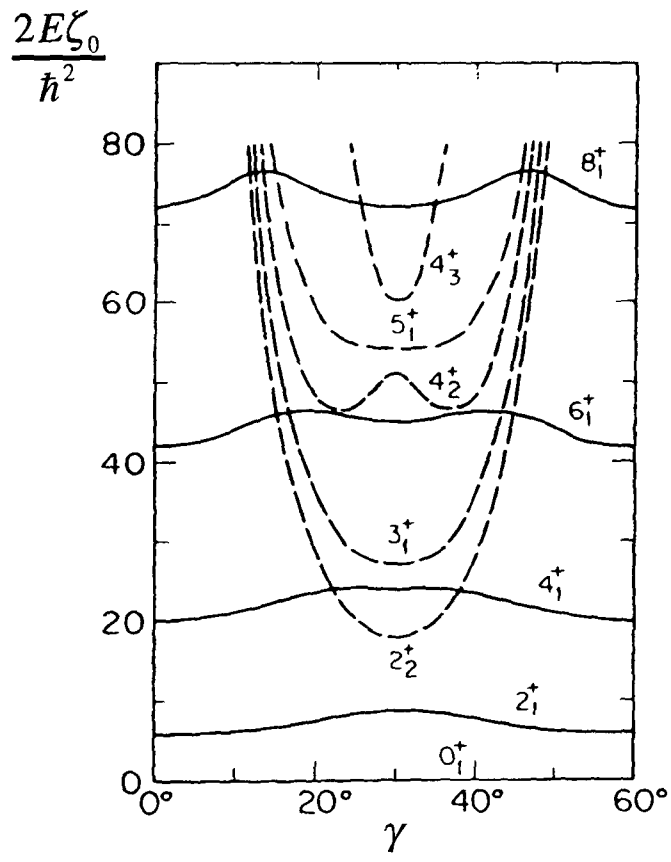


Fig 5.6. The energy eigenvalues of a deformed, asymmetric rotor with hydrodynamic moments of inertia[17]

5.3 The nuclear shell model

The theory of the shell model of the nucleus is based on the assumption that the nucleons in the nucleus move almost independently in the field created by all the other nucleons, despite the existence of the strong interaction between free nucleons. The interaction between them can be described by a self-consistent field that is assumed to be the same for all the nucleons and also the potential of this field is assumed to be static and spherically symmetric. In the shell model the independence of the motion of individual nucleons in the nucleus means that the mean free path of a nucleon in nuclear matter is large compared with dimensions of the nucleus while the liquid drop model of the nucleus is based on the assumption of the existence of strong coupling between the nucleons, which means that the mean free path of a nucleon in the nuclear matter is small compared with the the dimensions of the nucleus. Since the nuclear forces have a short range character, the potential of the self-consistent field varies in nearly the same way as the nuclear density. As a result, the one particle wave functions are not plane waves, but more complicated functions, which depend on the distance from the centre of the nucleus and go to zero outside the nucleus. The Pauli principle prevents the presence of more than one particle occupying a given state and, therefore, the effective interaction between the nucleons is considerably weakened. Thus, in spite of the presence of a strongly fluctuating potential, the motion of a nucleon will often be fairly smooth, since there are not many states available into which it can scatter. However there are two major problems in the study and description of nuclei. Firstly, it is a many-body system so we need to employ an approach in terms of pertubation theory with its accompanying problems of convergence. Secondly, the exact nature of the nucleon-nucleon interaction is not known.

An atomic shell model approach is very useful in describing nuclei but there are, however, some essential differences in the case of nuclei.

(i) The nuclear force is attractive and the nuclear interaction is quite different from the Coulomb interaction and it contains a strong spin-orbit interaction term.

(ii) The neutrons and the protons in the nucleus give rise to an additional quantum number, the isospin.

(iii) There is no heavy centre of force similar to that of the atom in the nuclear system.

For these reasons the maximum number of particles in successive shells differs for nuclei and atoms. Thus the shell closures occur at different particle numbers in the two systems.

The discrete and generally degenerate nuclear energy levels of the single-particle states in a central field are clustered in groups. Due to the Pauli principle each state or orbit of given j can be occupied only by a restricted number of identical fermions, thus forming a subshell. A group of orbits lying close in energy is referred to as a major shell. Each orbit is characterized by a particular value of the radial quantum number(n), the orbital quantum number(l) and the total angular momentum quantum number(j). Closed-shell states in nuclei are coupled to total spin J=0. The most stable configuration is obtained when there is a large energy gap between the highest occupied level and the lowest unfilled level. In general, the nucleus consists of a definite number of filled shells and a few outer nucleons in an unfilled shell. The hypothesis of the existence of shell structure in nuclei was put forward by Elsasser[24] and the modern theory of nuclear shells is based on the work of Goeppert-Mayer[25,26] and Haxel, Jensen and Suess[27,28], who assumed the existence of a strong spin-orbit interaction between the nucleons in nuclei. The only way to exite closed-shell nuclei is by promoting at least one nucleon to a higher-lying shell. Other nuclei with partly filled shells may have excited states that result from a recoupling of the angular momenta only. This usually results in appreciably smaller excitation energies for these states. The nucleon number at a shell closure is called a *magic number*. The closed-shell nuclei exhibit extra stability compared to neighbouring nuclei. After introducing a strong spin-orbit coupling term into the independent-particle Hamiltonian the magic numbers can be reproduced.

There exist several variations on the shell model of the nucleus. In the simplest of the these, the one-particle shell model, which is used to describe nuclei with odd values of the mass number A, it is assumed that all paired nucleons (including nucleons in the unfilled outer shell) form an inert core with zero spin, and the properties of the nucleus are entirely determined by the state of the last odd nucleon. In the many-particle shell model, the properties of the nucleus are determined by all the nucleons, both in the unfilled shell and in the filled shells.

5.4. One-particle shell model of nuclei

5.4.1 Spins and parities of the ground states of nuclei

The one-particle shell model can explain the special stability of magic nuclei and predict correctly the spins and parities of the ground states of most odd-A nuclei. According to the one-particle shell model, all the paired nucleons from a core with zero spin and, therefore, the spin and parity of the nucleus are determined by the state of the last unpaired nucleon. This model can only describe the properties of odd nuclei. The experimentally determined spins and parities of the ground states of odd nuclei, in almost all cases, coincide with the values predicted by the model for the last unpaired nucleon.

In a more sophisticated model, the nucleus is represented as consisting of a certain number of filled shells and outer neutrons and protons in unfilled shells. In this case, the properties of the nucleus are determined by these outer uncleons. Since, however, for a system of identical particles there are several different independent states differing in symmetry and, consequently, in total angular momentum, the spin of the nucleus is not uniquely determined. This indeterminacy is removed by introducing the residual interaction between the nucleons, which causes the degeneracy of the states to be lifted. If the range of the interaction is small compared with the dimensions of the nucleus, the spin s of the ground state of a group of identical particles in the j-shell turns out to be equal to 0 if the number of particles is even and j if it is odd. This agrees with the results of the simple one-particle model. Thus the spins and parities of the ground states of the odd-A nuclei can be determined by knowing the one-particle level scheme determining the order in which the shells are filled.

Deviations from this rule occur for nuclei in which the next shell up has a higher spin and begins to be filled. Since the pairing energy of two nucleons with high spin is greater than the pairing energy of nucleons with low spin, the order of occupation of the shells is inverted and occupation of the higher shell by one or more pairs of nucleons occurs. When inversion occurs, the state corresponding to the normal order of occupation of the shells is found to be a low-lying metastable state, since its spin differs greatly from that of the ground state. Deviations from the general rule are observed for heavy nuclei, this being connected with violation of the spherical symmetry of the nuclei.

There are two fundamental setbacks if the theory is to agree with experimental single-particle spectra;

(i) a strong spin-orbit term must be added in order to reproduce the magic

numbers

(ii) for heavy nuclei, the realistic average potential is rather flat in the interior of the nucleus compared to the harmonic oscillator and nucleons with high l-values feel a deep potential in the realistic case.

5.4.2. Single-particle magnetic dipole moments of nuclei

An equation for the magnetic 2^l-pole moment is given by

$$\vec{\mu}^{(l)} = \langle jj | \sum_{k=1}^{A} {}_N \left\{ \nabla(k) r^l(k) Y_{l0}(\hat{\boldsymbol{r}}(k)) \right\} \cdot \left\{ \frac{2g_l(k)}{l+1} \boldsymbol{l}(k) + g_s(k) \boldsymbol{s}(k) \right\} | jj \rangle \qquad (5.42)$$

where $\boldsymbol{l}(k)$ and $\boldsymbol{s}(k)$ are the operators of the orbital and spin angular momenta of the nucleon, and g_l and g_s are the orbital and spin gyromagnetic ratios.

According to the one-particle model, the magnetic dipole moment of an odd nucleus is determined by the magnetic dipole of the last unpaired nucleon. For the magnetic moment of an individual nucleon moving in the self-consistent field of the nucleon (l=0),

$$\vec{\mu}^{(1)} = \vec{\mu} = \langle jj | \sum_{k=1}^{A} \{ g_l(k) \boldsymbol{l}(k) + g_s(k) \boldsymbol{s}(k) \} | jj \rangle \mu_N \qquad (5.43)$$

Because of the spin-orbit interaction, the orbital and spin angular momenta are not separately conserved in the motion of the nucleus but only the total angular momentum of the nucleus is conserved, where

$$\boldsymbol{j} = \sum_{k=1}^{A} [\boldsymbol{l}(k) + \boldsymbol{s}(k)] \qquad (5.44)$$

Both operators are linear combinations of the orbital and spin angular momenta, but with different coefficients, since $g_l(k) \neq g_s(k)$ for the protons and neutrons. Thus the two operators $\vec{\mu}$ and $\boldsymbol{j}$ are not parallel. But the expectation values of these operators in a state $|jm = j\rangle$ can be compared.

The magnetic dipole moment μ is defined as the mean value of the projection of the vector $\vec{\mu}$ on the direction of the vector $\boldsymbol{j}$ of the total angular momentum of the nucleon in the state with the maximum value of the projection of the vector $\boldsymbol{j}$. The generalized Landé formula is

$$\langle jm|V|jm'\rangle = \frac{\langle jm|V\cdot j|jm\rangle}{j(j+1)}\langle jm|j|jm'\rangle \tag{5.45}$$

which can be applied to get the expression for the single-particle magnetic moments

$$\begin{aligned}\mu &= \langle jm=j|\mu|jm=j\rangle = \langle jj|g_l l_z + g_s s_z|jj\rangle\mu_N \\ &= \frac{\langle jj|g_l(l\cdot j)+g_s(s\cdot j)|jj\rangle}{j(j+1)}\langle jj|j_z|jj\rangle\mu_N \\ &= \left\langle \frac{\vec{\mu}\cdot j}{j^2} j_z \right\rangle_{m=j}\end{aligned} \tag{5.46}$$

or, noting that $\langle j_z\rangle = j$ and $\langle j^2\rangle = j(j+1)$

$$\mu = \frac{1}{j+1}\langle \vec{\mu}\cdot j\rangle_{m=j} \tag{5.47}$$

Substituting (5.43) into (5.47) the single-particle magnetic dipole moment can be written as

$$\mu = \begin{Bmatrix} (j-\frac{1}{2})g_l + \frac{1}{2}g_s, & j = l+\frac{1}{2} \\ \left[1+\frac{1}{2(j+1)}\right]jg_l - \frac{j}{(2j+1)}g_s, & j = l-\frac{1}{2} \end{Bmatrix} \tag{5.48}$$

since $2l\cdot j = j^2 + l^2 - s^2$ and $2s\cdot j = j^2 - l^2 + s^2$.

The orbital gyromagnetic ratio g_l is equal to zero for the neutron and one for the proton. The spin gyromanetic ratio g_s can be put equal to twice the value of the intrinsic magnetic moment of the neutron or proton. Thus, for the unpaired neutron, equation (5.48) can be rewritten as

$$\mu = \begin{Bmatrix} \mu_n, & j = l+\frac{1}{2} \\ -\frac{1}{j+1}\mu_n, & j = l-\frac{1}{2} \end{Bmatrix} \tag{5.49}$$

and for the unpaired proton

$$\mu = \begin{cases} j - \frac{1}{2} + \mu_p, & j = l + \frac{1}{2} \\ \left[1 + \frac{1}{2(j+1)}\right] j - \frac{1}{j+1}\mu_n, & j = l - \frac{1}{2} \end{cases} \qquad (5.50)$$

The formulae (5.49) and (5.50) lead to Schmidt curves for the dependence of the magnetic moment μ of the nucleus on the spin j (See fig 5.7). Also there is an additional magnetic moment associated with the protons in the nucleus but it is found to be small compared with (5.50).

5.4.3. Single-particle electric quadrupole moments of nuclei

The nuclear quadrupole moments vary widely in magnitude from nucleus to nucleus. Light nuclei usually can be considered as to consist of a spherical core with a small number of extra nucleons which can be coupled to pairs, and then the electric quadrupole moments of nuclei on the basis of the single-particle shell model is due to the last unpaired odd-proton.

The operator for an electric transition is given by

$$O(Elm) = \sum_{k=1}^{A} e(k) r^l Y_{lm}(\hat{\boldsymbol{r}}(k)) \qquad (5.51)$$

where $e(k)$ represents the charge of the nucleon numbered k and is zero for a neutron and e for a proton and the definition for the quadrupole moment is

$$\begin{aligned} Q &= \sum_k e(k) \langle jj | 3z^2(k) - r^2(k) | jj \rangle \\ &= \sqrt{\frac{16\pi}{5}} \sum_{k=1}^{A} e(k) \langle jj | r^2(k) Y_{20}(\hat{\boldsymbol{r}}(k)) | jj \rangle \end{aligned} \qquad (5.52)$$

Unlike the electric dipole moment, the quadrupole moment operator $e(3z^2 - r^2)$ is an even function under inversion of the coordinate system. Hence the parity rule does not prevent nuclei from having a permanent quadrupole moment.

The Wigner-Eckart theorem with a 3-j symbol is

$$\langle j'm' | \boldsymbol{T}_q^k | jm \rangle = (-1)^{j'-m'} \begin{pmatrix} j' & k & j \\ -m' & q & m \end{pmatrix} \langle j' \| \boldsymbol{T}^k \| j \rangle \qquad (5.53)$$

where $\boldsymbol{T}^k$ is the spherical tensor operator acting on the ψ_{jm} and produces a state that can be acted upon by the rotation operator $R(\alpha\beta\gamma)$, k the spherical tensor operator rank and q=-k,-k+1,...,k).

The reduced martix elements of spherical harmonics are

$$\left\langle l_a \frac{1}{2} j_a \| Y_l \| l_b \frac{1}{2} j_b \right\rangle = (-1)^{j_a+½} \sqrt{\frac{(2j_a+1)(2j_b+1)(2l+1)}{4\pi}} \times \begin{pmatrix} j_a & l & j_b \\ \frac{1}{2} & 0 & -\frac{1}{2} \end{pmatrix} \times \frac{1}{2}\left\{1+(-1)^{l_a+l+l_b}\right\} \tag{5.54}$$

Using equations (5.53), (5.54) and keeping the radial integral as a separate factor, equation (5.52) can be written as

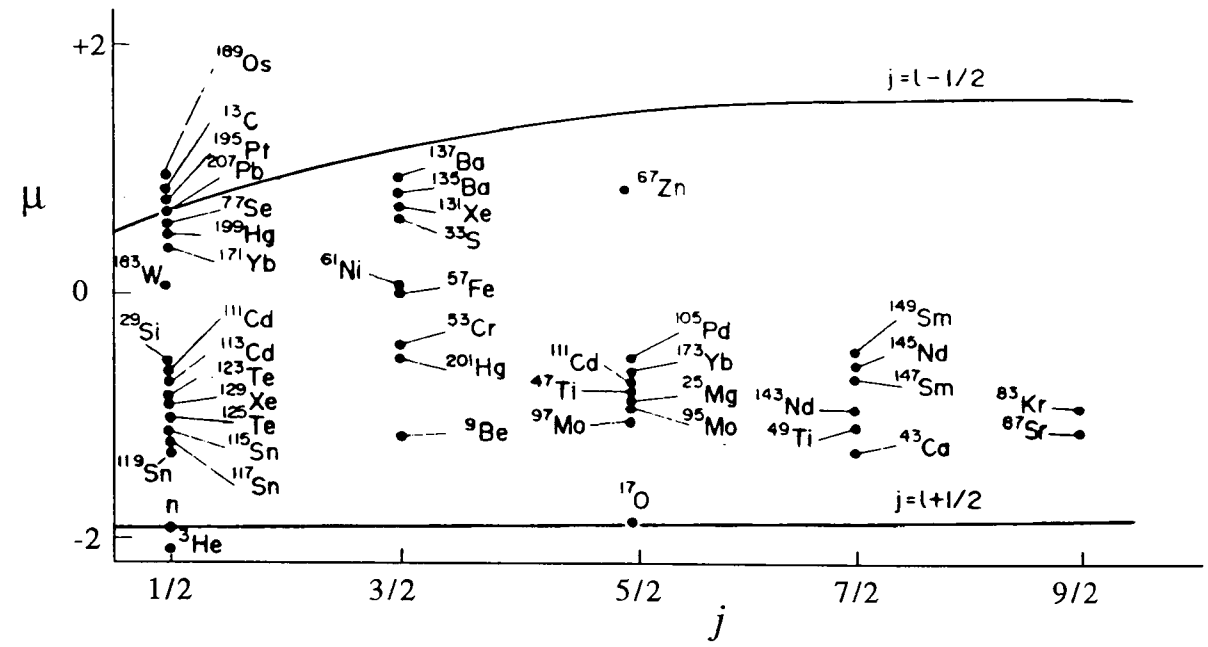
$$\begin{aligned} Q_{zz} &= e\sqrt{\frac{16\pi}{5}}\langle nl|r^2|nl\rangle \begin{pmatrix} j & 2 & j \\ -j & 0 & j \end{pmatrix} \left\langle l \frac{1}{2} j \| Y_2 \| l \frac{1}{2} j \right\rangle \\ &= -e\langle nl|r^2|nl\rangle \frac{2j-1}{2(j+1)} \end{aligned} \tag{5.55}$$

The minus sign in equation (5.55) indicates the fact that the density of a state $|jm=j\rangle$ is concentrated along the equator and the inequality $\langle 3z^2\rangle < \langle r^2\rangle$. The radial integral in equation (5.55) can be evaluated for harmonic-oscillator wave functions.

There is also a certain effective quadrupole moment for an unpaired neutron because of the recoil motion of the nuclear core, and the magnitude of the effective quadrupole moment of the neutron amounts to Z/A^2 of the magnitude of the proton quadrupole moment.

The electric quadrupole moments calculated using the single-particle model agree with the experimental values only in the case of nuclei containing one nucleon outside of a filled shell and differ both in sign and in magnitude in almost all other nuclei. The largest quadrupole moments are often observed in nuclei with half-filled shells. Although the periodic dependence of the nuclear quadrupole moments on the number of nucleons is evidence of the shell structure of nuclei the single-particle model is not useful for determining the magnitude of the nuclear quadrupole moments. This indicates that not only one but at least several nucleons contribute to the quadrupole moment.

(a)



(b)

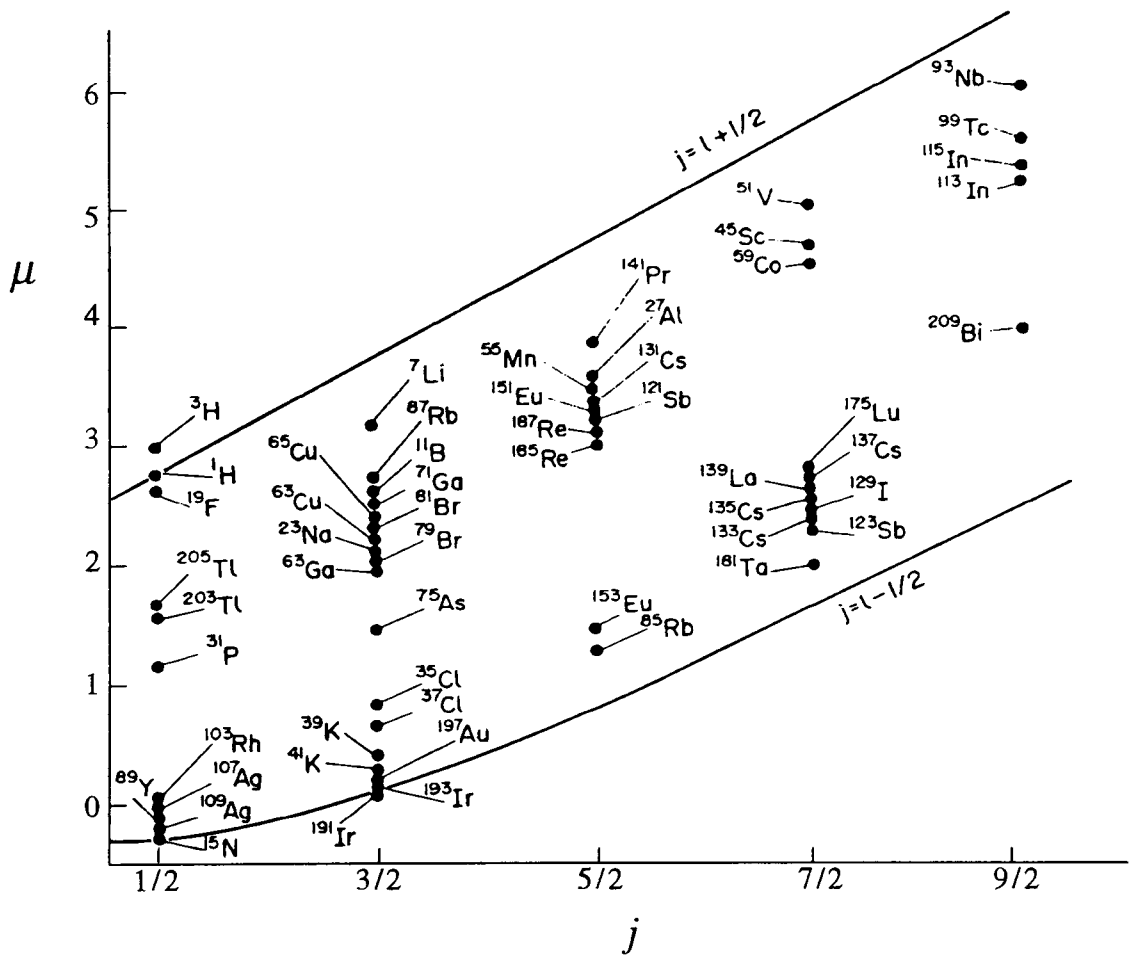


Fig 5.7 Schmidt curves and experimental values of the magnetic moments for nuclei (a) with an odd number of neutrons and (b) with an odd number of protons.
(j=l-1/2 ; Jacknife, j=l+1/2; Stretch)[23]

5.5 Deformed shell model

The assumption of approximately independent motion of nucleons in an average field is the basis of the shell model and of all microscopic theories of finite nuclei. This container potential is produced by the nucleons themselves and their mutual interaction. In a previous section the spherical potential is assumed for nuclei with closed or nearly closed shell and the spherical shell model is very successful for such nuclei. Though it works for nuclei which are far from closed shell with mass numbers $A \approx 25$, $150 < A < 190$ and $A > 220$, a deformed single particle potential must be assumed to explain many experimental facts;

(i) the existence of rotational bands
(ii) very large quadrupole moments
(iii) strongly enhanced quadrupole transition probabilities
(iv) hexadecapole matrix elements
(v) single particle structure
(vi) fission isomers

Since the nuclear forces have a small range ($\sim 1 fm$) compared to the nuclear diameter, it is expected that the deformed potential will be similar to the shape of the nuclear density distribution. This average potential can be represented by the Woods-Saxon potential

$$V(r,\vartheta,\varphi) = -V_0\left[1+\exp\left(\frac{r-R(\vartheta,\varphi)}{a(\vartheta,\varphi)}\right)\right]^{-1} \tag{5.56}$$

where the parameter a describes the surface diffuseness and is approximately constant over all spherical nuclei and does not depend on the curvature of the surface but has small dependence on the angle (ϑ,φ) to get a constant surface diffuseness.

5.5.1. The Anisotropic harmonic oscillator

Suppose the density of a deformed nucleus is an ellipsoidal distribution, then the anisotropic harmonic oscillator as an average field, which is equivalent to the potential (5.56), is

$$h_0 = -\frac{\hbar^2}{2m}\Delta + \frac{m}{2}\left(\omega_x^2 x^2 + \omega_y^2 y^2 + \omega_z^2 z^2\right) \tag{5.57}$$

where ω_x, ω_y and ω_z are frequencies and should be chosen propotional to the inverse of the half axes a_x, a_y and a_z of the ellipsoid.

$$\omega_\nu = \dot{\omega}_0 \frac{R_0}{a_\nu} \qquad (\nu = x, y, z) \tag{5.58}$$

The condition for volume conservation is

$$\dot{\omega}^2 = \omega_x \omega_y \omega_z = \text{const.} \tag{5.59}$$

The eigenstates are characterized by the quantum numbers n_x, n_y and n_z, and eigenvalues are

$$\varepsilon_0\left(n_x, n_y, n_z\right) = \hbar\omega_x\left(n_x + \frac{1}{2}\right) + \hbar\omega_y\left(n_y + \frac{1}{2}\right) + \hbar\omega_z\left(n_z + \frac{1}{2}\right) \tag{5.60}$$

In the case of axially symmetric shapes, the z-axis can be chosen as the symmetric axis and a deformation parameter δ can be introduced in the following definition

$$\begin{aligned} \omega_\perp^2 = \omega_x^2 = \omega_y^2 &= \omega_0^2(\delta)\left(1 + \frac{2}{3}\delta\right) \\ \omega_z^2 &= \omega_0^2(\delta)\left(1 - \frac{4}{3}\delta\right) \end{aligned} \tag{5.61}$$

where $\omega_0(\delta)$ is chosen to conserve volume. Taking terms up to quadratic in (5.59)

$$\omega_0(\delta) = \dot{\omega}_0\left(1 + \frac{2}{3}\delta^2\right) \tag{5.62}$$

Introducing a deformation dependent oscillator length $b(\delta) = \left(\hbar/m\,\omega_0(\delta)\right)^{1/2}$ that was introduced by Nilsson and dimensionless coordinates

$$h_0(\delta) = \hbar\omega_0(\delta)\left(-\frac{1}{2}\Delta' + \frac{1}{2}r'^2 - \frac{1}{3}\sqrt{\frac{16\pi}{5}}\delta r'^2 Y_{20}(\vartheta', \varphi')\right) \tag{5.63}$$

The equipotential surfaces are ellipsoids and can be represented by (5.7)

$$r' \sim \left(1+\beta Y_{20}(\vartheta',\varphi')\right) \tag{5.64}$$

with $\beta = \frac{1}{3}\sqrt{\frac{16\pi}{5}}\delta + \cdots = 1.057\delta + \cdots$. The deformation parameter δ of equation (5.61) is therefore roughly equal to β in equation (5.7).

In the case of axial symmetry cylindrical coordinate can be used. The eigenstates are characterized by quantum numbers n_x, n_y and n_z, and m_l is the projection of the orbital angular momentum onto the symmetry axis. Let

$$N = n_z + 2n_\rho + m_l = n_x + n_y + n_z \tag{5.65}$$

then from equation (5.60)

$$\begin{aligned} \varepsilon_0(n_x,n_y,n_z) &= \hbar\omega_z\left(n_z+\frac{1}{2}\right)+\hbar\omega_\perp\left(n_\rho+m_l+1\right) \\ &= \hbar\dot{\omega}_0\left\{\left(N+\frac{3}{2}\right)+\delta\left(\frac{N}{3}-n_z\right)\right\} \end{aligned} \tag{5.66}$$

where m_l is a good quantum number due to the axial symmetry.

The eigenstates of h_0 in the cylindrical basis can be characterized by the set of Nilsson quantum numbers $\Omega\pi[Nn_z m_l]$ where $\Omega = m_l + m_s = m_l \pm 1/2$ and π is the parity of the states.

5.5.2. Nilsson Hamiltonian

As discussed in section (5.2.1), the harmonic oscillator has two fundamental drawbacks concerning the agreement with experimental single-particle spectra. Therefore Nilsson added two terms to the deformed harmonic oscillator (5.57) and (5.63), and then used the Hamiltonian

$$\begin{aligned} h &= -\frac{\hbar^2}{2m}\Delta+\frac{m}{2}\omega_\perp^2(x^2+y^2)+\frac{m}{2}\omega_z^2 z^2 + Cl\cdot s + Dl^2 \\ &= \hbar\omega_0(\delta)\left(-\frac{1}{2}\Delta'+\frac{1}{2}r'^2-\beta r'^2 Y_{20}\right)-\kappa\hbar\omega_0^2\left(2l\cdot s+\mu l^2\right) \end{aligned} \tag{5.67}$$

where C gives the strength of the spin-orbit interaction with $C = -2\hbar\dot{\omega}_0\kappa$ and Dl^2 shifts the levels with higher l-values downward with $D = -\hbar\dot{\omega}_0\kappa\mu$. Equation

(5.67) can be rewritten as states with large N quantum numbers were observed,

$$h = -\frac{\hbar^2}{2m}\Delta + \frac{m}{2}\omega_\perp^2(x^2+y^2) + \frac{m}{2}\omega_z^2 z^2 + Cl\cdot s + D\left(l^2 - \langle l^2\rangle_N\right) \qquad (5.68)$$

where $\langle l^2\rangle_N = \frac{1}{2}N(N+3)$ is the expectation value of l^2 averaged over one major shell with quantum number N. In this case, only the states within the shells are shifted and the centre of gravity between different major shells remains unaffected.

The Nilsson Hamiltonian (5.68) contains no Coulomb term which is incorporated into an appropriate choice of the constants κ and μ. They are actually fitted such that the observed levels in deformed nuclei can be reproduced. The spherical single-particle energies that are obtained with these parameters agree qualitatively with the single-particle or single-hole spectra of near magic nuclei. However sometimes there are quantitative discrepancies.

5.6 The particle-plus-rotor model

5.6.1 Introduction

The particle-plus-rotor model has been applied with great success to nuclei in the region of small deformations and to transitional nuclei. To describe the interplay bewteen the motion of particles and the collective rotation, a few valence particles are needed to couple them to a collective rotor which stands for the rest of the particles. The unpaired nucleon in an odd-mass nucleus can be treated as a valence nucleon on an even-even core. In general, the Hamiltonian is divided into two parts, a phenomenological part H_{coll} and a intrinsic part H_{intr}. The former describes the rotation of the inert core and the latter describes microscopically a valence particle near the Fermi level. Therefore, the Hamiltonian can be written as

$$H = H_{intr} + H_{coll} \qquad (5.69)$$

The intrinsic part has the form

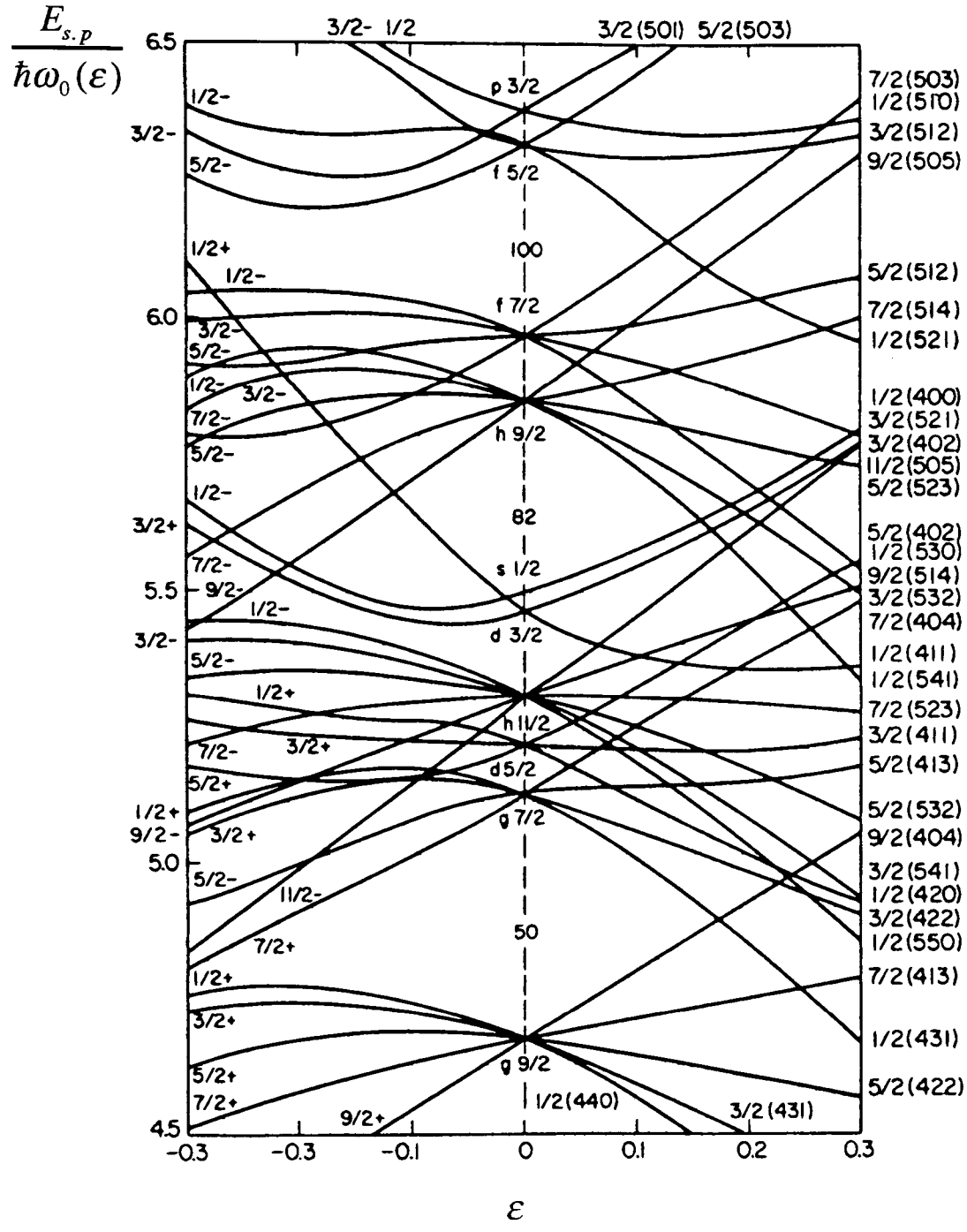


Fig 5.9. Level scheme of the Nilsson Model for heavy nuclei. The numbers on the lines correspond to the quantum number Ω, N, n_z, m_l. The single particle energy $E_{s.p}$ is in units of the oscillator energy the corresponding deformations $\varepsilon = \varepsilon_2$ for the Nilsson model in the oscillator shells N= 4 and 5. These energy levels are to be associated with odd-A nuclei in the range $50 < N$ or $Z < 82$ [2].

$$H_{intr} = \sum_k \varepsilon_k a_k^+ a_k + \frac{1}{4}\sum_{klmn} \overline{v}_{klmn} a_k^+ a_l^+ a_n a_m \tag{5.70}$$

where ε_k are single-particle energies in the deformed potential and $\overline{v}$ is the interaction between the valence particles which can be neglected. The collective part has the form

$$H_{coll} = \sum_{i=1}^{3} \frac{R_i^2}{2\zeta_i} \tag{5.71}$$

where the R_i are the body-fixed components of the collective angular momentum of the core.

The total angular momentum $\boldsymbol{I}$ is then

$$\boldsymbol{I} = \boldsymbol{R} + \boldsymbol{j} \tag{5.72}$$

where $\boldsymbol{j}$ is the angular momentum of the valence particle. H_{coll} can be decomposed into three parts

$$H_{coll} = H_{rot} + H_{rec} + H_{cor} \tag{5.73}$$

H_{rot} is the pure rotational operation of the rotor (see 5.28), which acts only on the degrees of the freedom of the rotor, and is given by

$$H_{rot} = \sum_{i=1}^{3} \frac{I_i^2}{2\zeta_i} \tag{5.74}$$

where

$$\begin{aligned} I_1 &= \frac{1}{i}\left(-\frac{\cos\gamma}{\sin\beta}\frac{\partial}{\partial\alpha} + \sin\gamma\frac{\partial}{\partial\beta} + \cos\gamma\tan^{-1}\beta\frac{\partial}{\partial\gamma}\right) \\ I_2 &= \frac{1}{i}\left(-\frac{\sin\gamma}{\sin\beta}\frac{\partial}{\partial\alpha} - \cos\gamma\frac{\partial}{\partial\beta} + \sin\gamma\tan^{-1}\beta\frac{\partial}{\partial\gamma}\right) \\ I_3 &= \frac{1}{i}\left(-\frac{\partial}{\partial\gamma}\right) \end{aligned} \tag{5.75}$$

The term H_{rec} represents a recoil energy of the rotor and is given by

$$H_{rec} = \sum_{i=1}^{3} \frac{j_i^2}{2\zeta_i} \tag{5.78}$$

The term H_{cor} is the Coriolis interaction which couples the degrees of freedom of the valence particle to the degrees of freedom of the rotor and is given by

$$H_{cor} = -\sum_{i=1}^{3} \frac{I_i j_i}{2\zeta_i} \tag{5.79}$$

The wavefunction of the system can be writen as

$$\left|\Psi_M^I\right\rangle = \sum_k \Phi_k |IMK\rangle \tag{5.80}$$

where Φ_k depends on the coordinates of the valence particle and the $|IMK\rangle$ depend on the Euler angles. The normalised wavefunctions $|IMK\rangle$ are defined as

$$|IMK\rangle = \sqrt{\frac{2I+1}{8\pi^2}} D_{MK}^{I*}(\Omega) \tag{5.81}$$

where $D_{MK}^{I*}(\Omega)$ are the Wigner functions under rotations around axis in the laboratory and in the body-fixed frame, and behave like spherical tensors of rank I with magnetic quantum number M under rotation of the laboratory frame. In this section the unit h=1 will be used.

5.6.2 The axially symmetric case

Assuming $\zeta_1 = \zeta_2 = \zeta$, there can then be no collective rotation around this axis and the 3-component of $\boldsymbol{R}$ has to vanish (see section 5.1.4). From (5.72), it follows that K, the 3-component of the total angular momentum $\boldsymbol{I}$, has to be equal to Ω, the 3-component of $\boldsymbol{j}$.

$$K = \Omega \tag{5.82}$$

From (5.69) and (5.73), it follows that

$$H_{rot} = \frac{\boldsymbol{I}^2 - I_3^2}{2\zeta} \tag{5.83}$$

$$H_{rec} = \frac{j_1^2 + j_2^2}{2\zeta} \tag{5.84}$$

$$H_{cor} = -\frac{I_1 j_1 + I_2 j_2}{2\zeta} = -\frac{I_+ j_- + I_- j_+}{2\zeta} \tag{5.85}$$

$$H_{intr} = \sum_{i,\Omega} \varepsilon_\Omega^i a_{i\Omega}^+ a_{i\Omega} \tag{5.86}$$

where the residual interaction has been neglected in (5.86). The single-particle levels in the axially symmetric well are labeled by $K = (i, \Omega)$ and the corresponding eigenfunctions will be denoted by Φ_Ω^i.

The strong coupling limit is realised when the Coriolis interaction martix elements are small compared with the level splitting of the single-particle energies in the deformed shell model for different values of Ω. In this case, K is a good quantum number and, therfore, it is called the strong coupling or deformation aligned limit. The angular momentum j of the valence particle is strongly coupled to the motion of the core (see fig 5.10a). In this limit, the Coriolis interaction can be neglected and the total energy spectrum for $K = 1/2$ can then be written as

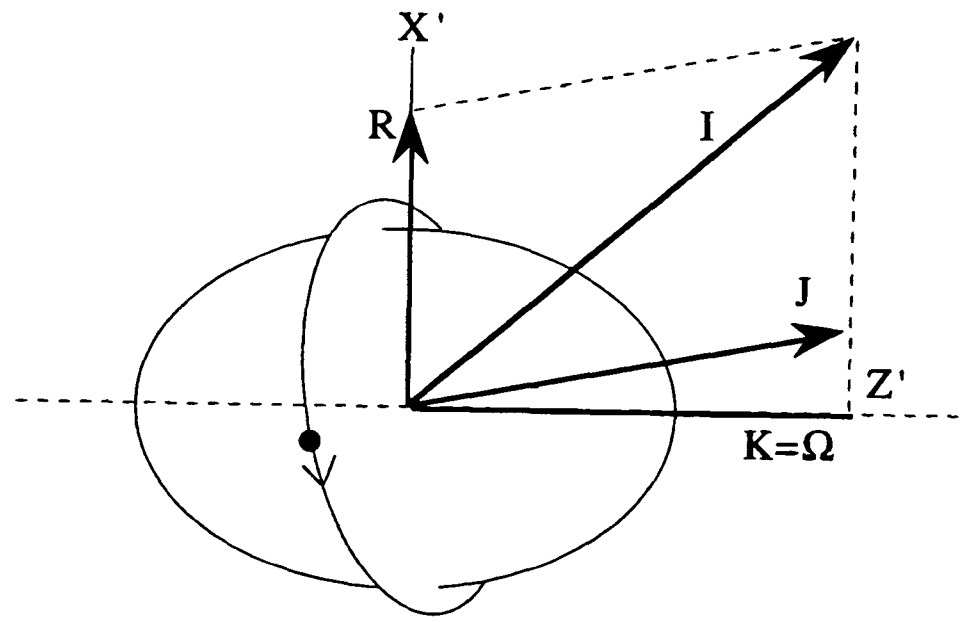
$$E_{K=1/2}^i = \varepsilon_{K=1/2}^i + \frac{1}{2\zeta}\left\{ I(I+1) - \frac{1}{4} + a^i (-1)^{I+\frac{1}{2}} \left(I + \frac{1}{2} \right) \right\} \tag{5.87}$$

where a^i is the decoupling factor and is given by

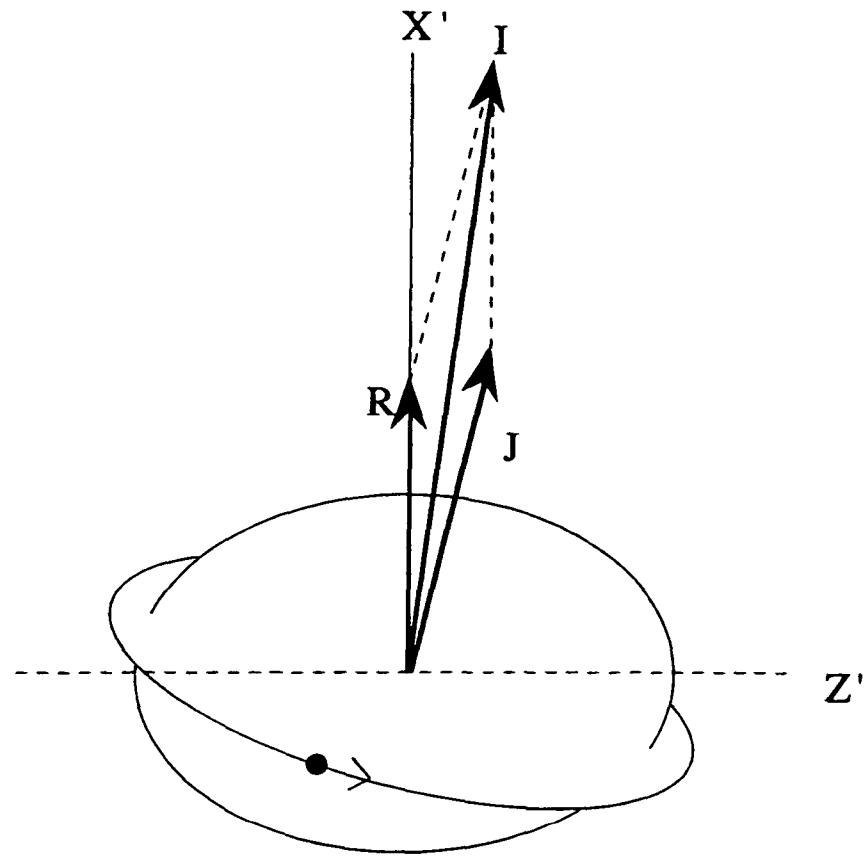
$$a^i = i \left\langle \Phi_{\frac{1}{2}}^i \middle| j_+ e^{-i\pi j_1} \middle| \Phi_{\frac{1}{2}}^i \right\rangle \tag{5.88}$$

(5.87) implies that for a positive decoupling factor (major component with $j + \frac{1}{2}$ odd) the levels with odd values of $I + \frac{1}{2}$ are shifted downwards.

In the weak coupling limit, the the Coriolis interaction martix elements are no longer negligible compared to the energy splitting of the single-particle levels belonging to different K values. For very small deformation, if the K-splitting of H_{intr} is totally neglected, the corresponding energy spectrum is



(a)



(b)

Fig 5.10 Vector Coupling Scheme in the case of (a) the strong-coupling (deformation aligned) (b) the weak-coupling (rotation aligned).

$$E(I) = E_{intr} + \frac{R(R+1)}{2\zeta} \tag{5.89}$$

with $|j - R| \le I \le j + R, \qquad R = 0, 2, 4$. This means that for each rotational quantum number R, j can have $2j+1$ orientations without changing the energy of the system (zero coupling).

In the case of the Decoupling limit (or Rotational alignment), the energy splitting in the intrinsic part of the Hamiltonian must be taken into account. In this case, the energy spectrum of the Hamiltonian is given by

$$\begin{aligned} E(I,\alpha) &= \frac{1}{2\zeta}\{I(I+1) + j(j+1) - 2I\alpha\} + const. \\ &= \frac{1}{2\zeta}(I-\alpha)(I-\alpha+1) + const. \\ &= \frac{1}{2\zeta}R(R+1) + const. \end{aligned} \tag{5.90}$$

where $R = I - \alpha = 0, 2, 4, \cdots$ must be even because of the symmetry condition.

5.6.3 The triaxial-rotor-plus-particle model

In this model, discussion will be restricted to one external particle in a high j-shell (e.g., $h_{11/2}$) and couple it to a triaxial rotor. The moment of inertia ζ_i depends on β and γ, and is given by (5.20). In this case, the Hamiltonian is

$$H_{rot} = \sum_{i=1}^{3} \frac{R_i^2}{2\zeta_i}(\boldsymbol{I}_i - \boldsymbol{j}_i)^2 \qquad (i = 1, 2, 3) \tag{5.91}$$

The dynamical behaviour of a system of an odd high-j particle coupled to a rotating triaxial core is determined by three physical effects.

(i) The core prefers to rotate around the axis with the maximal moment of inertia in order to minimize the rotating energy.

(ii) The particle moving in the deformed well prefers maximal mass overlap with the core because in this case its potential energy is minimal.

(iii) The Coriolis interaction tries to align the angular momenta of the particle $\boldsymbol{j}$ and the core $\boldsymbol{R}$.

5.6.4 Electromagnectic Properties

For particle states, the reduced matrix elements of $Q^{(c)}_{\lambda\mu}$, $Q^{(p)}_{\lambda\mu}$, and M are obtained in the form

$$\left\langle I'\alpha' \middle\| Q^{(c)} \middle\| I\alpha \right\rangle = F^{(c)}_{I'\alpha',I\alpha} Q_0 \tag{5.92}$$

$$\left\langle I'\alpha' \middle\| Q^{(p)} \middle\| I\alpha \right\rangle = F^{(2)}_{I'\alpha',I\alpha} q_{s.p} \tag{5.93}$$

and, for $(I'\alpha') \neq (I\alpha)$,

$$\left\langle I'\alpha' \middle\| M \middle\| I\alpha \right\rangle = F^{(1)}_{I'\alpha',I\alpha} \left(\mu_{s.p} - g_R j\right) \tag{5.94}$$

where $q_{s.p}$ and $\mu_{s.p}$ are the single-particle values for the quadrupole moment and the magnetic moment, and Q_0 is the intrinsic charge quadrupole moment,

$$q_{s.p} = -\frac{2j-1}{2j+2}\left\langle r^2 \right\rangle \tag{5.95}$$

$$\mu_{s.p} = \left(g_l + \frac{g_s - g_l}{2l+1}\right) j \tag{5.96}$$

$$Q_0 = \frac{3}{\sqrt{5\pi}} R_0^2 Z\beta \tag{5.97}$$

and $\left\langle r^2 \right\rangle \approx (n+3/2)A^{2/3}\left(fm^2\right)$ for the (n,j,l) shell. The F-factors contain the effect of the rotating core on the matrix elements and are given by

$$F^{(c)} = \sqrt{(2I'+1)(2I+1)} \sum_{KK'\Omega\nu}{}' w^{(I'\alpha',I\alpha,2)}_{K'\Omega,K\Omega} (-)^{I'-K'} \begin{pmatrix} I' & 2 & I \\ -K' & \nu & K \end{pmatrix} \frac{q_{2\nu}}{Q_0} \tag{5.98}$$

$$F^{(c)} = \sqrt{(2I'+1)(2I+1)} \sum_{KK'\Omega\nu}' w^{(I'\alpha',I\alpha,\lambda)}_{K'\Omega,K\Omega} (-)^{I'+j-K'-\Omega'}$$
$$\times \frac{\left\{ \begin{pmatrix} I' & \lambda & I \\ -K' & \nu & K \end{pmatrix} \begin{pmatrix} j & \lambda & j \\ -\Omega' & \nu & \Omega \end{pmatrix} + (-)^{I-j} \begin{pmatrix} I' & \lambda & I \\ -K' & \nu & K \end{pmatrix} \begin{pmatrix} j & \lambda & j \\ -\Omega' & \nu & -\Omega \end{pmatrix} \right\}}{\begin{pmatrix} j & \lambda & j \\ -j & 0 & j \end{pmatrix}} \quad (5.99)$$

for $\lambda = 1,2$. The amplitude $w^{(I'\alpha',I\alpha,\lambda)}_{K'\Omega,K\Omega}$ includes all the information about the wavefunction and is given by

$$w^{(I'\alpha',I\alpha,\lambda)}_{K'\Omega,K\Omega} = \sum_{\kappa,\kappa'=1}^{\left(j+\frac{1}{2}\right)} s^{j}_{\Omega'\kappa'}, t^{(I',j)}_{K'\kappa',\alpha'} \left(\mu_{\kappa'}\mu_{\kappa} - (-)^{\lambda} \upsilon_{\kappa'}\upsilon_{\kappa} \right) s^{j}_{\Omega\kappa} t^{(I,j)}_{K\kappa,\alpha} \quad (5.100)$$

From the reduced matrix elements (5.92), (5.93) and (5.94), the spectroscopic quadrupole moments and the magnetic moments can be obtained as

$$Q^{(sp)}_{I\alpha} = \begin{pmatrix} I & 2 & I \\ -I & 0 & I \end{pmatrix} \langle I\alpha \| Q \| I\alpha \rangle \quad (5.101)$$

$$\mu_{I\alpha} = g_R I + \begin{pmatrix} I & 2 & I \\ -I & 0 & I \end{pmatrix} \langle I\alpha \| M \| I\alpha \rangle \quad (5.102)$$

and for the reduced *E2* and *M1* transition probabilities

$$M(M1; I\alpha \to I\alpha') = \frac{\left| \langle I'\alpha' \| M \| I\alpha \rangle \right|^2}{(2I+1)} \quad (5.103)$$

$$B(E2; I\alpha \to I\alpha') = \frac{5}{16\pi} \frac{\left| \langle I'\alpha' \| Q \| I\alpha \rangle \right|^2}{(2I+1)} \quad (5.104)$$

Mixing ratios are defined as

$$\delta(I\alpha \to I\alpha') = \sqrt{0.7} E_\gamma \sqrt{\frac{5}{16\pi}} \frac{\left| \langle I'\alpha' \| Q \| I\alpha \rangle \right|}{\left| \langle I'\alpha' \| M \| I\alpha \rangle \right|} \quad (5.105)$$

where $E_\gamma = \left(E_I - E_{I'} \right)$ is the transition energy.

References

[1] J.M.Eisenberg and W.Greiner, in Nuclear models (North-Holland, 1987)

[2] A.deShalit and H.Feshbach, in Theoretical Nuclear Physics vol. 1 (Wiley, 1974)

[3] K.Kumar, in Nuclear models and the search for unity in nuclear physics (Universitetsforlaget, 1984)

[4] J.P.Davidson, in Collective models of the nucleus, (Academic press, 1968)

[5] L.Grodzins, Phys. Lett. **2**(1962)88

[6] J.Meyer-Ter-Vehn, Nucl. Phys. **A249**(1975)111

[7] E.Osnes et al., Nucl. Phys. **A253**(1975)45

[8] B.Harmatz and T.H.Handley, Phys. Rev. **128**(1962)1186

[9] J.P.Davidson, Rev.Mod. Phys. **37**(1965)105

[10] I.M.Irvine, in Nuclear Structure Theory (Pergaman Press, 1971)

[11] K.Heyde, Hyp. Int **75**(1992)69

[12] J.Dudek et al., J. Phys **G5**(1979)1359

[13] R.Wadsworth et al., J. Phys **G13**(1987)205

[14] A.S.Davydov and G.F.Filippov, Nucl. Phys **8**(1958)237

[15] V.M.Strutinsky, Nucl. Phys **A95**(1967)420

[16] S.G.Nilsson et al., Nucl. Phys **A131**(1969)1

[17] J.Meyer-Ter-Vehn., Nucl. Phys **A249**(1969)111

[18] J.Meyer-Ter-Vehn., Nucl. Phys **A249**(1969)141

[19] F.S.Stephens et al, Phys.Rev.Lett. **29**(1972)438

[20] S.E.Larsson et al., Nucl. Phys **A307**(1978)189

[21] L.Bennour et al., Nucl. Phys **A465**(1987)35

[22] A.Bohr and B.Mottleson, in Nuclear Sturcture vol. 1, 2 (Benjamin, 1975)

[23] M.G.Mayer and J.H.D.Jensen, in Elementary Theory of Nuclear Shell Structure (Wiley, 1955)

[24] W.Elsasser, J. Phys. Rad **5**(1934)625

[25] M.G.Mayer, Phys. Rev **75**(1949)1969

[26] M.G.Mayer, Phys. Rev **78**(1950)16

[27] O.Haxel et al., Phys. Rev **75**(1949)1766

[28] O.Haxel et al., Z. Phys **128**(1950)295

Chapter Six

Particle-triaxial-rotor calculation of light odd-A and odd-odd Eu and Sm nuclei ($137 \leq A \leq 143$)

6.1 Introduction

Light Eu and Sm nuclei have attracted attention as systems with a number of protons right below the Z=64 subshell gap and a number of neutrons approaching the N=82 major shell closure. Both proton and neutron states belong to the same major oscillator shell. Independent study of odd-proton Eu and odd-neutron Sm isotopes using the same even-even Sm core provides a suitable basis for calculation of odd-odd Eu nuclei. There are two interesting aspects of this investigation:

Firstly, Leander and Moller[1] predicted an onset of well developed deformation at N=73 in Pm(Z=61) and Sm(Z=62) nuclei. Indeed, $\beta_2=0.24\pm0.02$ has been extracted from the life-time measurement of the first 2^+ state in ^{138}Sm (N=76) and $\gamma\sim25^o$ has been calculated from the energy of the second excited 2^+ state. With these deformation parameters a decoupled band built on the $h_{11/2}$ ground state of the isotonic ^{139}Eu could be well described[2]. Similarly, the first 2^+ state in ^{136}Sm yields deformation $\beta_2=0.23\pm0.01$ and in ^{134}Sm $\beta_2=0.30(2)$[3].

Secondly, the effect of the Z=64 subshell gap below and above the N=82 magic number seems to be rather different. Large deformations, observed for neutron-hole states below N=82, do not appear for particle states above the shell. There, the Z=64 gap appears to be more relevant, resulting in a smaller deformation of N=88 ^{150}Sm (6 particles) nucleus ($\beta_2=0.165(2)$) than that of N=76 ^{138}Sm (6 holes)[15]. Similarly, $\beta_2=0.252(2)$ and 0.279(2) for ^{152}Sm and ^{154}Sm, respectively [data taken from current Nuclear data Sheets].

Our interest in this region has been prompted by nuclear orientation measurement by Singleton et al[4,5] of magnetic dipole moments of ^{138,139}Eu and ^{139m}Sm. Together with other known magnetic dipole and electric quadrupole

Nucleus	I^{π}	μ [n.m]	Q [eb]
^{139}Sm	$1/2^{+}$	-0.534(18)	
^{139m}Sm	$11/2^{-}$	1.1(2)	
^{141}Sm	$1/2^{+}$	-0.738(24)	
^{141m}Sm	$11/2^{-}$	-0.836(20)	+1.64(34)
^{143}Sm	$3/2^{+}$	+1.009(19)	+0.41(21)
^{138}Eu	7^{+}	5.3(7)	
^{139}Eu	$11/2^{-}$	6.1(8)	
^{141}Eu	$5/2^{+}$	+3.365(13)	+0.31(4)
^{142}Eu	1^{+}	+1.536(19)	+0.12(5)
^{142m}Eu	8^{-}	+2.978(11)	+1.41(6)
^{143}Eu	$5/2^{+}$	+3.673(8)	+0.51(3)

Table 6.1. Experimental data on magnetic dipole and electric quadrupole moments in neutron deficient Sm and Eu isotopes with N<82. Data were taken from Raghavan[6], Letokhov et al. [7] and Singleton et al.[4,5]

moments and nuclear spectroscopy data in the region, these results provide important additional information for nuclear model analysis. It is well known that to base a model calculation only on experimental energies of excited states (band members) is not good enough to find unambiguous information on the shape of a nuclear state. We summarize in Table 6.1 the up-to-date information on magnetic dipole and electric quadrupole moments in the Eu and Sm nuclei ($137 \leq A \leq 143$) and present model calculation of these values in the subsequent sections.

There have been several nuclear model calculations presented in the literature on Eu and Sm nuclei, including particle-triaxial rotor model with modified oscillator single particle potential ($^{133\text{-}143}$Sm[1], ^{138,139}Eu and ^{139m}Sm [4]), particle rotor model with Woods-Saxon single particle potential ($^{133\text{-}135}$Sm[24]) cranked shell model (^{137}Sm[9]), interacting boson-fermion approximation (^{143}Eu[10]), triaxial-weak-coupling model (^{143}Eu[10]), shell model (^{141}Sm[11]) and macroscopic-microscopic model of Moller and Nix[12]. We have attempted in this work to perform a systematic calculation using the Lund particle-triaxial rotor model of negative and positive parity states in odd-A Eu and Sm and use these results for a schematic calculation of odd-odd ^{138}Eu nucleus. In all cases the appropriate even-even Sm core was used.

The main aim of this Chapter is not only to obtain information about nuclear shapes, but also to examine in some detail to what extent this information is unambiguous. In particular, we investigate the role of nuclear moments in this analysis. Electromagnetic moments of nuclear ground and isomeric states are the

main results yielded in nuclear orientation experiments and to establish their significance in nuclear model investigations is one of our prime interests.

6.2 Calculation procedure and parameters of the model.

6.2.1.Odd-A nuclei

The Lund particle-triaxial rotor model has been described in detail in several papers [13-15]. The single-particle Hamiltonian used has the form[15]

$$H_{sp} = H_{ho}(\varepsilon_2, \gamma) - \kappa(N)\hbar\omega_0\left\{2\boldsymbol{l}\cdot\boldsymbol{s} + \mu(N)\left(\boldsymbol{l}^2 - \langle \boldsymbol{l}^2 \rangle N\right)\right\} \qquad (6.1)$$

where H_{ho} is the deformed harmonic-oscillator hamiltonian, and all the other symbols have their usual meaning. Diagonalization of the hamiltonian in the $|Nlj\Omega>$ basis and inclusion of pairing effects gives adiabatic quasi-particle energies and wave functions written as an expansion,

$$\chi_\nu = \sum_{Nlj\Omega} C^{(\nu)}_{Nlj\Omega}\phi_{Nlj\Omega} \qquad (6.2)$$

and their conjugate states

$$\bar{\chi}_\nu = \sum_{Nlj\Omega}(-1)^{(j-\Omega)} C^{(\nu)}_{Nlj\Omega}\phi_{Nlj-\Omega} \qquad (6.3)$$

where ν is the sequential number of a wave-function χ_ν. The even-even-core hamiltonian is defined as

$$H_{core} = \sum_{i=1}^{3}\left(\frac{\hbar^2}{2\zeta_i}\right)\left(\boldsymbol{I}_i - \boldsymbol{j}_i\right)^2, \; (i = 1,2,3 \text{ for } x,y,z) \qquad (6.4)$$

where **I** is the total nuclear angular momentum (spin) and **j** is the spin of the odd particle. ζ_i is the hydrodynamical moment of inertia, calculated as

$$\zeta_i(K) = 4B\varepsilon^2 \sin^2\left(\gamma + \frac{2K\pi}{3}\right) \qquad (6.5)$$

using Grodzin's empirical relation[25,27]

$$\frac{\hbar^2}{B} = \frac{1000}{A^{\frac{7}{3}}}(MeV) \tag{6.6}$$

where B is in units of moment of inertia.
H_{core} is exactly diagonalized in the strong-coupling basis

$$\Psi^{I(\nu)}_{MK} = \left[\frac{(2I+1)}{16\pi^2}\right]^{\frac{1}{2}} \sum_{Nlj\Omega} C^{(\nu)}_{Nlj\Omega}\left\{D^I_{MK}\phi_{Nlj\Omega} + (-1)^{(I-j)} D^I_{M-K}\phi_{Nlj-\Omega}\right\} \tag{6.7}$$

yielding energy levels and total wave-functions

$$\Phi^I_M = \sum_{K,\nu} a^{I(\nu)}_K \Psi^{I(\nu)}_{MK} \tag{6.8}$$

For odd A nuclei, five single-particle orbitals above and below the Fermi level were included in the diagonalization. The positive and negative parity systems were treated separately.

This choice of hamiltonian implies that the even-even core is approximated as a rigid body, in principle not including vibrations or effects like g-softness. Nevertheless, Larson et al[13] pointed out that there is some shape-vibration amplitude present in the model within the uncertainties of the core quadrupole components Q_{20} and Q_{22} which can contribute a sizeable fraction of the total deformation in transitional nuclei.

Standard BCS procedure was used for calculation of pairing parameters λ and Δ with G_{n0}=19.2 MeV and G_{n1}=7.4 MeV[16].

The only model parameters varied in our calculations were the deformations ε_2 and γ and the Coriolis attenuation factor ξ. All the other parameters were kept constant, including the strengths of the **l.s** and l^2 terms in the modified oscillator potential, κ and μ and the constant B in the expression (6.5) for the moment of inertia. The choice of κ and μ of Zhang et al[26] was adopted. The standard value of the constant B=1225, used for well deformed systems, gave less satisfactory agreement with experimental data. B=1000 was found to be more suitable in the region of A=140 transitional nuclei. For deformation parameters ε_2 and γ the following convention was used:

$\varepsilon_2 > 0$, $0^o \leq \gamma < 30^o$ prolate - "prolate-triaxial" shape

$\varepsilon_2 < 0$, $0^o \leq \gamma < 30^o$ oblate - "oblate-triaxial" shape

In variance with previous calculations, we did not use any of the other options of the model- namely variable moment of inertia or taking $E_{2+(1)}$ and

$E_{2+(2)}$ experimental energies of the core as input data for calculation of the moment of inertia. These options suppress any core-polarization effects by the odd-particle and are quite unsuitable in the region of light rare earths where the cores are extremely soft. Also, we treated the recoil term in the core hamiltonian as a one-body operator.

6.2.2. Odd-odd nuclei

A particle-triaxial rotor calculation for odd-odd nuclei has been performed using the code developed by Ragnarsson and Semmes[15]. The modified single particle potential was used for both the proton and neutron systems. In calculation of pairing parameters using standard BCS procedure, only the six orbitals closest to the Fermi level were used due to limitations in the present version of the program. The residual n-p interaction used in the model has been discussed in detail by Boisson et al[17]. In our calculation, only the central force contributions were included and a Gaussian shape of the radial dependence of the potential was taken. In the expression for V_{pn}

$$V_{pn} = exp\left(-\frac{r^2}{r_0}\right)\left(u_0 + u_1\sigma_p \cdot \sigma_n + u_2 P_M + u_3\sigma_p \cdot \sigma_n P_M\right) \qquad (6.8)$$

where P_M is the shape exchange operator and **s** is the Pauli spin matrix, values of u_0=-50.0 MeV, u_1=-9.22 MeV and u_3=-6.2 MeV, fitted by Boisson et al[17] were used. In this way, neither spin-orbit, nor tensor forces nor core polarization effects were taken into account. A full strength of residual interaction was applied.

In calculation of magnetic moments an effective g_S-attenuation factor of 0.7 was adopted.

The general strategy adopted throughout the calculation was to start from the simplest shape (i.e. assuming axial symmetry) and to keep as many additional parameters at their standard values as possible. We examined carefully the sensitivity of available experimental data to changes in the model parameters and aimed rather for determination of a region of possible shapes than one set of deformation parameters.

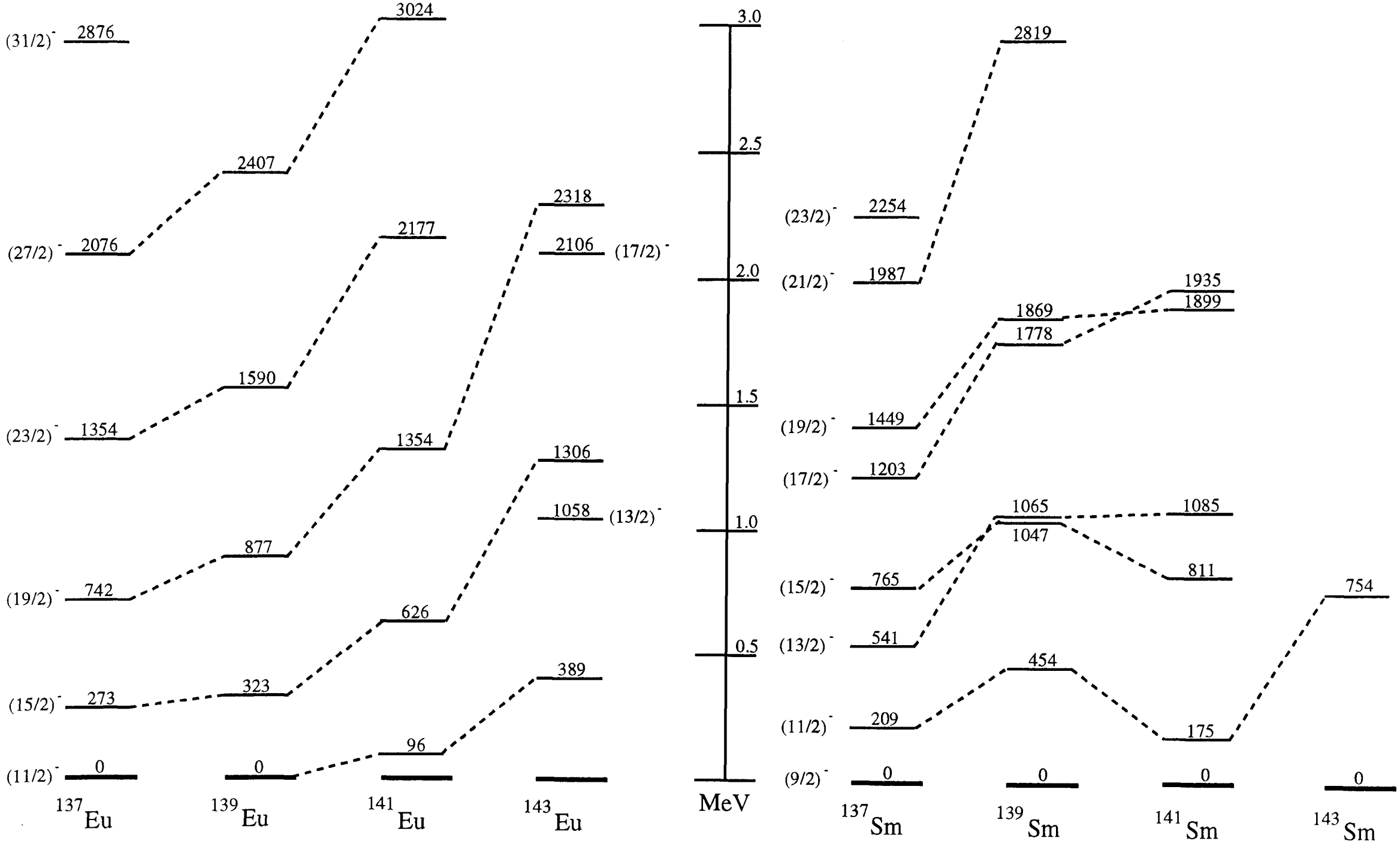


Fig 6.1 The systematics of negative parity yrast bands in $^{137\text{-}143}$Eu and $^{137\text{-}143}$Sm.
Data taken from current NDS and from Bazzacco [18]

6.3 Results

6.3.1 Negative parity states in $^{137-143}$Eu nuclei.

The systematics of negative parity states in odd-A light Eu and Sm nuclei are shown in Fig 6.1. A decoupled $\Delta I=2$ band built on a $h_{11/2}$ odd-proton state, which is believed to be the ground state, has been observed in $^{137-139}$Eu [2,19,20]. Calculation by Leander and Moller predicts a prolate shape and deformation $\varepsilon_2 \sim 0.27$[1] for ^{137}Eu. Results of our calculation are shown in Fig 6.2. Calculated energy levels for a prolate shape agree very well with this prediction, setting $\varepsilon_2 \sim$ 0.26-0.27. However, it can be seen that any deviation from an axially symmetrical shape, represented by a non-zero value of γ, would in combination with an appropriate value of ε_2, yield an equally reasonable agreement with experimental data. In other words, having at our disposal only data on energies of low-lying members of a $\Delta I=2$ band, no predictions can be made for values of g deformation and only an interval of possible ε_2 values can be obtained.

Experimental data for ^{139}Eu offer not only energy levels of the $\Delta I=2$ band built on the $11/2^-$ state but also absolute transition probabilities between the three lowest band members and the magnetic dipole moment of the $11/2^-$ band head. In our model calculation, we have examined apart from the three limiting shapes (prolate, triaxial and oblate) also the effect of the Coriolis attenuation factor used for the prolate shape. Examination of Fig 6.3 shows, as expected, that similarly to the case of ^{137}Eu, there is always an appropriate value of ε_2 which gives a very good agreement between experimental and calculated energies of the band members, i.e. the band energies themselves do not reveal unambiguous information about nuclear shape, giving a region of possible values of $0.24 \leq \varepsilon_2 \leq 0.28$. Results of our calculation of transition probabilities are summarized in Fig 6.4. Although the right order of magnitude of the probability of the $15/2^-$ - $11/2^-$ transition can be calculated for different shapes, the model predicts transition probability increasing with increasing spin of the initial state of a transition, contrary to experiment. Calculation with variable moment of inertia may be needed to improve on these results. Finally, the sensitivity of the magnetic dipole moment of the $11/2^-$ band-head to deformation is displayed in Fig 6.5. It is clear that the experimental error of the moment is prohibitively large and no distinction amongst possible shapes of the $11/2^-$ configuration can be made. Only a limit $\varepsilon_2 > 0.2$ can be extracted from the measured moment. Fig 6.5 also gives a measure of the precision of the magnetic moment needed in this case for meaningful comparison with model predictions. Clearly, a nuclear magnetic

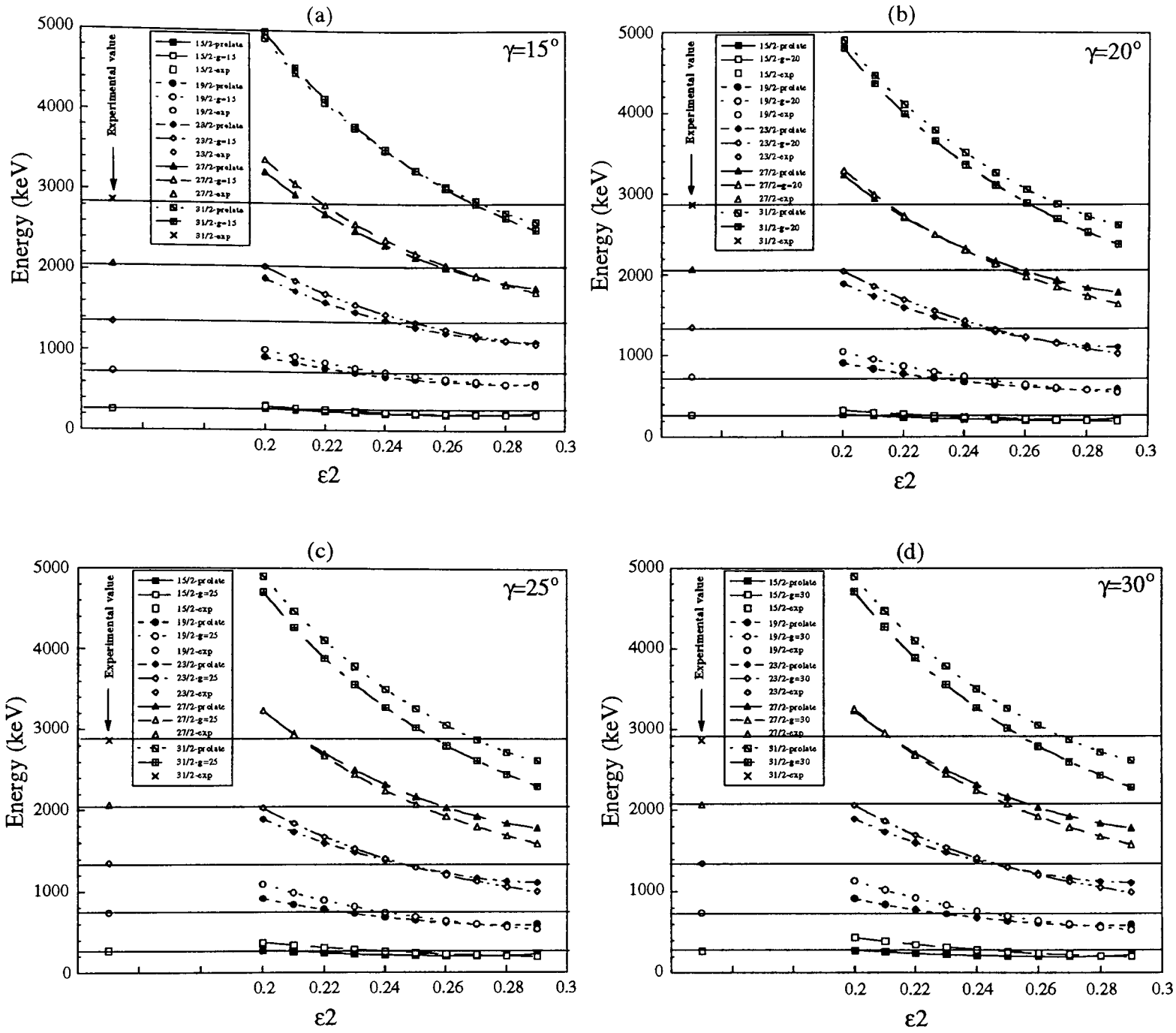


Fig 6.2 Calculated energies of negative parity states in ^{137}Eu as a function of γ-deformation with ξ=1. Experimental data are shown for comparison.

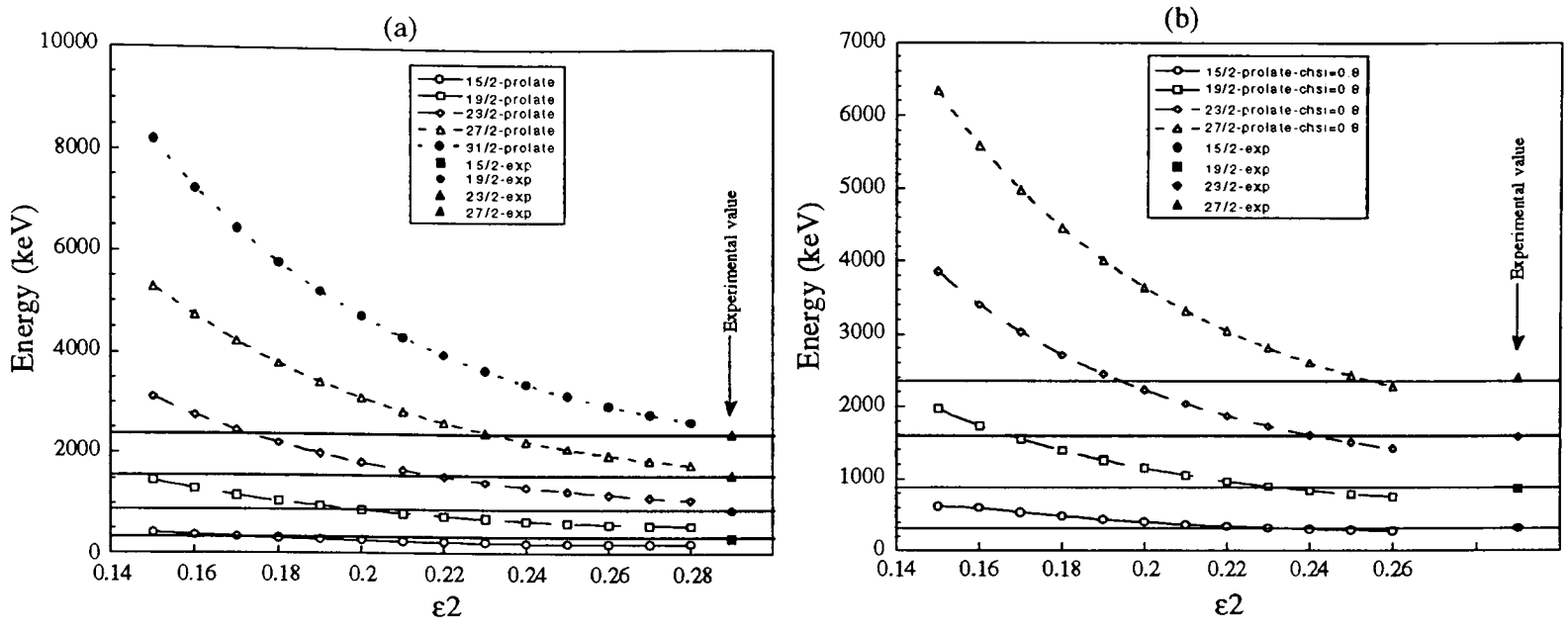


Fig 6.3 Experimental and calculated negative parity energy levels in ^{139}Eu for prolate (a), prolate with Coriolis attenuation factor ξ=0.8 (b), oblate (c), and triaxial (γ=30°) (d) shapes are shown. For oblate shape (c), only calculated bands are shown with the band-head forming the ground-state of ^{139}Eu.

resonance experiment would provide the accuracy needed.

The yrast negative parity ΔI=2 band was first observed by Lunardi et al [21]. Its $h_{11/2}$ proton particle band-head has been identified as an isomeric state 96 keV above the $I^{\pi}=5/2^{+}$ ground state. The band built on the $h_{11/2}$ proton state in ^{143}Eu is almost 400 keV above the $5/2^{+}$ ground state and in variance with the lighter odd-A Eu isotopes, members of both signatures were identified in an in-beam experiment by Aryaeinejad et al[22]. This helps enormously with shape identification of the band-head configuration in ^{143}Eu. We show in Fig 6.7 a fit to the energy levels up to spin $19/2^{-}$ for ε_2=-0.15 and $\gamma=25^{\circ}$. This result generally agrees with findings in ref.[10], where an oblate shape has been identified with β_2=0.154 and $\gamma=36.5^{o}$. This result also means that the shape of the Sm even-even cores in $^{137\text{-}143}$Eu, coupled to the $h_{11/2}$ proton, most probably develops from a prolate shape (only assumed, not identified in our calculation) for A=136 to close-to oblate in ^{142}Sm, possibly via a triaxial shape. We illustrate this notion using results of our calculation for ^{141}Eu (see Fig 6.6), where, similarly to ^{137}Sm and ^{139}Eu, the model does not distinguish between prolate, triaxial or oblate shape. Comparison with experiment indicates the optimal value of ε_2 is about -0.18 which is a reasonable value, in line with the expected decrease of deformation with increase of neutron number towards the N=82 shell.

6.3.2 Negative parity states in $^{137\text{-}143}$Sm nuclei.

It can be seen in Fig 6.1 that although the odd-neutron in $^{137\text{-}143}$Sm is in orbitals with the spherical $h_{11/2}$ origin, the yrast collective band, based on a coupled neutron orbital from the upper $h_{11/2}$ midshell, connects both signatures of a given configuration. This circumstance allows much more definite prediction of the intrinsic nuclear shape in the framework of the particle-triaxial rotor model. Magnetic dipole moments have been measured for the $11/2^{-}$ band-heads in ^{139m}Sm and ^{141m}Sm, accompanied by the quadrupole moment of the latter (see Table 6.1).

Results of our best results fit energy levels in $^{137\text{-}141}$Sm are summarized in Table 6.2. We have found out that for these nuclei the model was not only sensitive to changes in ε_2 and γ deformations, but also attenuation of the Coriolis coupling had to be employed. Our calculation indicates that all the Sm cores are triaxial, which is compatible with the general notion of large γ-softness of nuclei in this region.

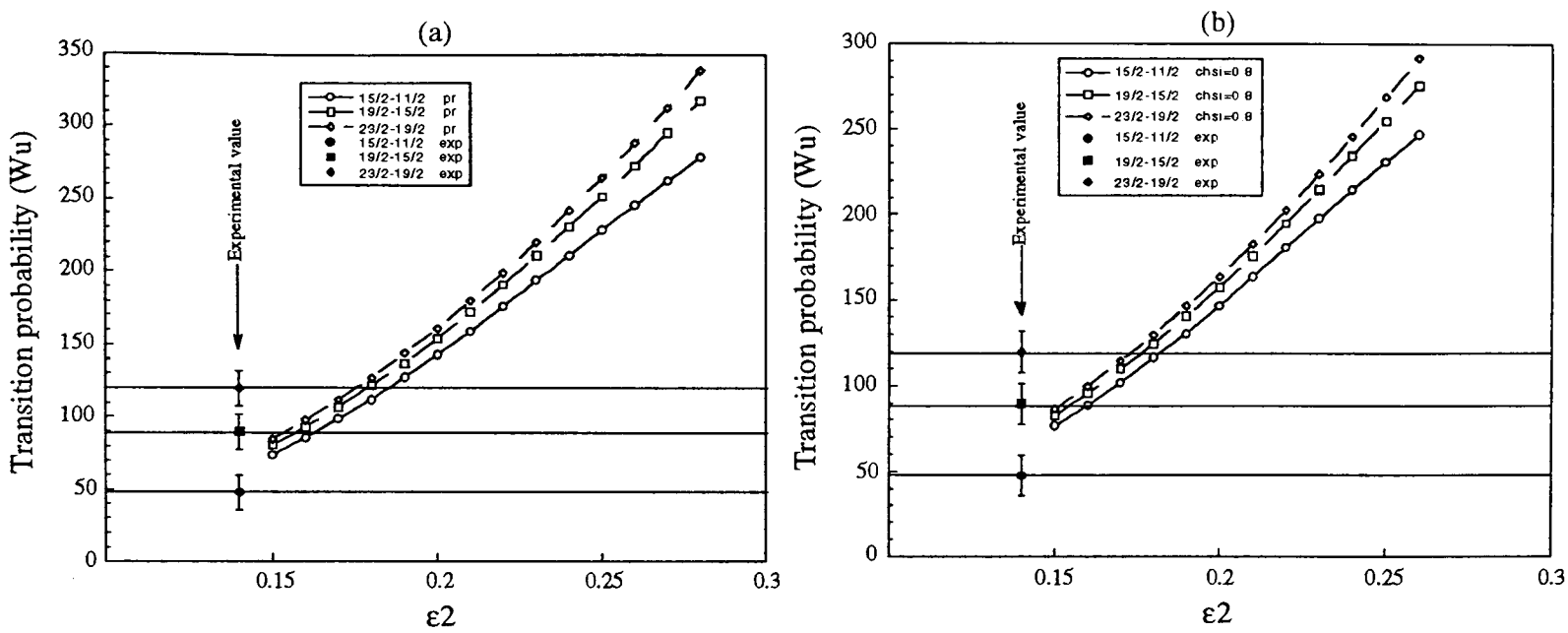


Fig 6.4 The same as fig 6.3 but for transition probabilities between low-lying band members.

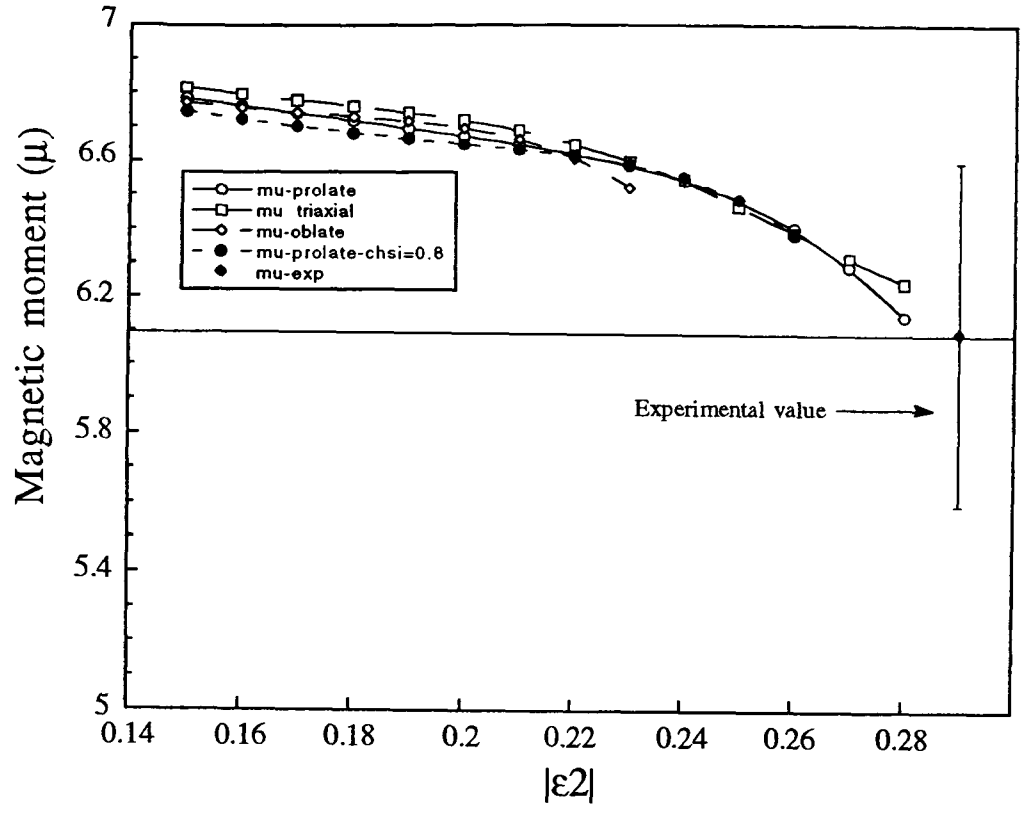


Fig 6.5 The same as fig 6.3 but for the magnetic dipole moment of the $(11/2)^-$ band-head. Experimental value is taken from Singleton[4].

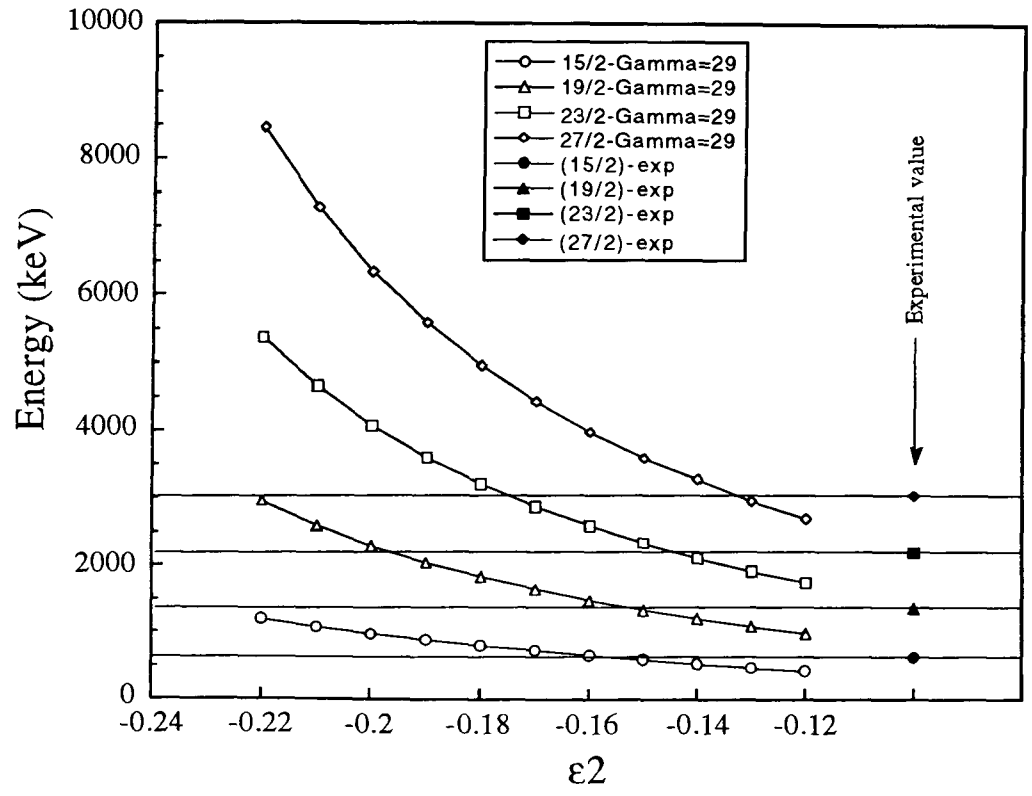


Fig 6.6 Calculated and experimental energy levels in ^{141}Eu for $\gamma=29^\circ$ as a function of ε2 (see text).

In Fig 6.8(a) we show the ε_2 dependence of the calculated magnetic dipole moment for the ^{139m}Sm $11/2^-$ band-head. It is obvious that with the current experimental precision this moment cannot be used for precise determination of the model parameters. However, it is compatible with ε_2, γ and ξ extracted from the fit to band member energies. Fig 6.8(b) illustrates the simultaneous compatibility of both magnetic dipole and electric quadrupole moments of the $11/2^-$ state in ^{141m}Sm with deformation parameters obtained from model analysis of energies of the band members. Although the error on the experimental magnetic moment is very small, uncertainty in the quadrupole moment still makes it difficult to use values of both moments for shape determination, but it demonstrates the potential of such a process. We show in Fig. 6.8(b) variation of the calculated moments with ε_2, keeping γ and ξ fixed just for illustration. More precise comparison of experimental values with model calculation with all three parameters variable would not bring a more meaningful outcome because of the large error on the quadrupole moment.

6.3.3 Positive parity states in $^{141\text{-}143}$Eu

The systematics of positive parity states in light Eu and Sm nuclei are shown in Fig 6.9. Positive parity single neutron and proton states in very neutron deficient Eu and Sm nuclei should have $g_{7/2}$, $d_{5/2}$, $d_{3/2}$ and $s_{1/2}$ spherical origin.

Because of the known softness of the even-even Sm core it is likely that different single-particle configurations and collective structures built on them would correspond to different intrinsic nuclear shapes. This makes comparison of excited state energies to calculations using a particle-rotor model difficult. The model assumes that all excited states correspond to the same core deformation. In its present version it cannot handle different core shapes and their interactions in one nucleus. For this reason we will concentrate in this paragraph on analysis of known ground state electromagnetic moments and take excited energy levels more as an illustration. There are precise experimental values of magnetic dipole and electric quadrupole moments of the $5/2^+$ ground state in $^{141\text{-}143}$Eu available in the literature (see Table 6.1). We have examined the first two lowest lying $5/2^+$ states in these nuclei and show their dependence on ε_2 (an axially symmetrical shape has been assumed for simplicity) in Fig 6.10. For a prolate core the model predicts two single-proton states 5/2[413] ($g_{7/2}$) and 5/2[402] ($d_{5/2}$) in the vicinity of the ground state. For $0.12 \leq \varepsilon_2 \leq 0.19$ the main component of the ground state wave functions is 5/2[413]. At $\varepsilon_2 \sim 0.20$ a dramatic change occurs

J^{π}	^{137}Sm ε_2 =0.24, γ =22° ξ =0.75		^{139}Sm ε_2 =-0.20, γ =28° ξ =0.80		^{141}Sm ε_2 =-0.17, γ =26.5° ξ =0.90	
	E_{exp}	E_{calc}	E_{exp}	E_{calc}	E_{exp}	E_{calc}
$(9/2)^-$	0	0	-	-	-	-
$(11/2)^-$	209	203	0	0	0	-
$(13/2)^-$	541	502	611	626	910	849
$(15/2)^-$	765	803	593	523	636	627
$(17/2)^-$	1203	1165	1324	1260	1760	1639
$(19/2)^-$	1449	1544	1415	1623	1724	2015
$(21/2)^-$	1987	2018	-	-	-	-
$(23/2)^-$	2254	2461	-	-	-	-

Table 6.2 Experimental and calculated energies of the one-neutron $h_{11/2}$ band members with $I^{\pi} \leq (23/2)^-$.

resulting in the 5/2[402] becoming the major contribution to the ground state and a $5/2^+$ collective excitation built on 3/2[411] comes within 75 keV of the ground state. Magnetic dipole and electric quadrupole moments of this configuration agree exactly with the moments of the $5/2^+$ experimental ground state. Having in mind uncertainty of the absolute position of the model ground state, caused mostly by simplifications in the treatment of pairing, it is highly likely that the experimental moment values reflect the change in the $5/2^+$ state make-up. Turning to ^{143}Eu, the calculated composition of the first and second $5/2^+$ states is very similar to the one for ^{141}Eu. An excellent agreement between experimental and calculated moments can be achieved for ε_2~0.13 (see Fig 6.11).

We note that oblate core has been also taken into consideration for both ^{141}Eu and ^{143}Eu but no agreement with experiment for the electromagnetic moments could be achieved.

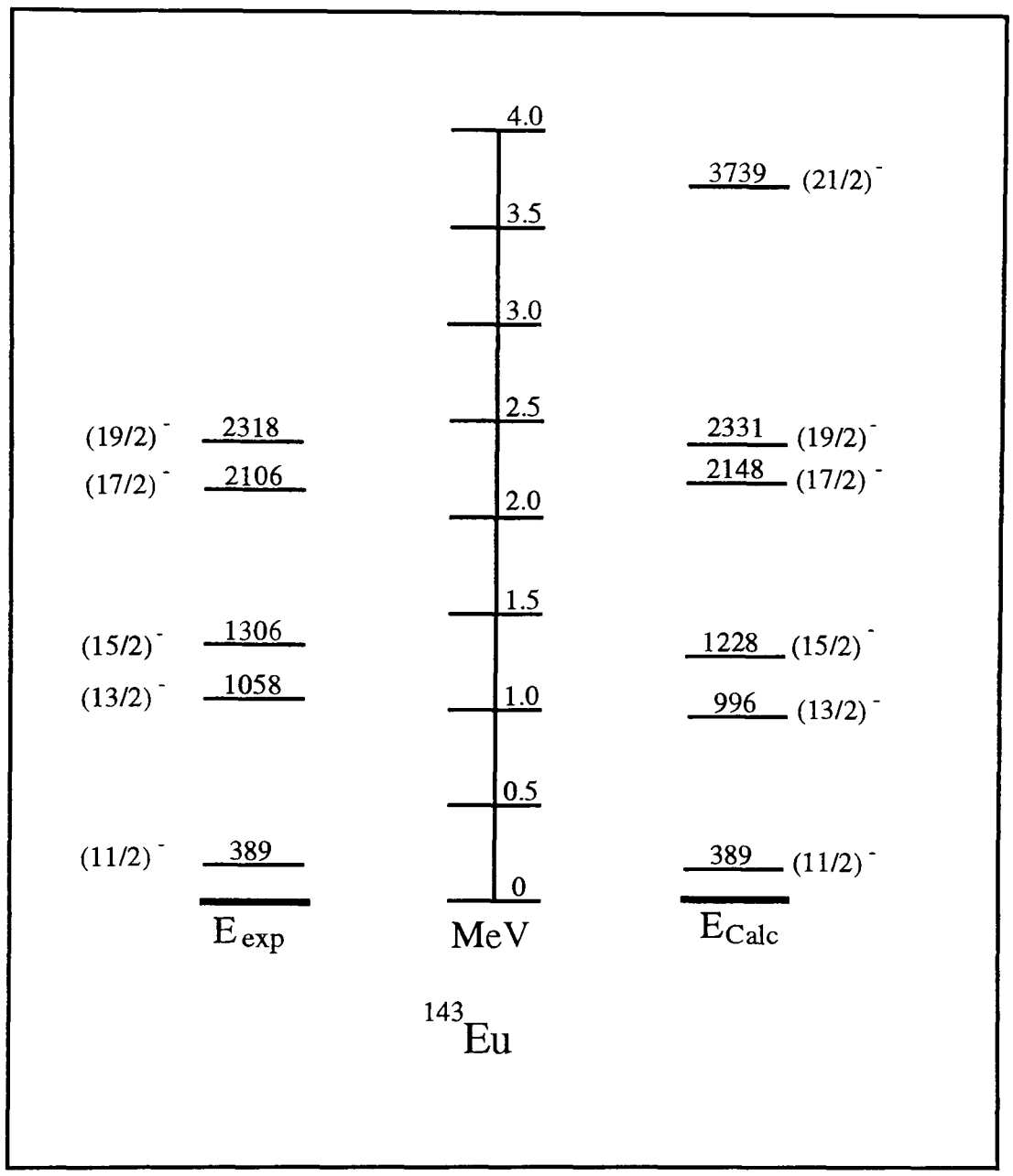


Fig 6.7 Experimental and calculated energy level of the yrast negative parity band in ^{143}Eu for ε_2=-0.15 and γ=25°

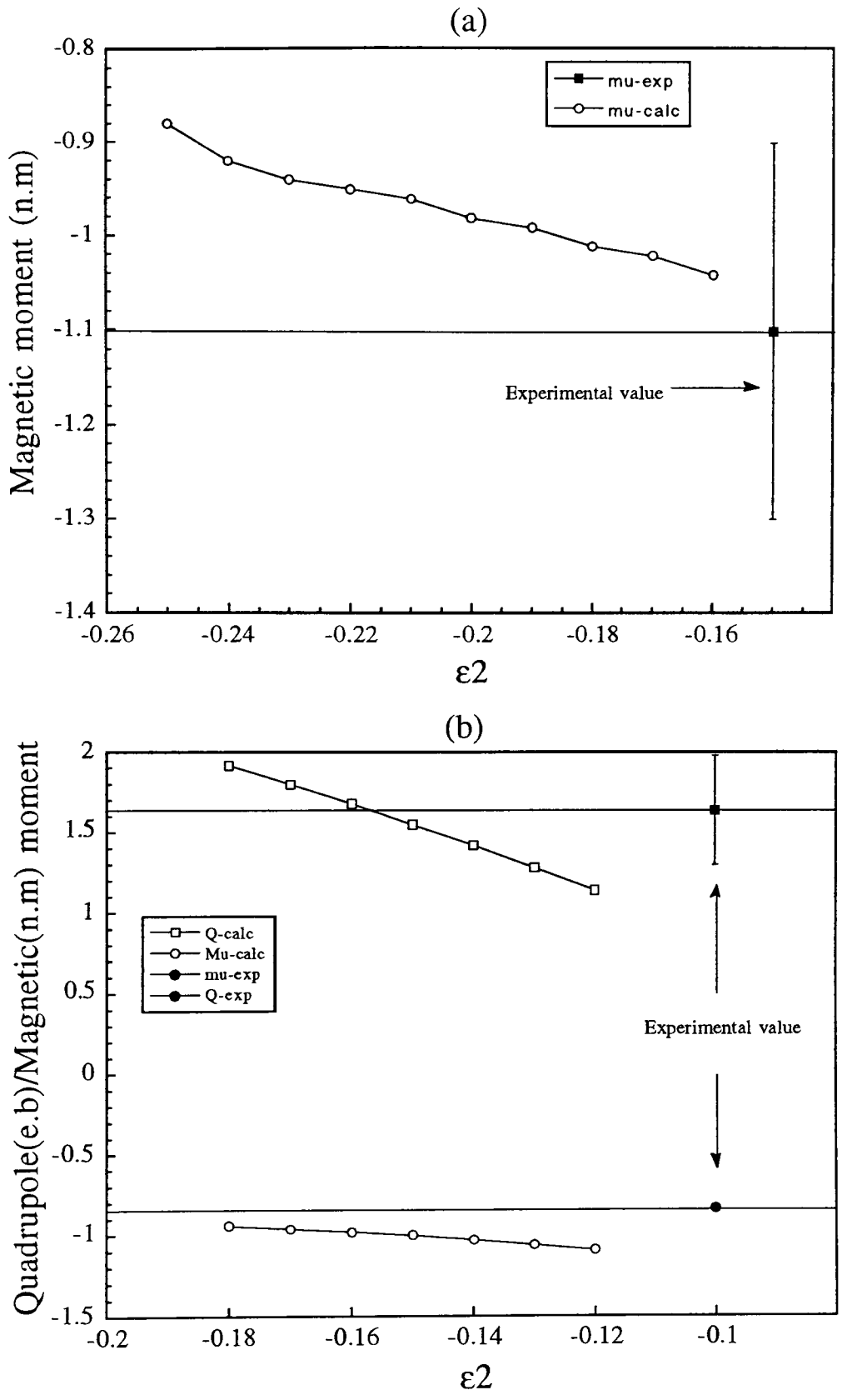


Fig 6.8 Calculated and experimental moments of the $(11/2)^-$ band heads in ^{139m}Sm (a) for $\gamma=28^\circ$ and $\xi=0.8$ and ^{141m}Sm (b) for $\gamma=26.5^\circ$ and $\xi=0.9$ as a function of $\varepsilon_2 < 0$.

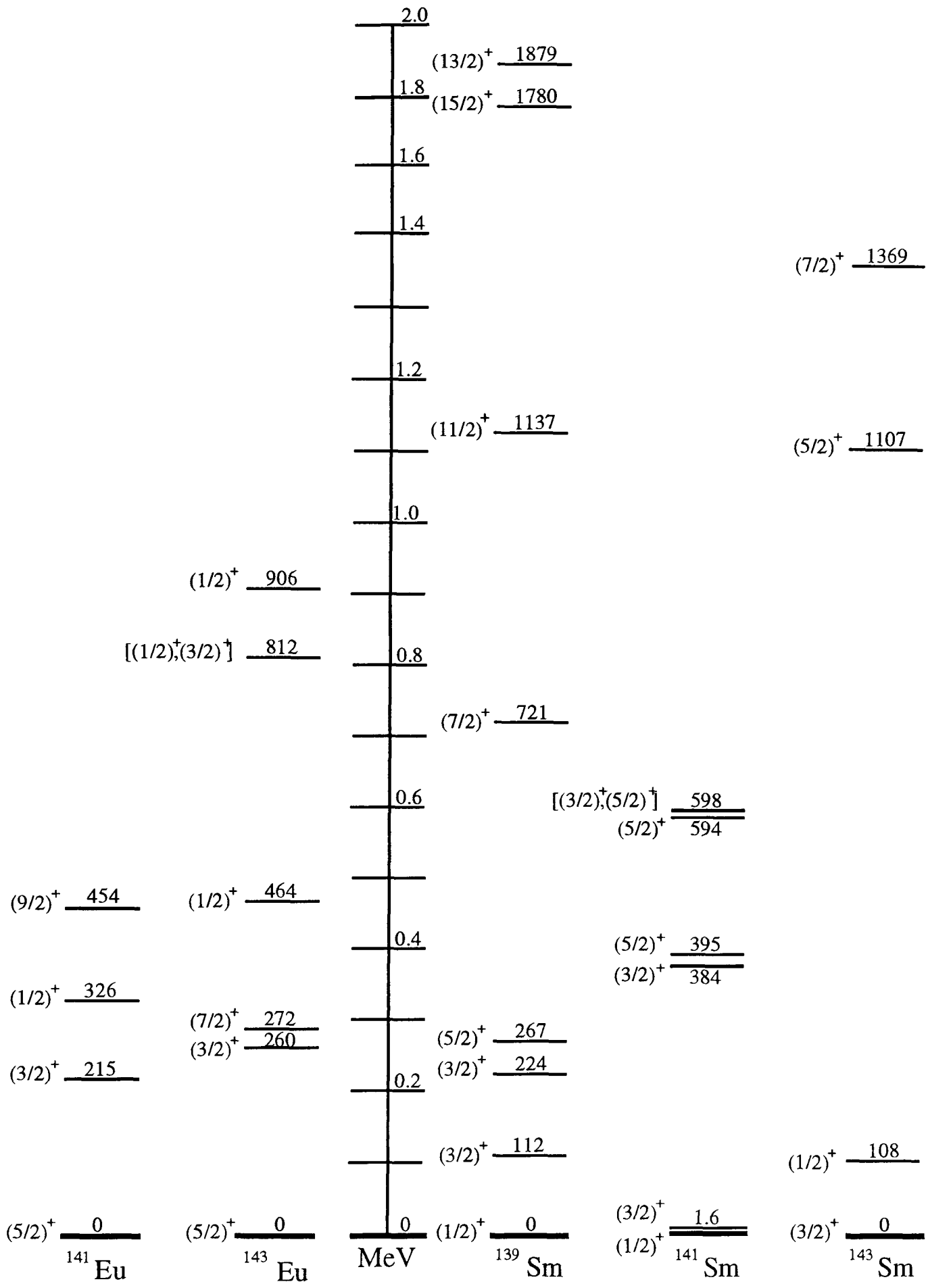


Fig 6.9 The systematics of experimental positive parity states in $^{141\text{-}143}$Eu and $^{139\text{-}143}$Sm.

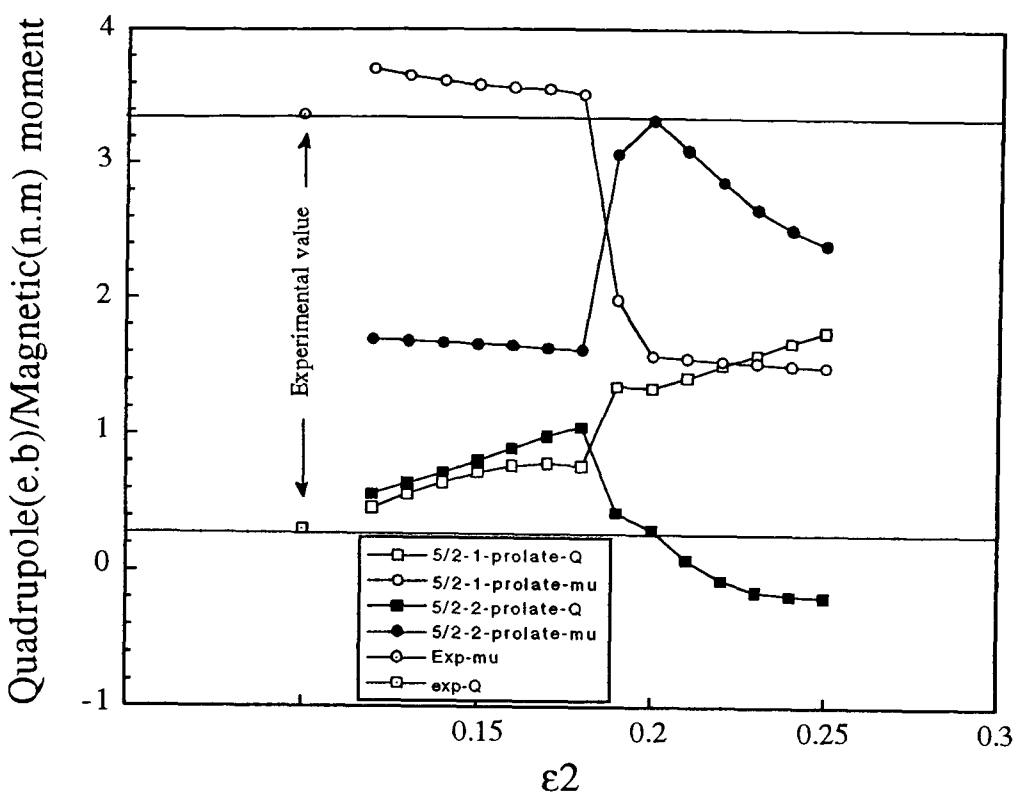


Fig 6.10 Dependence of the calculated values of μ and Q on ε_2 for the two lowest $(5/2)^+$ states in ^{141}Eu.

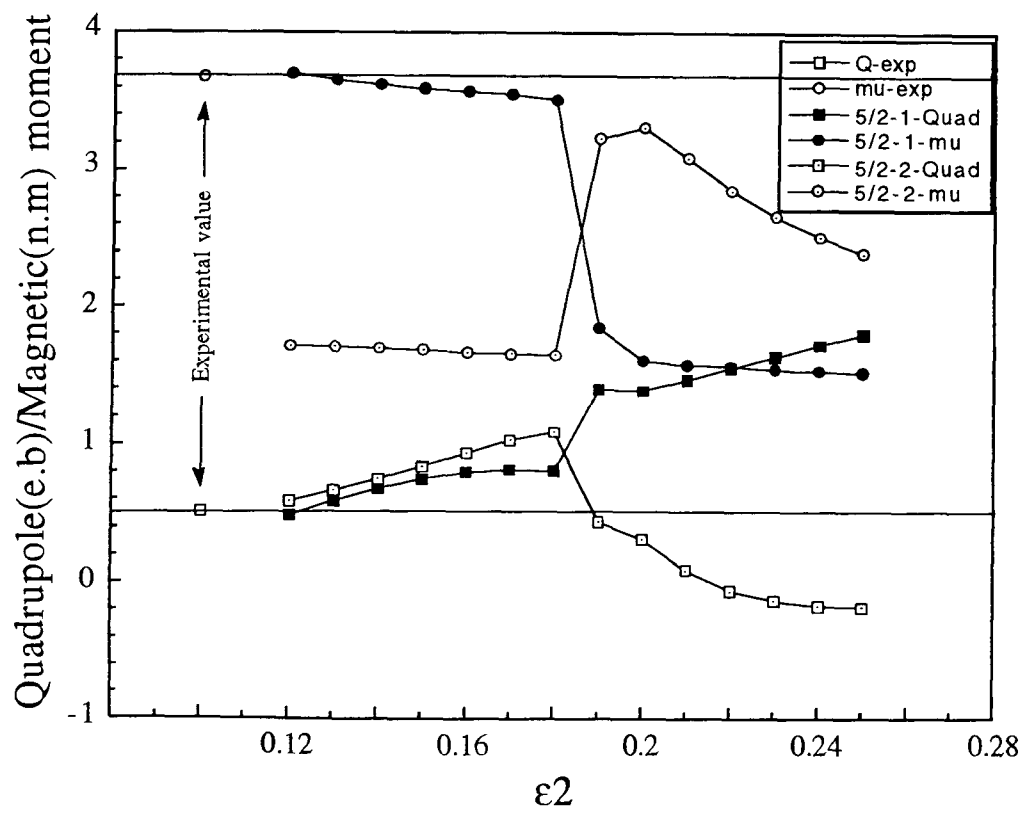


Fig 6.11 The same as Fig 6.10 but for ^{143}Eu.

6.3.4 Positive parity states in $^{139\text{-}143}$Sm

The particle-triaxial rotor model identifies the two lowest lying positive parity states in the odd-neutron $^{139\text{-}143}$Sm as states of the $d_{3/2}$ spherical origin with main components 1/2[411] ($I^{\pi}=1/2^{+}$) and 3/2[402] ($I^{\pi}=3/2^{+}$). The next two states ($3/2^{+}$ and $5/2^{+}$) are collective excitations built on the single-neutron configurations. Deformation dependence of the calculated magnetic dipole moment is displayed in Fig 6.12. The experimental value of the moment clearly rules out a prolate shape but is not sensitive to an unambiguous simultaneous choice of ε_2 and γ. Possible additional information which can be taken into account with caution (see section 6.3.3) comes from a comparison of the calculated and experimental values of the first three excited states in ^{139}Sm (see Table 6.3). We cannot expect a good agreement with experiment of predictions of relative positions of different single-particle configurations. However, collective excitations built on these configurations should be realistically estimated in the model. We see from Table 6.3 that the agreement between calculated and experimental energy differences $(3/2+)_2$ - $(1/2+)_1$ and $(5/2+)_1$ - $(3/2+)_1$ becomes systematically better with increasing γ. Therefore it is plausible to choose ε_2~0.21, $\gamma=29^{o}$ as the most probable deformation parameters of the ^{138}Sm core.

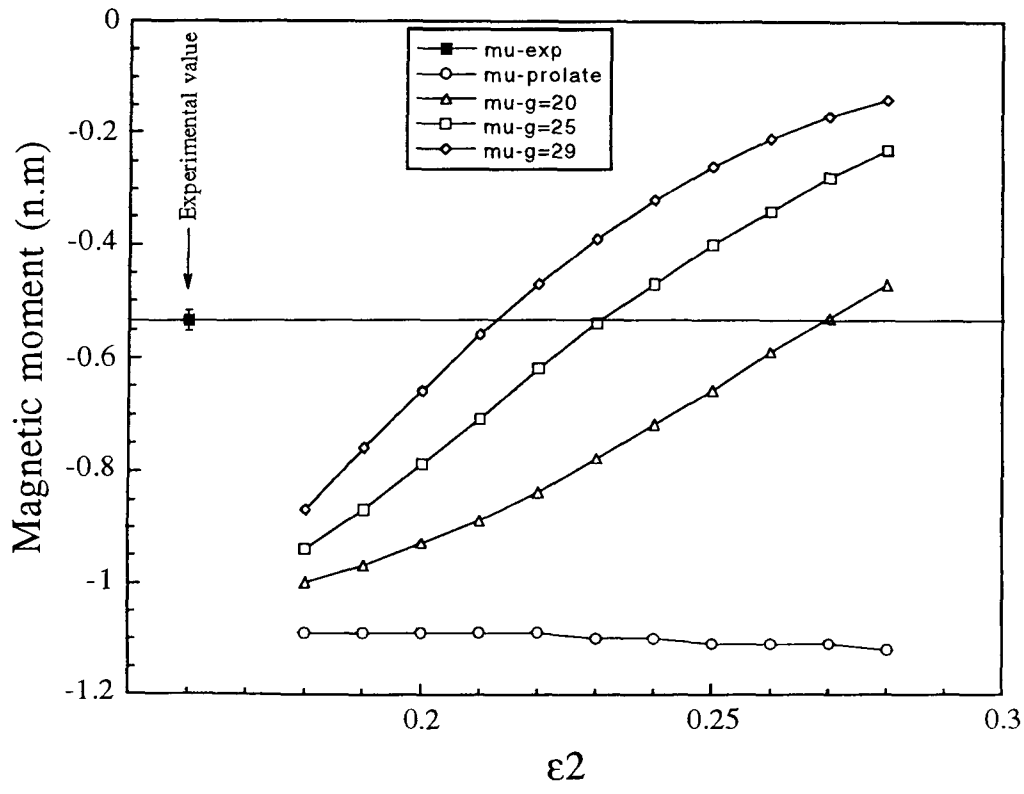


Fig 6.12 Deformation dependence of the magnetic dipole moment of the $I^{p}=(1/2)^{+}$ ground state of ^{139}Sm.

The same procedure as above can be applied in the case of the magnetic dipole moment of the ^{141}Sm $I^{\pi}=1/2^{+}$ ground state. Our results are illustrated in Fig 6.13 and Table 6.4. We can identify a clear preference for an "oblate-triaxial" shape of the ^{140}Sm core with $|\varepsilon_2|\leq 0.21$ and $\gamma\geq 25^{o}$. Both magnetic dipole and electric quadrupole moments are known for the $I^{\pi}=3/2^{+}$ ground state of ^{143}Sm. The model predicts $I^{\pi}=3/2^{+}$ only for $\varepsilon_2<0$. Calculated values of the magnetic dipole moment are rather insensitive to γ deformation in the whole region of $0^{o}\leq\gamma\leq 30^{o}$ for $\varepsilon_2<0$ (see Fig 6.14a).The large uncertainty in the experimental value of the quadrupole moment makes this quantity less useful for comparison with model calculation. The calculated energy of the first excited state in ^{143}Sm best fits the experimental value for an "oblate-triaxial" shape with $\varepsilon_2 \leq |0.14|$ (see Fig 6.14 b).

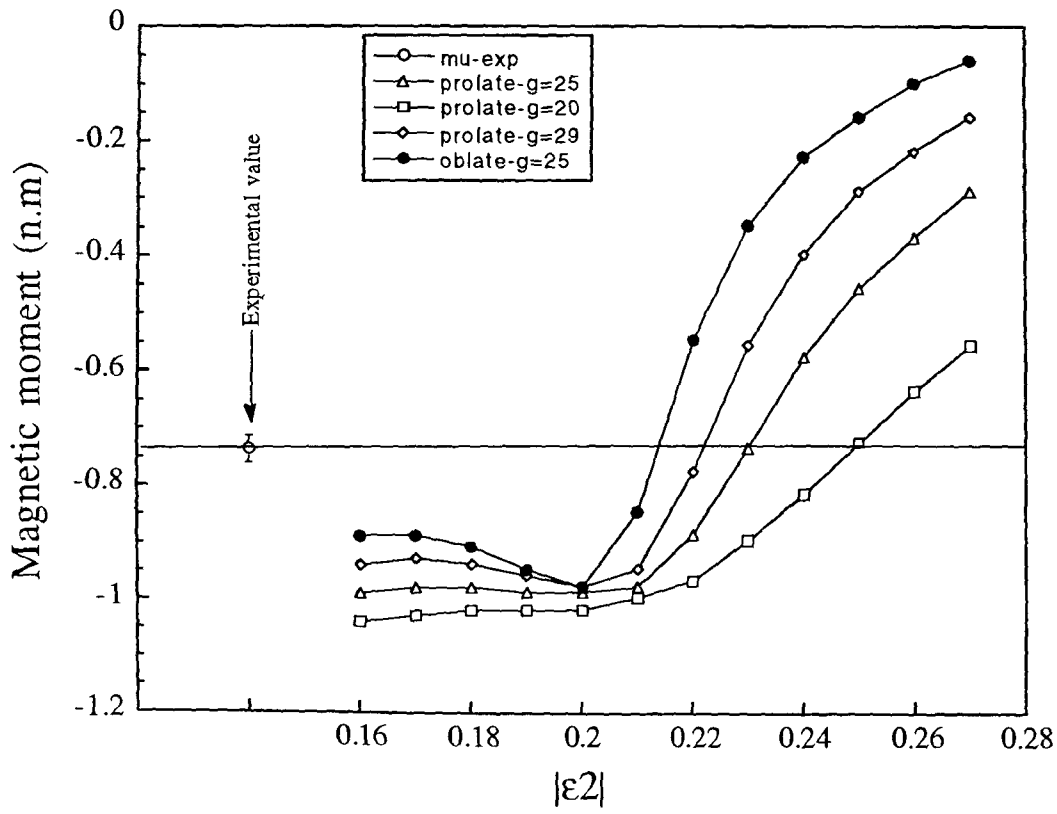


Fig 6.13 The same as fig 6.12 but for ^{141}Sm.

J^{π}	E_{exp}	$\varepsilon_2 = 0.27$ $\gamma = 20^{\circ}$	$\varepsilon_2 = 0.23$ $\gamma = 25^{\circ}$	$\varepsilon_2 = 0.21$ $\gamma = 29^{\circ}$
$(1/2)_1^+$	0	0	0	0
$(3/2)_1^+$	112	42	32	15
$(3/2)_2^+$	224	114	136	164
$(5/2)_1^+$	267	130	154	174

Table 6.3 Experimental and calculated energies (in keV) of the first three lowest-lying states in ^{139}Sm.

J^{π}	E_{exp}	$\varepsilon_2 = 0.25$ $\gamma = 20^{\circ}$	$\varepsilon_2 = 0.23$ $\gamma = 25^{\circ}$	$\varepsilon_2 = 0.22$ $\gamma = 29^{\circ}$	$\varepsilon_2 = -0.21$ $\gamma = 25^{\circ}$
$(1/2)_1^+$	0	0	0	0	4.6
$(3/2)_1^+$	1.6	45	26	11	0
$(3/2)_2^+$	384	129	146	174	223
$(5/2)_1$	395	147	162	183	219

Table 6.4 The same as table 6.3 but for ^{141}Sm.

6.3.5 The odd-odd ^{138}Eu nucleus.

The yrast band in the odd-odd Eu nucleus showing states with both signatures has been identified by Liang et al [23]. Both the odd-proton and the odd-neutron in ^{138}Eu lie within the high-j $h_{11/2}$ subshell. Yrast bands in odd-odd nuclei in this mass region are built on the $\pi h_{11/2}\, \nu h_{11/2}$ configuration. Singleton et al[4,5] measured the magnetic dipole moment of the ground state of ^{138}Eu and gave preference to spin-parity assignment of 6^- to the ground state as a result of coupling of the π5/2[532] and ν7/2[404] single particle configurations to the ^{136}Sm core.

We have re-examined the calculation and illustrate the results in Fig 6.15 and Table 6.5. Assuming a prolate shape of the ^{136}Sm core, we have found two $I^\pi=7^+$ states within 200 keV above the ground state. One of the states forms a band-head of a strongly coupled band, the other has decoupled band associated with it. The two 7^+ band-heads come very close together at $\varepsilon_2 \sim 0.24$ and interchange their mutual position at about 60 keV. As a result of interaction of these states a large increase in the magnetic moment of the lower 7^+ state takes place, and reaches agreement with experimentally measured value. The large uncertainty on the experimental value of μ allows us to set a lower limit for the value of ε_2, i.e. $\varepsilon_2 \geq 0.24$. The main proton orbitals involved in the make-up of the two 7^+ states are 3/2[541] and 5/2[532]. The main contributing neutron orbitals are 9/2[514] and 11/2[505]. The calculation was performed both with and without the proton-neutron residual interaction. The effect was small on the value of the calculated magnetic dipole moment (see Fig 6.15), but the presence of the residual interaction considerably increases energies of the band members, bringing them closer to experimental values.

I^π	E_{exp} (keV)	E_{res} (keV)	E_{nores} (keV)
7^+	0	0	0
8^+	105	156	97
9^+	272	245	219
10^+	545	536	345
11^+	807	708	687
12^+	1169	1045	810
13^+	1490	1349	1291

Table 6.5 Experimental and calculated energies of the $I^\pi=7^+$ decoupled band (see text) with and without the residual p-n interaction.

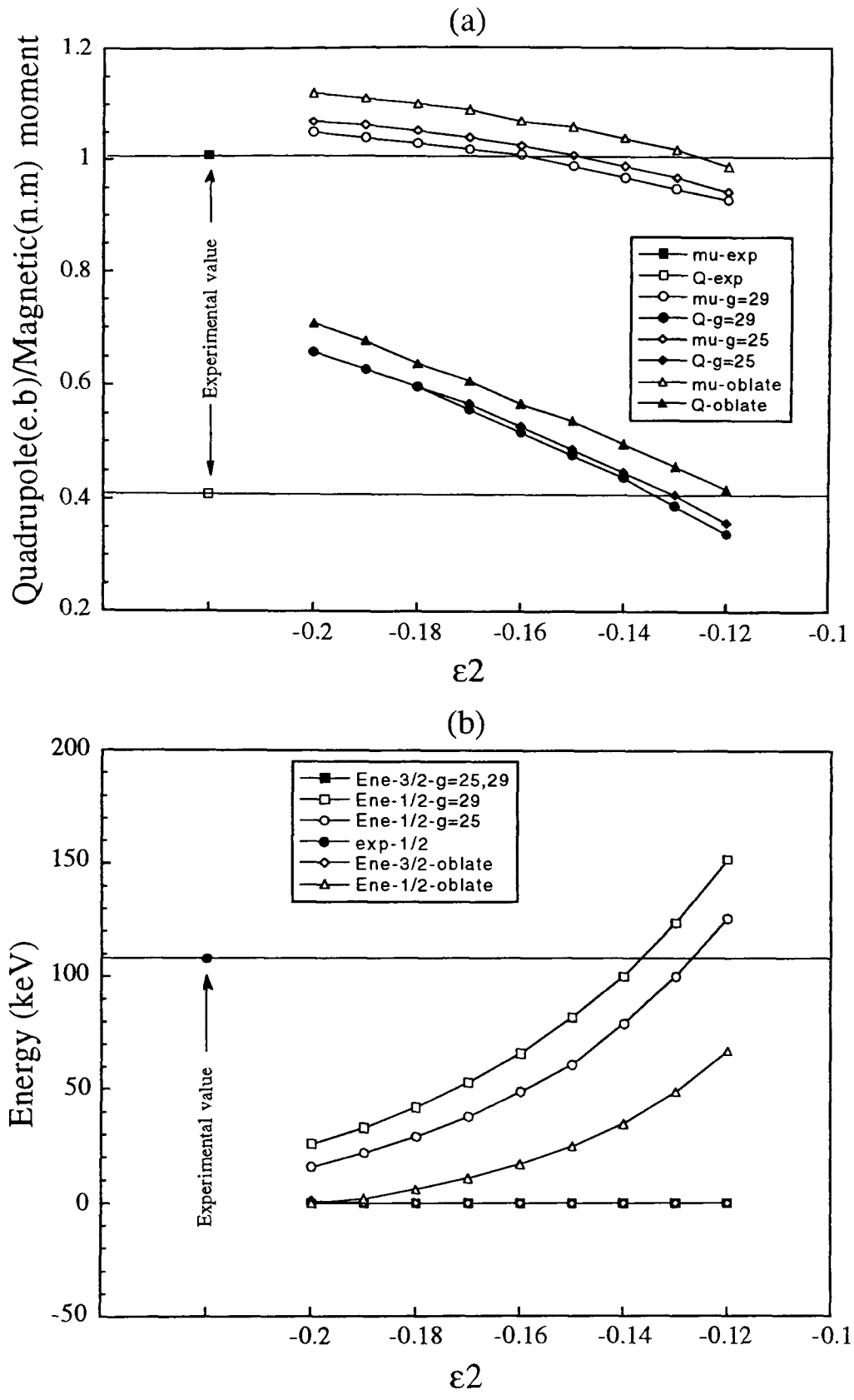


Fig 6.14 (a) Deformation dependence of μ and Q-values of the $I^{\pi}=(3/2)^{+}$ ^{143}Sm ground state (b) Experimental and calculated energies of the lowest lying $(1/2)^{+}$ and $(3/2)^{+}$ states in ^{143}Sm as a function of deformation. The calculated lowest $(3/2)^{+}$ state remains ground state for all γ.

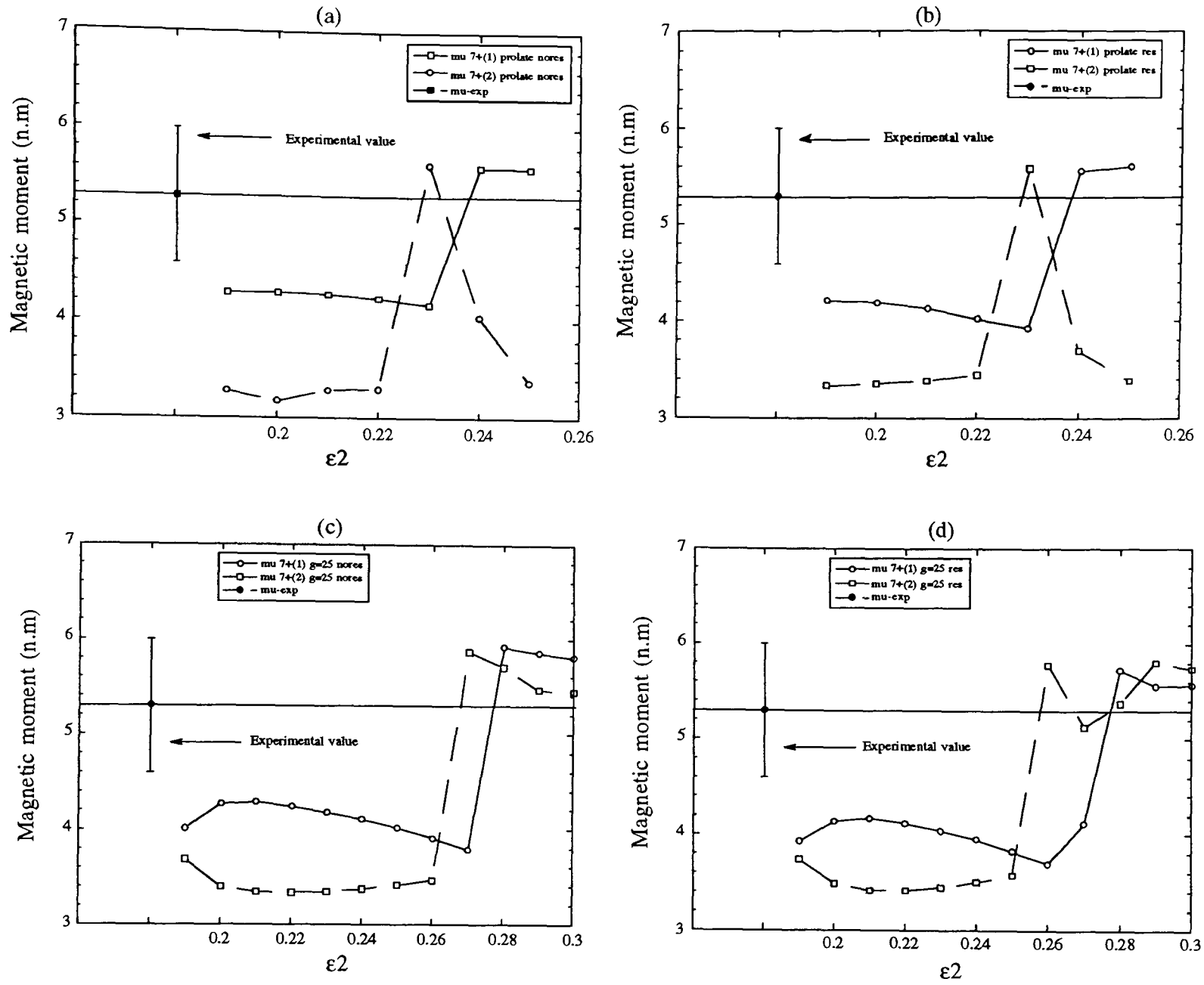


Fig 6.15 Deformation dependence of the calculated magnetic dipole moments of the $7^+(1)$ and $7^+(2)$ states in ^{138}Eu for prolate and triaxial shapes with and without the residual p-n interaction.

Liang et al[23] pointed out that observation of signature splitting in doubly odd nuclei in this region is indicative of a triaxial shape of the core. Whereas the low W $h_{11/2}$ protons favour prolate shape, the high Ω $h_{11/2}$ neutrons drive towards an oblate shape. As a result, a triaxial shape can be expected. Therefore we repeated our calculation for $\gamma=25^{o}$. We observed a lowering in energy of the two 7^{+} configurations with one of them always forming a ground state for $0.19 \leq \varepsilon_2 \leq 0.30$. At $\varepsilon_2 \sim 0.27$ the ground state becomes the band-head of the decoupled band, with a magnetic moment in line with the experimental value. We show in Table 6.5 a comparison of experimental and calculated energies of the decoupled band based on the 7^{+} state both with and without the residual interaction. It is clear that the residual interaction brings the band-members energies closer to the experimental values.

A more detailed calculation is being done at present on this system. No change in the physics content is expected, but more restricted values of ε_2 and γ of the ^{136}Sm core will be obtained. To summarize, our present result shows the 7^{+} configuration as a valid alternative to the previous $I^{\pi} = 6^{-}$ spin parity assignment.

6.4 Conclusions

Odd-proton, odd-neutron and odd-odd systems in the A=140 region have been investigated in the framework of the particle-triaxial rotor model. Attention have been paid mainly to explanation of the experimental magnetic dipole and electric quadrupole moments of ground and isomeric states. Together with additional information provided by experimental energy levels of nuclear collective excitations built on these states, model predictions for deformation parameters of $^{136\text{-}142}$Sm even-even cores have been extracted. It is clear that the cores are extremely soft and their shape is very much dependent on the configuration of the odd particle they couple with. We show these results in Table 6.6 in comparison with calculations by Moller and Nix[12] (their model considers only axially symmetrical shapes) and results of some previous calculations. Generally our deformation parameters are higher than predictions of the macroscopic-microscopic model but reasonably in line with results from the literature, although we stress that more attention must be paid to incorporation of experimental uncertainties into the error on the calculated parameters.

	present calculation		[12]	previous calculation		
	ε_2	γo	ε_2	ε_2	γo	ref.
(a)negative parity states						
137Eu	~ 0.26	?	0.272			
139Eu	~ 0.26	?	0.198	0.18	0	[20]
				0.19	<20	[25]
				0.27	29	[4]
141Eu	(~ -0.20)	(29)	0.151			
143Eu	~ -0.15	25	-0.144	-0.154	24	[10]
137Sm	~ 0.24	22	0.198			
139Sm	~ -0.20	28	0.158	-0.20	27.5	[4]
141Sm	~ -0.17	26.5	-0.144			
(b) positive parity states						
141Eu	~ 0.20	0	0.151			
143Eu	~ 0.13	0	-0.144	-0.12	0	[10]
139Sm	~ 0.21	29	0.158			
141Sm	≤ -0.21	≥ 25	-0.144			
143Sm	< 0	?	0.050			
c) odd-odd						
138Eu	≥ 0.27	~ 25	0.192	0.24	25	[4]

Table 6.6 Summary of deformation parameters calculated in the particle-triaxial rotor model: for odd-A $^{137\text{-}143}$Eu, $^{137\text{-}143}$Sm isotopes and odd-odd ^{138}Eu.

References

[1] G.A.Leander and P.Moller, Phys. Lett **110B**(1982)17

[2] S.Lunardi et al., Z. Phys **A321**(1985)177

[3] R.Wadsworth et al., J. Phys **G13**(1987)205

[4] B.D.D.Singleton, PhD. Thesis, Surrey, 1991

[5] B.D.D.Singleton et al., Hyp. Int **75**(1992)471

[6] P.Raghavan, ANDT **42**(1989)189

[7] V.S.Letokhov et al. J. Phys **G18**(1992)1177

[8] P.B.Semmes, Hyp. Int **75**(1992)85

[9] R.Ma et al, Phys. Rev **C40**(1989)156

[10] R.Aryaeinejad et al., Phys. Rev **C40**(1989)1429

[11] M.Lach et al., Z. Phys **A345**(1993)427

[12] P.Moller and J.R.Nix, ANDT **26**(1981)165

[13] S.E.Larson et al., Nucl. Phys **A307**(1978)189

[14] Ch.Vieu et al., J. Phys **G4**(1978)
and Z. Phys **A290**(1979)301

[15] I.Ragnarsson and P.B.Semmes, Hyp. Int **43**(1988)424

[16] S.G.Nilsson et al., Nucl. Phys **A313**(1969)1

[17] P.Boisson et al., Phys. Rep **26**(1976)99

[18] D.Bazzacco et al. Z. Phys **A335**(1990)363

[19] L.Goettig et al. Nucl. Phys **A475**(1987)569

[20] P.J.Bishop et al., J.Phys **G14**(1988)995

[21] S.Lunardi et al., Z. Phys **A324**(1986)433

[22] R.Aryaeinejad et al., Phys. Rev **C23**(1981)194

[23] Y.Liang et al., Phys. Rev **C38**(1988)2432

[24] J.Meyer-ter-vehn, Nucl. Phys **A249**(1975)111

[25] L.Ragnarson, Particle-rotor model code (unpublished)

[26] J.Zhang et al., Phys. Rev **C39**(1989)714

[27] L.Grodzins, Ann Rev. Nuc Sci **18**(1968)291

Appendix A

Chart of the nuclides showing which are accessible for NO.

A.1

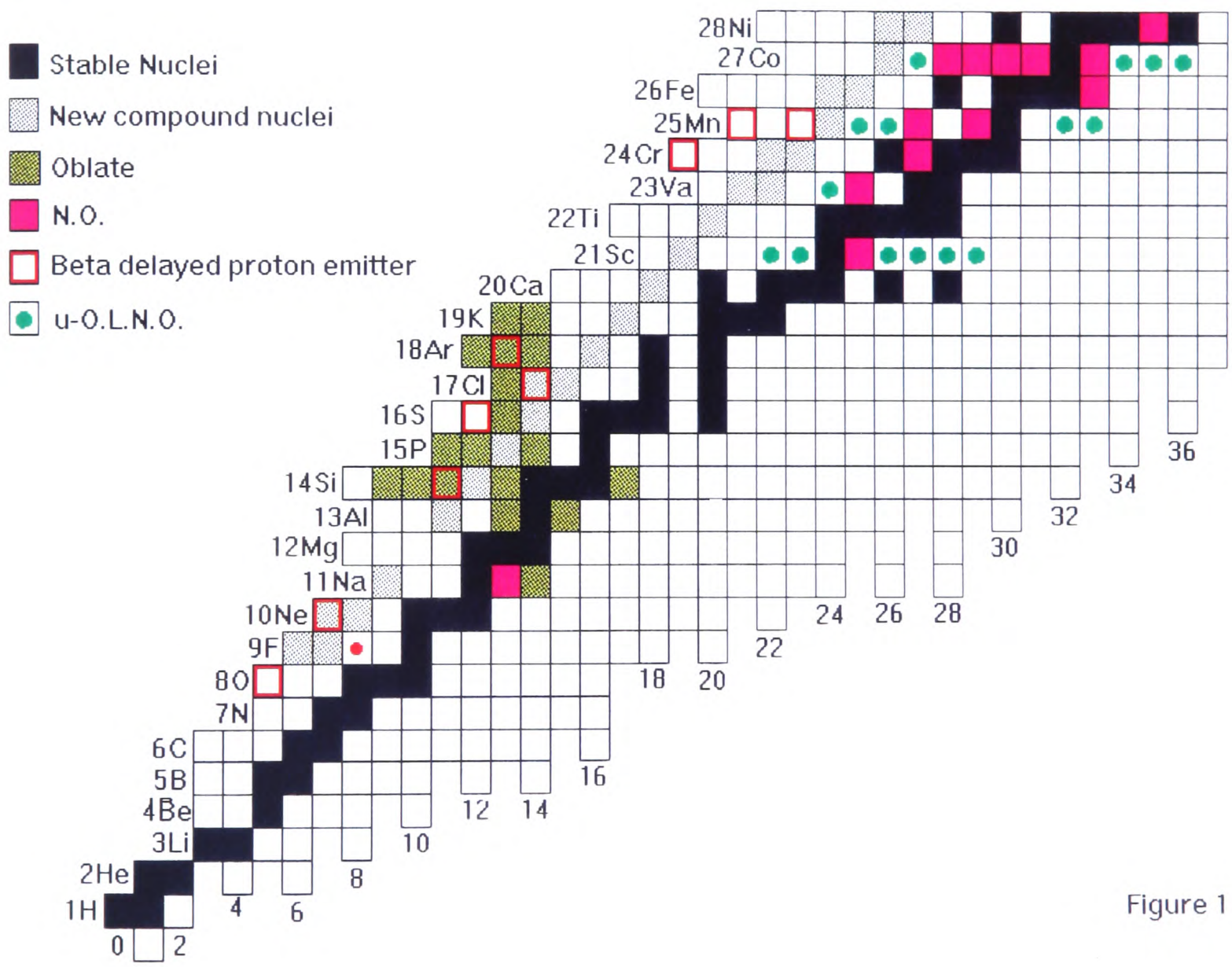


Figure 1

A.2

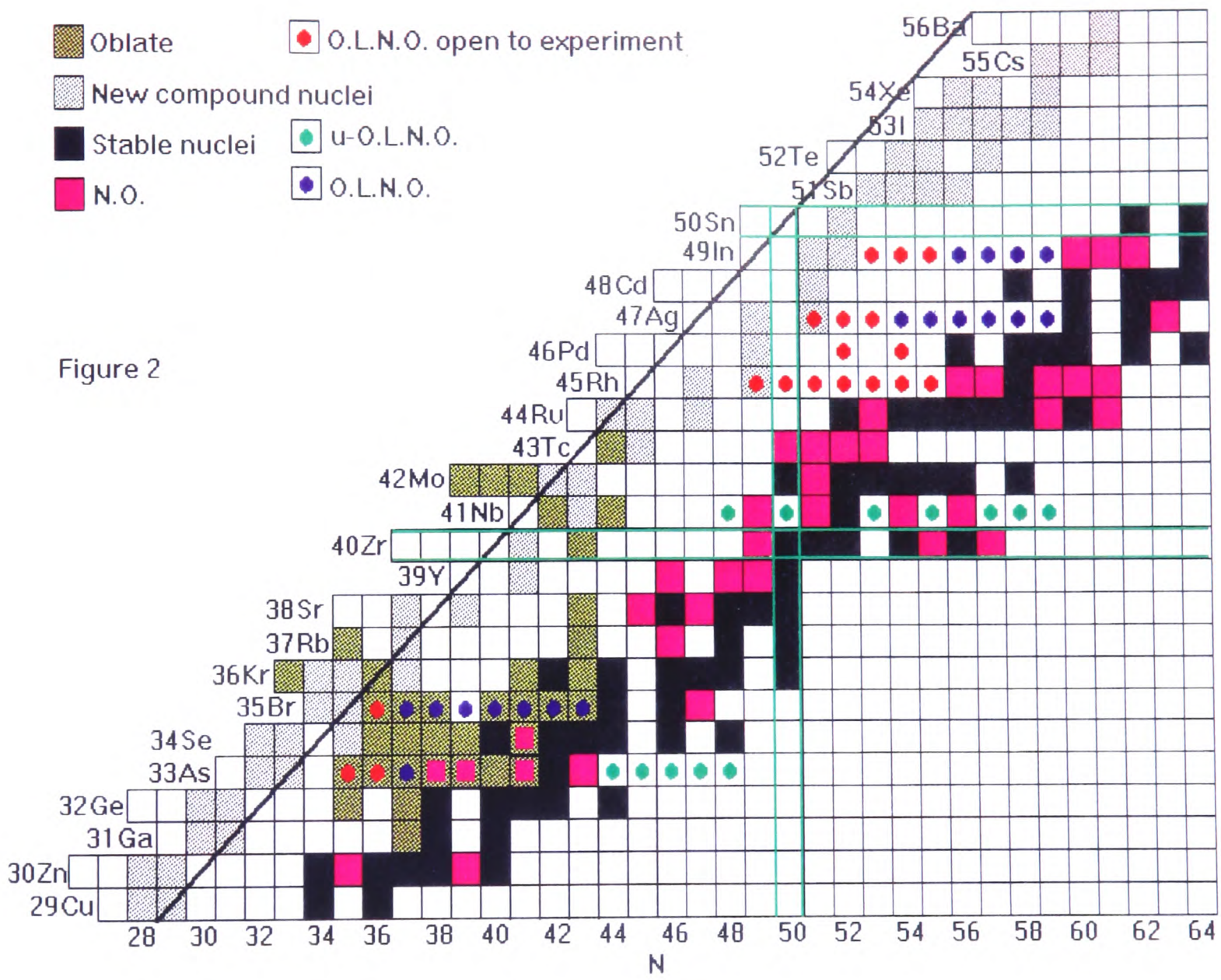

Oblate
New compound nuclei
Stable nuclei
N.O.
O.L.N.O. open to experiment
u-O.L.N.O.
O.L.N.O.
56Ba
55Cs
54Xe
53I
52Te
51Sb
50Sn
49In
48Cd
47Ag
46Pd
45Rh
44Ru
43Tc
42Mo
41Nb
40Zr
39Y
38Sr
37Rb
36Kr
35Br
34Se
33As
32Ge
31Ga
30Zn
29Cu
28 30 32 34 36 38 40 42 44 46 48 50 52 54 56 58 60 62 64
N

Figure 2

A.3

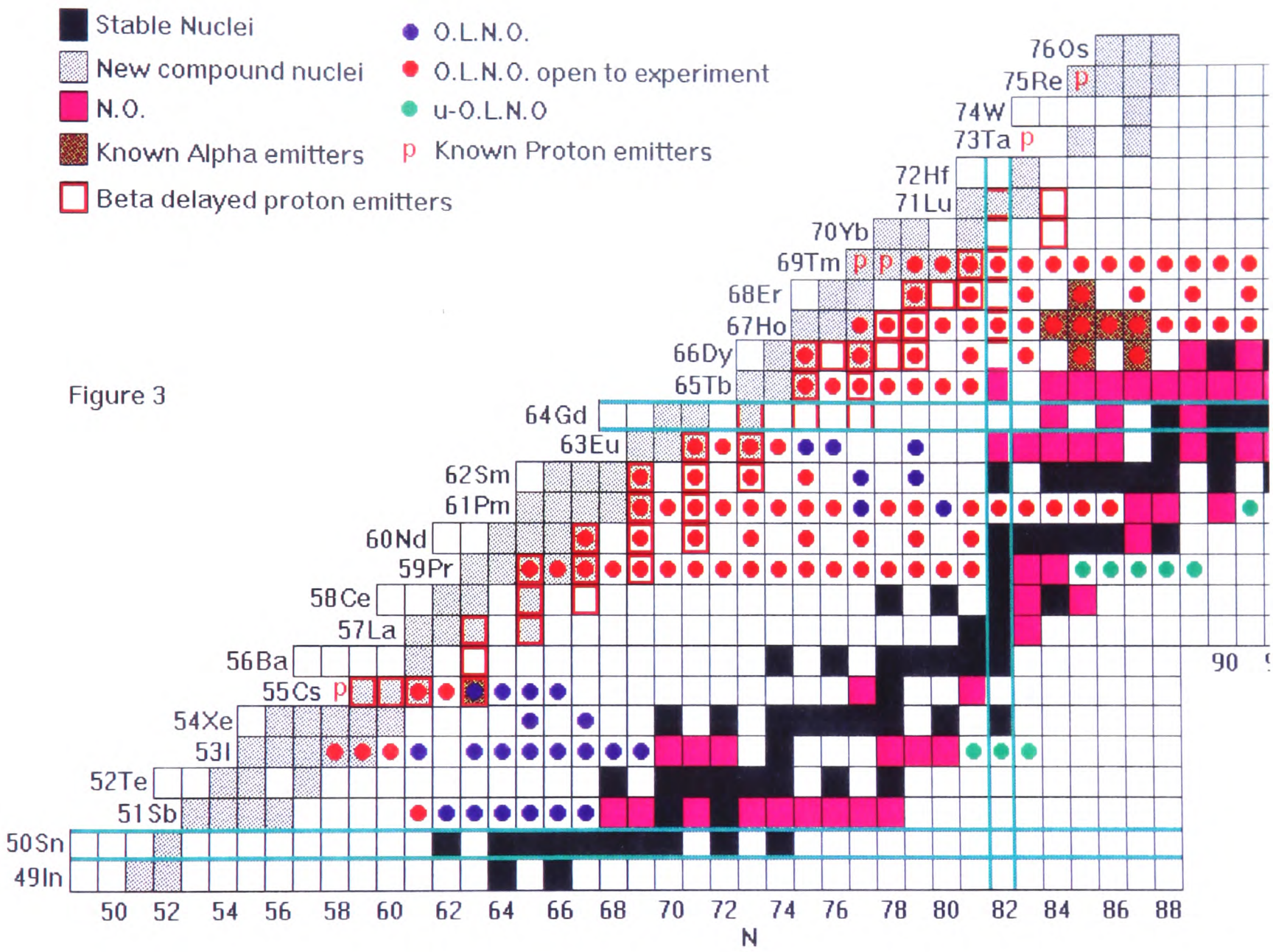

Stable Nuclei
New compound nuclei
N.O.
Known Alpha emitters
Beta delayed proton emitters
O.L.N.O.
O.L.N.O. open to experiment
u-O.L.N.O
p Known Proton emitters
76Os
75Re p
74W
73Ta p
72Hf
71Lu
70Yb
69Tm p p
68Er
67Ho
66Dy
65Tb
64Gd
63Eu
62Sm
61Pm
60Nd
59Pr
58Ce
57La
56Ba
55Cs p
54Xe
53I
52Te
51Sb
50Sn
49In
50 52 54 56 58 60 62 64 66 68 70 72 74 76 78 80 82 84 86 88
90
N

Figure 3

A.4

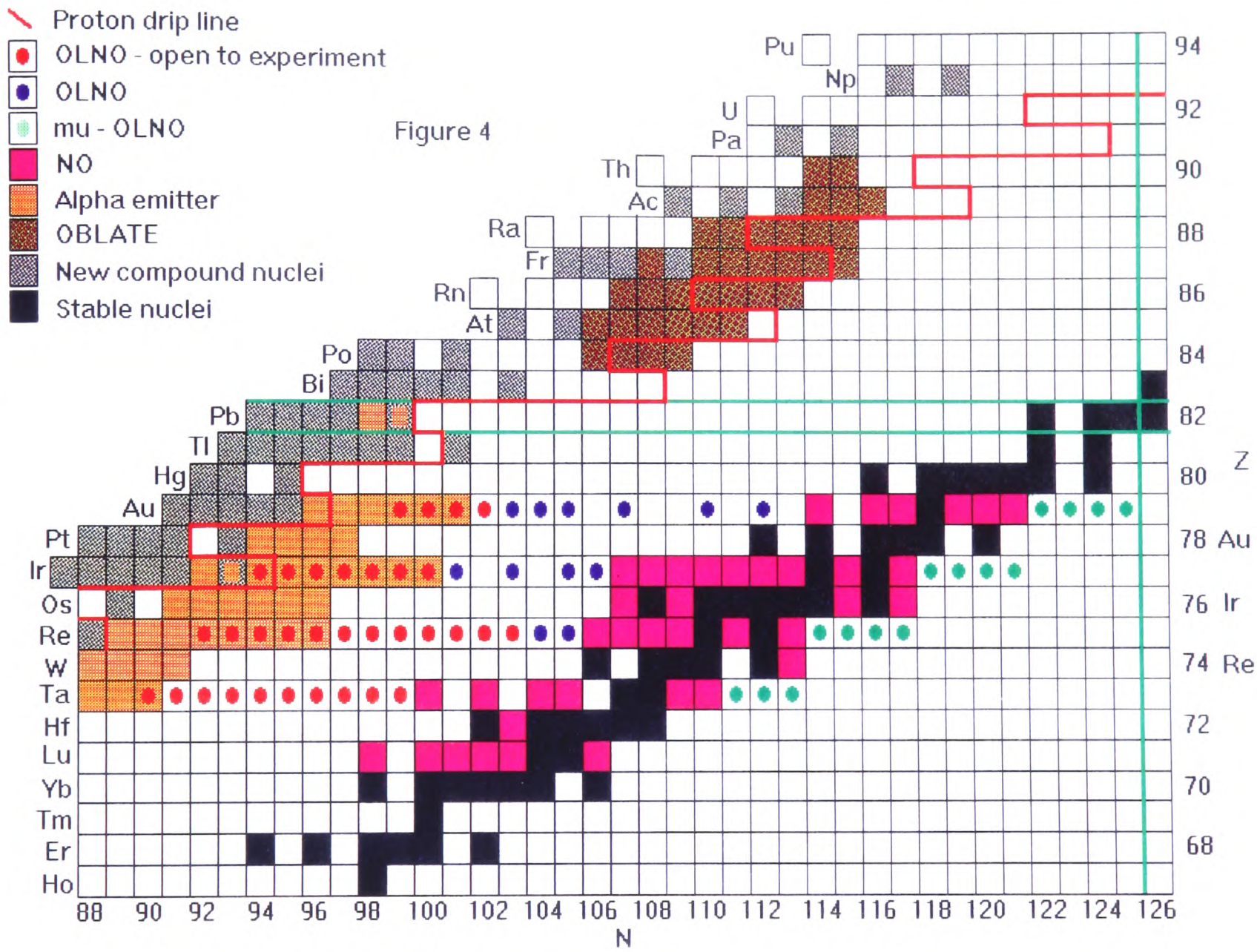

Proton drip line
OLNO - open to experiment
OLNO
mu - OLNO
NO
Alpha emitter
OBLATE
New compound nuclei
Stable nuclei
Pu
Np
U
Pa
Th
Ac
Ra
Fr
Rn
At
Po
Bi
Pb
Tl
Hg
Au
Pt
Ir
Os
Re
W
Ta
Hf
Lu
Yb
Tm
Er
Ho
94
92
90
88
86
84
82
80
78 Au
76 Ir
74 Re
72
70
68
Z
88 90 92 94 96 98 100 102 104 106 108 110 112 114 116 118 120 122 124 126
N

Figure 4

Appendix B

Angular Momentum

Properties of a free nucleus do not depend on the orientation of the nucleus in space. The rotational invariance of the nuclear Hamiltonian implies that the total angular momentum $\boldsymbol{J}$ of the nucleus is a good quantum number. For the construction of the independent-particles states in the shell model the isotropic harmonic-oscillator potential is employed.

In classical mechanics the angular momentum of a system of n-particles is defined with respect to the origin O of the coordinate frame as the vector product and is given by

$$\boldsymbol{l} = \sum_{i=1}^{n} (\boldsymbol{r}_i \times \boldsymbol{p}_i) = \sum_{i=1}^{n} \boldsymbol{l}_i \tag{B1}$$

where $\boldsymbol{r}_i$, $\boldsymbol{p}_i$ and $\boldsymbol{l}_i$ are the position vector with respect to O, the linear momentum, and angular momentum respectively of the ith particle. For the force which act along the radius vector (a central potential), it can be deduced that $\boldsymbol{l}$ is a constant of motion. The quantum mechanical definition of the orbital angular momentum operator is

$$\hbar \boldsymbol{l} = \boldsymbol{r} \times \boldsymbol{p} \tag{B2}$$

Substituting by $\boldsymbol{p} = i\hbar\nabla$ into equation (6.64) the expression for the operator $\boldsymbol{l}$ that is dimensionless is obtained

$$\boldsymbol{l} = i\boldsymbol{r} \times \nabla \tag{B3}$$

In quantum mechanics the components of position and linear momentum of a particle obey the commutation relations

$$\begin{aligned} &[x_i, p_i] = i\hbar\delta_{ij} \\ &[x_i, x_i] = 0 \qquad\qquad \textit{where} \quad i, j = 1,2,3 \\ &[p_i, p_i] = 0 \end{aligned} \tag{B4}$$

Applying these relations the commutation rules for the components of angular momentum is as follows;

$$\begin{aligned}\left[l_x, l_y\right] &= \left(yp_z - zp_y\right)\left(zp_x - xp_z\right) - \left(zp_x - xp_z\right)\left(yp_z - zp_y\right) \\ &= yp_x\left(p_z z - zp_z\right) + xp_y\left(zp_z - p_z z\right) \\ &= i\hbar\left(xp_y - yp_x\right)\end{aligned} \tag{B5}$$

Thus following relations are obtained

$$\begin{aligned}\left[l_x, l_y\right] &= i\hbar l_z \\ \left[l_y, l_z\right] &= i\hbar l_x \\ \left[l_z, l_x\right] &= i\hbar l_y\end{aligned} \tag{B6}$$

The differential operator forms of angular momentum with $p_x = -i\hbar\left(\frac{\partial}{\partial x}\right)$ are

$$\begin{aligned}l_x &= -i\hbar\left(y\frac{\partial}{\partial z} - z\frac{\partial}{\partial y}\right) \\ l_y &= -i\hbar\left(z\frac{\partial}{\partial x} - x\frac{\partial}{\partial z}\right) \\ l_z &= -i\hbar\left(x\frac{\partial}{\partial y} - y\frac{\partial}{\partial x}\right)\end{aligned} \tag{B7}$$

and in terms of the spherical polar coordinates

$$\begin{aligned}l_x &= i\hbar\left(\sin\varphi\frac{\partial}{\partial\vartheta} + \cot\vartheta\cos\varphi\frac{\partial}{\partial\varphi}\right) \\ l_y &= i\hbar\left(-\cos\varphi\frac{\partial}{\partial\vartheta} + \cot\vartheta\cos\varphi\frac{\partial}{\partial\varphi}\right) \\ l_z &= -i\hbar\frac{\partial}{\partial\varphi}\end{aligned} \tag{B8}$$

Thus the angular momentum operators are proportional to the operators of infinitesimal rotations.

The square of the total angular momentum is defined as $\boldsymbol{l}^2 = l_x^2 + l_y^2 + l_z^2$

and in terms of the spherical differential operators

$$l^2 = -\hbar^2\left[\frac{1}{\sin\vartheta}\frac{\partial}{\partial\vartheta}\left(\sin\vartheta\frac{\partial}{\partial\vartheta}\right)+\frac{1}{\sin^2\vartheta}\frac{\partial^2}{\partial\varphi^2}\right] \tag{B9}$$

These relations can be used for the intrinsic angular momentum. The orbital angular momentum and the spin refer to independent degrees of freedom and therefore commute with each other

$$[l,s]=0 \tag{B10}$$

Thus the sum vector can be defined as

$$j = l + s \tag{B11}$$

Appendix C

Equation of motion of a nucleon in the self-consistent field of the nucleus

Assume that the potential V(r) of the self-consistent field is characterized. Let the single-particle wave functions $\Psi(\mathbf{r})$ describing the motion of the nucleon be the solutions of the Schrödinger equation

$$\left\{\left(\hbar^2/2M\right)\nabla^2 + V(\mathbf{r}) - E\right\}\Psi(\mathbf{r}) = 0 \qquad \text{(C.1)}$$

where ∇^2 is the Laplacian operator, $\mathbf{r}$ the particle coordinate and E represent the single particle energies. Because of the spherical symmetry of the potential $V(\mathbf{r})$, the angular momentum of the nucleon is a constant of the motion and the wave function, $\Psi(\mathbf{r})$, can be represented in the form of a product of a radial function with an angular function.

$$\Psi_{nlm}(\mathbf{r}) = R_{nl}(r)Y_{lm}(\vartheta,\varphi) \qquad \text{(C.2)}$$

The angular function $Y_{lm}(\vartheta,\varphi)$ is the eigenfunction of a state in which the angular momentum l and its component m have well-defined values. The radial function, $R_{nl}(r)$, satisfies the equation

$$\frac{d^2R_{nl}(r)}{d^2r} + \frac{2}{r}\frac{dR_{nl}(r)}{dr} + \frac{2M}{\hbar^2}\left[E_{nl} - V(r) - \frac{\hbar^2}{2M}\frac{l(l+1)}{r^2}\right]R_{nl}(r) = 0 \qquad \text{(C.3)}$$

and the boundary conditions that the function $R_{nl}(r)$ be finite at the point r=0 and go to zero at infinity. The energy eigenvalues $E_{nl} \prec 0$ of the bound states of the nucleon are determined from the condition that the radial function $R_{nl}(r)$ go to zero at infinity. Here n is the principal quantum number, which characterizes the energy eigenvalue E_{nl} of the nucleon and is equal to the number of nodes of the radial function $R_{nl}(r)$ plus one.

Since the energy eigenvalues E_{nl} do not depend on the quantum number m, each level is characterized by $(2l+1)$-fold degeneracy. In addition, each level is doubly degenerate with respect to the spin, and is also doubly degenerate with respect to the charge if the Coulomb interaction is neglected. Thus, the mean spacing between the degenerate levels found to be considerably greater than the spacing predicted by the statistical theory.

The radial functions, $R_{nl}(r)$, like the sequence of single-particle levels, E_{nl} , depend on the shape of the potential $V(r)$. Information on the shape of the potential can be obtained from the nucleon scattering experiments and from these experiments the depth of the potential well $V(r)$ is almost constant inside the nucleus and rapidly drop to zero close to the nuclear surface.

The problem of the motion of a nucleon in the self-consistent field $V(r)$ can be solved in explicit form by approximating the true potential $V(r)$ by an oscillator potential well or a square potential well. The results for the true potential can be then obtained by interpolation from the results obtained for these idealized potentials.

Appendix D

Spin-orbit interaction

As the nucleon moves in the self-consistent field of the nucleus an additional interaction appears due to the presence of the spin of the nucleon. The energy of this interaction depend on three parameter, namely, **s**, $\boldsymbol{r}$ and $\boldsymbol{v}$ - an axial vector, a true vector and the velocity of the nucleon respectively. A scalar expression can be constructed from these as follows:

$$f(r)[\boldsymbol{r}\times\boldsymbol{v}] \tag{D.1}$$

where $f(r)$ is a scalar function of the coordinates. Since the vector product in equation (D.1) $\boldsymbol{r}\times\boldsymbol{v}$ is proportional to the nucleon orbital angular momentum $\boldsymbol{l}$, and equation (D.1) can be regarded as a spin-orbit interaction which has relativistic character as $\boldsymbol{v}\to 0$ and is considerably weaker than the nucleon interaction with the self-consistent field.

Consider the interaction of a moving particle with momentum $\boldsymbol{p}$ and a magnetic moment $\mu = \left(e\hbar/Mc\right)\boldsymbol{s}$, with an electrostatic field $\boldsymbol{E} = -\left(1/e\right)grad\, V$. The magnetic field intensity is equal to $\boldsymbol{H} = \left(1/c\right)\left[\left(\boldsymbol{p}/M\right)\times\boldsymbol{E}\right]$, and, consequently, the magnetic interaction energy is given by

$$U = -\mu\bullet\boldsymbol{H} = -\frac{\hbar}{M^2c^2}[\boldsymbol{p}\times\nabla V]\bullet\boldsymbol{s} \tag{D.2}$$

for spherically symmetric potential, equation (D.2) can be rewritten as

$$U = \left(\frac{\hbar}{Mc}\right)^2\left(\frac{1}{r}\right)\left(\frac{\partial V}{\partial r}\right)(\boldsymbol{l}\bullet\boldsymbol{s}) \tag{D.3}$$

since $grad\, V = \left(\boldsymbol{r}/r\right)\left(\partial V/\partial r\right)$ and $\boldsymbol{r}\times\boldsymbol{p} = \hbar\boldsymbol{l}$.

When a nucleon is moving in the self-consistent field $V(r)$ of the nucleus, the spin-orbit interaction can be chosen by analogy with (D.3), providing an additional dimensional factor $-\lambda$ that is characterizing the magnitude of the spin-orbit coupling.

$$U = -\lambda\left(\frac{\hbar}{Mc}\right)^2\left(\frac{1}{r}\right)\left(\frac{\partial V}{\partial r}\right)(\boldsymbol{l}\bullet\boldsymbol{s}) \tag{D.4}$$

Because of the spin-orbit interaction, the orbital and spin angular momenta $\boldsymbol{l}$ and $\boldsymbol{s}$ of the nucleon are not separately conserved but only the total angular momentum $\boldsymbol{j} = \boldsymbol{l} + \boldsymbol{s}$ of the nucleon conserved. Noting that $2\boldsymbol{l}\bullet\boldsymbol{s} = j(j+1) - l(l+1) - s(s+1)$ the spin-orbit interaction energy of a nucleon in a state with a well-defined value of the total angular momentum can be represented as in the form

$$U = \left(\frac{a}{r}\right)\left(\frac{\partial V}{\partial r}\right) \tag{D.5}$$

where

$$a = \left(\frac{\lambda}{2}\right)\left(\frac{\hbar}{Mc}\right)^2 \times \begin{Bmatrix} l, & \text{for } j = l + \frac{1}{2} \\ -(l+_1), & \text{for } j = l - \frac{1}{2} \end{Bmatrix} \tag{D.6}$$

The Schrödinger equation for the motion of a nucleon in the self-consistent field $V(r)$ in the presence of spin-orbit interaction has the form

$$\left\{-\left(\frac{\hbar^2}{2M}\right)\nabla^2 + V(r) - \left(\frac{a}{r}\right)\left(\frac{\partial V}{\partial r}\right) - E\right\}\Psi = 0 \tag{D.7}$$

The wave function that is the solution of equation (D.7) can be written in the form of product of radial and spin-angle functions

$$\Psi_{nlm} = R_{nl}(r)\zeta_{l(1/2)jm} \tag{D.8}$$

The spin-angle function

$$\zeta_{lsjm} = \sum_{m_l + m_s = m} (lm_l sm_s | jm) Y_{lm_l}(\vartheta, \varphi)\chi_{sm_s} \tag{D.9}$$

is the eigenfunction of a state in which the total angular momentum j and its component m have well defined values. In this state, the squares of the orbital and spin angular momenta, characterized by the quantum numbers l and s, also have well-defined values.

The radial function $R_{nl}(r)$ in the presence of spin-orbit interaction satisfies the

equation

$$\frac{d^2R_{nl}}{dr^2}+\frac{2}{r}\frac{dR_{nl}}{dr}+\frac{2M}{\hbar^2}\left[E_{nlj}-V(r)+\frac{a_{lj}}{r}\frac{dV(r)}{dr}-\frac{\hbar^2}{2M}\frac{l(l+1)}{r^2}\right]R_{nl} \qquad \text{(D.10)}$$

Since the coefficient a_{lj} depends on the value j of the total angular momentum, the degeneracy of the energy levels with respect to j is lifted in the presence of spin-orbit interaction and the nucleon energy levels E_{nlj} depend on three quantum numbers n, l and j.